UNIVERSITY OF Southampton

Faculty of Physical Sciences and Engineering
School of Electronics and Computer Science

# Label-free Single Particle Analysis and Separation

by

**Carlos Honrado**

Thesis for the degree of Doctor of Philosophy

August 2018

**UNIVERSITY OF SOUTHAMPTON**

# ABSTRACT

FACULTY OF PHYSICAL SCIENCES AND ENGINEERING
School of Electronics and Computer Science

Doctor of Philosophy

## LABEL-FREE SINGLE PARTICLE ANALYSIS AND SEPARATION

Carlos Manuel Fernandes Honrado

Analysing and separating single particles are crucial processes in many biomedical applications. Particles (cells) are usually present as heterogeneous populations, and retrieval and analysis of single particles frequently relies on specific biochemical "labels" (which commonly involve expensive and complex protocols). As a result, there is an increasing interest in performing analysis and separation with "*label-free*" methods, *i.e.*, solely relying on the particle's inherent biophysical properties or phenotype, such as size or dielectric properties.

This thesis describes methods for the analysis of human pathogenic organisms using microfluidic impedance cytometry (MIC), a label-free, single-cell analysis technique. The first of these is the water-borne protozoan *Cryptosporidium parvum*. Current detection methods cannot speciate or assess the viability these pathogens. Experiments with MIC revealed both a high degree of discrimination between viable and non-viable parasites, and a high level of discrimination between pathogenic (*C. parvum* and *Giardia lamblia*) and non-pathogenic (*C. muris*) species.

Cells infected with intracellular pathogens, specifically malaria parasite-infected erythrocytes and leishmania-infected macrophages, were also analysed using MIC. By fitting the impedance data with multi-shell models the dielectric properties of erythrocytes and malaria parasites were estimated at various stages of infection. Finally, dielectric analysis of leishmania-infected macrophages at different activation states were also analysed, but these showed little variation in their biophysical characteristics.

Label-free methods for the separation of single particles were also described. This was done using deterministic lateral displacement (DLD), a label-free, size-based sorting technique. This technique was integrated with MIC, permitting single-cell level identification of enriched target cells. The integrated system was used to enrich for the blood dwelling parasites *Trypanosoma cyclops* from a blood sample with high specificity and sensitivity.

In summary, the integration of label-free methods for analysis and separation of rare single particles moves a step forward towards the goal of simpler point-of-care analytical technologies to diagnose and analyse human pathogens.

# List of Contents

# Acknowledgements

I would not be able to be writing these words if it was not for my supervisor, Prof. Hywel Morgan, granting me this opportunity, and for that I am incredibly grateful. Back in 2014, when I made the choice to pursue my PhD at the University of Southampton, I was not fully aware of how lucky I was to get the chance to work with one of the best in the microfluidics and AC electrokinetics fields - I know better now. I must also mention Dr. Daniel Spencer, my co-supervisor, with whom I spent a considerable amount of time discussing results, debugging MATLAB codes or just getting those darn lasers aligned – thank you Dan for your patience and help. The mentoring and guidance of my supervisors throughout this project was invaluable and I am thankful for that.

I was tremendously fortunate to be part of the LAPASO Project, an European consortium that brought together some of the leading research groups in the microfluidics, parasitology and microbiology fields. Thanks to this project I was not only capable of travelling and be part of fascinating scientific projects and discussions, but to meet and socialize with incredible people in a non-scientific environment. I established a priceless network that I am sure will accompany me after the conclusion of my PhD. Out of the fear of missing someone, I will just give a collective "*Thank you*" to everyone that was part of this amazing LAPASO experience.

As the reader will attest, this PhD project was built on a series of collaborations and I must take time to acknowledge everyone involved. From Heriot-Watt University, thank you Dr. Helen Bridle and Dr. John McGrath for reaching out and collaborating on the water-borne pathogens sub-project. I had barely started my PhD and could not feel more helpless when doing the first experiments, but John stuck with me and we managed to accomplish what we set for – thank you for that. From Glasgow University, and partners in the LAPASO Project, thank you Dr. Lisa Ranford-Cartwright and Prof. Michael Barrett for welcoming me in rainy Glasgow and making the experiments on intra-cellular parasites possible. Thank you Clément Regnault and Laura Ciuffreda for sharing with me the grunt work back in Glasgow – one more time-course and I swear I would have quit! Also from the LAPASO Project, thank you Dr. Simone Tanzi, Dr. Wilfred Buesink and Dr. Maciej Skolimowski from Micronit Microtechnologies for receiving me in cold Enschede and helping solve many of the technical issues on my technological integration work. Finally, I must thank fellow LAPASO partners at Lund University: Prof. Jonas Tegenfeldt, Dr. Jason Beech, Dr. Stefan Holm, Bao Dang Ho and everyone else in Jonas Lab. From day one they helped me on everything DLD-related and I am thankful for the valuable discussions we had. They also welcomed me in their lab

and made the work on blood-dwelling parasites possible. A special thank you to Stefan and Bao, who shared with me a lot of sorting-related headaches in the lab – our color-coded "*Team Parasite*" will not be forgotten.

Back in Southampton, I would be negligent if I did not acknowledge all the help and support from everyone in the Centre for Hybrid Biodevices. Whenever I felt lost in the lab, aid was always around the corner and everyone was available to help. I would also like to thank the technical support from Sarah Helps and Ying Tran, whom not only kept the lab from descending into chaos, but also had the time to fabricate my devices in the cleanroom.

On a personal note, I would like to thank all the friends I made in the CHB for making sure that these past four years were everything but boring. Thank you Miguel and Catarina for being a much-needed Portuguese refuge in Southampton, and, specifically, Miguel for being my LAPASO "*partner in crime*". Thank you Antonio, Anna, Josip, Riccardo, Roel, Kri, Paul, Billy, Kai, Yuetao, Victor, Marios, Josh … (the list could go on) for these past years. People came and went, but we always managed to be there for each other, venting on bad lab-days but also celebrating and having fun whenever we felt like it (*Stag's* will always be our second home!).

Last (but definitely not least), I would like to thank my family and friends back in Portugal for all their love and support. I am deeply thankful to my parents for everything they made for me. I know they missed me dearly (with the feeling being reciprocal), but they were always supportive of my choice to move to the UK and provided me with good counselling at all times. I would like to extend my gratitude to my brother, beloved grandmother and the rest of my closest family. Thank you Filipa, for sharing with me most of this journey; your love and extraordinary support will stay with me forever. To all my friends, thank you for your friendship throughout the years. You were always capable of making me feel as if I never really went away. Independently of what the future might bring, I am sure that every holiday back in Portugal will be as if nothing had changed.

And thank you, the reader, for taking time to explore a portion of all the work I put into this PhD. I do hope you find it useful, and that the work I did can help you (even if in a small detail) in your own scientific journey…

The author acknowledges the European Commission through the Label-free particle sorting (LAPASO) ITN project from the People Programme (Marie Curie Actions) of the European Union's Seventh Framework Programme FP7/2007-2013 under REA grant agreement no 607350 ITN for funding this work.

# List of Figures

# List of Tables

# Academic Thesis: Declaration of Authorship

I, Carlos Manuel Fernandes Honrado, declare that this thesis, entitled *Label-free Single Particle Analysis and Separation*, and the work presented in it are my own and has been generated by me as the result of my own original research.

I confirm that:

1. This work was done wholly or mainly while in candidature for a research degree at this University;
2. Where any part of this thesis has previously been submitted for a degree or any other qualification at this University or any other institution, this has been clearly stated;
3. Where I have consulted the published work of others, this is always clearly attributed;
4. Where I have quoted from the work of others, the source is always given. With the exception of such quotations, this thesis is entirely my own work;
5. I have acknowledged all main sources of help;
6. Where the thesis is based on work done by myself jointly with others, I have made clear exactly what was done by others and what I have contributed myself;
7. Parts of this work have been published as:

    i. J. S. McGrath, **C. Honrado**, D. C. Spencer, H. L. Bridle, and H. Morgan, "Microfluidic impedance cytometry for species-level discrimination of waterborne protozoa," in *MicroTAS 2015 - 19th International Conference on Miniaturized Systems for Chemistry and Life Sciences*, 2015;

    ii. **C. Honrado**, L. Ciuffreda, D. Spencer, L. Ranford-Cartwright, and H. Morgan, "Dielectric characterisation and identification of malaria-infected red blood cells using microfluidic impedance cytometry," in *20th International Conference on Miniaturized Systems for Chemistry and Life Sciences, MicroTAS 2016*, 2016;

    iii. J. S. McGrath[†], **C. Honrado**[†], D. Spencer, B. Horton, H. L. Bridle, and H. Morgan, "Analysis of Parasitic Protozoa at the Single-cell Level using Microfluidic Impedance Cytometry," *Sci. Rep.*, vol. 7, no. 1, 2017.

    iv. **C. Honrado**, L. Ciuffreda, D. Spencer, L. Ranford-Cartwright, & H. Morgan, "Dielectric characterization of Plasmodium falciparum -infected red blood cells using microfluidic impedance cytometry," *J. R. Soc. Interface*, vol. 15, no. 147, p. 20180416, 2018.

Signed: .....

Date: .....

# List of Abbreviations

| | |
|---|---|
| µTAS | Micro Total Analysis System |
| AC | Alternating current |
| BMMs | Bone marrow macrophages |
| CAD | Computer aided design |
| *c*-BMMs | Control bone-marrow macrophages |
| CL | Cutaneous Leishmaniasis |
| *c*-RBCs | Control red blood cells |
| CTCs | Circulating tumour cells |
| DAPI | 4'6-diamidino-2-phenylindole |
| DC | Direct current |
| DEP | Dielectrophoresis |
| DLD | Deterministic lateral displacement |
| dpi | Days post-invasion |
| EP | Electrophoresis |
| FACS | Fluorescence-activated cell sorting |
| FCP | Fluidic Connect Pro |
| FITC | Fluorescein isothiocyanate |
| FMIC | Fluorescence-coupled Microfluidic impedance cytometry |
| GFP | Green fluorescent protein |
| HAT | Human African trypanosomiasis |
| *h*-BMMs | Phagocytosed heat-killed parasites bone marrow macrophages |
| HIP | Heat-inactivated *C. parvum* oocysts |
| hpi | Hours post-invasion |
| *i*-BMMs | Infected bone-marrow macrophages |
| IC-DLD | Impedance cytometry- deterministic lateral displacement |
| *i*-RBCs | Infected red blood cells |
| LOC | Lab-on-a-chip |
| MACS | Magnetic-activated cell sorter |
| MEMS | Microelectro mechanical systems |
| MIC | Microfluidic impedance cytometry |
| MMT | Maxwell's mixture theory |
| nDEP | Negative dielectrophoresis |
| PCB | Printed circuit board |
| PCR | Polymerase chain reaction |
| pDEP | Positive dielectrophoresis |
| PDMS | Polydimethylsiloxane |
| PI | Propidium iodine |

| | |
|---|---|
| PoC | Point-of-Care |
| RBCs | Red blood cells |
| RDTs | Rapid diagnostic tests |
| ROT | Electrorotation |
| RPMI | Roswell Park Memorial Institute medium |
| SDS | Sodium dodecyl sulfate |
| TC | Time-course |
| twDEP | Travelling wave dielectrophoresis |
| *u*-BMMs | Uninfected bone-marrow macrophages |
| *u*-RBCs | Uninfected red blood cells |
| UTP | Untreated *C. parvum* oocysts |
| VL | Visceral Leishmaniasis |
| WBCs | White blood cells |
| WHO | World Health Organization |
| YFP | Yellow fluorescent protein |

# List of Symbols

| | |
|---|---|
| $\alpha$ | Polarisability ($F\ m^{-2}$) |
| $\beta$ | Compressibility ($Pa^{-1}$) |
| $\mathbf{\Gamma}_{ROT}$ | Electrorotation torque ($N\ m$) |
| $\delta$ | Transit time ($s$) |
| $\varepsilon$ | Permittivity ($F\ m^{-1}$) |
| $\tilde{\varepsilon}$ | Complex permittivity |
| $\varepsilon_0$ | Vacuum permittivity ($8.85 \times 10^{-12}\ F\ m^{-1}$) |
| $\varepsilon_r$ | Relative permittivity |
| $\eta$ | Dynamic viscosity ($Pas$) |
| $\theta$ | Angle (°) |
| $\lambda$ | Distance between post-centres ($m$) |
| $\Delta\lambda$ | Row shift ($m$) |
| $\Lambda$ | Acoustic wavelength ($m$) |
| $\mu_o$ | Vacuum permeability ($4\pi \times 10^{-7}\ H\ m^{-1}$) |
| $\rho$ | Density ($kg\ m^{-1}$) |
| $\boldsymbol{\rho}_b$ | Bound charge density ($C\ m^{-3}$) |
| $\boldsymbol{\rho}_f$ | Free charge density ($C\ m^{-3}$) |
| $\sigma$ | Conductivity ($S\ m^{-1}$) |
| $\Sigma$ | Peak width |
| $\tau$ | Relaxation time ($s$) |
| $\varphi$ | Volume fraction |
| $\phi$ | Acoustic contrast factor |
| $\chi$ | Susceptibility of the dielectric |
| $\omega$ | Angular frequency ($rad\ s^{-1}$) |
| $a$ | Peak amplitude |
| $A$ | Area ($m^2$) |
| $A_n$ | Depolarising factor |
| $B$ | Magnetic induction ($T\ m^{-1}$) |
| $C$ | Capacitance ($F$) |
| $d$ | Thickness ($m$) |
| $d_{exp}$ | Expected particle size ($m$) |
| $D$ | Diffusion ($m^2\ s^{-1}$) |
| $D_c$ | Critical diameter ($m$) |
| $D_{corr}$ | Corrected estimated particle size ($m$) |
| $D_{est}$ | Estimated particle size ($m$) |
| $D_p$ | Post diameter ($m$) |

| | |
|---|---|
| $\mathbf{D}$ | Electric flux density ($C\ m^{-2}$) |
| $\mathbf{E}$ | Electric field ($V\ m^{-1}$) |
| $\tilde{f}_{CM}$ | Clausius-Mossotti factor |
| $\mathbf{f}$ | Applied force ($N$) |
| $F_{acoustic}$ | Acoustic force ($N$) |
| $F_D$ | Dean drag force ($N$) |
| $\langle \mathbf{F}_{DEP} \rangle$ | Time averaged dielectrophoretic force ($N$) |
| $F_H$ | Hydrodynamic force ($N$) |
| $F_L$ | Lift force ($N$) |
| $F_m$ | Magnetic force ($N$) |
| $G$ | Post gap distance ($m$) |
| $h$ | Channel height ($m$) |
| $\tilde{I}$ | Electrical current ($A$) |
| $k_B$ | Boltzmann's constant ($1.38\times10^{-23}\ J\ K^{-1}$) |
| $\widetilde{K}_n$ | Polarisability magnitude ($F\ m^{-2}$) |
| $L$ | Length scale of system ($m$) |
| $N$ | Post period |
| $p$ | Pressure ($Pa$) |
| $\Delta P$ | Pressure difference ($Pa$) |
| $\mathbf{p}$ | Dipole moment ($C\ m$) |
| $Pe$ | Péclet number |
| $P_0$ | Acoustic pressure ($Pa$) |
| $q$ | Ratio of ellipsoid semi-axis |
| $Q$ | Fluid flow rate ($m^3\ s^{-1}$) |
| $r$ | Particle radius ($m$) |
| $\langle r_{diffusion} \rangle^2$ | Diffusion displacement |
| $R$ | Resistance ($\Omega$) |
| $Re$ | Reynolds number |
| $R_h$ | Hydrodynamic resistance ($Pa\ s^{-1}\ m^3$) |
| $t$ | Time ($s$) |
| $t_c$ | Individual signal centre |
| $T$ | Temperature ($K$) |
| $\widetilde{U}$ | Complex signal ($V$) |
| $\mathbf{v}$ | Velocity ($m\ s^{-1}$) |
| $V_{particle}$ | Particle volume ($m^3$) |
| $\Delta x$ | Difference in magnetic susceptibility |
| $w$ | Channel width ($m$) |
| $Z$ | Impedance ($\Omega$) |

# Chapter 1

# Introduction

## 1.1 Motivation

Characterization, separation and sorting of particles underpins many biomedical applications. Cell sorting is commonly used to enrich for cell types into well-defined populations, which can be used as the first step in many diagnostic and therapeutic practices. Often, the particles or cells of interest are present in heterogeneous populations, either in culture, tissue or suspension. Techniques to retrieve and analyse valuable single cells usually rely on methods requiring specific "labels", usually by attaching magnetic particles or fluorescent tags, to identify and retrieve the desired cells. This labelling process could have secondary effects on the viability of labelled cells, limiting their post-sorting utilisation. Label-based sorting methods are frequently complex and lengthy processes. Moreover, the labels used are costly materials, which are impeditive for many clinical settings in impoverished regions.

Thus, the need for label-free alternatives is increasing, with recent approaches taking advantage of the intrinsic biophysical properties of cells. Furthermore, the scale of microfluidic systems provides an optimal interface for manipulating single cells and harness these intrinsic properties for analysis and separation. Therefore, there is a growing interest in exploring microfluidic techniques to manipulate and analyse single particles in a label-free fashion. The main goal of this project is to develop label-free methods for analysing and sorting rare single particles. The progress towards this objective is presented, starting with a brief introduction to the core aspects behind the project.

### 1.1.1 Biological particles

Many of the biomedical processes performed in research laboratories, clinical environments and even industrial setups can be broken down to successive analysis and decomplexing steps, where the constituent parts or particles are counted,

separated and retrieved from usually heterogeneous mixtures. These biomedical decomplexing and analysis processes can be applied to break down a wide variety of biological samples and particles that make up living systems, ranging from entire micro-organisms and single cells to simpler (but smaller) DNA strands or proteins (**Figure 1.1**). One of the best examples of such a biological sample is human blood, probably one of the most widely used source of diagnostic information. By breaking down a blood sample to its various constituents, it is possible to determine whether the different blood cell types are found at correct concentrations and even if pathogenic foreign bodies (as parasites) are present.

Decomplexing of biological samples is usually possible as long as there are significant differences in the biophysical properties of the particles to sort. Alternatively, specific "labels" can artificially generate these differences. Examples of intrinsic characteristics used for separation are size, volume, shape, deformability, density, magnetic susceptibility or dielectric properties. Size and density are prime examples of properties that have been used to identify and separate cells, *e.g.* size or deformability-based filtration methods to identify pathogenic cells (Cranston *et al.*, 1983; Nash *et al.*, 1989; Athanassiou *et al.*, 2010; Suresh, 2010). Particle size cannot be simplified to a given diameter value, as many biological cells have complex shapes. A good example is the red blood cell characteristic discoid shape, which can be altered due to disease states (Turchetti *et al.*, 1997), genetic conditions (Barabino, Platt and Kaul, 2010) or drugs (Sheetz and Singer, 1976), for example, without a significant alteration in its apparent size/volume. Thus, when considering single cell separation methods all the different properties of the particles must be considered.

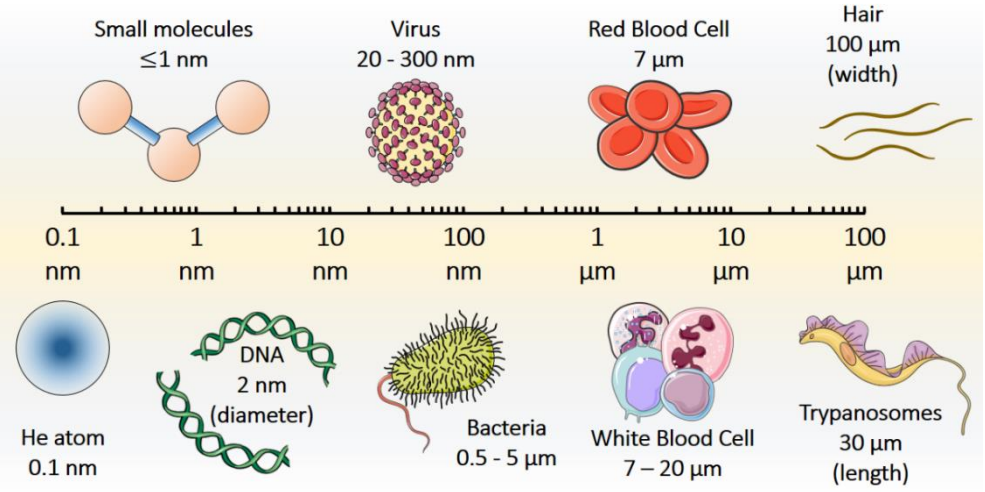


**Figure 1.1:** Sub-millimetre biological particles cover a wide range of sizes and shapes, ranging from small molecules and DNA strands to larger blood cells and parasites.

### 1.1.2 Separation of single particles

Separation is usually a central aspect of many analytical processes performed for clinical analysis or diagnostics. It is not uncommon for the targets of separation and detection to be found at extremely low concentrations in highly complex samples. An example of this is the arduous process of detecting parasites or parasite-infected cells in a blood sample. These can be at concentrations of <1 per µL, while red blood cells are found at ~5 million per µL (Chappuis *et al.*, 2005). The same issue can be found when dealing with other types of rare cells, such as circulating tumour cells or skeletal stem cells.

Existing microfluidic separation techniques can be approximately divided into active and passive methods (Bhagat *et al.*, 2010; Lenshof and Laurell, 2010; Wyatt Shields IV, Reyes and López, 2015). Active methods rely on the application of external forces and fields, such as electrical and magnetic fields, to perform separation. On the other hand passive methods rely simply on microfluidic phenomena and the interactions between particles and the forces that occur as samples flow through the device.

However, separation is not limited to decomplexing of complex samples and should, in many cases, be considered an analytical method per se. While the aim of a separation method could be to simplify a mixture of particles for further analysis, in other cases the separation method infers the ability to identify and analyse the sorted particles. Examples of this would be the sorting of particles based on their intrinsic magnetic or dielectric properties, where the act of separating particles is in itself an analytic process, which could be used to measure specific properties and even quantify changes in that property.

### 1.1.3 Analysis of single particles

In other biomedical processes, decomplexing is not a requirement as long as it is possible to quantify and analyse the particles in the biological sample. For example, the enumeration of different blood cells is used to help diagnose different medical conditions, such as anaemia or pneumonia, and to infer other health conditions such as leukaemia. However, this requires the processing and analysis of large numbers of particles in ideally a short period of time. Current analysis methods include the haemocytometer, considered the reference cell counting method. In this method, single cells are counted directly using microscopy while they are trapped in a transparent chamber of fixed volume. The fact that counting is

performed manually potentially introduces human errors and is slow process, resulting in long turnover times for analysis of a samples and rare cell detection is difficult.

An alternative analysis method is flow cytometry, where individual particles flow in a liquid medium through a detection region. Properties of single particles are measured in this detection region usually using light- or electrical-based methods. The optical flow cytometry is an example of a light-based approach, making use of fluorescence and optical properties to identify and count single particles (Shapiro, 2003). Particles of interest are usually fluorescently labelled, often with antibodies conjugated to fluorescent molecules. The particles flow through a narrow detection region through a sheet of light from a focused laser beam. By detecting fluorescent and scattered light at different angles, the size, granularity and surface markers of individual particles can be measured. While having high throughput (up to 100,000 cells/s), optical flow cytometers are large and expensive systems, thus limiting their applicability in resource scarce regions of the globe.

An example of an electrical flow cytometer is the Coulter counter (Coulter, 1956). In this technique, particles suspended in an electrolyte pass through an aperture between two reservoirs, each containing a measurement electrode. By applying a voltage between the two electrodes and measuring the resultant current, it is possible to detect single particles as they transverse the apertures and reduce the current flow. This change in current is proportional to particle volume and thus single particles can be counted and sized. Microfluidic impedance cytometry, a technique for single cell analysis and characterization, is based on this same principle and will be thoroughly explored later in this thesis. Due to its implementation in a microfluidic context, the impedance-based flow cytometry technique is naturally smaller and simpler than conventional optical cytometry, offering an alternative for low-cost single cell analysis and characterization and being an ideal candidate for future Point-of-Care (PoC) diagnostics.

### 1.1.4 Point-of-Care Testing

The development of novel devices capable of performing Point-of-Care (or PoC) testing or diagnostics is the objective of much of the research conducted in the microfluidics field. PoC diagnostics would allow the quick detection of health issues using a device that is close to the patient, independent of the location and without extensive laboratory testing (Linder, 2007; Sia and Kricka, 2008; Sorger, 2008). Existing PoC tests include urine pregnancy tests, blood glucose level tests for

diabetics, blood cholesterol tests and even HIV and syphilis diagnosis (Chin *et al.*, 2011). PoC tests offer the possibility to quickly perform tests near a patient's bed in a hospital, at the patient's home for continued monitoring or even in the field, like disease-stricken rural areas of impoverished nations. Without PoC tests samples must be directed to a clinic or laboratory for testing which usually takes a long time for the return of results, causing a delay in treatment that can be critical for the patient. PoC testing and diagnosis could greatly minimise this issue, holding the potential to transform the health care industry, especially in the developing world where these waiting periods for results can extend to days (Yager *et al.*, 2006). By creating low cost and portable PoC systems, a new paradigm of personalized medicine, adapted precisely to each patient, can be put to practice. This has the potential to speed up treatment, reduce misdiagnosis occurrence and decrease the overall health costs for governments and patients.

## 1.2 Objective

The main goal of this project is to develop label-free methods for analysis, characterization and sorting of rare particles. Rare particles of particular interest are human pathogens (or pathogen-infected cells) such as waterborne pathogenic protozoa, malaria parasite-infected red blood cells, leishmania parasite-infected macrophages and blood dwelling parasites (trypanosomes).

Microfluidic impedance cytometry is used to analyse the dielectric properties of single particles at high throughput. The overarching goal of implementing this technique is to explore whether different cell conditions and characteristics (*e.g.*, viability, species or parasitization) can be identified by alterations in the cell dielectric properties and therefore used as an alternative detection method. If identifiable, this technique could then be implemented as a future PoC testing system for the various rare cells.

Particle separation is performed using deterministic lateral displacement. The separation process is based on particle size and permits the sorting of different cell types by their size and shape. The latter was explored to enrich for blood-dwelling parasites. One of the goals of this project is to develop a sample-to-answer system for PoC field detection. This was explored by integrating single cell sorting and analysis in a single device using the two techniques previously mentioned.

## 1.3 Thesis Outline

The thesis structure has the following outline:

**Chapter 1** introduces the motivation and background of the research project, and highlights the main subject areas of the research conducted.

**Chapter 2** outlines the theory of microfluidics and the behaviour of particles in fluids. It then explores some of the most relevant label-free microfluidic techniques for single particle sorting.

**Chapter 3** presents an overall, theoretical background to the field of AC Electrokinetics along with descriptions of some of the available characterisation and sorting techniques within this field, with special emphasis on microfluidic impedance cytometry.

**Chapter 4** describes efforts made to perform viability and species level discrimination of water-borne pathogens from the *Cryptosporidium* and *Giardia* genus using impedance cytometry.

**Chapter 5** discusses the dielectric studies performed on cells parasitized by intra-cellular parasitic protozoa using fluorescence-coupled impedance cytometry. The dielectric properties of malaria parasite-infected RBCs are modelled for the different parasitic stages of the disease. Leishmania parasite-infected macrophages were also dielectrically analysed.

**Chapter 6** starts with a brief introduction to the theory of DLD, followed by the initial trials conducted to integrate this technology with AC electrokinetics. The first results of an integrated device are presented and the Chapter concludes with the sorting and identification of blood dwelling parasites in blood samples using an optimized integrated system.

# Chapter 2

# Label-free Microfluidics

## 2.1 Introduction

When in 1979 photolithography was used for the first time to fabricate an operational chromatograph on a silicon wafer (despite being three orders of magnitude smaller than its conventional industrial homologous), the first steps into the miniaturisation of electro-mechanical systems was taken (Terry, Jerman and Angell, 1979). The successful miniaturisation of other systems during the 1980s gave rise to what was termed MEMS (micro electro mechanical systems). With the field constantly expanding, the applications of MEMS eventually encompassed the handling of fluids for chemical, biological and biomedical functions. In 1990, Manz proposed the integration of modules with these capabilities into a single chip: the Micro Total Analysis System, or μTAS, was born (Manz, Graber and Widmer, 1990). With almost 30 years passed since, much work has been done on the development of numerous microsystems, with the paradigm slowly changing from μTAS to a broader notion of "Lab-on-a-chip" (LOC) systems. As the name suggests, the technological focus of LOC systems not only includes the biochemical analysis of samples but also includes the miniaturization in a microchip of many other chemical, biological or physical processes currently performed in laboratory conditions (*e.g.* the separation of single particles based on size or surface labels).

The miniaturization and diversification of the various processes involved in μTAS/LOC logically gave rise to the field of Microfluidics: a crossroad of science and engineering, defined as the study of flows circulating in artificial microsystems (Tabeling and Chen, 2005; Nguyen and Wereley, 2006). The characteristic small dimensions of microfluidic systems allow the generation of predictable and stable flow regimes, permitting a precise sample control at the microscale (the scale of a typical biological cell, for example) (Beebe, Mensing and Walker, 2002). The advantages of miniaturization arising from microfluidics include increased portability, speed, resolution, automation and parallelization capabilities (Craighead, 2006; Dittrich and Manz, 2006; Mark *et al.*, 2010; Mosadegh *et al.*, 2011). Consequently, microfluidic systems have been extensively applied to

various fields including chemical analysis, biotechnology and medical science (Nguyen and Wereley, 2006). Being at the core of the single particle analysis and separation technologies an understanding of the underlying microfluidics principles is necessary and will be presented first.

## 2.2 Microfluidics Principles

Fluids at the macro scale are part of the daily life of any person, with knowledge from how to handle them arriving mostly from experience. For example, fluids can be moved through body forces such as gravity (picture a raindrop falling), shear forces causing viscosity or normal forces such as pressure (visualise a stone dropped in a pool). From these effects, inertial effects dominate fluid flow on the macro scale. However, at the micrometre scale of microfluidic devices, the situation is quite different. As inertia becomes almost negligible and viscous forces govern flow, many physical phenomena that have a lesser influence at macro scale begin to rise in prominence at the micro scale. Thus, effects such as laminar flow, diffusion, surface tension and resistance have a greater impact on the fluidics in microchannels. In this section, the theory describing these effects is presented, (Nguyen and Wereley, 2006; Bruus, 2008; Hauke, 2008).

### 2.2.1 Fluid flow characteristics

A fluid is defined as a substance which continually deforms under the action of shear stress, and thus the notion of describing its motion through a centre of mass must be rejected. Instead, one must consider it as a continuous medium rather than a discrete mass. Consequently, fluids are better described in terms of continuous fields and not with discrete values. These notions can be used to describe the local density of the fluid, which obeys the conservation of mass, *i.e.*, the change of mass rate, in a certain volume, is equal to the flux of mass through the surface enclosing the volume. The continuity equation can then be written as:

$$\frac{d\rho}{dt} + \rho\nabla \cdot \mathbf{v} = 0 \qquad (2.1)$$

here $\mathbf{v}$ is the velocity of the fluid and $\rho$ the mass density. However, assuming an incompressible fluid where $\rho$ is constant in both time and space, the equation for the continuity or conservation of mass can be simplified to:

$$\nabla \cdot \mathbf{v} = 0 \qquad (2.2)$$

### 2.2.2 The Navier-Stokes equation and the Reynolds number

The Navier-Stokes equation describes the motion of fluids:

$$\rho\left[\frac{\partial v}{\partial t} + (\mathbf{v}\cdot\nabla)\mathbf{v}\right] = -\nabla p + \eta\nabla^2\mathbf{v} + \mathbf{f} \qquad (2.3)$$

where $p$ is the pressure, $\eta$ is the dynamic viscosity and $\mathbf{f}$ is the applied body force. In this equation, inertial terms are located on the left while force terms are on the right. Inertial terms correspond to both the "local" acceleration $(\partial\,\mathbf{v}/\partial t)$, describing changes at a fixed point; and convective acceleration $\left((\mathbf{v}\cdot\nabla)\mathbf{v}\right)$, describing changes along the movement. Force terms consist of the pressure gradient $(-\nabla p)$, the viscous effects $(\eta\nabla^2\mathbf{v})$, and other forces acting on the fluid $(\mathbf{f})$, as gravity or electrical forces.

Due to the presence of the convective acceleration (a non-linear term) in the formula, an analytical solution is generally not feasible to obtain. As an alternative, the equation can be simplified based on the assumption that conditions found at the small scale of microfluidic devices are used. For instance, the inertial terms can be represented in the form:

$$F_{inertial} \propto \rho\mathbf{v}\frac{\partial\mathbf{v}}{\partial t} \qquad (2.4)$$

If this is extended to a measure of flow inertia, it can also be expressed in terms of a characteristic, or average, velocity $(V)$ and characteristic, or length scale of system, length $(L)$:

$$F_{inertial} \rightarrow \rho\frac{V^2}{L} \qquad (2.5)$$

Using the same process, the viscous effects can be represented in the form:

$$F_{viscous} \propto \eta\frac{\partial^2\mathbf{v}}{\partial x^2} \qquad (2.6)$$

which can similarly be defined in terms of $V$ and $L$:

$$F_{viscous} \rightarrow \eta\frac{V}{L^2} \qquad (2.7)$$

The ratio of inertial and viscous forces can be defined by the ratio of **Equations 2.5** and **2.7**:

$$\frac{F_{inertial}}{F_{viscous}} = \frac{\rho LV}{\eta} \equiv Re \qquad (2.8)$$

$Re$ is a dimensionless number named Reynolds number and describes the relationship between the two forces acting in a moving fluid. If $Re \ll 1$, the viscous terms dominate the dynamics of the fluid, while for $Re \gg 1$ the inertial terms dominate. In the case of microfluidic systems, the length scale is typically ~$10^{-4}$ m, the characteristic velocity is in the ~$10^{-2}$ - $10^{-3}$ m/s range, and, given that aqueous solutions are commonly used, $\rho$=$10^{3}$ kgm$^{-3}$ and $\eta$=$10^{-3}$ kgm$^{-1}$s$^{-1}$. $Re$ is then of the order 0.1 – 0.01, where viscosity dominates, and the fluid is said to be in the viscous limit. In practical terms, if a fluid is moving under an applied pressure or force, when such external force stops the fluid is expected to stop immediately as well. **Equation 2.3** can then be simplified to represent the fluid velocity:

$$\rho \frac{\partial \mathbf{v}}{\partial t} = -\nabla p + \eta \nabla^2 \mathbf{v} + \mathbf{f} \qquad (2.9)$$

### 2.2.3 Laminar Flow

In microfluidic systems, the microchannels used to guide the fluid throughout the device have dimensions in the order of ~10 μm to 1 mm. At this scale, the fluid flow will be characterised by a low $Re$ and have a laminar profile, *i.e.*, it follows distinct streamlines, and free of turbulence. A good example is to consider two fluids flowing in independent channels that meet at a Y-shaped intersection. If both arrive at the intersection in a laminar flow, the two fluids will continue to flow next to each other without total mixing (since no turbulence is present). If no other force is applied, the only transport between the two flows would be due to diffusion (later discussed), forming an uniform interface with mixed fluids.

Another aspect to consider in a laminar flow is the velocity profile. Since there are viscous forces present in the system, a viscous drag will be present at the microchannel walls, making the flow velocity zero at those points; a condition known as no-slip boundary. As the flow distances from the wall, the viscous drag effect reduces. Thus, at the centre of the channel, the point furthest from the walls, the velocity has its maximum value. The end result is a parabola-shaped flow profile between the two parallel walls. This steady-state flow is also referred to as Poiseuille flow.

### 2.2.4 Hydrodynamic Resistance

The influence of microchannel geometry is not limited to defining the expected $Re$ or the fluid flow velocity profile. The parameters of channel length, cross sectional shape and pressure gradient across the microchannel define the hydrodynamic resistance, ($R_h$) to the liquid. Depending on this resistance and the pressure difference ($\Delta P$) applied across the microchannel it is possible to calculate the resultant fluid flow rate, $Q$:

$$Q = \frac{\Delta P}{R_h} \tag{2.10}$$

Microfluidic devices usually have channels and sections that can be closely approximated to a rectangular-shaped microchannels. For these type of channels, a simplified formula, derived by Bruus (2008), can be used:

$$R_h = \frac{12\eta L}{wh^3}\left[1 - \frac{h}{w}\left(\frac{192}{\pi^5}\sum_{n,odd}^{\infty}\frac{1}{n^5}\tanh\left(\frac{n\pi w}{2h}\right)\right)\right]^{-1} \tag{2.11}$$

where $w$ is the channel width and $h$ its height. For a cross section where $w \gg h$, the expression can actually be further simplified to:

$$R_h = \frac{12\eta L}{wh^3} \tag{2.12}$$

In the cases where the cross sections is closer to a square shape, a rough numerical estimate gives:

$$R_h \approx \frac{29\eta L}{w^4} \tag{2.13}$$

For other cases, an approximation to **Equation 2.11** can usually be used without much error:

$$R_h = \frac{12\eta L}{wh^3}\left[1 - 0.63\,\frac{h}{w}\right]^{-1} \tag{2.14}$$

If for instance, $w = 2h$ the error is only 0.2%, while for $w = h$ the error escalates to 13%. However, since obtaining perfectly rectangular microchannels is quite difficult fabrication-wise (corners come usually rounded or the sidewalls not exactly parallel), a certain error is always associated with any calculation.

### 2.2.5 Diffusion

Due to the micrometre scale of microfluidic devices, diffusion needs to be taken into consideration when designing a system. It is caused by the Brownian motion of particles, *i.e.*, the random movement originated from collisions with atoms and molecules in the fluid. The movement caused by such motion can be quantified in terms of the mean square of displacement ($\langle r_{diffusion} \rangle^2$) and is given by:

$$\langle r_{diffusion} \rangle^2 = 2nDt \qquad (2.15)$$

with $n$ denoting the number of dimensions to consider, $D$ being the diffusion constant and $t$ the time. This diffusion constant is, in turn, given by the Stokes-Einstein equation:

$$D = \frac{k_B T}{6\pi r \eta} \qquad (2.16)$$

where $k_B$ is Boltzmann's constant, $T$ is the absolute temperature and $r$ the radius of the particle.

Usually diffusion is regarded as factor to consider when the sample consists of particles on the size scale of 1 µm, however even for larger particles (up to 10 µm, for instance) it can be an interfering effect. This is clearly visible if the microfluidic application requires a long residence time of the particles in the device or channel, as it is the case of batch mode analysis, where the diffusion effect is increased.

### 2.2.6 Convection

In microfluidics, convection is related to the transfer of mass that happens due to fluid movement, *i.e.,* the transport of suspended molecules in flow. The Péclet number ($Pe$) is a dimensionless number that expresses the ratio of rates of convection and diffusion of particles, being estimated by:

$$\frac{diffusion\ time}{convection\ time} = \frac{L^2/D}{L/V} = \frac{LV}{D} \equiv Pe \qquad (2.17)$$

If $Pe$ is high, convection exceeds diffusion, which limits the mixing of fluids. In microfluidic channels, the $Pe$ is usually high over the length of the channel and the stream remains well defined. This effect, together with the typical low $Re$ found in microchannels, results in long mixing time for fluids and a high predictability of the fluid flow (Squires and Quake, 2005). In certain microfluidic techniques, such as deterministic lateral displacement, it is essential that high Péclet numbers are achieved since individual streams must be generated within the device and maintained without blurring due to diffusion.

## 2.3 Label-free Separation Methods

Until recently, conventional cell sorting methods relied on molecular markers on the cell surface. These molecules, if specific to a certain cell type, can be used to achieve separation. Ion exchange columns are used to attract particles to surfaces by surface charge and perform separation of for example parasites (of the *Trypanosoma* genus) from blood cells (Lumsden, Kimber and Strange, 1977; Lumsden *et al.*, 1979). Custom labelled surfaces can also be used to adhere cells based on surface markers and enrich specific cell types (Didar and Tabrizian, 2010). Alternatively, the particles could be labelled with biomolecules which would induce differences in their physical properties and can be used for identification or separation. Some of the most common labels used are antibodies as they can be highly specific to target cell types and are easily attached to fluorescent or magnetic markers. For example, fluorescence-activated cell sorting (FACS) separates particles accordingly to their fluorescent labelling by the application of electric fields (Boeck, 2001; Johnson, Dooner and Quesenberry, 2007). Another case is magnetic-activated cell sorting (MACS), where superparamagnetic nanoparticle labels allow separation of target cells from a bulk population using strong magnetic fields (Grützkau and Radbruch, 2010). While effective at separating cells based on very specific properties, the labelling process might have secondary negative effects on the viability of labelled cells. This could be a major drawback in cases where the sorted cells are aimed for culturing or therapeutic use. Furthermore, label-based sorting methods are usually lengthy processes, with labelling being a complex and costly process.

By contrast, "label-free" methods function by harnessing physical biomarkers of particles to perform sorting, *i.e.,* the separation force/action is dependent on the difference in inherent physical properties of the particles. These methods do not require additional labelling steps and are generally cheaper and simpler, and eliminate secondary effects from labels on sorted cells. Commonly utilized biomarkers are size, shape, density, deformability, polarisability, dielectric properties, hydrodynamic properties or magnetic susceptibility. Additionally, for separation of a particle of interest from a population to be possible, such biomarkers must be coupled to a fractionation method or sorting method. Some recent reviews highlight the various existing techniques, their benefits and limitations (Gossett *et al.*, 2010; Wyatt Shields IV, Reyes and López, 2015; Huang *et al.*, 2017; Liu and Hu, 2017). Hence, some of the possible methods currently available will be discussed in the following sub-sections.

### 2.3.1 Acoustophoresis

Acoustophoresis is the induced movement of particles in response to an acoustic pressure wave. Recently, application of acoustic forces in microfluidic schemes led to the development of new techniques for cell sorting. The use of acoustic forces for cell separation is possible since they allow a rapid and precise spatial control of cells within microfluidic devices without affecting the viability of the cells (Laurell, Petersson and Nilsson, 2007; Lenshof, Magnusson and Laurell, 2012; Burguillos *et al.*, 2013). The core principle of acoustophoresis takes advantage of pressure gradients resulting from the application of ultrasonic standing waves. The applied acoustic force $F_{acoustic}$, the ultrasound wavelength $\lambda$ and pressure amplitude $P_0$ are described by (Hawkes and Coakley, 2001; Laurell, Petersson and Nilsson, 2007; Petersson *et al.*, 2007):

$$F_{acoustic} = -\left(\frac{\pi {P_0}^2 V_{particle} \beta_{medium}}{2\Lambda}\right) \phi(\beta, \rho) \sin\left(\frac{4\pi x}{\Lambda}\right) \quad (2.18)$$

$$\phi(\beta, \rho) = \frac{5\rho_{particle} - 2\rho_{medium}}{2\rho_{particle} + \rho_{medium}} - \frac{\beta_{particle}}{\beta_{medium}} \quad (2.19)$$

The strength of the acoustic force depends on three main properties: the volume of the particle $V_{particle}$ and its distance $x$, to a pressure node; the relative compressibility $\beta$, of the medium (with most microfluidic systems using a liquid medium as the working fluid) and particle; and the relative density $\rho$, of the medium and particle.

Differences in compressibility and density between particles and medium result in an acoustic contrast factor $\phi$ (**Equation 2.19**) (Kapishnikov, Kantsler and Steinberg, 2006; Laurell, Petersson and Nilsson, 2007; Lenshof, Magnusson and Laurell, 2012). Particles with differing contrast factors may be separated by being concentrated in different locations within the microchannel. Typically, acoustophoresis systems create a single pressure node at the centre of the microchannel (Lenshof and Laurell, 2011). Thus, if $\phi$ is positive (as the case for most solid particles and cells in aqueous conditions), particles will move to pressure nodes, *i.e.*, regions were the pressure change is zero, at the centre of the microchannel. If $\phi$ is negative (as in air bubbles or oil droplets, for instance), particles move to pressure antinodes where maximum pressure change occurs, near the microchannel walls (Lenshof and Laurell, 2011). After the separation of particles separation can be accomplished by collecting each section of the flow (**Figure 2.1a** and **b**).

In the case where particles have similar contrast factors, separation can also be performed based on the particle size. Bigger particles will feel a stronger force ($F_{acoustic} \propto V_{particle}$) and, when displacing, will be aligned into different positions within the microchannel, allowing for the collection of particles at different outputs (**Figure 2.1c** and **d**) (Petersson *et al.*, 2007; Lenshof and Laurell, 2011; Lenshof, Magnusson and Laurell, 2012).

Petersson *et al.* presented in 2007, a device capable of performing separation of polymer beads and cells of different properties using free flow acoustophoresis. Depending on the volume, density, compressibility or a combination of these properties, different particles were successfully aligned and sorted within the microchannel (**Figure 2.1c** and **d**). The system was used to separate white blood cells (WBCs), red blood cells (RBCs) and platelets. Collections of pure samples comprising 79% of platelets, 86% of RBCs, and 92% of WBCs were attained. By optimizing this technique, it would be possible to enrich different blood components, creating concentrates of the different cells. Modern transfusion therapy, for instance, requires leukocyte-depleted concentrates of platelets, with high purity and yield, processed in a cost-effective manner. Acoustophoresis is a possible solution to tackle these needs.

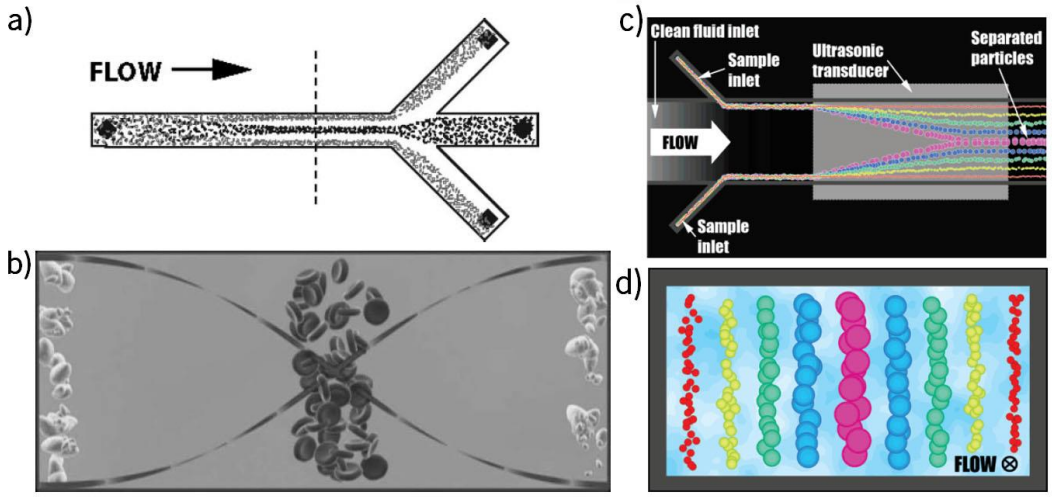


**Figure 2.1:** **a)** Acoustic separation of positive $\phi$-factor particles (black) from negative $\phi$-factor particles (grey). **b)** Cross-section, from dashed line in **a)**, illustrating the particle separation within the microchannel, with positive $\phi$-factor particles (erythrocytes in this example) collected at the pressure node and negative $\phi$-factor particles (lipid particles in this example) concentrated in the pressure antinodes by the microchannel walls. **c)** Acoustic separation of particles based on their size, with particles being moved toward the centre at a rate increasing with their size. **d)** Cross section view, after the ultrasonic transducer, where the particles attained a stable position within the microchannel and will be sorted based on this. **a)** and **b)** adapted from Laurell *et al.* 2007. **c)** and **d)** adapted from Petersson *et al.* 2007.

### 2.3.2 Deterministic Lateral Displacement

In 2004, Huang *et al.* reported a new microfluidic sorting technique called deterministic lateral displacement (DLD), which was capable of efficiently sorting particles based on size. It is a continuous flow sorting technique and has been applied for various particle and cell sorting. Some if its main advantages are having a 20 nm minimal separation size (Wunsch *et al.*, 2016) and a resolution in the order of 2% of the particle size, ideal for sorting microscale bioparticles of close size (Huang *et al.*, 2004; Morton *et al.*, 2008). In this technique, control over sorting is deterministically decided by the design of an array of features (usually circular posts) throughout the device. Depending on the geometry of the array, particles that are smaller than a predefined critical size follow the flow streamlines, while larger particles are laterally displaced and move in a direction predefined by the array, as presented in **Figure 2.2**. The critical particle size for separation is dependent on the gap between posts and their offset.

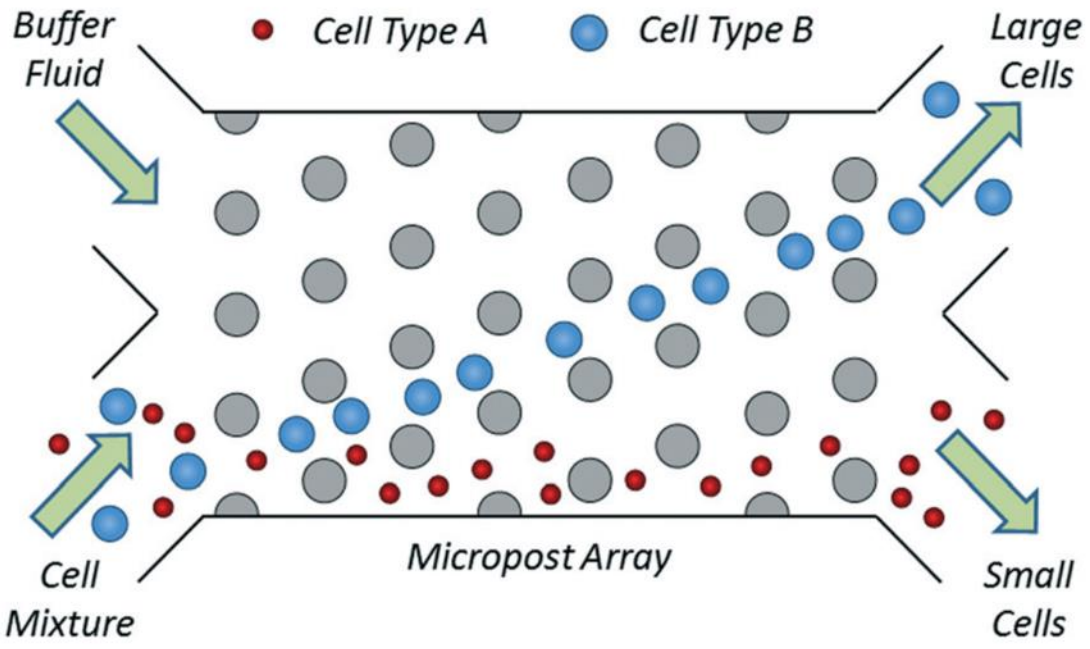


**Figure 2.2:** Illustration of the separation principle of DLD. Usually, a sample containing the cells to sort and a buffer for sheath flow are introduced at the inlets. As a small particle (cell type A) interacts with the post it is capable of following the fluid flow, while a large particle (cell type B) will be laterally displaced and move at a predefined migration angle. These effects result in larger cells to be collected at a different outlet than smaller cells. Adapted from Wyatt Shields IV, Reyes and López, (2015).

Due to its scalability and adaptability to different size-ranges of particles, DLD has already been used for multiple applications, from sorting (un)diluted whole blood samples to retrieval of WBCs, RBCs and platelets; to isolating cancer cells or even human pathogens such as trypanosomes or bacteria (summarised by McGrath *et al.* in 2014). Besides purely size-based sorting, it has been shown that shape and deformability can also be harnessed to perform separation in a DLD device (Beech *et al.*, 2012), Moreover, coupling of other external forces (such as electrokinetics) can also enhance the sorting capability (Beech, Jönsson and Tegenfeldt, 2009), which could be an interesting factor to explore. DLD will be thoroughly discussed later on this thesis (**Chapter 6**).

### 2.3.3 Electrokinetics

Electrokinetics refers to a family of mechanisms originating from the interaction of particles or cells with an applied electric field and the resultant particle movement (Voldman, 2006). These interactions can be explored in various ways, and are dependent on the type of electric field applied and how it is integrated in the microfluidic device. In the case of a DC field, motion is due to electrophoresis (EP). In this technique, particles are attracted to an oppositely charged electrode, and since most cells possess a minor negative charge on their membrane (due to a mosaic of chemical groups in their surface, *e.g.*, glycoproteins, carbohydrates or glycolipids), they are attracted to a positive electrode, allowing separation from other positively charged particles (Voldman, 2006).

In contrast to EP, dielectrophoresis (DEP) refers to the motion of particles in a non-uniform electric field, AC field based on their polarisability. Unlike the case of EP, the particles do not need to possess a significant surface charge, as the field induces a dipole moment across the particle, polarizing it (Voldman, 2006; Pethig, 2010). As particles are exposed to the AC field, they will move either toward or away from the region with higher electric field strength depending on their polarisability. Particles more polarisable than the medium migrate towards the high field strength region, termed positive DEP. Contrastingly, if the medium is more polarisable particles are repelled from the regions of high AC field strength, termed negative DEP. By controlling the AC field frequency and the medium properties, sorting of particles with different DEP responses can be achieved. DEP will be further discussed in detail in **Chapter 3**.

### 2.3.4 Inertial Focusing

In microfluidic devices it is usually assumed that flow is laminar and particles will follow fluid streamlines. There is a large range of flow rates used in microfluidic devices, and when working at the higher end, Reynolds numbers are typically 1 - 100 $Re$ and inertial effects cannot be neglected (Segré and Silberberg, 1961). Instead, particles that were initially randomly dispersed will concentrate in a narrow region, around 0.6 times the channel radius (for a circular channel), due to lift forces ($F_L$) acting on the particles (Di Carlo, 2009).

The lift caused by these inertial forces come from the interplay of boundary effects of fluid flowing near the microchannel walls and the parabolic flow profile. These effects are more prominent if curved microchannels are used, hence the high number of applications based on serpentine or spiral designs (Di Carlo, 2009). In these curved channels a second inertial effect arises due to the higher momentum of fluid at the microchannel centre which displaces lower momentum fluid near the channel walls. The result is the creation of counter-rotating vortices, perpendicular to the primary flow direction, generating a secondary flow within the channel termed Dean flow. This gives rise to a secondary force on the particles called a Dean drag force ($F_D$). Interplay between this force and the lift force in curved microchannels can be exploited for size-based sorting, as initially randomly distributed particles will, above a certain critical size, migrate to specific equilibrium positions (Di Carlo, 2009; Russom *et al.*, 2009).

It was demonstrated that cells could be differentially focused and sorted using a laminar flow in a serpentine design, as seen in **Figure 2.3a** and **b** (Di Carlo *et al.*, 2007). This method had high throughput (approximately 1.5 mL/min) without needing sheath flow, making it very appealing for rare cell sorting (where large amounts of sample must be used). Likewise, spiral designs were proposed to focus and sort cells, taking advantage of the differential focusing observed within the channel, *i.e.*, cells will focus in different region within the microchannel; collected by simply branching the outlet (**Figure 2.3c** and **d**) (Kuntaegowdanahalli *et al.*, 2009; Russom *et al.*, 2009). Another example was presented by Hou *et al.* (2013), who developed a device to retrieve CTCs from blood using Dean flow fractionation. One of the downsides of using these methods for blood-related sorting is their limited effect when a large RBCs background is present. The common level of haematocrit (~45%) greatly hinders the cell-cell interactions needed for appropriate focusing so samples must be diluted (50 – 100 times) before sorting, increasing the processing time.

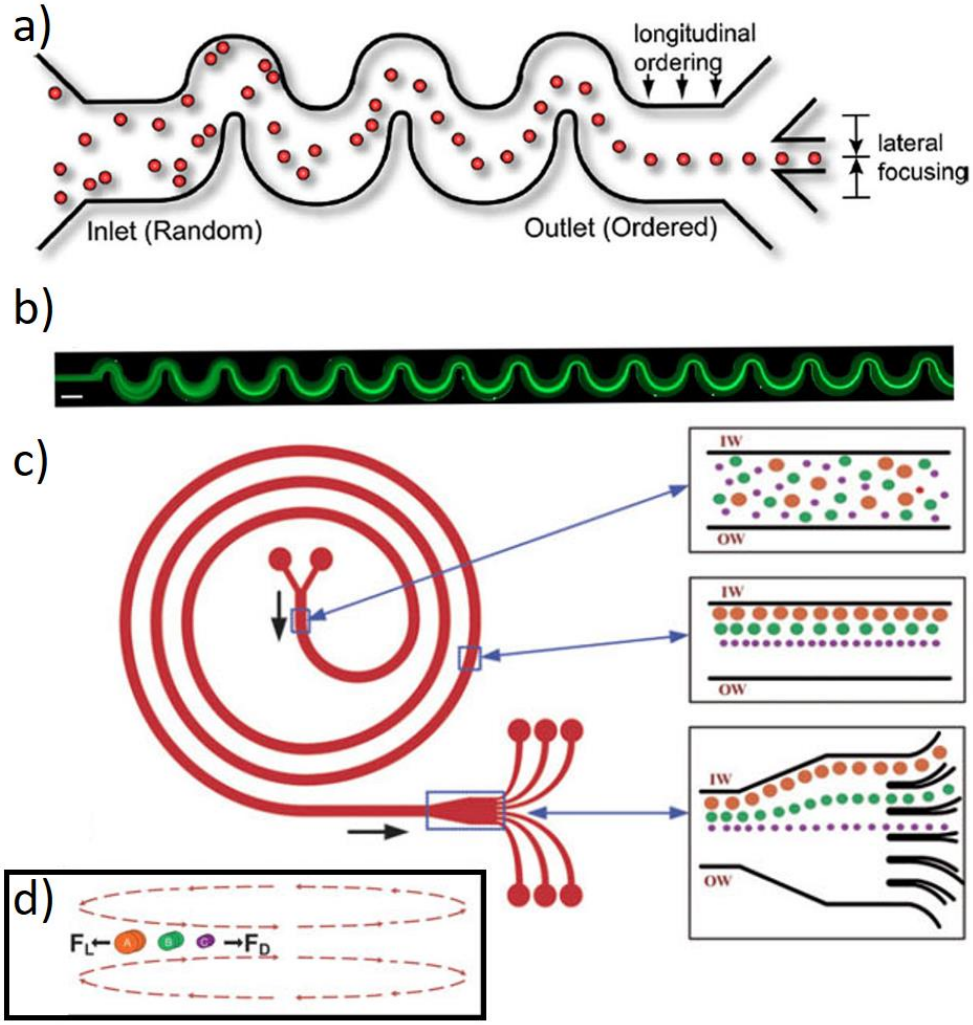


**Figure 2.3: a)** Schematic representation of the inertial focusing process in a serpentine device. Precise ordering of initially randomly distributed particles is observed along the flow direction and laterally across the microchannel. **b)** Example of inertial focusing of fluorescent particles, forming a tighter streamline as they go from the inlet, on the left, to the outlet, on the right (Scale bar of 160 μm). **c)** Schematic representation of the inertial focusing process in a spiral device. The initially scattered particles focus at different equilibrium positions along the inner wall (IW) of the spiral microchannel. Individual streams can then be collected at the outlet by branching the multiple outlet region. **d)** Cross-section of the channel, representing the effects of $F_L$ and $F_D$ on the particles. **a)** and **b)** adapted from.Di Carlo *et al.* (2007); **c)** and **d)** adapted from Kuntaegowdanahalli *et al.* (2009).

### 2.3.5 Magnetophoresis

Particle sorting through magnetophoresis is centred on the use of permanent magnets or electromagnetic coils to apply forces on cells with intrinsic magnetic properties, cells labelled with magnetic particles, or even cells suspended in a ferrofluid. Separation is possible since because a magnetic force, $F_m$, is exerted on the particles, expressed by:

$$F_m = \frac{V_{particle}\,\Delta x}{\mu_o}(B \cdot \nabla)B \qquad (2.20)$$

where $V_{particle}$ is the particle volume, $\Delta x$ is the difference in magnetic susceptibility of the particle and fluid, $B$ is the magnetic induction and $\mu_o$ the permeability of the vacuum (constant at $4\pi \times 10^{-7}$ T/mA). Thus, in order to induce a magnetic force on a particle, both a difference in the magnetic susceptibility and a gradient in the magnetic field are necessary.

In the case of magnetic labelling, cell surface markers usually contain iron and aim to either isolate rare cells or remove specific cell populations (Zborowski and Chamers, 2011). A magnetic field gradient isolates the magnetic markers, separating the cells as well. This is core principle of techniques such as MACS (Magnetically Actuated Cell Sorting), which is capable of processing up to $10^{11}$ cells in 30 min (Thiel, Scheffold and Radbruch, 1998).

RBCs are naturally magnetic cells due to the high iron content present in haemoglobin. Using this property, Qu *et al.* proposed in 2008 a microfluidic system where a magnetic gradient is created in the centre of the device, using a 69 μm diameter nickel wire with ferromagnetic properties, and RBCs were collected in this region (**Figure 2.4**). By initially treating the haemoglobin with $NaNO_2$, it is changed to its paramagnetic form, *i.e.*, attracted to an applied magnetic field (contrasting with the natural repelling, diamagnetic form of WBCs). Under a 0.2 T magnetic field, separation of RBCs was then accomplished with a 93.5% efficiency, using a concentrated sample (1:40 dilution). Some of the drawbacks of this technique are its low recovery and non-optimal cell purity, however it could perform a quick separation of RBCs, possibly coupled with other more specific separation techniques.

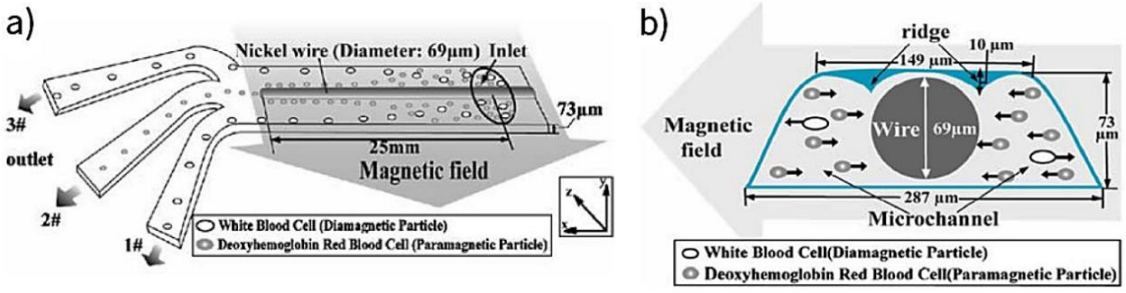


**Figure 2.4:** A label-free magnetic separation system for RBC isolation. **a)** Schematic of the device used and **b)** cross-section view of the microchannel. A ferromagnetic nickel wire, located at the centre of the separation channel, creates a magnetic gradient, inducing the concentration of RBCs at the central region, with WBCs being repelled from this region. Adapted from Qu *et al.* (2008).

## 2.4 Summary

The development of microfluidic single cell analysis and separation technology has the potential to improve current biomedical and clinical sciences. First, the use of microfluidics results in a significant reduction of reagents and sample volume leading to cheaper, less invasive protocols and to quicker processing times. Furthermore, microfluidic systems could be designed as miniaturized, self-contained, and portable devices. Thus, easy-to-use systems can be created and even used in harsh field conditions, where there is severe deficiency of well-equipped clinical labs and skilled personnel.

Current label-free microfluidics technologies for analysis and separation have already demonstrated to be capable of sorting and characterizing individual rare cells from a heterogeneous population. These technologies use only the inherent biophysical properties of the cells to perform separation, requiring no further labelling. They have the potential to develop into systems of higher sensitivity and accuracy than current methods, giving faster results in a controlled and reproducible way. The creation of integrated systems, capable of performing a series of decomplexing tasks, separation and analysis could be on the horizon for the label-free microfluidics field. However, the lack of such systems currently leaves open the opportunity to develop novel approaches, as presented later on this thesis.

# Chapter 3

# AC Electrokinetics: Theory & Application

## 3.1 Theoretical Background

The electrical demonstration of the existence of the cell membrane by Höber in the 1910s, or the determination of canine RBC's membrane capacitance (as 8.1 $mFm^{-2}$) and thickness (as 3.3 nm) by Fricke in 1924/25, are some examples of the first dielectric studies (Morgan *et al.*, 2007). Since these early studies, different approaches have been developed to measure cell dielectric properties, such as dielectrophoresis (Pethig, 2010; Pethig *et al.*, 2010; Gascoyne and Shim, 2014), electrorotation (Goater, Burt and Pethig, 1997; Goater and Pethig, 1998; Dalton *et al.*, 2001) and electrical impedance spectroscopy (Holmes, Sun, *et al.*, 2007; Morgan *et al.*, 2007; Sun, Bernabini and Morgan, 2010). In this chapter, the underlying theory of the AC electrokinetic characterisation of particles is presented, as well as techniques for single particle analysis and/or separation.

### 3.1.1 Dielectric polarisation

Dielectric materials contain charges which polarise under the influence of an applied electric field. These charges are bound within the material, being able to move short distances when the field is applied, with positive and negative charges moving opposite to each other, forming induced dipoles. Some materials also consist of molecules with a permanent dipole (*e.g.* pure water molecules) which polarise by orienting with the applied electric field.

The formation of the induced dipole creates a dipole moment (a vector) from the negative to the positive charge. In a dielectric material, the average dipole moment ($\mathbf{p}_{av}$) of all the constituent molecules will be proportional to the applied electric field magnitude:

$$\mathbf{p}_{av} = \alpha \mathbf{E}' \qquad (3.1)$$

where $\mathbf{E}'$ is the local electric field, close to the dipole; and $\alpha$ the polarisability, representing the dielectric's response to the applied field, *i.e.*, the average dipole moment per unit field strength ($Fm^2$). The polarisation and displacement of the charge gives rise to a net charge at points in the dielectric or at the surface. These charges are referred to as bound or polarisation charges, with the bound volume charge density ($\boldsymbol{\rho}_b$) being given by:

$$\boldsymbol{\rho}_b = -\nabla \cdot \mathbf{P} \tag{3.2}$$

Dielectric materials can be classified as polar and non-polar. Polar dielectrics contain molecules possessing permanent dipole moments, independent of the application of an electric field. Non-polar dielectrics are materials containing molecules which do not possess a permanent dipole moment. However, when an electric field is applied, a slight displacement of individual charges within or around the molecules gives rise to an induced dipole.

There are three basic molecular polarisation mechanisms: electronic, atomic and orientational. In electronic polarisation ($\alpha_e$), the applied electric field causes a displacement of the electron cloud relative to the nuclei in each atom; whereas in atomic polarisation ($\alpha_a$), the displacement is of the atomic nuclei relative to one another. In the case the material is an ionic crystal, then apart from the ions being polarized individually, the negative and positive ions will be displaced with respect to each other – this effect is called ionic polarisation. As for orientational polarisation ($\alpha_o$), it arises from the alignment of molecules possessing permanent dipole moments.

There is a fourth, long-range polarisation, known as interfacial polarisation ($\alpha_i$), that occurs due to the accumulation of charge carriers at the interface between two materials of different dielectric properties. Interfacial polarisation is critical in the formation of induced dipoles on particles and plays an important role in AC electrokinetics. Assuming that each polarisability acts independently, the total polarisability ($\alpha_T$) of a dielectric is given by the sum of the different polarisability mechanisms:

$$\alpha_T = \alpha_e + \alpha_a + \alpha_o + \alpha_i \tag{3.3}$$

Considering again the net charges generated by the polarisation, these can be either free or bound to the dielectric, resulting in two individual charge densities for free ($\boldsymbol{\rho}_f$) and bound ($\boldsymbol{\rho}_b$) charges. Using Gauss's Law to relate the electric field vector ($\mathbf{E}$) to the volume electric charge density:

$$\nabla \cdot \mathbf{E} = \frac{\boldsymbol{\rho}_f + \boldsymbol{\rho}_b}{\varepsilon_0} \tag{3.4}$$

the expression can be further simplified using **Equation 3.2**:

$$\nabla \cdot (\varepsilon_0 \mathbf{E} + \mathbf{P}) = \boldsymbol{\rho}_f \tag{3.5}$$

with $\varepsilon_0$ being the constant, vacuum permittivity (8.85× $10^{-12}$ $Fm^{-1}$). The component $(\varepsilon_0 \mathbf{E} + \mathbf{P})$ is a vector (usually represented as $\mathbf{D}$) and is called the electric flux density (in C $m^{-2}$). Its divergence is thus equivalent to the free volume charge density ($\nabla \cdot \mathbf{D} = \boldsymbol{\rho}_f$). Since most dielectrics are linear and isotropic, $\mathbf{P}$ is proportional to $\mathbf{D}$ such that:

$$\mathbf{P} = \varepsilon_0 \, \chi_{ae} \, \mathbf{E} \tag{3.6}$$

where $\chi_{ae}$ is the electric susceptibility of the dielectric. Therefore, for an ideal dielectric, *i.e.*, linear and isotropic, with zero conductivity, the electric flux density is given by:

$$\mathbf{D} = \varepsilon_0 \, (1 + \chi_{ae}) \mathbf{E} = \varepsilon_0 \, \varepsilon_r \mathbf{E} \tag{3.7}$$

where $\varepsilon_r = 1 + \chi_{ae}$ is a dimensionless number referring to the relative permittivity of the dielectric. The permittivity of the dielectric is thus $\varepsilon = \varepsilon_0 \, \varepsilon_r$, being the constant of proportionality between $\mathbf{D}$ and $\mathbf{E}$.

### 3.1.2 Complex permittivity

When dealing with a non-ideal dielectrics, the movement of charge and the polarisation mechanism becomes more complicated (especially if AC fields are used). As previous, equivalent circuits can be helpful in modelling the physical system comprising of a non-ideal dielectric with permittivity $\varepsilon$ and conductivity $\sigma$. First, consider a parallel plate capacitor containing a homogeneous dielectric with no unbound charge (**Figure 3.1a**). The plates of the capacitor are separated by a distance $d$ and have an area of $A$, with a potential $V$ of angular frequency $\omega$ being applied between them. For a loss-free dielectric of permittivity $\varepsilon$ filling the gap the impedance is

$$Z = \frac{1}{i\omega C} = \frac{d}{i\omega \varepsilon A} \tag{3.8}$$

where $i^2 = -1$ and $C$ is the capacitance ($C = \varepsilon(A/d)$). Some dielectrics are almost loss-free and can be considered to have a constant permittivity, however this does not apply to most dielectrics. In the case of a non-ideal, "*lossy*" dielectric (containing

unbound charge), the polarisation of the medium depends on the frequency of the applied AC field. If the material is considered lossy, with both conductivity $\sigma$ and permittivity $\varepsilon$ (**Figure 3.1b**), it can be modelled as a parallel combination of a loss-free capacitor (capacitance $C$) and a resistor ($R = (1/\sigma)(d/A)$. The impedance is then:

$$Z = \frac{1}{\frac{1}{R}+i\omega C} = \frac{R}{1+i\omega RC} \tag{3.9}$$

The capacitance of a lossy dielectric is now given by:

$$C = \tilde{\varepsilon}\frac{A}{d} \tag{3.10}$$

where $\tilde{\varepsilon}$ is the complex permittivity of the dielectric, which represents the AC field frequency dependence of the material permittivity. It is given by:

$$\tilde{\varepsilon} = \varepsilon_0\varepsilon_r - i\frac{\sigma}{\omega} \tag{3.11}$$

The impedance is then simplified to:

$$Z = \frac{d}{A(\sigma+i\omega\tilde{\varepsilon})} \tag{3.12}$$

By multiplying both the numerator and denominator of the impedance expression by the complex conjugate of the component containing the imaginary part (*i.e.*, by $(\sigma - i\omega\tilde{\varepsilon})$) it is possible to simplify the expression so that the Real and Imaginary parts of impedance can be separated:

$$\mathrm{Re}(Z) = \frac{d}{A\sigma\left(1+\left(\frac{\omega\tilde{\varepsilon}}{\sigma}\right)^2\right)} \tag{3.13}$$

$$\mathrm{Im}(Z) = -i\frac{d}{A\omega\tilde{\varepsilon}\left(1+\left(\frac{\sigma}{\omega\tilde{\varepsilon}}\right)^2\right)} \tag{3.14}$$

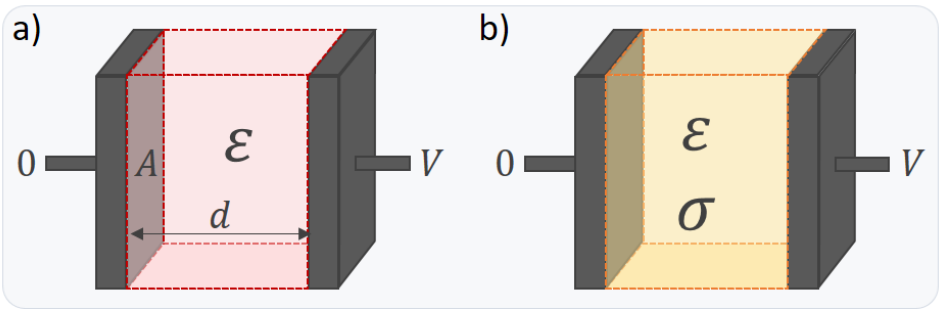


**Figure 3.1:** Representation of a parallel plate capacitor, with **a)** a conductor, **b)** a dielectric with no unbound charge and **c)** a dielectric with unbound charge placed between the two electrodes planes.

### 3.1.3 Dielectric relaxation

When a dielectric is polarised, the induced dipole created requires the displacement of unbound charges, which takes a certain time to occur. Similarly, when the electric field is removed, there is a time period before the induced dipole and polarisation disappears. If a low frequency AC field is being applied, the dipoles have enough time to orient with the field. For increasing frequencies, this time period for alignment decreases. In other words, the particles have less time to "relax" and follow the field - this time is termed the relaxation time, $\tau$.

With increasing frequency, there will be a moment when the relaxation time equals that of the time period required for maximum polarisation. For higher frequencies, maximum polarisation no longer occurs and, for very high frequencies, polarisation ceases to exist as the dipoles are no longer able to move in response to the changing field. This frequency dependent reduction in polarisability is termed dielectric relaxation.

### 3.1.4 Orientational polarisation

Amongst the basic polarisation mechanisms, orientational polarisation has the longest relaxation time. Electronic and atomic polarisations will align with the field up to frequencies of the order of $10^{14}$ Hz, and thus are considered virtually constant. The orientational polarisation takes the form of **Equation** $\mathbf{P} = \varepsilon_0 \chi_{ae} \mathbf{E}$ (3.6 but with a characteristic relaxation time $\tau_{or}$, associated with the time taken for the permanent dipoles to re-orient with the field and is given by

$$\mathbf{P}_{or} = \frac{\varepsilon_0 \chi_{or}}{1+i\omega\tau_{or}} \mathbf{E} \qquad (3.15)$$

where $\chi_{or}$ is the low frequency limit for the orientational susceptibility of the dielectric. The total frequency dependent polarisation is then

$$\mathbf{P}_{tot} = \varepsilon_0 \left(\chi_{ae} + \frac{\chi_{or}}{1+i\omega\tau_{or}}\right) \mathbf{E} \qquad (3.16)$$

At the low frequency limit $\chi = \chi_{ae} + \chi_{or} = \varepsilon_s - 1$, where $\varepsilon_s$ is the relative permittivity measured in a static electric field. At the high frequency limit, $\chi = \chi_{ae} = \varepsilon_\infty - 1$, where $\varepsilon_\infty$ is the relative permittivity at sufficiently high frequency where no orientational polarisation occurs. As a result, $\chi_{or} = \varepsilon_s - \varepsilon_\infty$, and total frequency dependent polarisation can be written as

$$\mathbf{P}_{tot} = \varepsilon_0(\tilde{\varepsilon}_d - 1)\,\mathbf{E} \qquad (3.17)$$

where $\tilde{\varepsilon}_d$ is a complex term given by

$$\tilde{\varepsilon}_d = \varepsilon_\infty + \frac{\varepsilon_s - \varepsilon_\infty}{1 + i\omega\tau_{or}} \qquad (3.18)$$

The total complex permittivity of the dielectric is therefore

$$\tilde{\varepsilon} = \varepsilon_0\left(\varepsilon_\infty + \frac{\varepsilon_s - \varepsilon_\infty}{1 + i\omega\tau_{or}}\right) - i\frac{\sigma}{\omega} \qquad (3.19)$$

The complex permittivity can be written in the form of $\tilde{\varepsilon} = \varepsilon' - i\varepsilon''$, with $\varepsilon'$and $\varepsilon''$ being given by Debye relations:

$$\varepsilon' = \varepsilon_0\left(\varepsilon_\infty + \frac{\varepsilon_s - \varepsilon_\infty}{1 + \omega^2\tau_{or}{}^2}\right) \qquad (3.20)$$

$$\varepsilon'' = \varepsilon_0\left(\frac{(\varepsilon_s - \varepsilon_\infty)\,\omega\tau_{or}}{1 + \omega^2\tau_{or}{}^2}\right) + \frac{\sigma}{\omega} \qquad (3.21)$$

The variation of $\varepsilon'$and $\varepsilon''$ with $\omega$ gives a dispersion in the relative permittivity – see **Figure 3.2**.

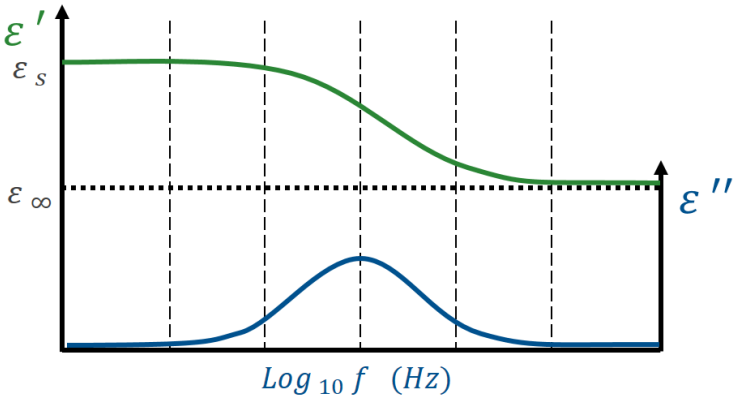


**Figure 3.2:** The real and imaginary components of the complex permittivity versus frequency for a single Debye relaxation

### 3.1.5 Interfacial polarisation

Polarisation can occur at the interface between two materials with different dielectric properties. In systems using AC electrokinetics, this interface (or discontinuity) arises between a dielectric medium (usually electrolyte) and the dielectric particles in suspension. Given the frequency dependency of each dielectric polarisability, the total complex permittivity is mainly affected by the interfacial polarisation. For instance, if a single particle is suspended between the two parallel plates from **Figure 3.1b**, the charges will be distributed across its surface, resulting in the formation of an induced dipole. How the system then takes

advantage of this dipole, by creating motor or rotational forces, for instance, varies according to the AC electrokinetic technique.

One of the simplest examples to consider is that of a single, homogenous, solid particle suspended in a homogenous dielectric medium. If an electric field $\mathbf{E}$ is applied across the medium, the induced dipole moment, $\mathbf{p}$ can be calculated through:

$$\mathbf{p} = 4\pi r^3 \varepsilon_{medium} \frac{\tilde{\varepsilon}_{particle} - \tilde{\varepsilon}_{medium}}{\tilde{\varepsilon}_{particle} + 2\tilde{\varepsilon}_{medium}} \mathbf{E} \qquad (3.22)$$

where $\tilde{\varepsilon}_{medium}$ and $\tilde{\varepsilon}_{particle}$ are the complex permittivity of the medium and particle, respectively, and $r$ the particle radius. This effective dipole moment can also be re-written in terms of the particle volume, $V_p$, and the effective polarisability, $\tilde{\alpha}$:

$$\mathbf{p} = V_p \tilde{\alpha} \mathbf{E} \qquad (3.23)$$

$$\tilde{\alpha} = 3\varepsilon_{medium} \frac{\tilde{\varepsilon}_{particle} - \tilde{\varepsilon}_{medium}}{\tilde{\varepsilon}_{particle} + 2\tilde{\varepsilon}_{medium}} = 3\varepsilon_{medium} \tilde{f}_{CM} \qquad (3.24)$$

with $\tilde{f}_{CM}$ referring to the Clausius-Mossotti factor:

$$\tilde{f}_{CM} = \frac{\tilde{\varepsilon}_{particle} - \tilde{\varepsilon}_{medium}}{\tilde{\varepsilon}_{particle} + 2\tilde{\varepsilon}_{medium}} \qquad (3.25)$$

The $\tilde{f}_{CM}$ is complex, describing the polarisability of the particle with a relaxation time of:

$$\tau = \frac{\varepsilon_{particle} + 2\varepsilon_{medium}}{\sigma_{particle} + 2\sigma_{medium}} \qquad (3.26)$$

### 3.1.6 Maxwell's Mixture Theory

For the case where various particles are suspended in the dielectric medium, dielectric spectroscopy can be used to measure the dielectric properties of the suspension (Pethig, 1979). This mixture of particles and medium can be approximated to that of a single dispersion. To do so, Maxwell's Mixture theory (MMT) (Maxwell, 1881) can be used to combine the dielectric properties of all particles into an overall complex permittivity of the mixture ($\tilde{\varepsilon}_{mix}$):

$$\tilde{\varepsilon}_{mix} = \tilde{\varepsilon}_m \left(1 + 3\,\varphi\,\tilde{f}_{CM}\right) \qquad (3.27)$$

with $\varphi$ the volume fraction of particles in the medium. In practical terms, $\tilde{\varepsilon}_{mix}$ describes the change in the medium permittivity due to the presence of a certain

volume of particles, and can only be used if the volume fraction is small, *i.e.*, $\varphi \ll 1$.

### 3.1.7 Shell Model for biological particles

For the case of a single shelled particle, *e.g.* cell, in suspending medium, MMT can be used to define the dielectric properties of the cell, the volume fraction and the complex impedance of the suspension (Maxwell, 1881; Morgan and Green, 2002). Specifically, MMT based, multi-shell models can be used to retrieve the dielectric properties of the cell (Hanai, Koizumi and Irimajiri, 1975; Irimajiri, Hanai and Inouye, 1979; Huang *et al.*, 1992; Wang *et al.*, 1994). While cells have an intricate internal structure, surrounded by a membrane, a simpler approximation can be used for some cells, *e.g.* red blood cells, where a single-shell model (**Figure 3.3a**) is applicable.

In this model, there are two dispersions, corresponding to each of the existing interfaces (membrane-medium and cytoplasm-membrane). For a single shell model, the induced dipole moment and the effective polarisability of the cell in the mixture are given by:

$$\mathbf{p} = 4\pi r^3 \varepsilon_{medium} \tilde{f}_{CM,mix} \mathbf{E} \tag{3.28}$$

$$\tilde{\alpha} = 3\varepsilon_{medium} \tilde{f}_{CM,mix} \tag{3.29}$$

with the mixture Clausius-Mossotti factor:

$$\tilde{f}_{CM,mix} = \frac{\tilde{\varepsilon}_{cell} - \tilde{\varepsilon}_{medium}}{\tilde{\varepsilon}_{cell} + 2\tilde{\varepsilon}_{medium}} \tag{3.30}$$

The complex permittivity of the cell, $\tilde{\varepsilon}_{cell}$, in a single shell model (**Figure 3.3b**) can be calculated as:

$$\tilde{\varepsilon}_{cell} = \tilde{\varepsilon}_{membrane} \frac{\gamma^3 + 2\tilde{f}_{CM,cell}}{\gamma^3 - \tilde{f}_{CM,cell}} \tag{3.31}$$

with,

$$\tilde{f}_{CM,cell} = \frac{\tilde{\varepsilon}_{cytoplasm} - \tilde{\varepsilon}_{membrane}}{\tilde{\varepsilon}_{cytoplasm} + 2\tilde{\varepsilon}_{membrane}} \tag{3.32}$$

$$\gamma = \frac{r_{cytoplasm} + d_{membrane}}{r_{cytoplasm}} \tag{3.33}$$

where $\tilde{\varepsilon}_{cytoplasm}$ and $\tilde{\varepsilon}_{membrane}$ are the complex permittivity of cytoplasm and membrane, $r_{cytoplasm}$ the inner radius of the cell and $d_{membrane}$ the thickness of the cell membrane ($d_{membrane} \ll r_{cytoplasm}$).

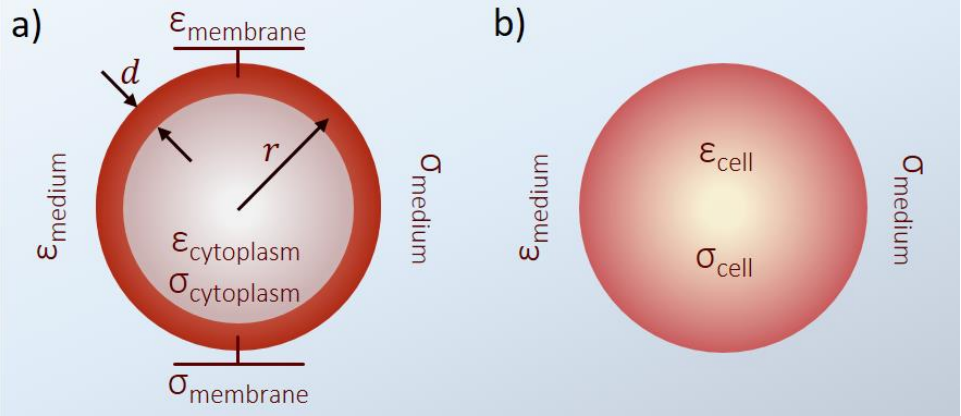


**Figure 3.3: a)** Representation of a single shell model of a biological cell in a suspending medium. **b)** Equivalent model of a cell, obtained through Maxwell's mixture theory.

## 3.2 AC Electrokinetics Techniques

### 3.2.1 Dielectrophoresis

The term dielectrophoresis (DEP) refers to the movement of particles due to their dielectric properties in a non-uniform AC field. Consider a single spherical particle, of high conductivity and low permittivity, located between two electrodes and suspended in a low conductivity and high permittivity electrolyte. Starting with an uniform AC field, if $\tilde{\alpha}_{particle} > \tilde{\alpha}_{medium}$, more charges exist within the interface than outside, resulting in a difference of charge density on either side of the particle (**Figure 3.4a**). An induced net dipole across the particle, following the applied field direction, is thus generated. Conversely, if $\tilde{\alpha}_{particle} < \tilde{\alpha}_{medium}$, more charges are accumulated on the interface outside and the induced net dipole is now contrary to the field direction (**Figure 3.4b**). If a non-uniform AC field is now applied, the density of electrical field lines is unbalanced between the poles, meaning that the forces on the induced dipole will also be unbalanced, resulting in particle movement. For $\tilde{\alpha}_{particle} > \tilde{\alpha}_{medium}$, the dipole is oriented with the field and positive DEP occurs (**Figure 3.4c**); while negative DEP arises in the opposite situation (**Figure 3.4d**).

Based on the behaviour in an AC field, the dielectrophoretic force, $\mathbf{F}_{DEP}$ applied to a particle can be described as:

$$\mathbf{F}_{DEP} = (\mathbf{p} \cdot \nabla)\mathbf{E} \qquad (3.34)$$

A clear conclusion from this equation is that for a uniform electric field the force is zero.

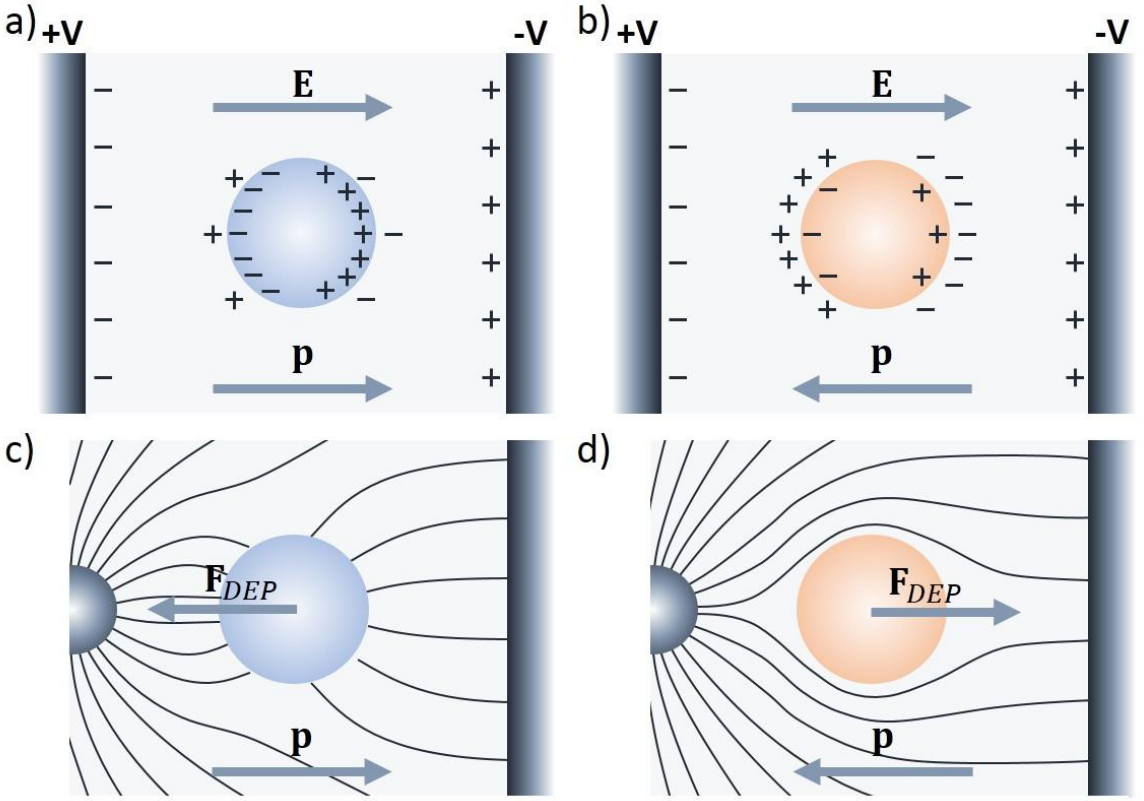


**Figure 3.4:** Depending on the difference in polarisability between particle and medium, different polarisations occurs. **a)** Polarisation when $\tilde{\alpha}_{particle} > \tilde{\alpha}_{medium}$, under a uniform electric field. **b)** Polarisation when $\tilde{\alpha}_{particle} < \tilde{\alpha}_{medium}$, under a uniform electric field. **c)** When the particle in **a)** is placed under a non-uniform field, positive DEP occurs. **d)** When the particle in **b)** is placed under a non-uniform field, negative DEP occurs.

The dielectrophoretic force is commonly expressed in terms of the time-averaged force being applied to the particle:

$$\langle \mathbf{F}_{DEP} \rangle = \frac{1}{2} V_p \mathrm{Re}[\tilde{\alpha}] \nabla |\mathbf{E}_{\boldsymbol{rms}}|^2 \qquad (3.35)$$

It is apparent that $\mathbf{F}_{DEP}$ is not only dependent on the gradient of the field magnitude but also on the volume of the particle, which are both variable parameters in experiments. Furthermore, the dependence on the particle effective polarisability means that not only the permittivity and conductivity of both medium and particle influence the resultant force but also that it is dependent on the frequency of the electric. Substituting for the effective polarisability of a sphere gives the expression:

$$\langle \mathbf{F}_{DEP} \rangle = 2\pi\varepsilon_m r^3 \mathrm{Re}\left[\tilde{f}_{CM}\right] \nabla |\mathbf{E}_{rms}|^2 \qquad (3.36)$$

the $r^3$ term means the time averaged force is proportional to particle volume. The frequency dependence is in this case defined by the real part of the Clausius-Mossotti factor. As earlier described, for particles more polarisable than the medium, *i.e.*, $\mathrm{Re}\left[\tilde{f}_{CM}\right] > 0$, positive DEP ensues, with the particles moving to areas of higher electric field strength. For cases where $\mathrm{Re}\left[\tilde{f}_{CM}\right] < 0$, the medium is more polarisable, so negative DEP occurs and particles are repelled from the regions of high field strength. Furthermore, due to the frequency dependent nature of the Clausius-Mossotti factor, particles can experience positive and subsequently negative DEP by changing the applied frequency. The frequency at which this change occurs is not the same for particles of different conductivity/permittivity. Therefore, by selecting appropriate frequency values, a dynamic separation of particles based on DEP is achievable. This effect has been widely explored for particle separation, as summarized by Pethig in 2010.

### 3.2.2 Electrorotation

When a uniform electric field is applied to a particle, the induced dipole experiences a torque, so that the dipole moves parallel to the field. Furthermore, there is a finite period needed for the dipole moment to become aligned with the field vector and, if the field vector changes direction during this time, the induced dipole moment vector has to realign itself with the electric field vector. Electrorotation (ROT) is based on this phenomenon, occurs when a particle is located in an electric field with a rotating field vector and spatially dependent phase. One simple example where ROT arises is the case of a rotating polarised electric field, generated by the superposition of two phase-shifted AC signals (**Figure 3.5**).

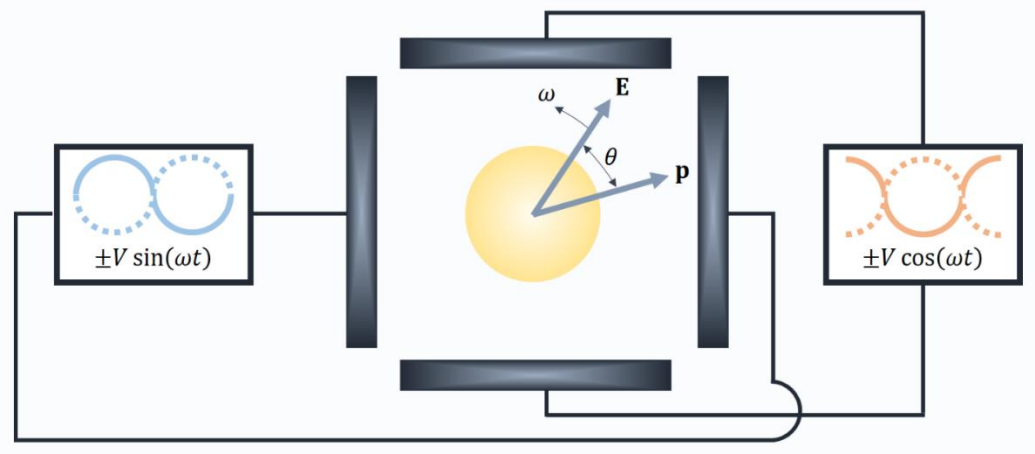


**Figure 3.5:** Schematic representation of the ROT setup, with a particle surrounded by four electrodes. At each electrode a signal 90° out of phase of the next signal is

applied. The induced dipole moment (**p**) will then always lag behind the rotating electric field (**E**, of a certain angular frequency **ω**), by a phase angle (**θ**)

As the induced dipole is constantly trying to align itself with the rotating electric field vector, the particle experiences a constant torque, rotating around its axis. This torque will be zero when the phase angle between the polarisation vector and field is zero; and maximum when the phase angle is ±90°. By analysing the generated torque on a biological particle it is then possible to measure its dielectric properties (Holzel, 1997; Yang *et al.*, 1999; Dalton *et al.*, 2004). The time-averaged first order torque on the particle is:

$$\mathbf{\Gamma}_{ROT} = -V_p \mathrm{Im}[\tilde{\alpha}]|\mathbf{E}|^2 \qquad (3.37)$$

which, substituting for the effective polarisability of a sphere, gives the commonly used form

$$\mathbf{\Gamma}_{ROT} = -4\pi\varepsilon_m r^3 \mathrm{Im}\left[\tilde{f}_{CM}\right]|\mathbf{E}|^2 \qquad (3.38)$$

As with DEP, there is a frequency dependence associated to the torque, this time reliant on the imaginary part of the Clausius-Mossotti factor ($\mathrm{Im}\left[\tilde{f}_{CM}\right]$). The particle will rotate with or against the applied rotating electric field if $\mathrm{Im}\left[\tilde{f}_{CM}\right]$ is negative or positive, respectively.

In the case where a particle is under the effect of a moving electric field and under appropriate parameters, travelling wave dielectrophoresis (twDEP) can induce the movement of the particle (Masuda, Washizu and Iwadare, 1987; Fuhr *et al.*, 1991; Morgan *et al.*, 1997). As in ROT, twDEP is based on the application of an electric field which is spatially dependent. However in this case, instead of a rotating electric field, a travelling electric field is used. This effect can be generated by using phase-quadrature sinusoidal signals at frequencies varying between 50 Hz to 100 MHz.

### 3.2.3 Impedance Spectroscopy

In impedance spectroscopy a frequency-dependent AC signal is applied to the sample and, by measuring current in the system the dielectric properties can be retrieved. This complex signal ($\tilde{U}$) generates an electrical current ($\tilde{I}$), from which the complex impedance ($\tilde{Z}$) can be calculated:

$$\tilde{Z}(j\omega) = \frac{\tilde{U}(j\omega)}{\tilde{I}(j\omega)} = \mathrm{Re}\left(\tilde{Z}\right) + \mathrm{Im}(\tilde{Z}) \qquad (3.39)$$

where $\mathrm{Re}\left(\tilde{Z}\right)$ and $\mathrm{Im}(\tilde{Z})$ are the Real and Imaginary parts of the complex impedance, respectively. The real part is commonly referred to as resistance while the

imaginary part is termed reactance. As for the magnitude ($|\tilde{Z}|$) and phase ($\phi\tilde{Z}$) components of the complex impedance, they can be calculated through

$$|\tilde{Z}| = \sqrt{\mathrm{Re}(\tilde{Z})^2 + \mathrm{Im}(\tilde{Z})^2} \quad (3.40)$$

$$\phi\tilde{Z} = \arctan\left(\frac{\mathrm{Im}(\tilde{Z})}{\mathrm{Re}(\tilde{Z})}\right) \quad (3.41)$$

By measuring the complex impedance of a suspended particle it is then possible to obtain the complex impedance of the mixture of particle and medium:

$$\tilde{Z}_{mix} = \frac{1}{j\omega\tilde{C}_{mix}} \quad (3.42)$$

where $\tilde{C}_{mix}$ is the complex capacitance of the system. Using MMT, the equivalent complex permittivity of the mixture is retrieved and the dielectric properties of the particle derived. When comparing with DEP or ROT, impedance spectroscopy differs in that the polarisability of individual particles is not measured. This requires the volume fraction of the particle in the mixture to be known in order to retrieve dielectric properties. However, DEP and ROT only measure the real and imaginary parts of the Clausius-Mossotti factor, respectively, meaning that a full characterization of the particle requires the measurements of both DEP properties and ROT spectrum. By contrast impedance spectroscopy not only fully characterizes a particle with a single measurement but also does it in much quicker manner - ROT assays take several seconds per cell, for instance, while impedance spectroscopy performs several measurements per second.

## 3.3 Microfluidic Impedance Cytometry

### 3.3.1 Technology Principles

Microfluidic Impedance Cytometry, or MIC, is a technology based on impedance spectroscopy, exploring single particle analysis for counting and discrimination of single cells (Gawad, Schild and Renaud, 2001; Küttel *et al.*, 2007; Morgan *et al.*, 2007; Holmes *et al.*, 2009; Kim *et al.*, 2010). In this technique, cells flow in a glass microchannel through pairs of electrodes, located at the bottom and top, which apply an AC field across the channel (**Figure 3.6**). The detection region consists of pairs of parallel facing platinum electrodes, fabricated within the microfluidic channel. The sample is diluted adequately so that only a single particle passes the

detection region between the electrodes at any one time. An AC signal is applied to the top electrodes; and the difference in current flowing through the channel is acquired by the bottom electrodes and measured by a custom detection circuit. The circuit consists of transimpedance amplifiers, which convert current (I) to voltage (V), and a differential amplifier. Lock-in amplification (HF2LI, Zurich Instruments) is then used to retrieve the different components of the signal, with the input signal used as a reference.

When a particle passes the detection region, it disrupts the electric field – **Figure 3.6** shows the idealised differential signal that results when a particle passes the centre of the detection region and the corresponding steps of the sequence are annotated ($t_0$, $t_1$, $t_2$, $t_3$ and $t_4$). In the situation where no cell is present between the electrode pair ($t_0$, $t_2$ and $t_4$), the medium is modelled as a capacitor in parallel with a resistor, having a specific complex impedance. When a particle is now present between a pair of electrodes ($t_1$ and $t_3$), the complex impedance being acquired is altered. MMT can be used, as previously demonstrated, to derive the properties of the particle.

The impedance changes caused by the presence of a particle between the electrode pair are then translated into a change in the current signal being measured, as the current path becomes disturbed. The current flowing through each bottom electrode is converted to voltage using transimpedance amplifiers, built within the custom detection circuit. Afterwards, a differential amplifier is used to retrieve a single output signal. Lock-in amplification then separates the real and imaginary parts of the signal at each applied frequency. In the case of a cell or polymer bead, for instance, their insulating properties (at lower frequencies in the case of a cell), result in an increased impedance, leading to a drop of the current being measured. This in turn results in a positive peak, for the first pair of electrodes ($t_1$), and the opposite for the second pair ($t_3$). The time taken from $t_1$ to $t_3$ is known as the transit time. Signal processing and data analysis are used to retrieve individual particle signals (see **Sections 3.3.2.2** and **3.3.2.3**). These individual signals are later used to plot population distribution, modelling and to retrieve the dielectric properties of the particle under study.

Using MIC it is possible to acquire single-cell measurements at a rate of hundreds of cells per minute, usually at a flow rate of 40 µL/min. Furthermore, it does not require re-suspension of cells in a low-conductivity medium, allowing the measurements to be performed at physiological conditions (Spencer, Hollis and Morgan, 2014).

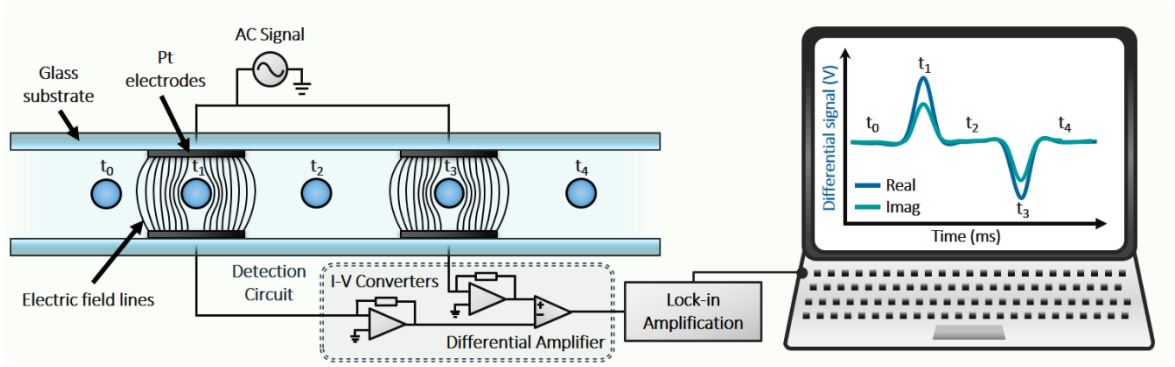


**Figure 3.6:** Schematic of the MIC system, showing the impedance detection section. Particles flow through the microchannel, between pairs of electrodes, in the detection region. The acquired differential signal is stored for further analysis.

The system has been used for discrimination of different cell types, including leukocytes (Holmes *et al.*, 2009; Holmes and Morgan, 2010), stem cells (Song *et al.*, 2013; Xavier *et al.*, 2017), circulating tumour cells (Spencer, Hollis and Morgan, 2014), protozoan parasites (Du *et al.*, 2013), phytoplankton (Benazzi *et al.*, 2007) or yeast cells (Rodriguez-Trujillo *et al.*, 2007; Nikolic-Jaric *et al.*, 2009). There is still, however, a myriad of possible applications, some of which will be addressed later on this thesis.

### 3.3.2 Experimental Details

#### 3.3.2.1 Chip Fabrication

The MIC system uses microfluidic glass chips (**Figure 3.7**). The chips used in this thesis were fabricated using standard photolithography techniques by Ying Tran at the Southampton Nanofabrication Centre, University of Southampton. The lithography masks were designed previously by Dr. Daniel Spencer.

The fabrication details have been detailed previously in literature and can be found elsewhere (Holmes, She, *et al.*, 2007; Spencer, Elliott and Morgan, 2014; Spencer, Hollis and Morgan, 2014). Briefly, the platinum electrodes for impedance detection (200 nm thickness, 30 µm width and separated by 10 µm) were patterned on a glass wafer. SU8 photoresist was used to define the microchannel, with a detection region of 40 µm by 30 µm, by photolithography. Full wafer thermal bonding was used to bond the top and bottom layers of the microfluidic chip. After dicing, inlet and outlet channels were etched using a $CO_2$ laser (Mini 18, Epilog Laser). The microfluidic chip was clamped to a 3D-printed holder housing fluidic and electrical connections. Samples were flushed through the chip at 40 µL/min (unless stated otherwise) using a syringe pump (Fusion 400, Chemyx). Between samples, the chips

were flushed with 1 mL DI water and 1 mL phosphate buffered saline (PBS) using a syringe. Periodic cleaning steps were taken to remove debris from electrode surfaces by introducing 1 M sodium hydroxide into the system before rinsing with 1 mL DI water.

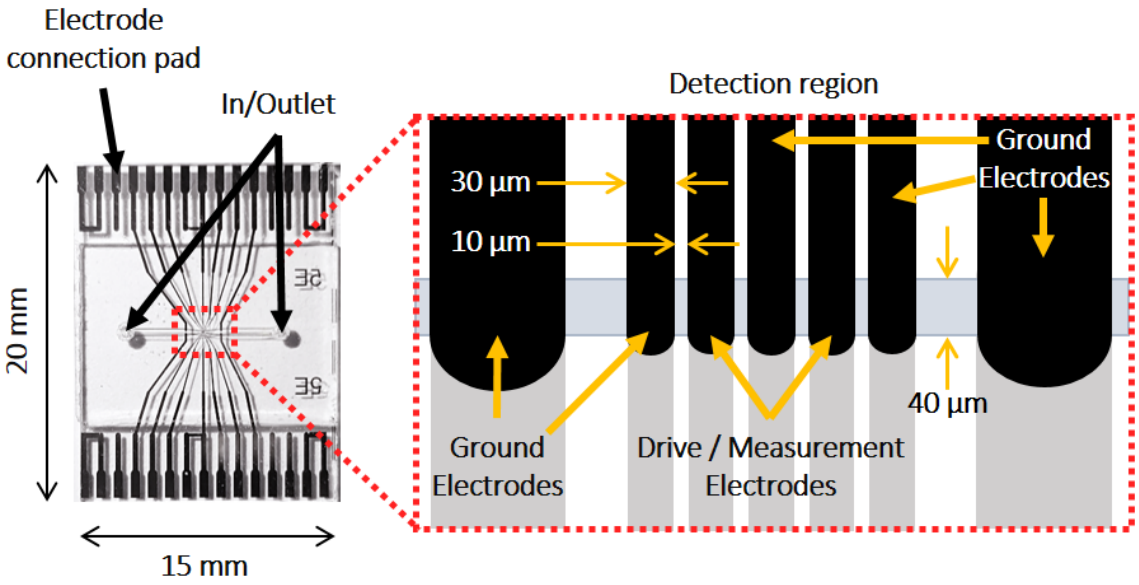


**Figure 3.7:** Photograph of a MIC glass chip with platinum electrodes. Insert shows a schematic of the impedance detection region.

### 3.3.2.2 Signal Processing

The raw data from MIC experiments requires post-experiment signal processing to extract single particle impedance signals. An example of the raw signal of two particles (7 µm polystyrene beads) passing through the detection region can be seen in **Figure 3.8a**. The differential current signal of each particle follows the expected asymmetric double Gaussian pattern, as previously explained (**Figure 3.6**). The simplest method to identify single particle signals would be to define a trigger level and detect when the signal rises above this threshold. However, this method is susceptible to errors in noisy signals therefore requiring a large signal-to-noise ratio, which is not guaranteed for smaller particles. Furthermore, it can fail when the smaller secondary peaks are present in the signal, or coincident events occur.

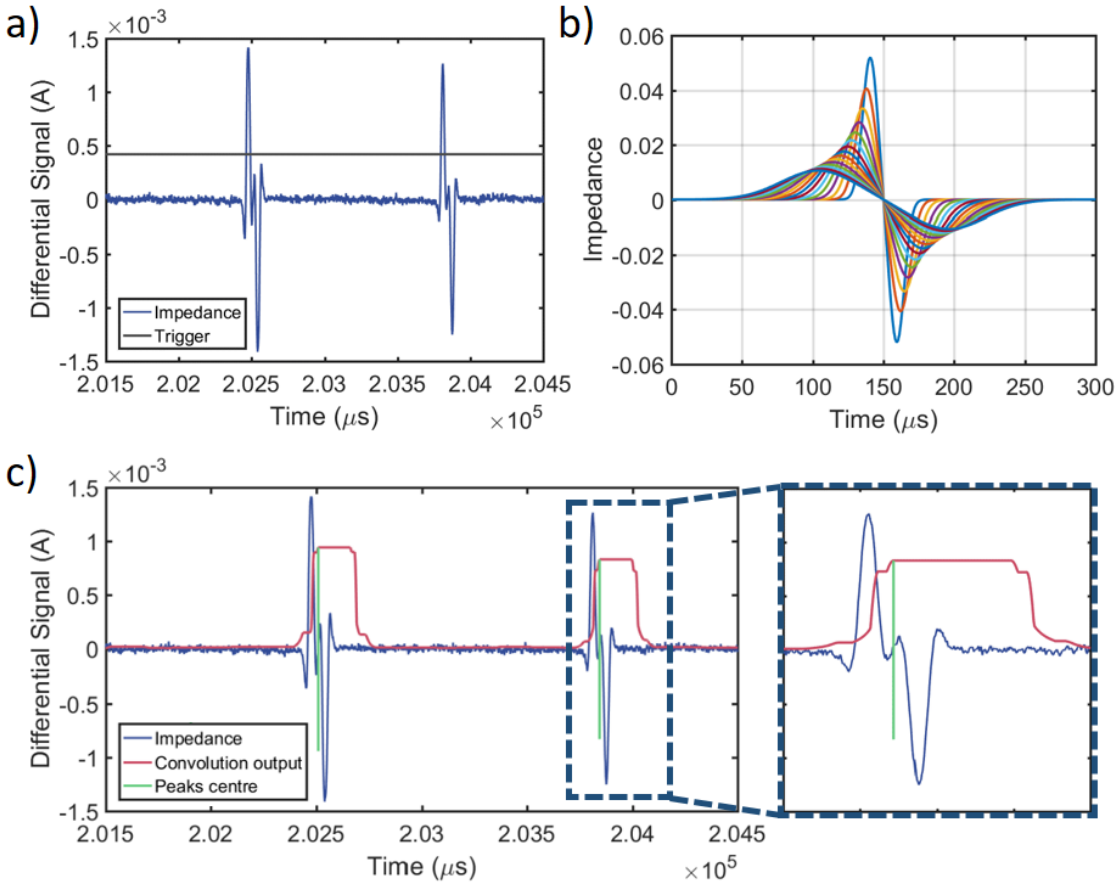


**Figure 3.8: a)** A section of experimental data showing two individual particles detected by the system and a trigger level set to identify the two events. **b)** A set of 15 template signals, each with different transit times, used to detect individual signals through convolution. **c)** Result of the maximum filter applied to the convolution output on the experimental data and the detected centres for each individual signals.

To avoid these issues a better processing method is to convolute the signal with a template signal (an anti-symmetric double Gaussian signal). Custom scripts in Matlab (R2016a) were created for signal processing. In order to accommodate the possible transit times of different particles, a range of template signals needs to be tested. The range minimum and maximum can be calculated based on the known flowrate and channel dimensions. **Figure 3.8b** shows the convolution template signals used on the data from **Figure 3.8a**. Each template signal is convoluted with the data and the optimal template signal will have the highest convolution output. A running maximum filter is then applied to identify the position where the maximum convolution outputs are present. The peaks of this filter give the position of each individual impedance signals (centre and height), as shown in **Figure 3.8c**. Each signal can then be stored for further data analysis.

### 3.3.2.3 Data Analysis

The individual data of each impedance signal is stored for post-processing in the forms of its real and imaginary parts. These can be used to plot the acquired data – as an example, the experimental data at 18.3 MHz of 7 µm polystyrene beads and red blood cells (RBCs) is plotted in **Figure 3.9**. The analysis of MIC experimental data starts by plotting the real versus the imaginary parts of each individual signal in a scatter plot (**Figure 3.9a**). In the example of **Figure 3.9**, the two particle populations (beads and cells) are clearly identifiable and can be gated. The magnitude and phase of each individual signal are calculated, respectively, and plotted against each other (**Figure 3.9b**). These plots will be used in this thesis for comparison between cell/particle populations. Polystyrene beads are usually added to samples as a reference as they have a well- defined size and known dielectric properties. They can be used for the normalization of magnitude and phase of the impedance signal, allowing direct comparison between different particle populations and/or experiments. For example, the normalized magnitude values of different populations relates to the size of each particle (Morgan and Green, 2002) and, as such, can be used to discriminate different cells/particles based on their size. **Figure 3.9b** shows this effect as the 7 µm polystyrene beads (≈180 fL) have a higher mean magnitude than RBCs (≈100 fL).

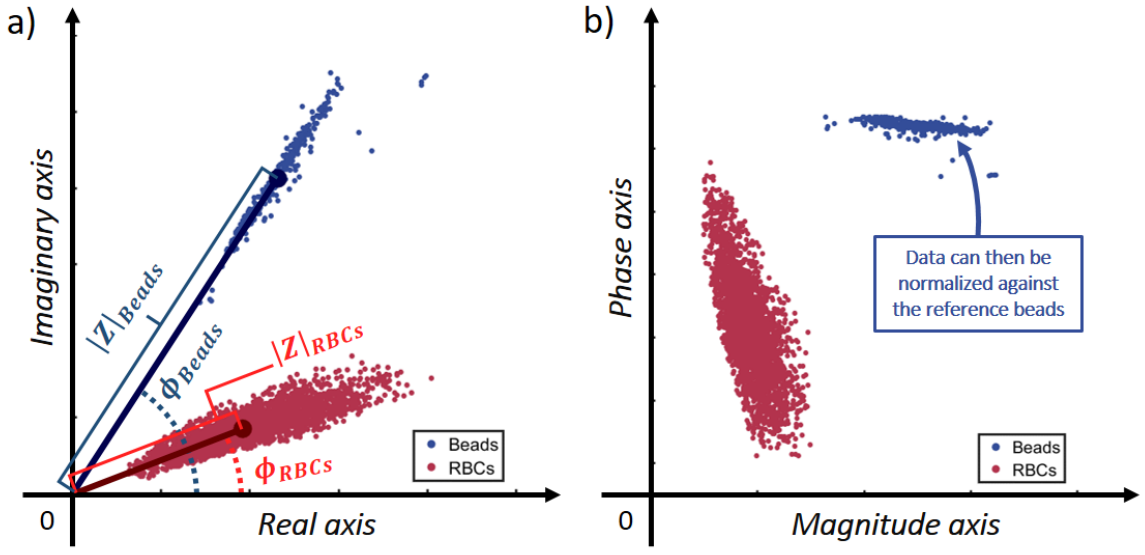


**Figure 3.9: a)** Scatter plot of the real versus the imaginary parts of impedance of a sample containing 7 µm polystyrene beads and RBCs at 18.3 MHz. The mean (●) of each population is identified and used as an example on how to calculate the magnitude and phase of individual signal. **b)** Scatter plot of the magnitude versus the phase of impedance.

## 3.4 Fluorescence-coupled Impedance Cytometry

### 3.4.1 Previous implementations

In the case where the dielectric properties or size of certain cell types overlap (due to similar mean values or considerable spread due to high standard deviation), the MIC system will struggle to properly discriminate between the cell types. To tackle this, a useful add-on to this label-free technique would be to couple fluorescence detection to the system. Fluorescent tags could label certain cell types to discriminate target cells from a background in cases where the dielectric properties of target and non-target cells are similar. It can also be used as a reference to label each data point in the dielectric analysis as target/non-target and observe whether dielectric differences alone are significant to separate cells.

Such systems have already been implemented in different forms. Holmes *et al.* (2009) joined the impedance system to a lab-based confocal microscope, to acquire both impedance and fluorescence data. The integrated system was capable of identifying fluorescently labelled leukocytes, distinguishing different cell sub-populations. However, it was very sensitive to cell position within the microfluidic channel, resulting in a high variation in fluorescence signals. Spencer *et al.* presented in 2014 a fully integrated system. The system made use of an optical fibre for light delivery, which was coupled to the chip itself. This setup was capable of discriminating different leukocyte sub-populations, presenting a similar sensitivity to that of a commercial flow cytometer. More recently, Xavier *et al.* (2017) used fluorescence-coupled MIC system as part of broader study on the biophysical properties of skeletal stem cells. The system was custom built in lab, combining the regular MIC setup to a bench-fixed rig comprised of a light source (635 nm laser), a full set of optical filters and a photomultiplier for data acquisition. By using this setup, it was possible to discriminate the various cell populations under study and properly correlate variations in their properties along the duration of the study.

### 3.4.2 System Overview

All of the previous fluorescence-coupling approaches share the characteristic of being bench-top, fixed setups in lab. While not a major drawback, this limits their applicability in certain scenarios. For example, in the case where the sample being measured can only be handled in a controlled environment, as a biological safety

cabinet, or in a specific area of the laboratory, moving the entire setup becomes an arduous task, if not impossible. This is the case when handling samples of malaria-parasite infected RBCs or Leishmania-parasite infected macrophages, for example, which are discussed later in this thesis. Thus, the main requirement of a fluorescence-coupled MIC (FMIC) system was its portability. Furthermore, to reduce the complexity of the setup, a single wavelength of 488nm was used. This is a commonly used wavelength in flow cytometry, as it excites common fluorophores (*e.g.*, fluorescein isothiocyanate (FITC), green fluorescent protein (GFP), yellow fluorescent protein (YFP), and propidium iodine (PI)). **Figure 3.10** shows a schematic of the idealized FMIC system.

The implementation of the FMIC system can be found on **Figure 3.11** and **Figure 3.12**. As seen on **Figure 3.10**, a particle first flows through the impedance detection region, where a standard MIC measurement is performed. Afterwards, the particle flows through the fluorescence detection region. Here, the laser interacts with the particle, exciting any fluorophores present. The path taken by the optical signal can be seen in more detail in **Figure 3.11**. The 488 nm laser is first filtered by a band-pass filter of 488/15 nm. The signal is then reflected by a dichroic filter of 495 nm; and directed to a 20x objective, where it is focused down to the fluorescence detection region, covering the exact width of the microfluidic channel. Any correction in the position of the light beam can be made using the $xyz$ stage to move the MIC chip setup or re-focus the optical signal. If a fluorophore is excited and emits a fluorescent signal, it is collected by the 20x objective and directed to the dichroic filter.

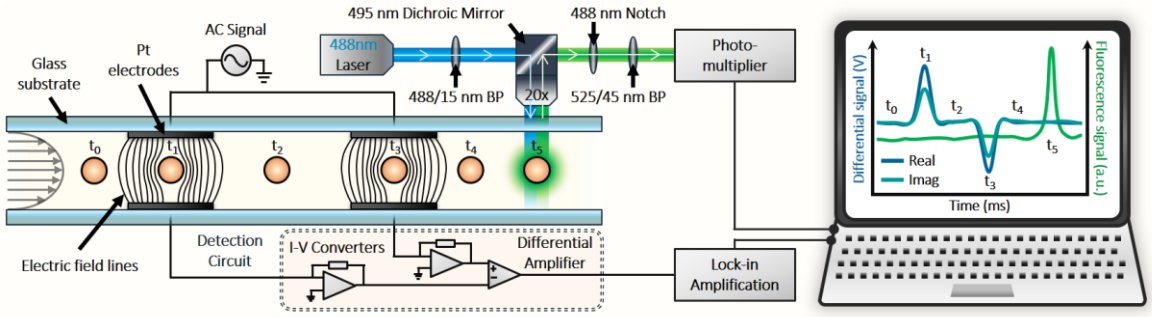


**Figure 3.10:** Schematic of the FMIC system, showing impedance and fluorescence detection sections. Particles flow through the microchannel, between pairs of electrodes and the fluorescence detection region. The acquired differential signal is coupled to the fluorescent signal and stored for further analysis.

The signal is then filtered twice: first by a band-pass filter of 525/45 nm, which is specific for FITC or GFP, for example; and then by a notch filter of 488 nm, which removes any background or scattered light coming from the original 488 nm light beam. Post filtering, the optical signal is split in two parts by a pellicle: 8% of the signal is directed to a camera, which permits the observation of the detection region; while 92% of the signal is directed to a photomultiplier for amplification and acquisition. The acquired fluorescence data is then coupled with the impedance data being measured. Each individual particle will then present both an impedance and fluorescence value, which will be used in further data analysis.

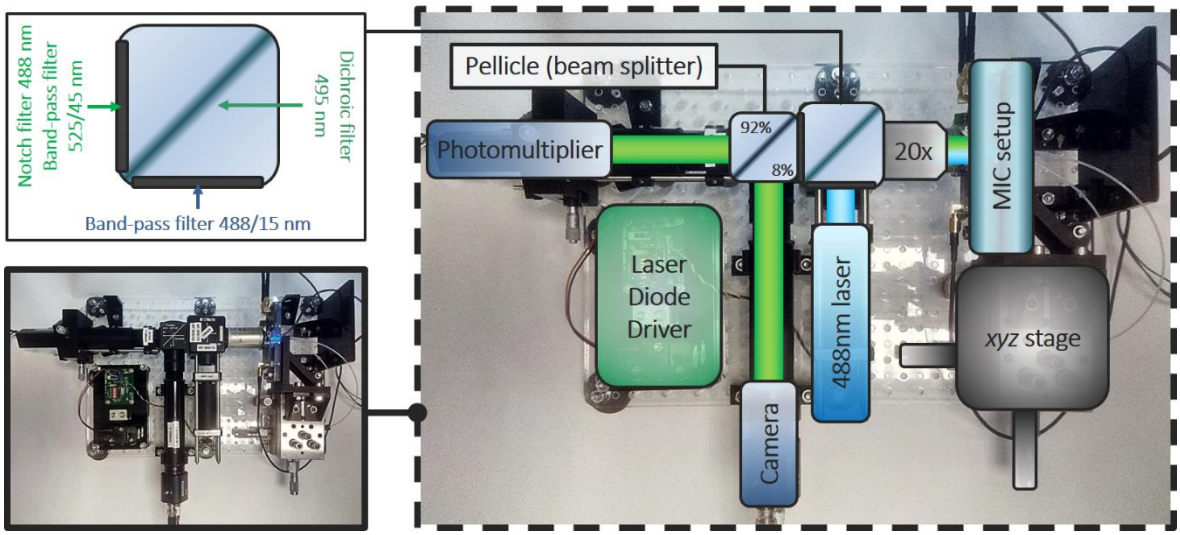


**Figure 3.11:** Diagram of the implemented, portable FMIC system components.

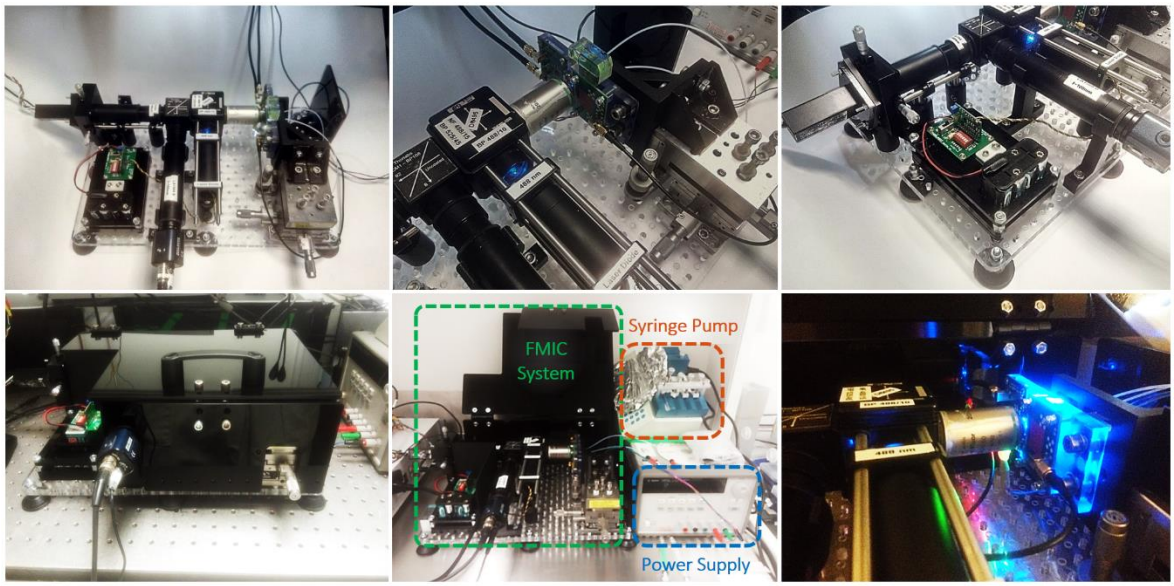


**Figure 3.12:** Photographs of the portable FMIC system: before enclosing (*top three*); after enclosing (*bottom left*); within a biological safety cabinet, with the remaining equipment needed for a measurement (*bottom middle*); and during an experiment (*bottom right*).

### 3.4.3 Signal Processing

In order to retrieve and couple single particle impedance and fluorescence signals, a similar signal processing method to that of MIC measurements must be applied to FMIC raw data. An example of the raw signals of four particles (6 µm polystyrene beads tagged with yellow-green fluorescence) passing through the detection region can be seen in **Figure 3.13**.

The impedance and fluorescence signals of individual particles are acquired together. The standard convolution-based, identification method used for impedance signals is first applied to the signal. Since the fluorescence signal will always come after the impedance signal, a time window is created using the peaks centre (see the insert of **Figure 3.13**). A maximum filter is then applied within that fluorescence time window, with the peak value being stored as the fluorescence value of the particle. This value is then coupled to the correspondent impedance signal, permitting further data analysis.

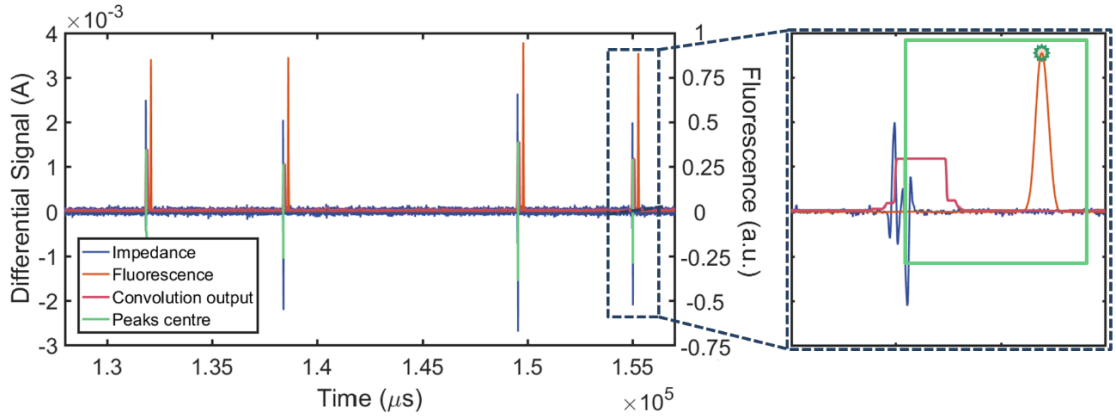


**Figure 3.13:** A section of experimental data showing four individual particles detected by the system. Both impedance and fluorescence signals are acquired. The convolution output, used to identify individual signals, and the peaks centre are also represented. The insert shows the time window (*green box*) used to identify the maximum of the fluorescence signal (*star*) and retrieve its value.

### 3.4.4 System Optimization

The efficiency of the FMIC system was evaluated by comparing it with a standard flow cytometry setup. Measurements were performed on populations of 6 µm polystyrene beads with 6 peaks of fluorescence, *i.e.*, there are 6 individual sub-populations with different fluorescence levels. Measurements performed by flow cytometry (BD Accuri™ C6), showed the presence of these six individual peaks in fluorescence and their relative percentage within the beads population (**Figure 3.14a**). Thus, the FMIC system optimization should render the setup comparable to these results.

This process involved the optimization of the various lenses and filters positions and the system focal point. For example, a too small focal point would not cover the entire detection region, thus missing a considerable percentage of particles; while a too wide focal point would add background noise from the auto-fluorescence of the chip SU8. Furthermore, the position of the focal point also required optimization as a point too close to the platinum electrodes would reduce the signal acquired, while a point too far away would increase the overall measurement volume and increase the chance of coincidence. The FMIC system was successfully optimized so it was capable of identifying the six individual peaks in fluorescence as shown in **Figure 3.14b**.

**Table 3.1** shows the percentages (mean ± standard deviation) for each sub-population obtained from standard flow cytometry and the FMIC system (N = 3). The fluorescence peaks are counted from dimmest to brightest (left to right as seen in **Figure 3.14**). Comparing the values obtained, the percentages obtained for each fluorescent sub-population are very similar. Statistical analysis, using Student's t-test, showed no significant difference between the percentages obtained from each system. Thus, the FMIC system can be confidently used in future experiments (refer to **Chapter 5** for further details).

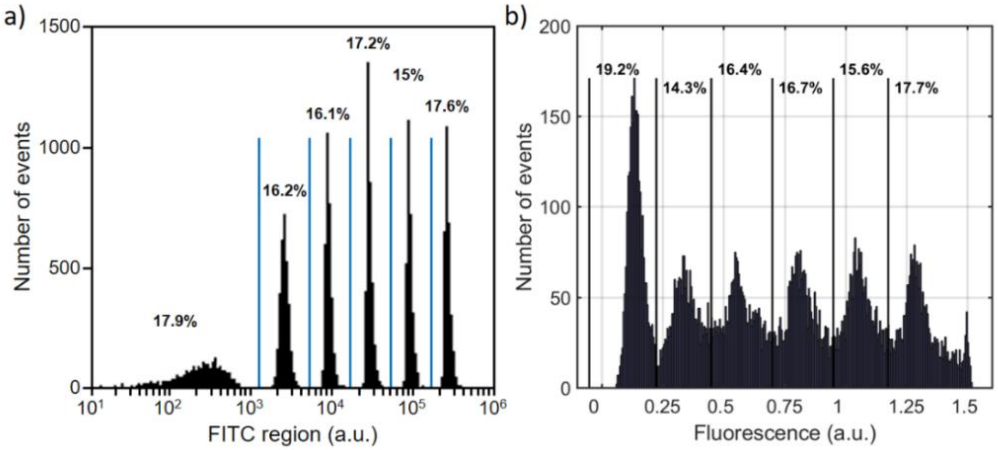


**Figure 3.14:** Fluorescence measurements of 6 µm polystyrene beads, with 6 peaks of fluorescence, using **a)** standard flow cytometry and **b)** the FMIC system.

**Table 3.1:** Percentages of the six peaks of fluorescence of the 6 µm polystyrene beads using standard flow cytometry and the FMIC system

| Technique | Percentage of sub-populations fluorescence | | | | | |
|---|---|---|---|---|---|---|
| | Peak 1 | Peak 2 | Peak 3 | Peak 4 | Peak 5 | Peak 6 |
| Flow cytometry | 17.2 ± 0.9 | 16.6 ± 1.2 | 16.3 ± 1.3 | 16.8 ± 1.1 | 16.5 ± 1.4 | 16.7 ± 1.1 |
| FMIC | 18.7 ± 2.0 | 15.5 ± 2.3 | 15.3 ± 0.8 | 17 ± 1.5 | 16.3 ± 1.1 | 17.1 ± 1.7 |

## 3.5 Summary

In this chapter, the underlying theory of AC electrokinetics and different techniques based on it were described. Amongst them, microfluidic impedance cytometry (or MIC) will be used throughout this thesis for single cell identification and analysis. A summary of the MIC system concept, implementation and experimental details was presented. Briefly, the MIC glass chips were fabricated using standard photolithography and connected to a custom setup for experiments. The signal processing and data analysis used to process the raw impedance data throughput this thesis was then introduced.

Finally, a portable fluorescence-coupled MIC system (or FMIC) was presented. The concept and execution of such system was presented, with the necessary signal processing and system optimization needs explained. A portable system allows its utilization in any scenario or location (*e.g.* within a biological safety cabinet). Furthermore, such system would be useful in situations where the dielectric properties and/or size of cell types are too similar to permit discrimination with impedance data alone. Fluorescence could then work as a reference in the experiment, confirming the identification of desired cell types, which will be explored later on this thesis.

# Chapter 4

# Dielectric Analysis of Water-borne Parasitic Protozoa

## 4.1 Introduction

Poor sanitation, lack of hygiene and unsafe water still remains an important cause of mortality, with an estimated 871,000 associated deaths in 2012 (World Health Organization, 2017b). Approximately one third of the world's population (32%) did not have access to improved sanitation in 2015 (World Health Organization, 2017b). At the same time, both developing and developed countries alike face population growth and urbanization problems, which translates to increasing cases of waterborne diseases. Caused by bacteria, viruses or protozoan parasites, these diseases lead to an increase in occurrence of diarrhoea, which affects approximately four billion people worldwide each year (World Health Organization, 2017b). Hence, the development of an alternative quick, sensitive and cost-effective method for assessing water contamination could prevent future waterborne infections.

*Cryptosporidium parvum* is one of these water-borne pathogens. It is a human pathogenic species, usually transmitted in water as infective oocysts. Ingestion of the pathogen normally causes self-limiting gastroenteritis, which can last 4 to 14 days, in immunocompetent individuals. However, in extreme cases this parasitic disease can be fatal to the elderly, infants or immunocompromised patients (Bridle *et al.*, 2012; Chalmers and Katzer, 2013). Oocysts are characterized by being highly infective, resistant to chlorination, are produced at high concentrations ($10^7$/g of faeces) and avoid the current filtration systems at low numbers (Davies and Chalmers, 2009). With only 10 oocysts capable of initiating cryptosporidiosis (Okhuysen *et al.*, 1999; King and Monis, 2007) waterborne monitoring for the presence of this pathogen is therefore essential (Scottish Water, 2013). Regulation in the UK requires investigation and disinfection procedures if 1 oocyst in 10 L is found (Bridle *et al.*, 2012).

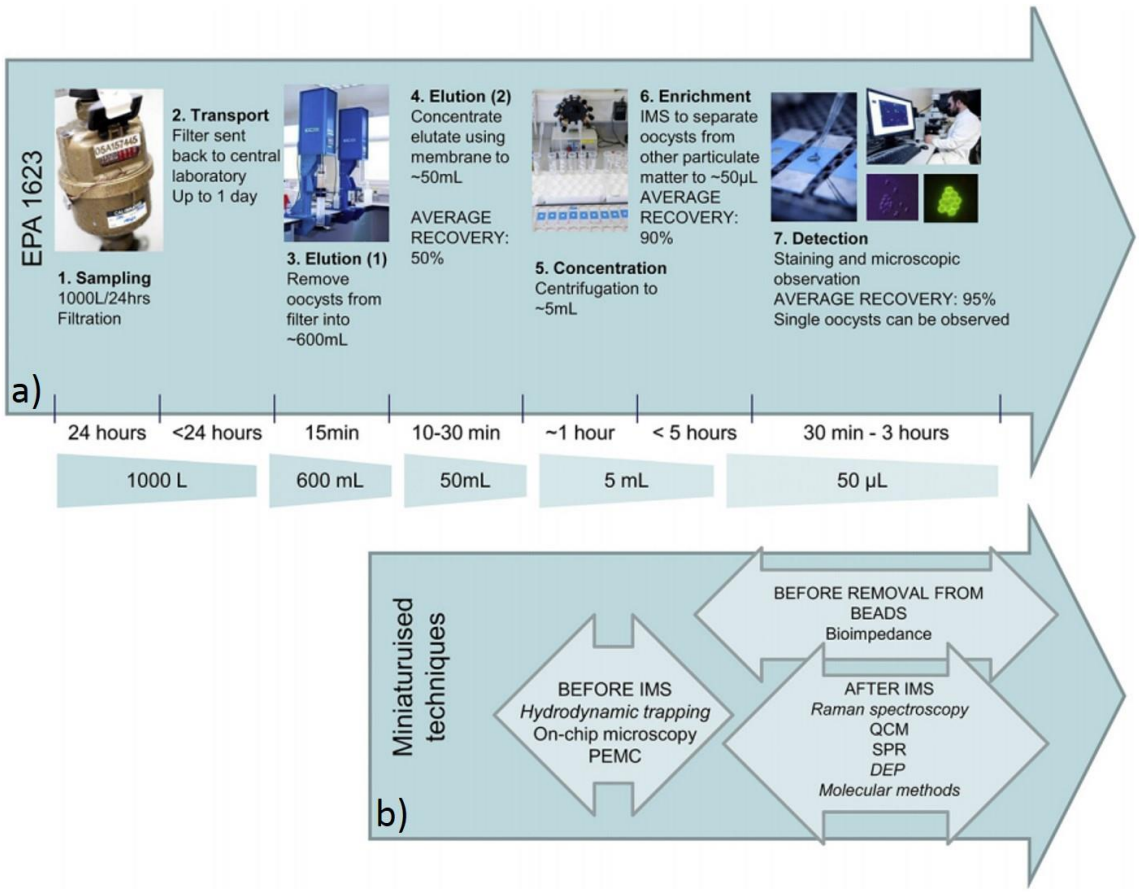


**Figure 4.1: a)** U.S EPA 1623 filtration method. The various steps are shown together with the time-scale of each step plus the volume of sample obtained. **b)** Some of the miniaturized or microfluidic approaches that could be, in the future, integrated into the existing method. Reported techniques capable of single oocyst detection are shown in italics. Adapted from Bridle *et al*. (2012).

The standard method of isolation and detection for *Cryptosporidium* oocysts present in treated water supplies, EPA 1623 (Environmental Protection Agency, 2012), typically involves the processing of 50-100 L of water (*e.g*., on site) or 1000 L (*e.g*., at the treatment works) to a 50 µL volume, before highly-skilled microscopists confirm detection using specialised techniques (Bridle *et al*., 2012) (method represented in **Figure 4.1**). This process also simultaneously recovers cysts of the *Giardia* genus – protozoan parasites that may also cause gastroenteritis if ingested by humans (Environmental Protection Agency, 2012). Not only is this procedure complex, time consuming and requires specialized personnel, but it does not confer any species-level information or viability status of recovered pathogens. Viability usually defines if an oocyst still possesses physical integrity and metabolic activity, *i.e*., in practical terms, if they still possess the capability to initiate the disease (Bridle *et al*., 2012).

The ability to rapidly enumerate and discriminate *Cryptosporidium* oocysts (post-recovery *via* EPA 1623.1) based on viability status and/or species in an automated process would reduce detection time, reduce the level of human intervention required, aid in better assessing the risk posed to human health and contribute to the saving of resources (Bridge *et al.*, 2010). At the moment, viability is often assessed through microscopic imaging (by analysing the morphology and internal content of the oocyst) and staining protocols (inclusion of membrane permeable nucleic acid stain, such as 4'6-diamidino-2-phenylindole (DAPI), or exclusion of a membrane impermeable nucleic acid stain, *e.g.* propidium iodine (PI). However it is known that measuring viability solely using inclusion/exclusion of nucleic acid stains overestimates viability. Therefore, there has been an interest in utilizing microfluidics for viability assessment as well as enrichment of parasites (Bridle *et al.*, 2012; Bridle, Miller and Desmulliez, 2014). Dielectric studies, focused on identifying viable oocysts, have shown promising results and will be described in the following section.

## 4.2 Literature Review

AC electrokinetics techniques have been used to discriminate and sort oocysts based on viability. Goater *et al.* described a device where ROT and twDEP were integrated capable of concentrating and determining the viability of oocysts (Goater, Burt and Pethig, 1997), see **Figure 4.2a**. They generated a travelling electric field directing radially from the centre of the device to the periphery. At the same time, a clockwise rotating field was created in the centre of the device. For a frequency range that caused co-field ROT, any movement caused by twDEP follows the propagation of the travelling field and *vice versa*. This effect was used to discriminate between viable and non-viable oocysts. It was observed that at 1.5 MHz they displayed anti-field and co-field rotation, respectively (**Figure 4.2b**). This value was obtained using a previously described method by the same group (Huang *et al.*, 1992). Oocysts were concentrated (**Figure 4.2c**) and differentiated with a concentration efficiency of approximately 90%. Nonetheless, as in previous examples, this system relied on microscopy to confirm efficiency or differentiate oocysts, making it more complex and prone to human-error.

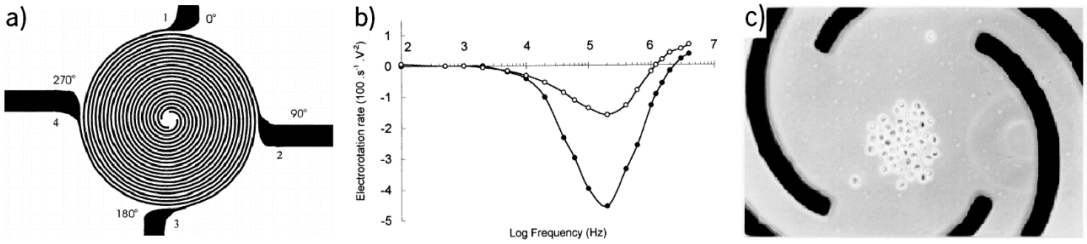


**Figure 4.2: a)** Schematic design of the twDEP-ROT electrode array, with the four parallel spiral elements. Sinusoidal voltages are applied at electrodes from 1 to 4 with relative phases shifting by 90˚. **b)** Electrorotation response for viable (●) and non-viable (○) oocysts, suspended in a 4 mS/m phosphate-buffered saline solution, using the system described in Huang *et al*. 1992. **c)** Oocysts concentrated in the centre region of the electrode array, under a 1.5 MHz rotating electrical field. Adapted from Goater *et al*. 1997.

Unni *et al*., in 2012, used DEP to trap, characterize and separate water-borne pathogens. In their work, samples containing *C. parvum*, *C. muris* and *Giardia lambia* oocysts were flushed through a microchannel with patterned interdigitated electrodes (**Figure 4.3**). When sufficiently high voltage was applied, oocysts were trapped at the edges of the electrodes, as the $\mathbf{F}_{DEP}$ surpassed the hydrodynamic lift force ($\mathbf{F}_H$). At a specific critical voltage, the two forces were balanced and oocysts were released from the electrodes. This release voltage varied with frequency (as $\mathbf{F}_{DEP}$ varies with frequency – see **Section 3.2.1**), thus the dielectric properties of the oocysts were determined based on this effect. Oocysts of different species had different trapping voltages and frequencies, and thus discrimination was attained. Despite its capability in terms of trapping, this system was limited. First, the need to perform microscopy in order to confirm trapping increases the complexity in analysis. Furthermore, with the analysis performed in bulk (averaging the results for the whole population), it would be impossible to distinguish between viable and non-viable oocysts in mixed samples.

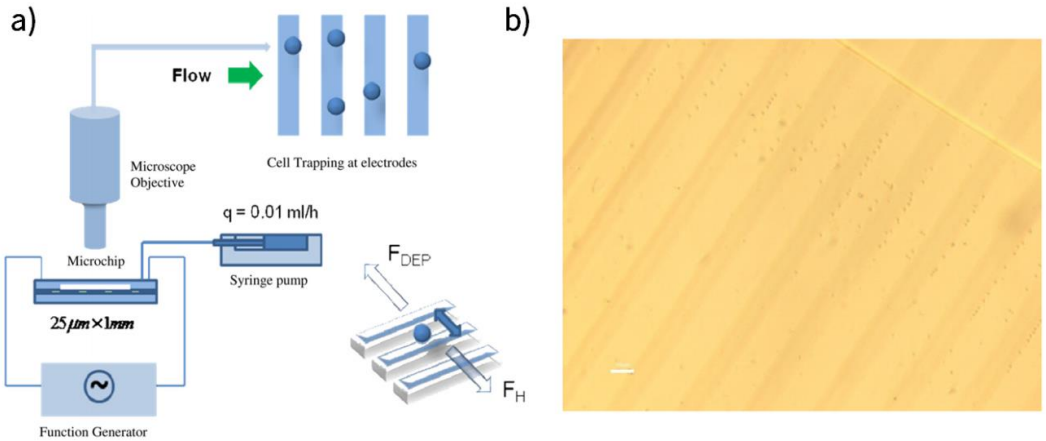


**Figure 4.3: a)** Experimental setup used for cell trapping and its working principle. **b)** Microscopy view of the trapped oocysts at the electrodes with a voltage of 5 Vpp at 200 kHz. Adapted from Unni *et al*. 2012.

Su *et al.* also used DEP to trap and characterize oocysts (Su *et al.*, 2014). A "constriction chip" (**Figure 4.4a** and **b**) was used to trap and differentiate untreated and heat-treated oocysts. Under the right conditions, positive DEP force caused translation of oocysts to the constriction tip and negative DEP force caused the opposite effect (**Figure 4.4c** and **d**). Calculated force values were fitted to a single-shell model and the dielectric properties retrieved. Oocyst translation due to dielectrophoretic force was later confirmed through fluorescence imaging (**Figure 4.4e** and **h**). It was observed that untreated oocysts would respond to negative DEP from frequencies between 1 kHz to 200 kHz approximately, shifting to a positive DEP force afterwards (**Figure 4.4e** and **f**). As for heat treated oocysts, they were continuously trapped at the constriction zone for the frequencies analysed (**Figure 4.4g** and **h**). This allowed a separation between populations if a frequency lower than 200 kHz was used (as the case of 100 kHz in **Figure 4.4e** and **g**). Nonetheless, some major drawbacks of this system were limitations in terms of retention, as there was a visible drop in DEP force for heat treated oocysts; as well as the inability to perform counting of trapped oocysts, allowing only a qualitative analysis of the populations.

Houssin *et al.* proposed an impedance-based system (**Figure 4.5**) to discriminate viable and non-viable *C. parvum* oocysts (Houssin *et al.* 2010). The system comprised four sensors, fabricated on a Pyrex substrate. Each sensor comprises an 8 mm circular array of interdigitated fingers (4 µm width; 4 µm spacing) (**Figure 4.5a** and **b**). Four circular sample wells were made in a PDMS block, covering the exact area of the sensors. Impedance measurements were performed by applying an AC signal of 10 mV, with a frequency range of 100 Hz to 1 MHz. Control measurements were first conducted by loading the sample wells with the suspending buffer and recording its impedance. Afterwards, the sample wells were emptied and suspensions of *C. parvum* (either viable or non-viable) were loaded. Measurements were made in bulk, after a stabilization period of 5 min, with the impedance of oocyst suspension recorded and compared to the control. Results showed a 15% difference in impedance magnitude when using a low conductivity buffer containing either viable or non-viable *C. parvum*, with a reported detection limit < 10 oocysts/µL.

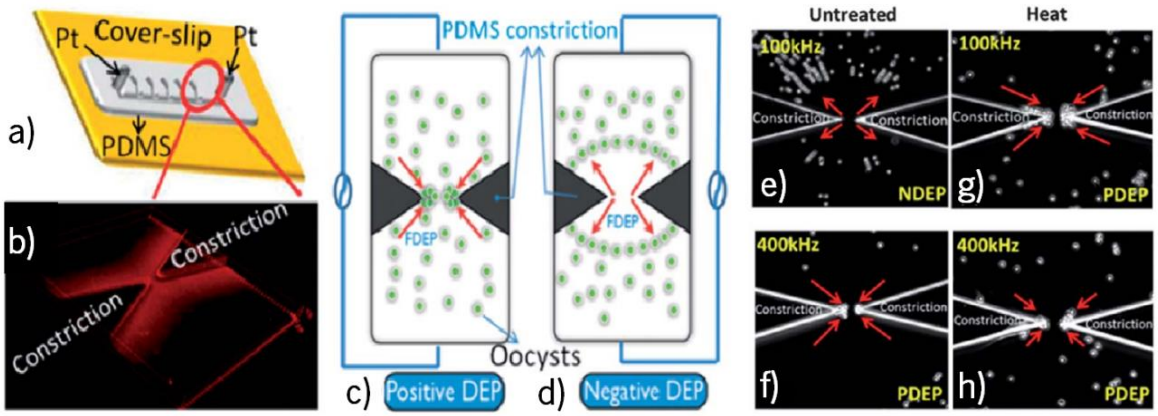


**Figure 4.4: (Left) a)** Setup of the device used. **b)** Confocal image of the "constriction chip". Oocysts trapped at the constricton region due to **c)** positive DEP and **d)** negative DEP. **(Right)** Fluorescence images of oocysts dielectrophoretic behaviour in the constriction chip after application of an AC field at 100 kHz (**e** and **g**) and 400 kHz (**f** and **h**) on untreated (**e** and **f**) and heat-treated (**g** and **h**) oocysts. Adapted from Su *et al*. 2014.

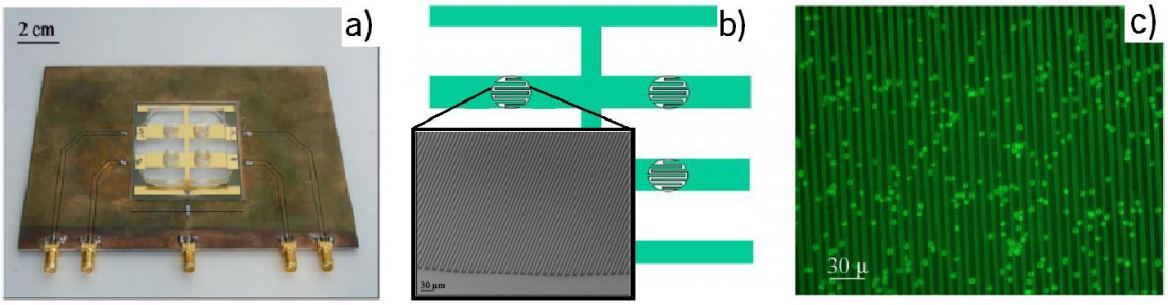


**Figure 4.5: a)** Picture of the system used. **b)** Schematic of the electrodes configuration with inset representing a SEM picture of the electrodes on the array edge. **c)** Fluorescent picture of oocysts, stained with a green fluorescent marker, on top of the electrodes array. This picture was used to confirm the location of oocysts. Adapted from Houssin *et al*. 2010.

Oocysts in any real sample, *e.g*., those recovered using EPA 1623.1, could be of mixed viability meaning that any impedance system used for detection can discern the viability of single oocysts. Therefore, **Sections 4.4** and **4.5** report on performing dielectric analysis of *Cryptosporidium* and *Giardia* species using the MIC system (**section 3.3**), aiming to perform both viability and species discrimination based solely on impedance spectroscopy.

## 4.3 Experimental Methods

### 4.3.1 Sample Preparation

The waterborne parasites used were kindly supplied by Dr. Helen Bridle, from Heriot-Watt University. Culturing of parasites, sample maintenance and preparation were performed by Dr. John McGrath, from Heriot-Watt University.

Four different stock samples were used in the analysis of untreated and heat-inactivated *C. parvum*. Samples from different stocks and ages were used to mimic the variation found in field samples, as well as test if the system was robust against different samples sources. Samples were obtained in suspensions containing PBS + 2% antibiotics + 0.01% Tween 20, and were as follows:

- A batch of calf-sourced *C. parvum* (termed WC1) obtained from Waterborne Inc. (Iowa strain; US) and used within one month of propagation;
- A second batch of calf-sourced *C. parvum* (termed WC2) obtained from Waterborne Inc. (Iowa strain) and used within 1-2 months of oocyst propagation;
- A batch of mouse-sourced *C. parvum* (termed WM) from Waterborne Inc. (Iowa strain) and used within 1-2 months of oocyst propagation;
- A batch of calf-sourced *C. parvum* (termed MC) obtained from Moredun Scientific (Moredun Strain; UK) and used when aged approximately 2-3 months.

From each stock, samples containing untreated or heat-inactivated *C. parvum* were independently prepared and the impedance measured separately. Heat-inactivation was used as a model for natural loss of viability in oocysts. In each sample, oocysts were diluted to a final concentration of ~100 oocysts/μL in PBS. The effect of varying buffer conductivity was examined using different PBS concentrations, ranging from $\sigma_{medium}$ = 0.76 – 7.10 S/m. Each buffer also contained 0.1% Tween 20 to prevent the oocysts from aggregating. Calibration polystyrene beads of 7 μm diameter were added to each sample to a final concentration of 100 beads/μL. The measured impedance of (oo)cysts was normalised with respect to the beads. For impedance analysis of untreated *Cryptosporidium spp*. and *G. lamblia*, individual samples containing either *C. parvum*, *C. muris* or *G. lamblia* (obtained from Waterborne Inc.) were prepared in PBS + 0.1% Tween 20 ($\sigma_{medium}$ = 1.6 S/m). Mixed samples were diluted to contain a total of ~100 (oo)cysts/μL and 100 beads/μL of sample; mixed samples were prepared to include equal numbers of each pathogen.

### 4.3.2 Data Analysis

Custom scripts were written in Matlab (R2016a) for data processing and statistical analysis. Samples containing each population were first measured separately. Using the comparison of untreated and heat-inactivated *C. parvum* as an example, the impedance signal was first normalised relative to the frequency-independent impedance response of the polystyrene beads. Then the *C. parvum* oocyst populations were gated from smaller debris and the larger reference beads using normalised impedance data gathered at the reference frequency (18.3 MHz). Upon gating, the normalised impedance response of gated pathogens at probe frequency (ranging from 0.25 to 50 MHz) were then plotted and analysed.

By considering the spread and orientation of the data and assuming a normal distribution, it was possible to estimate the level of discrimination achieved across both impedance dimensions (real and imaginary) at a given frequency between any two populations. Firstly, the covariance matrix was calculated to identify the directions in which the 2-D data of a single population varied most – the largest and smallest eigenvectors of this matrix indicate the direction of the data spread and the magnitude of this spread was given by the eigenvalues of the matrix. Secondly, with respect to spread and orientation of each population, confidence ellipses containing all events within 1×, 2× and 3× standard deviations of the mean were plotted. To identify the positions of equal probability deviation between two clusters, the intersection of the equivalent confidence ellipses defined the boundary where a data point has equal probability of belonging to either population. A line of equal probability deviation was then fitted to the points of intersection. Subsequently, the discrimination confidence was calculated by counting the number of oocysts from each population that plotted either side of the line of equal probability deviation. Also, scatter plots of cell populations were drawn with a mean and an elliptical boundary containing 50% of each population.

### 4.3.3 Optical Flow Cytometry

Conventional flow cytometric analysis of parasite suspensions was carried out using a BD Accuri C6 flow cytometer (BD Biosciences) with two lasers (488 nm and 640 nm). Data were exported as standard FCS files and the forward and side scattered light (FSC and SSC) signals were analysed using Matlab.

### 4.3.4 Oocyst Inactivation

In order to inactivate oocysts, samples prepared as described for untreated *C. parvum* in the previous section were subjected to heat-treatment at 70˚C for 5 mins in a heating block (Stuart Scientific, UK) before measurement. This treatment is reported in the literature as the minimum treatment required to induce loss of infectivity in the mouse model (Fayer, 1994; Su *et al*., 2014).

### 4.3.5 Excystation Assay

The waterborne parasites used were kindly supplied by Dr. Helen Bridle, from Heriot-Watt University. The excystation assay was performed by Dr. John McGrath, from Heriot-Watt University, and by Dr. Ben Horton, from Moredun Scientifc.

The viability rates of the live *C. parvum* stock samples were estimated using an *in vitro* excystation assay developed at Moredun Research Institute (UK) (Blewett, 1988), to evaluate original stock sample quality and provide a reference for comparison of untreated and heat-inactivated *C. parvum*. Upon completion of the assay, oocysts were visualised using a differential interference contrast microscope (BX50, Olympus) and the number of intact oocysts and empty shells were counted until 250 events had been recorded. For each sample, three counts were performed. The following formula was used to calculate excystation percentage: number of empty shells / (number of empty shells + number intact oocysts). The mean sample viability rates for the original *C. parvum* stock samples were: 95% for WC1, 86% for WC2; 87% for WM; and 88% for MC (see **Table 4.1** for detailed excystation assay results).

**Table 4.1**- Excystation assay results for *C. parvum* samples

| Sample | Treatment | Viability (%) | Sp/ Sh |
|---|---|---|---|
| **WC1** | Untreated | 95 | 3.1 |
| | Heat-inactivated | 9 | 0 |
| **WM** | Untreated | 87 | 2.7 |
| | Heat-inactivated | 18 | 0 |
| **WC2** | Untreated | 86 | 2.9 |
| | Heat-inactivated | 12 | 0 |
| **MC** | Untreated | 88 | 2.2 |
| | Heat-inactivated | 33 | 0 |

*Sp = sporozoite; Sh = shell.*

## 4.4 Viability Discrimination of *C. parvum*

### 4.4.1 Impedance Analysis of *C. parvum* oocysts

As previously discussed in Chapter 3, the simplest electrical model that describes the properties of a cell is the single-shelled model (**Figure 3.3**). Biological cells, as *C. parvum* oocysts (**Figure 4.6**), are insulating at low frequencies (kHz), due to the presence of the lipid cell membrane, but become increasingly conductive at higher frequencies (MHz) due to capacitive coupling across the membrane (Schwan, 1957; Morgan and Green, 2002; Raicu and Feldman, 2015). Therefore, for a viable cell the impedance at low frequencies (< 1 MHz) measures oocyst volume, while at intermediate frequencies (1 - 10MHz) becomes a function of the outer wall properties. At higher frequencies (> 10 MHz), the electric field capacitively couples across the outer wall and the impedance signal reflects the oocyst internal properties. Consequently, in the intermediate frequency range, viable oocysts of equivalent size may show differences in their impedance due to variations in the composition and/or structure of the outer wall and the interior. As the signal frequency increases further (> 30 MHz), the impedance is further influenced by the sporozoites and nucleus (Schwan, 1957; Morgan and Green, 2002; Raicu and Feldman, 2015).

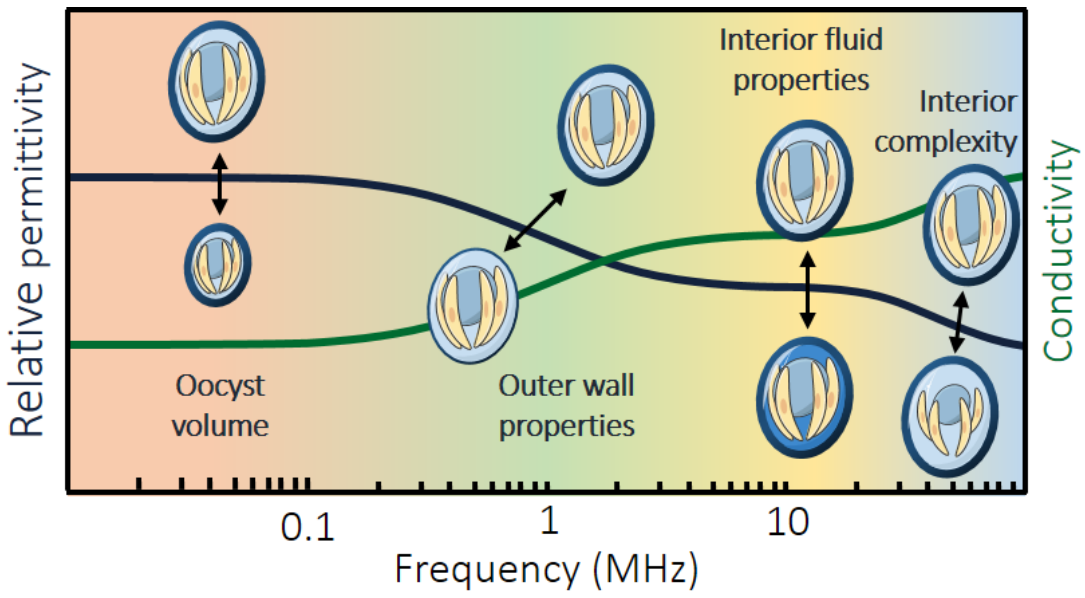


**Figure 4.6:** Illustration of the frequency-dependent dielectric response of a *C. parvum oocyst*, likely to experience multiple relaxations due to the polarisation of successive shells as the frequency increases. The relationships between some of the dielectric properties and behaviour at specific frequencies are highlighted. Note that the frequency window for these relaxations depends on the conductivity of the suspending medium.

The disruption of the selectively permeable membrane of a biological cell is typically measured using a viability stain such as propidium iodide - PI. Upon entering cells with compromised membranes, PI binds to DNA, intercalating between the bases and increasing the fluorescence significantly. If a compromised cell membrane is permeable to PI, then ions will be able to move freely across, *i.e.*, the cell is electrically "leaky" (**Figure 4.7**), which manifests as changes in impedance (Spencer, Hollis and Morgan, 2014). Therefore, non-viable cells may appear smaller in electrical volume but not optical volume.

Non-viable cells become incapable of regulating ion transfer and maintaining osmotic pressure as efficiently as viable cells (Shafiee *et al.*, 2010; Spencer, Hollis and Morgan, 2014). Upon inactivation, oocysts no longer regulate ion transfer as efficiently as viable oocysts. Viable oocysts persist in the environment for long durations due to their strict regulation of ion transfer. Thus, the internal composition of the inactivated oocyst may become compromised. For example, the microscope images of untreated (**Figure 4.8a**) and heat-inactivated (**Figure 4.8b**) *C. parvum* show that the interior constituents appear less granular in heat-inactivated oocysts, which may indicate a change in their internal composition. Therefore, by suspending oocysts in non-isosmotic conditions, it may be possible to induce change in the ionic composition of an oocyst and consequently change its intermediate and/or high frequency impedance.

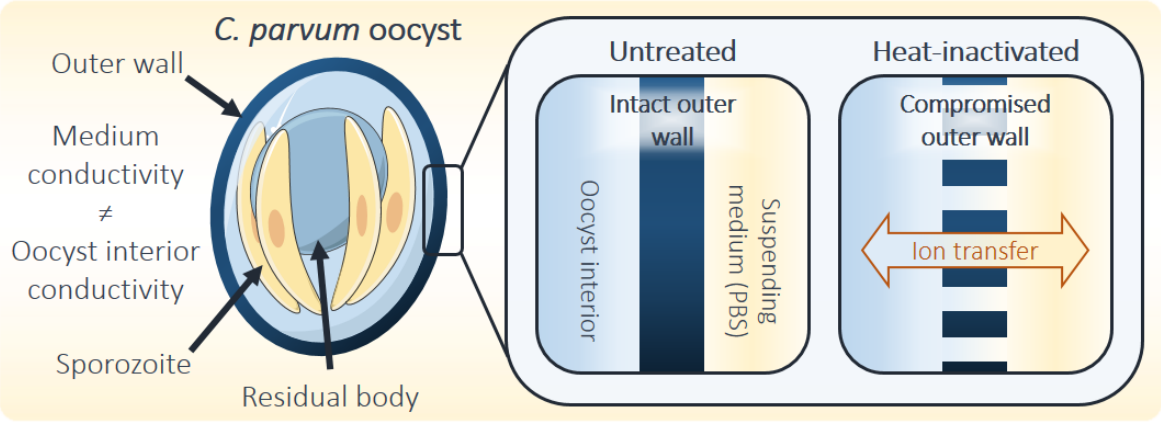


**Figure 4.7:** Schematic showing hypothetical effect of heat-inactivation on oocysts suspended in PBS. The *C. parvum* oocyst generally consists of a trilaminar outer wall, which contains four naked, sporozoites and a membrane-enclosed residual body. Upon inactivation, the direction of ion transfer is influenced by buffer conductivity/osmolality.

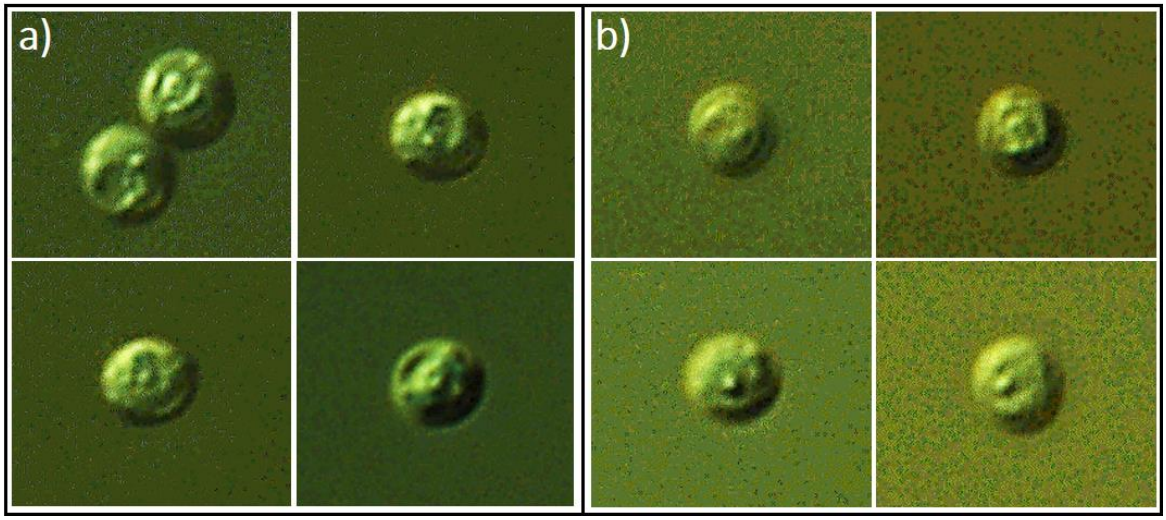


**Figure 4.8:** Microscope images of **a)** untreated and **b)** heat-inactivated oocysts (in PBS), viewed with oil immersion (100x) DIC microscopy.

**Figure 4.9** shows impedance data of the four different untreated *C. parvum* populations suspended in 0.5x PBS ($\sigma_{medium}$ = 0.76 S/m), at a reference frequency of 18.3 MHz. With environmental aging, *e.g.*, exposure to natural stress like UV light and temperature variations, or alternatively sample transit and processing when used in a laboratory setting, some oocysts may become collapsed, distorted or even excysted (Environment Agency, 2010). In these cases, the infective sporozoites may be lost and consequently oocysts become "empty shells" or "ghosts". Empty shells are routinely detected in environmental drinking-water samples (Kostrzynska *et al.*, 1999) and the impedance data in **Figure 4.9** shows the presence of such damaged/excysted oocysts. Shells have lower impedance magnitude (as they are electrically leaky) and phase on average. The subplots of **Figure 4.9a-d** are in ascending order of age. Interestingly, the youngest and oldest *C. parvum* samples have the least and most shells present respectively: a = 6%, b = 6%, c = 8% and d = 41%, which implies that the number of shells increases with environmental age.

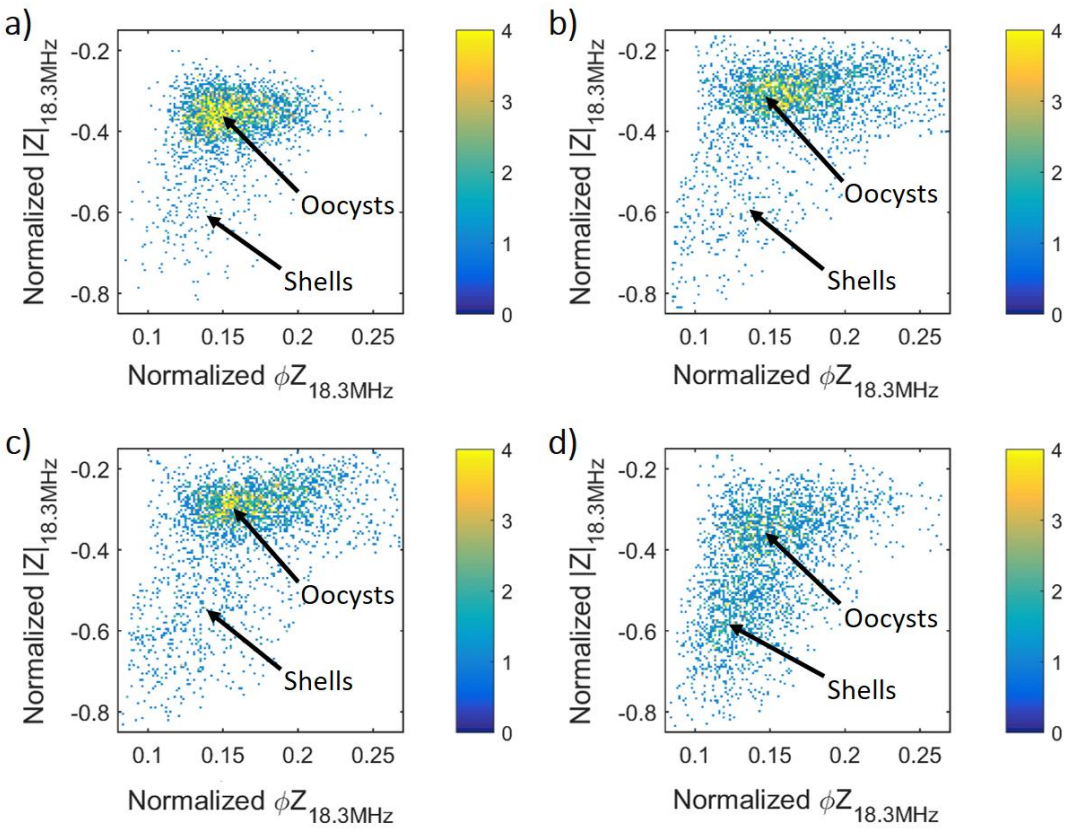


**Figure 4.9:** Normalized impedance scatter plots (magnitude - |Z| versus phase – ΦZ), at reference frequency of 18.3 MHz, for four untreated *C. parvum* samples. Each data point is a single oocyst and colour represents data density. **a)** Calf-sourced oocysts (Iowa strain) measured within 1 month of oocyst propagation. **b)** Mouse-propagated oocysts (Iowa strain) used within 1–2 months. **c)** Different sample of calf-sourced oocysts (Iowa strain) used within 1–2 months. **d)** Calf-sourced oocysts (Moredun strain) measured within 2–3 months.

### 4.4.2 Impedance Data Modelling of *C. parvum* oocysts

Generally, the dielectric behaviour of biological cells in suspension is defined by Maxwell's mixture theory – MMT, as previously discussed in **Section 3.1.5** (Maxwell, 1881). MMT-based, multi shell models have been used to model the dielectric properties of cells (Hanai, Koizumi and Irimajiri, 1975; Irimajiri, Hanai and Inouye, 1979; Huang *et al.*, 1992; Wang *et al.*, 1994). Single shell models describe cells with just a membrane and no interior organelles, while double shell models are applied for more complex cells with interior organelles. The frequency-dependent behaviour of these models can be plotted in terms of Debye relaxations (Debye and Falkenhagen, 1928). Single shells have a single relaxation and double shells have two (the first associated with the cell membrane and the second with the interior organelles - **Figure 4.6**) (Pethig, 1979; Morgan and Green, 2002; Raicu and Feldman, 2015). Thus, the integrity and complexity of a cell can be inferred by fitting data to these models.

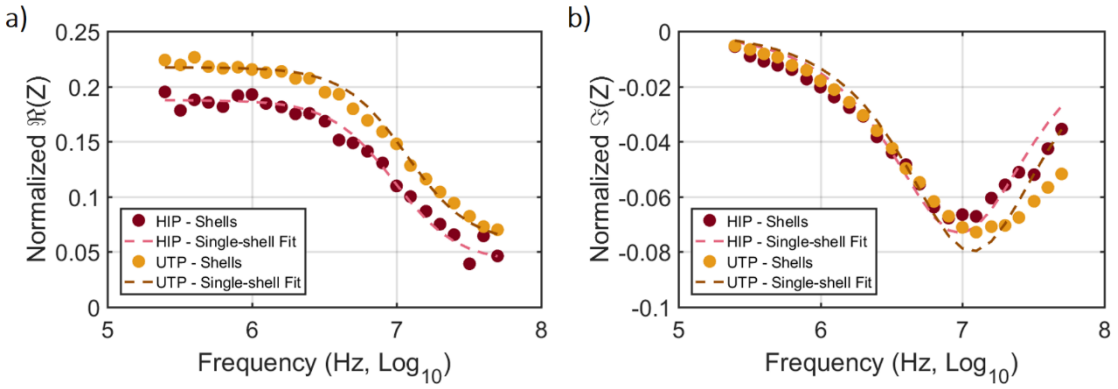


**Figure 4.10:** Normalized **a)** real and **b)** imaginary parts of impedance of shells from untreated (UTP) and heat-inactivated *C. parvum* (HIP) samples, across the measured probe frequency spectrum. The optimal Debye single-shell fits (*dashed lines*) are plotted on top of individual probe frequency mean values (*circles*).

Untreated (UTP) and heat-inactivated *C. parvum* (HIP) oocysts, suspended in 0.5x PBS ($\sigma_{medium}$ = 0.76 S/m), were measured (probe frequencies 250 kHz to 50 MHz). The impedance data for the empty shells in UTP and HIP samples was modelled by fitting the data to a single Debye relaxation representing a single shell (**Figure 4.10**). As expected, the simple structure of the oocyst shell, where no sporozoites or other organelles are present, fits well to a single relaxation (UTP: $R^2$ = 0.9994; HIP: $R^2$ = 0.9993). Moreover, heat-inactivation results in physical disruption of the membrane, leading to an apparent reduction in the magnitude of the low frequency impedance (**Figure 4.10a**).

The main oocyst population was also fitted to a single shell model (**Figure 4.11**), but poor fits were obtained, specifically to the imaginary part of impedance (UTP: $R^2_{imaginary}$ = 0.9983; HIP: $R^2_{imaginary}$ = 0.9985). This indicates that this model does not fully represent the intricacies of the oocyst structure.

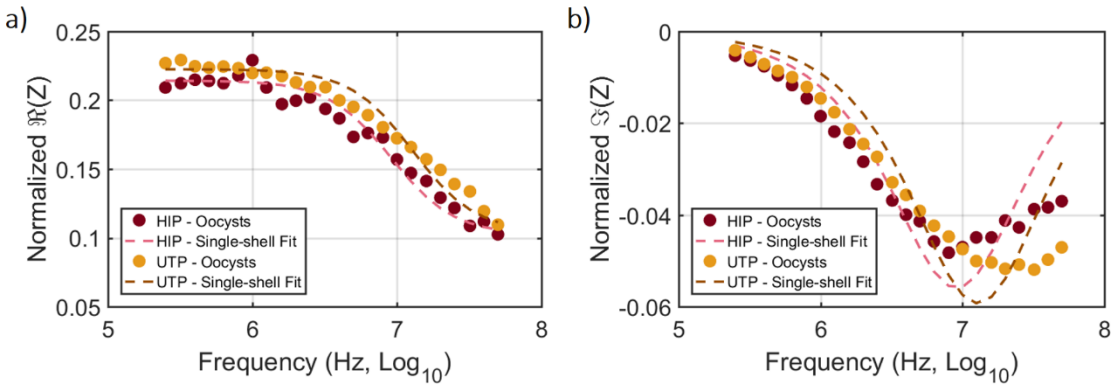


**Figure 4.11:** Normalized **a)** real and **b)** imaginary parts of impedance of oocysts from untreated (UTP) and heat-inactivated *C. parvum* (HIP) samples, across the measured probe frequency spectrum. The optimal Debye single-shell fits (*dashed lines*) are plotted on top of individual probe frequency mean values (*circles*).

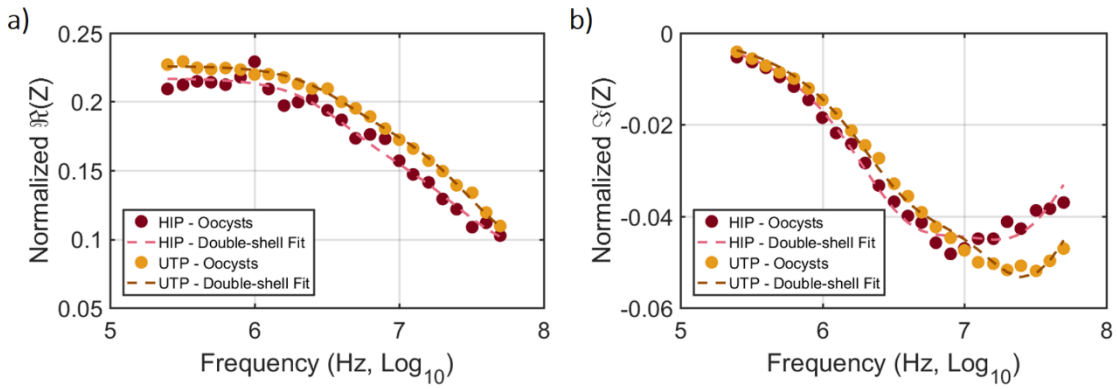


**Figure 4.12:** Normalized **a)** real and **b)** imaginary parts of impedance of oocysts from untreated (UTP) and heat-inactivated *C. parvum* (HIP) samples, across the measured probe frequency spectrum. The optimal Debye double-shell fits (*dashed lines*) are plotted on top of individual probe frequency mean values (*circles*).

Data was then fitted to a double shell model (**Figure 4.12**), which provided an optimal fit (UTP: $R^2$ = 0.9999; HIP: $R^2$ = 0.9999), *i.e.*, it correctly represents the relaxation the oocyst membrane (~1-10 MHz) followed by the relaxation of the interior content (>10 MHz). Furthermore, as seen for the shells, heat-inactivation and consequent outer wall disruption causes a small drop in low frequency impedance (**Figure 4.12a**). Thus, these simple models confirmed that the two populations were correctly identified in **Figure 4.9**, meaning that the *C. parvum* shells can be excluded from future analysis of the oocysts.

### 4.4.3 Discrimination at Optimal Suspension Conductivity

**Figure 4.13** shows the mean impedance magnitude and phase of the untreated and heat-inactivated *C. parvum* populations suspended in 1x PBS ($\sigma_{medium}$ = 1.51 S/m). With increasing buffer conductivity, the relaxation frequency of the outer wall shifted towards higher frequencies, as expected (Pethig, 1979; Morgan and Green, 2002). Furthermore, **Figure 4.13** indicates that the dielectric properties of untreated and heat-inactivated *C. parvum* are different, especially at higher frequencies (see **Figure 4.13c-e**), where the signal is influenced by the properties of the oocyst interior.

The ability of MIC to probe different layers of the oocyst structure means that impedance analysis enabled clearer discrimination than optical flow cytometry (see **Figure 4.14**). Generally, the *C. parvum* oocyst interior consists of four (nuclei-containing) sporozoites – the infective agents of the oocyst – and a membrane-enclosed residual body. The residual body contains a large lipid body, numerous amylopectin granules, a crystalline protein inclusion, ribosomes and

cytomembranes (Fayer and Xiao, 2012). For heat-inactivated *C. parvum*, the integrity and/or composition of the internal fluid and interior organelles was presumably compromised; and the osmolality difference between the oocyst interior and suspending medium was greater in 1xPBS than the 0.5x PBS buffer. Thus, the difference in the high frequency impedance of the parasite populations was greater for those re-suspended in PBS (**Figure 4.13e**). These findings suggest that the parasites were exposed to hyperosmotic conditions when suspended in PBS. The data in **Figure 4.13a** and **b** also indicated no difference in either the magnitude or phase, regardless of strain or source of the *C. parvum* oocysts.

Following these findings, oocysts were re-suspended in a high conductivity, hyperosmotic buffer (5x PBS; $\sigma_{medium}$ = 7.10 S/m), which gave rise to the largest difference in the impedance of untreated and heat-inactivated *C. parvum* (**Figure 4.15**). High frequency impedance (50 MHz) enabled the clearest discrimination of the parasite populations.

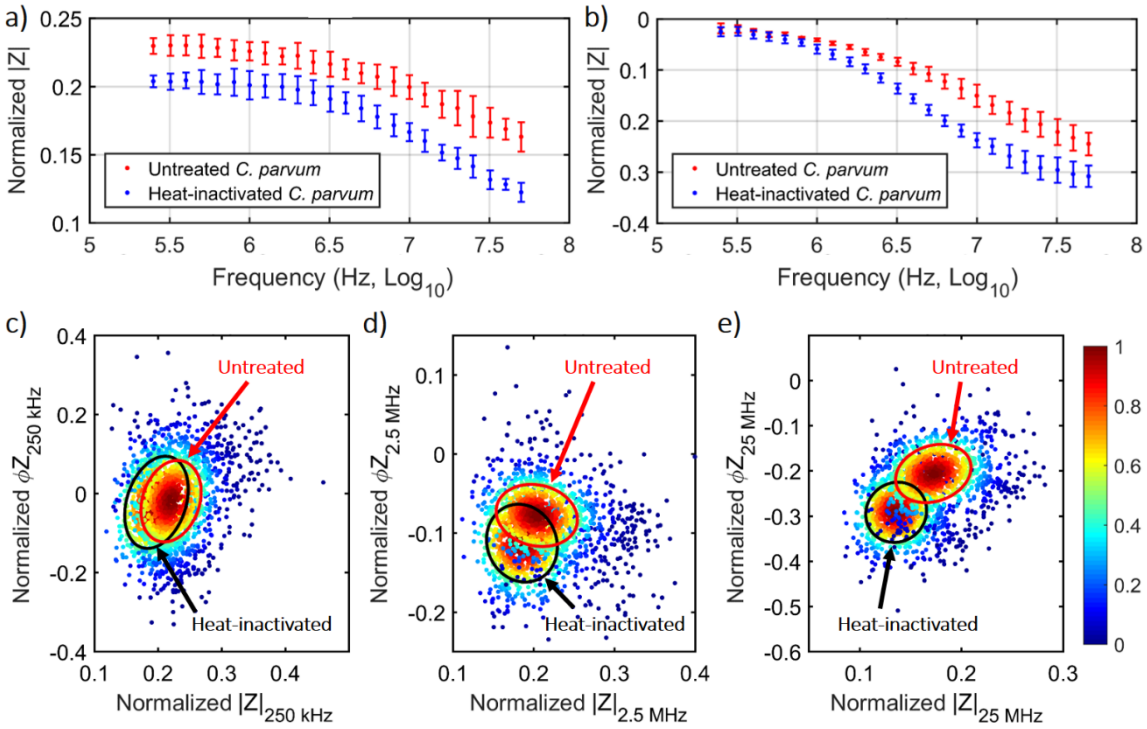


**Figure 4.13: a)** Impedance magnitude and **b)** phase of untreated (*red*) and heat-inactivated (*blue*) *C. parvum* as a function of frequency for all four *C. parvum* samples (mean ± standard deviation; N = 4). Normalized impedance scatter plots (magnitude - |Z| versus phase – ΦZ), at probe frequency of **c)** 250 kHz, **d)** 2.5 MHz and **e)** 25 MHz, of untreated and heat-inactivated *C. parvum* plotted together. The annotated confidence ellipses contain 50% of each population and the colour of each datapoint represents the normalized proximity of each event to the respective population mean. Scatter plots data from the "merged" sample.

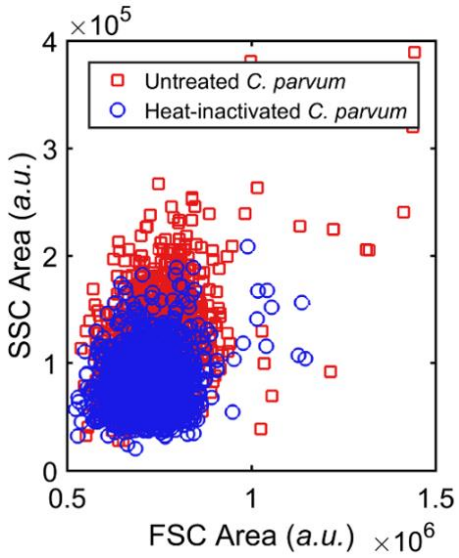


**Figure 4.14:** Conventional flow cytometry data (SSC *vs* FSC) for untreated and heat-inactivated *C. parvum* in PBS. Individual optical scatter data for viable or non-viable *C. parvum* are plotted together.

To quantify the discrimination between populations, the mean point of each population was first calculated assuming a 2D Gaussian distribution (along magnitude and phase). Ellipses containing 50%, 95% and 99% of each population were then defined and the intersection of the same ellipse type of each population gave the threshold of equal probability. This threshold indicated where a detected event has equal probability of belonging to either populations and is an estimate of confidence in the discrimination between untreated and heat-inactivated *C. parvum*.

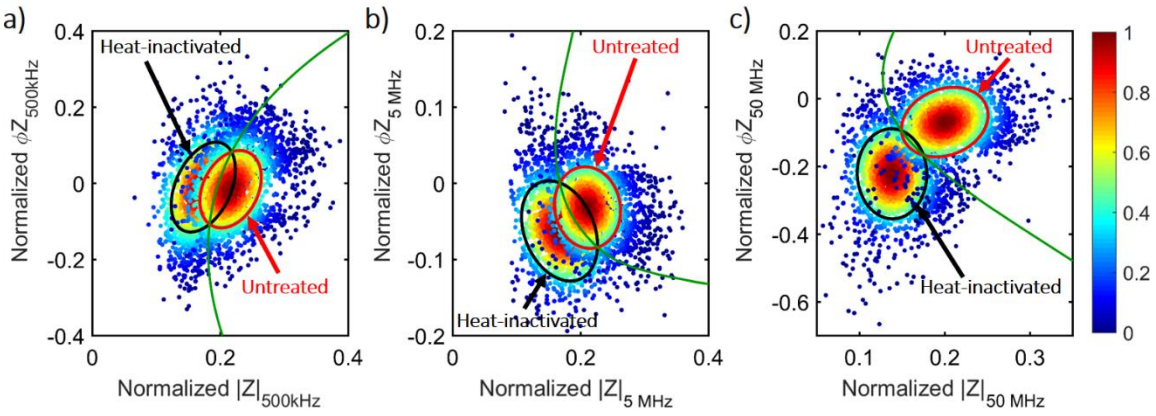


**Figure 4.15:** Normalized impedance scatter plots (magnitude - |Z| versus phase – ΦZ), at probe frequency of **a)** 500 kHz, **b)** 5 MHz and **c)** 50 MHz, of untreated and heat-inactivated *C. parvum* plotted together. The annotated confidence ellipses contain 50% of each population and the colour of each datapoint represents the normalized proximity of each event to the respective population mean. The threshold of equal probability is also represented (*green line*). Data from the "merged" sample.

Using the threshold, the identification confidence for each individual sample was calculated (**Table 4.2**). A "merged" sample was also created by joining 1000 random events of each sample. This sample should be a better representation of an environmental sample, where any oocysts present could have different ages, strains and sources (**Figure 4.15** shows data from this sample). For example, at 50 MHz, where the clearest discrimination was achieved (**Figure 4.15c**), 91% of the events to the right of the equal probability boundary were from the untreated *C. parvum* population and 92% of the events to the left were from the heat-inactivated *C. parvum* population. Considering all samples (N = 4), 89 ± 4% of untreated events and 89 ± 5% of heat-inactivated events were correctly gated. Thus, MIC enabled the identification of untreated or heat-inactivated *C. parvum* with approximately 90% confidence in these experimental conditions. Results also demonstrated that sample age and/or sample viability negatively affects the discrimination level. For example, confidence in heat-inactivation identification fell from 97% for the 1 month old, WC1 sample, to 84% for the 2 month old, WM sample.

**Table 4.2:** Identification confidence for untreated and heat-inactivated *C. parvum* oocysts, from samples of different age, at a frequency of 50 MHz in 5x PBS

| Sample (N = 250 events) | Sample age (months) | Identification confidence (%) | |
|---|---|---|---|
| | | Untreated | Heat-inactivated |
| **WC1** | 0 – 1 | 95 | 97 |
| **WC2** | 1 – 2 | 87 | 86 |
| **WM** | 1 – 2 | 85 | 84 |
| **MC** | 2 – 3 | 88 | 90 |
| **Merged*** | - | 91 | 92 |
| **Mean** | | 89 ± 4 | 89 ± 5 |

**Constituted of 1000 events of each sample*

## 4.5 Species discrimination of *C. parvum*, *C. muris* and *G. lamblia*

There are at least 27 valid species and 60 genotypes within the genus *Cryptosporidium* (Nichols *et al.*, 2010), each varying in the significance of risk it poses to human health. The standard EPA 1623.1 isolation method is not a *C. parvum* specific detection technique and it does not confer any species-level information o of recovered pathogens (Environmental Protection Agency, 2012; Bridle *et al.*, 2012). Thus, the impedance of pathogens which are commonly isolated using EPA 1623.1 was measured to assess the suitability of MIC for species- and genus-level discrimination of waterborne parasites. Specifically, samples containing *C. parvum*, *C. muris* and *G. lamblia* suspended in PBS ($\sigma_{medium}$ = 1.61 S/m) were analysed. Flow cytometry measurements were first conducted with these pathogens (**Figure 4.16a**). A high level of overlap between the different populations was observed in flow cytometry data.

To properly gate and characterise the impedance of each population, samples were firstly measured independently (**Figure 4.16b**). The cube root of the low frequency impedance magnitude is proportional to particle diameter (Spencer, Elliott and Morgan, 2014; Spencer, Hollis and Morgan, 2014). Using this data, the average diameter of the parasites was determined as: *C. parvum* = 4.3 ± 0.3 µm; *C. muris* = 5.9 ± 0.4 µm; and *G. lamblia* = 9.3 ± 0.4 µm (mean ± standard deviation from N = 3 samples). These values correlate well with dimensions obtained from optical imaging (LeChevallier, Norton and Lee, 1991; Chalmers and Katzer, 2013).

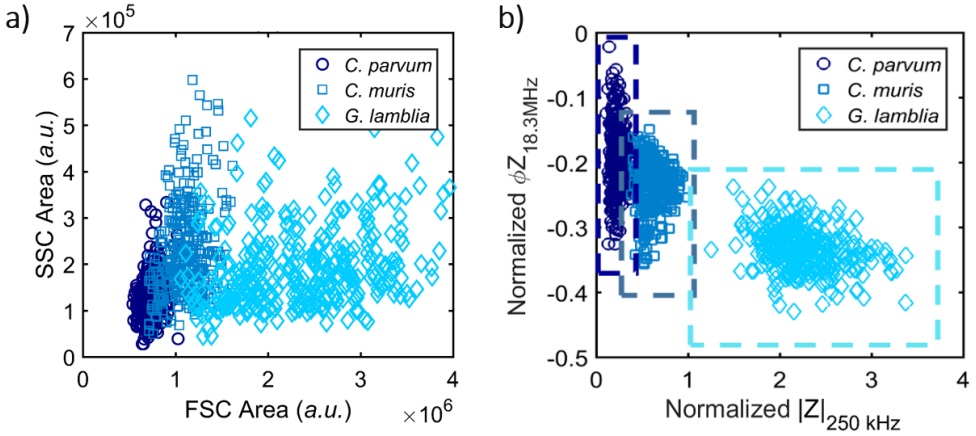


**Figure 4.16: a)** Conventional flow cytometry data (SSC vs FSC) for all parasite species in PBS. Individual optical scatter data for each population plotted together. **b)** Normalized impedance scatter plot (magnitude - |Z| at probe frequency 250 kHz versus phase – ΦZ at reference frequency 18.3 MHz), of *C. parvum*, *C. muris* and *G. lamblia* samples plotted together.

A sample containing all the different populations was then measured - **Figure 4.17** shows the data plotted as high frequency phase (18 MHz) versus low frequency magnitude (250 kHz), which effectively plotted variations in internal structure/composition versus size. Using the gates pre-defined in **Figure 4.16b**, the three populations were identified. Thresholds of equal probability were defined neighbouring populations, *i.e.*, *C. parvum/C. muris* and *C. muris/G. lamblia*. Thus, it was possible to identify *C. parvum* with 98% confidence, *C. muris* with 93% confidence and *G. lamblia* with over 99% confidence. These results suggest that impedance analysis allowed discrimination of these pathogens with a high degree of confidence, especially when compared to conventional flow cytometry (**Figure 4.16a**).

Two *Cryptosporidium* species (*C. parvum* and *C. hominis)* are estimated to be responsible for over 90% of human cases of cryptosporidiosis (Bouzid *et al.*, 2013). However, other species (*C. meleagridis*, *C. canis, C. cuniculus* and *C. felis*) have also been associated with human infection and are considered "major human-pathogenic species". In terms of oocyst dimensions, all these "major" species are typically reported within the size range of 4.0-5.0 x 5.0-5.5 µm (Chalmers and Katzer, 2013). MIC may be able to discriminate oocysts of this size from other species outside this size range that pose little to no risk. However, analysis of distinct species that have similar dimensions is required to assess whether inter-species variations in oocyst wall and interior structure/composition may facilitate impedance-based discrimination of such oocysts.

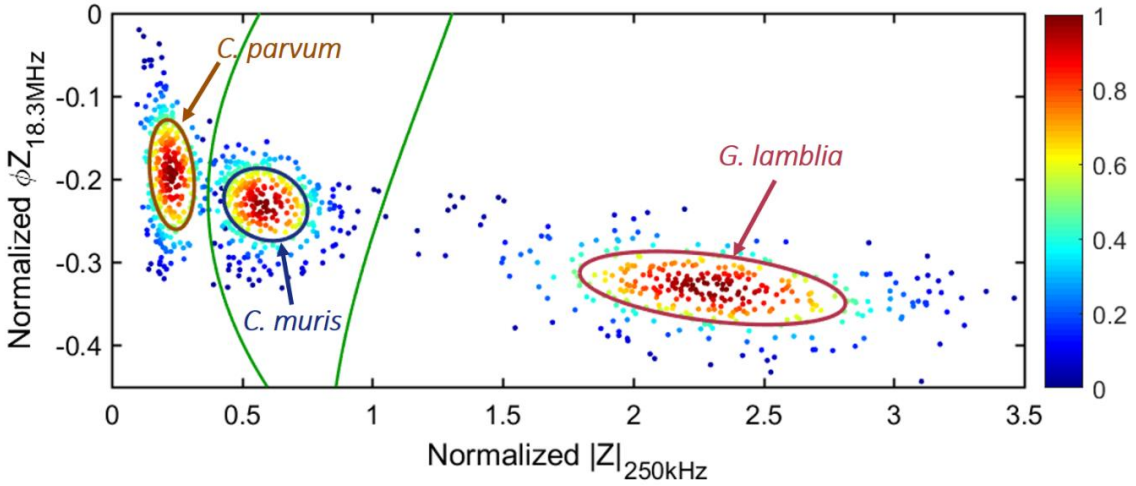


**Figure 4.17:** Normalized impedance scatter plot (magnitude - |Z| at probe frequency 250 kHz versus phase – ΦZ at reference frequency 18.3 MHz), of a sample containing *C. parvum*, *C. muris* and *G. lamblia*. The annotated confidence ellipses contain 50% of each population and the colour of each datapoint represents the normalized proximity of each event to the respective population mean. The thresholds of equal probability are also represented (*green lines*).

## 4.6 Summary

MIC has shown capable of assessing the species and viability status at the single (oo)cyst level. The impedance properties of *C. parvum* oocysts of varying source, strain and age were measured in buffers of different conductivity. The impedance data of the oocyst and shell populations within each sample were fitted to either a single or double shell model. The results indicated that it was possible to identify the presence of damaged/ excysted oocysts (termed shells) and that shell numbers increased with environmental age.

The results showed that untreated and heat-inactivated *C. parvum* could be identified with over 90% certainty at high frequencies when suspended in 5x PBS. It is hypothesised that optimal discrimination at higher conductivity buffer is because the non-viable parasites lose the ability to regulate ion transfer, resulting in an inward flux of ions that increases the electrical "contrast" between untreated and heat-inactivated *C. parvum*.

The ability of MIC to probe different layers of the oocyst structure meant that impedance analysis enabled a clearer discrimination than other label-free techniques (*e.g.* optical flow cytometry). Previous attempts to discriminate viable and non-viable oocysts using impedance spectroscopy had only shown a 15% difference between the two populations (Houssin *et al.*, 2010). Furthermore, this value was attained with bulk measurements and not at a single-cell level, as MIC is capable of.

Other AC electrokinetics techniques have also been used for discrimination, with ROT and twDEP integrated system capable of discriminating viable from non-viable with 90% efficiency (Goater, Burt and Pethig, 1997). While the level of discrimination is comparable to that obtained by MIC, the system has major problems, including analysis of low numbers of oocysts (~55 per experiment) or small sample volumes (~1.45 µL), while the MIC system processes samples of hundreds of oocysts at higher volumetric flows (~40 µL/min).

In addition, single *C. parvum*, *C. muris* and *G. lamblia* (oo)cysts were identified with over 93% certainty from the high frequency phase *vs* low frequency magnitude data (when suspended in PBS). Unni *et al.* had previously used DEP to separate the same species, however did not present any quantitative value for its efficiency (Unni *et al.*, 2012). Furthermore, the system was limited in its application, performing

measurements in bulk and requiring microscopy for separation assessment, which does not occur in MIC experiments.

In summary, MIC technology could potentially be useful for water utilities in, *e.g.,* a warning system which more rapidly identifies single Cryptosporidium and Giardia (oo)cysts in a standard 50 µL post-recovery sample, via EPA 1623.1. As demonstrated, the system can simultaneously provide an indication of the viability and species of recovered (oo)cysts, which may reduce the requirement for skilled microscopists and the associated labour demands.

# Chapter 5

# Dielectric Characterization of Intra-cellular Parasitic Protozoa

## 5.1 Introduction

The World Health Organization (WHO) has frequently reorganized its framework to properly manage infectious, parasitic diseases, such as human malaria and leishmaniasis. Parasitic infections are typically prevalent in resource-scarce regions of the globe, particularly in tropical areas (Tay *et al.*, 2016). It is widely accepted that rapid and efficient diagnosis is a critical aspect for controlling infectious diseases. An early detection of infection facilitates a timely access to care, delays the development of treatment resistance by the parasite, and saves money on secondary treatments (Wongsrichanalai *et al.*, 2007). A wide range of methods are currently used for diagnosis, including physical examinations, staining and microscopy techniques, or serological tests for pathogenic markers. These methods usually require a sample of bodily fluid (as blood or urine). However, there are still several hurdles affecting the diagnosis process including high costs, lack of controlled environments, prolonged turnaround times and the need of highly trained personnel (Ibrahim *et al.*, 2015).

The WHO has suggested that new diagnosis tools for parasitic diseases, endemic to developing countries, should aim to be: affordable, sensitive, specific, user-friendly, rapid and robust, equipment free and deliverable to end-users. These criteria are usually referred to using the acronym ASSURED (Martinez, Phillips and Whitesides, 2010). Many of these characteristics are shared by various microfluidic technologies, leading to an increase in research efforts, especially over the past decade, to develop new methods to facilitate low-cost diagnosis of parasitic infectious diseases (Ibrahim *et al.*, 2015; Tay *et al.*, 2016).

Despite increasing efforts to enhance current diagnostic tools, many aspects of parasitic infections are still not fully understood. In particular, the host cell

requirements and alterations during the life cycle of some protozoan parasites are not well studied (Leirião *et al.*, 2004). These intracellular parasites have developed ways to exploit host cell resources efficiently, ensuring their survival, differentiation and replication (Leirião *et al.*, 2004; Sibley, 2011). Such processes have consequences for the host cell, and might result in changes in the biophysical properties of the cell. Therefore, a study of the dielectric properties of intracellular parasitic protozoa could reveal new information and help in the development of new strategies for diagnosis. This chapter focuses on the dielectric characterization of two important parasitic diseases: human malaria and leishmaniasis.

### 5.1.1 Human Malaria

Malaria is undeniably one of the most serious health problems in the world today, and is a social and economic burden to many developing countries where the disease is endemic. **Figure 5.1** shows countries with ongoing transmission. Estimates of more than 200 million new cases and a death toll of approximately 445 000 for 2016 alone, put malaria as the world's most life-threatening parasitic disease (World Health Organization, 2017c). To date, five species of *Plasmodium* parasite are known to transmit human malaria: *P. falciparum*, *P. malariae*, *P. ovale*, *P. vivax* and the simian parasite *P. knowlesi*. Of these, *P. falciparum* is responsible for the most serious symptomatology and the highest number of deaths, mainly in sub-Saharan Africa.

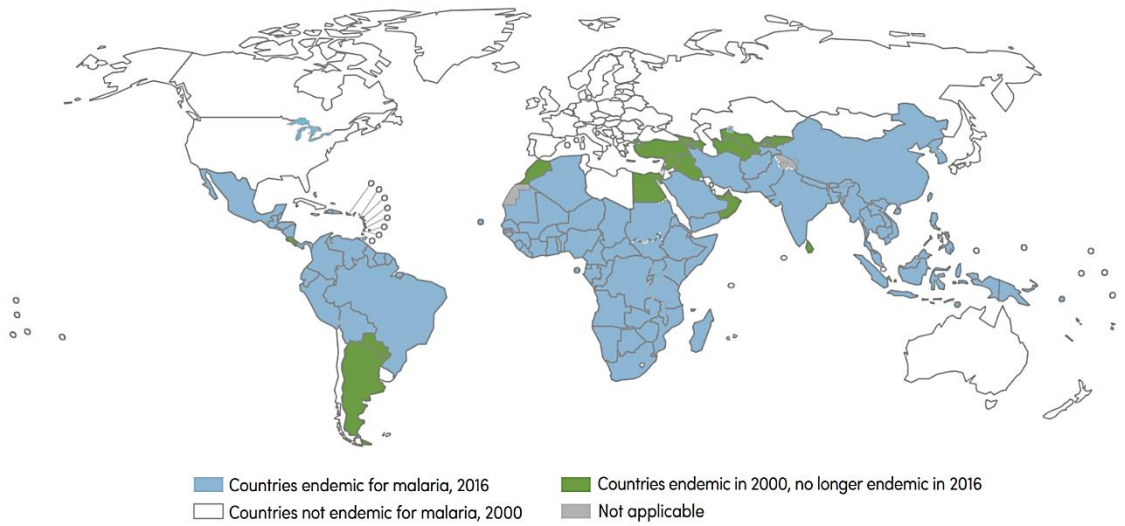


**Figure 5.1:** World map presenting the countries with ongoing transmission of malaria as of 2016. Adapted from the annual World Malaria Report by the WHO (2016).

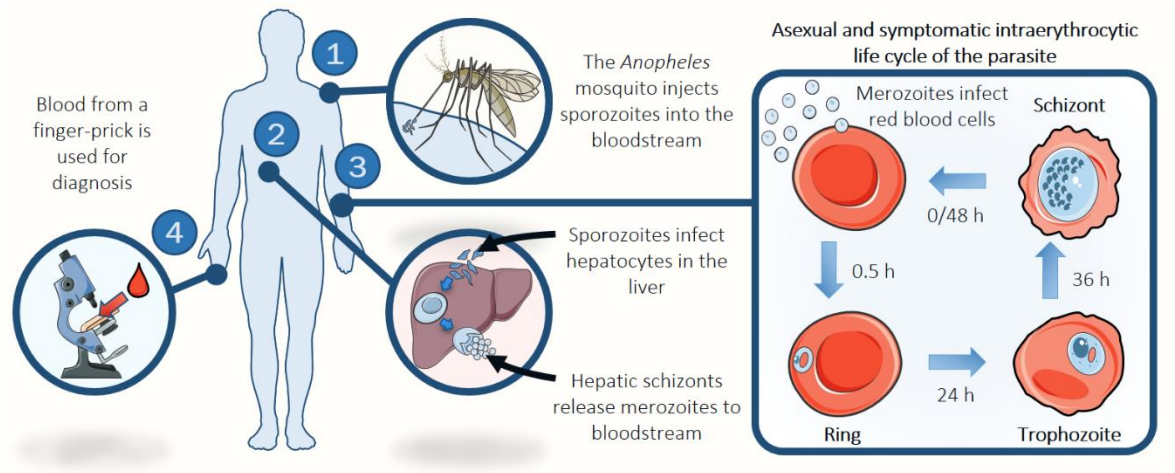


**Figure 5.2:** Representation of the *P. falciparum* life-cycle in the human host and the common diagnosis method. This includes: 1 – injection of parasitic sporozoites into the host by an *Anopheles* mosquito; 2 – invasion of hepatic cells, and consequent production and release of parasitic merozoites into the bloodstream; 3 – invasion of RBCs, proceeded by the intraerythrocytic life cycle of the parasite; 4 – diagnosis using microscopy, the current "gold-standard" method, to detect infected RBCs in a blood sample.

*Plasmodium* parasites have a complex life cycle, which involves multiple stages in the mosquito vector and human host (**Figure 5.2**). The infection is established when an infected mosquito of the genus *Anopheles* bites a human host and injects parasites in the sporozoite form, into the bloodstream. The parasites reach the liver and invade the hepatocytes, developing into the hepatic schizont, which produces and releases thousands of daughter cells, called merozoites into the bloodstream. These invade the red blood cells (RBCs). During the intraerythrocytic period, the parasite matures progressively into ring, trophozoite and schizont stage from which newly formed merozoites are released, ready to invade new red blood cells and start a new cycle (Cowman *et al.*, 2016).

The intraerythrocytic stage is responsible for the symptomatology of malaria and has a different time length depending on the *Plasmodium* species (24h for *P. knowlesi*, 48h for *P. falciparum*, *P. ovale*, *P. vivax*, 72h for *P. malariae*). Throughout the development of the parasite within the host RBC, the host cell is increasingly modified. Although parasite invasion and growth does not cause a significant change in volume of the infected cell (Esposito *et al.*, 2010), the host cell membrane is profoundly affected. Parasite infection alters the membrane lipid composition and parasite proteins are actively transported to the membrane, not only creating new permeation pathways for metabolite transportation, but also altering the underlying membrane cytoskeleton (Cranston *et al.*, 1983; Ginsburg *et al.*, 1985; Hsiao *et al.*, 1991; Vial and Ancelin, 1998; Kirk, 2001; Ginsburg and Stein, 2004).

A consequence of these membrane changes is the progressive stiffening of the infected RBCS (*i*-RBCs) membrane as the parasite matures (Cranston *et al.*, 1983; Nash *et al.*, 1989; Shelby *et al.*, 2003; Suresh *et al.*, 2005). Suresh *et al.* observed a significant increase in cell stiffness at later stages of infection, attributing this fact to the presence of the large and non-deformable parasite within the cell, resulting in an increase in internal viscosity (Suresh *et al.*, 2005). The parasite growth also causes the *i*-RBCs to become more spherical, reducing their surface area to volume, and consequently leading to a reduced cell deformability (Nash *et al.*, 1989; Herricks, Antia and Rathod, 2009). Furthermore, the active transport of parasite proteins to the membrane leads to its stiffening; and the accumulation of parasite proteins at the host cell membrane underside cause the appearance of small angular elevations ("*knobs*") at later stages, altering the membrane structure and surface area (Bannister *et al.*, 2000; Hanssen, McMillan and Tilley, 2010). In the case of *P. falciparum* *i*-RBCs, these knobs work as platforms for the presentation of a membrane-embedded cytoadherence protein – *P. falciparum* erythrocyte membrane protein 1 (Baruch, 1999; Weatherall *et al.*, 2002). By adhering to the endothelium of blood capillaries, the *i*-RBCs escape phagocytic clearance in the spleen (Miller *et al.*, 2002; Weatherall *et al.*, 2002; Maier *et al.*, 2009). This phenomenon is called "sequestration" (Berendt, Ferguson and Newbold, 1990). As a consequence, only ring stage parasites are able to circulate in the peripheral blood of an infected patient and therefore, are the only stage that can be detected for diagnosis.

The *"gold standard"* method currently used for malaria diagnosis in endemic areas is microscopy and is based on the identification of the parasite in red blood cells on a slide after Giemsa staining. Microscopy is cheap and does not require sophisticated equipment; however, the need for highly skilled technicians, presence of artefacts or low parasite levels (<50 parasites/μL) can affect the diagnostic accuracy and yield false results (Wongsrichanalai *et al.*, 2007). Immuno-chromatographic tests, called rapid diagnostic tests (RDTs), are also widely used in the field because of their simplicity and being relative inexpensive. However, RDTs can give inaccurate results and can be unreliable for level of parasitaemia below 200 parasites/μL (McMorrow, Aidoo and Kachur, 2011). Molecular methods, such as nested polymerase chain reaction (PCR), can also be used for malaria diagnosis and have higher sensitivity and specificity compared to microscopy and RDTs (Singh *et al.*, 1999). Nevertheless, the high cost of the equipment needed and the time necessary between sample processing and the evaluation of the results make them unusable in resource-limited settings where malaria is endemic (Hänscheid

and Grobusch, 2002). The presence of asymptomatic individuals with very low parasite densities highlights the necessity of new diagnostic tools with high sensitivity, especially for areas aiming to eradicate malaria (The malERA Consultative Group on Diagnoses, 2011). Microfluidics techniques might be able to address some of the drawbacks associated with malaria diagnosis. One possible approach could be using label-free cell sorting to enrich infected cells present in the sample, which can then be detected using current diagnostic methods (Tay *et al.*, 2016).

### 5.1.2 Leishmaniasis

The term leishmaniasis refers to a set of vector-borne diseases caused by obligate intracellular protozoan parasites of the genus *Leishmania*. *Leishmania* infections have been reported in 98 countries worldwide, and are endemic in tropical and subtropical regions (Pace, 2014). The true disease burden of leishmaniasis is unknown due to a lack of proper epidemiological surveillance and diagnostic methods. Recent estimates point to 1.3 million new cases per year, with approximately 200 million people at risk of infection (World Health Organization, 2017a). Of the 1.3 million estimated cases, only 600,000 are actually reported (Alvar *et al.*, 2012). The WHO considers leishmaniasis as one of the prominent global causes of death by infectious disease (World Health Organization, 2017a). Amongst all parasitic diseases, mortality from leishmaniasis is second only to malaria. It is also the third most common cause of morbidity in terms of disability adjusted life years, which is the number of years lost due to ill-health, disability or early death (Pace, 2014). Despite this, it is still considered one of the neglected tropical diseases, with less surveillance, scientific research on diagnostic techniques and funding in comparison with other parasitic diseases (Hotez *et al.*, 2007).

The genus *Leishmania*, consisting of trypanosomatid protozoans from the *Kinetoplastida* order, has more than 20 different species. Transmission of leishmaniasis occurs primarily via the bite of infected female sand-flies of the genera *Phlebotomus* in Europe, Asia and Africa, and *Lutzomyia* in the Americas. Survival of the *Leishmania* parasite is dependent on a successful transmission between the sand-fly vector and a mammalian reservoir (Bern, Maguire and Alvar, 2008). In the parasite life cycle (**Figure 5.3**) there are two main morphological forms: an extracellular 15 – 20 μm long flagellated promastigote present in the sand-fly (Bates, 2008); and an obligate intracellular 3 - 5 μm long nonflagellated

amastigote within the monocyte-macrophage cells of the mammalian host (Hommel, 1999). After a blood meal by an infected sand-fly, promastigotes are injected into the skin of the mammalian host, which are then phagocytized by macrophages. However, the parasites resist phagocytosis and transform into the amastigote form, growing and multiplying within the host cell. The host cell eventually bursts, releasing the parasites into the blood stream, where they can infect new macrophages, repeating their obligate intracellular cycle. If an infected macrophage is ingested by a sand-fly during a blood meal, it is digested, releasing the parasite in the sand-fly gut. There, amastigotes re-transform back into flagellated promastigotes, multiply and migrate to the proboscis, where they are ready to infect a new mammalian host.

Leishmaniasis have two main clinical forms: the visceral (VL) form and the tegumentary forms, which includes the cutaneous (CL), diffuse, and mucocutaneous leishmaniases (World Health Organization, 2017a), however it is not uncommon for infections to remain asymptomatic (Ostyn *et al.*, 2011). The distribution of VL and CL around the globe can be seen in **Figure 5.4**. VL is the most severe form of the disease and, if left untreated, is usually fatal; while CL is the most prevalent form and manifests in skin lesions that can heal spontaneously.

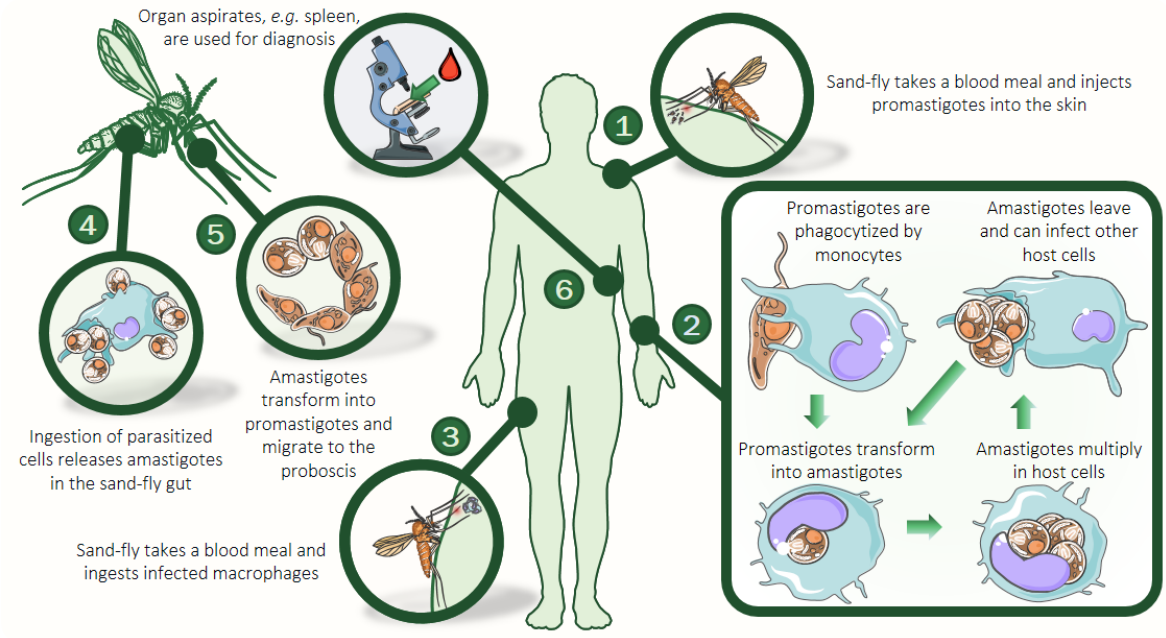


**Figure 5.3:** Representation of the *Leishmania* spp. life-cycle in the human host and sand-fly vector, and the common diagnosis method. This includes: 1 – injection of promastigotes into the host by a female sand-fly; 2 – obligate intracellular life cycle of the parasite within macrophages; 3 – ingestion of infected macrophages by a female sand-fly; 4 – release of amastigotes into the sand-fly gut; 5 – amastigotes re-transform into promastigotes; 6 – diagnosis using microscopy, the current "gold-standard" method, to detect infected macrophages in an aspirated sample.

Diagnosis of VL includes microscopic observation and culture from adequate samples, antigen detection, serological tests, and detection of parasite DNA (Elmahallawy *et al.*, 2014). Visual confirmation of infection by microscopy using Giemsa stained aspirates from bone marrow, spleen or lymph node is the "gold standard" diagnostic method (Murray *et al.*, 2005; Alvar *et al.*, 2012). The sensitivity of Giemsa stained bone marrow smears is only 60 – 85% (Sundar and Rai, 2002), while splenic smears have a sensitivity of 93% (Srivastava *et al.*, 2011). However, the tissue sampling required for this method is invasive, time-consuming and cumbersome, and must be performed by a trained technician. Moreover, splenic aspirations carry the risk of serious or fatal haemorrhages (Bezuneh *et al.*, 2014; Pace, 2014). PCR is an alternative to smears, especially if the parasite load is low (Sundar and Rai, 2002). Serological tests might be useful for further confirmation, but are unable to distinguish between a past treated infection and a current infection requiring treatment (Sundar and Rai, 2002). As for CL, it may be diagnosed clinically, with presence of characteristic skin lesions, or by a skin smear/biopsy observation to detect the presence of amastigotes. As with VL, PCR can also be used in situations when the parasitaemia is low (Neitzke-Abreu *et al.*, 2013).

As one of the WHO neglected tropical diseases, there is a clear lacks of tools to achieve control and erradication, with the absence of a vaccine being one of the flagrant examples (Hotez *et al.*, 2007; Pace, 2014). Moreover, the relative low sensitivity of current diagnostic methods is a clear hurdle on the path to the eradication of leishmaniasis. Besides the complex and burdensome methods still needed for diagnosis, this lack of sensitivity can also be explained by a lack of investment and research in the fight against leishmaniasis (Hotez *et al.*, 2007). As such, there are opportunities to develop new tools for diagnosis. One possibility could be implementing current microfluidic label-free techniques for enrichment of infected cells, which would increase the sensitivity of detection (Tay *et al.*, 2016). Moreover, obtaining pure populations of parasitized cells is of great interest for *in vitro* and *in vivo* characterization. For these reasons, **Section 5.5** will focus on investigating if the size and dielectric properties of macrophages are modified upon infection with *Leishmania mexicana*; and if these biophysical characteristics have potential as biomarkers for future diagnosis tools.

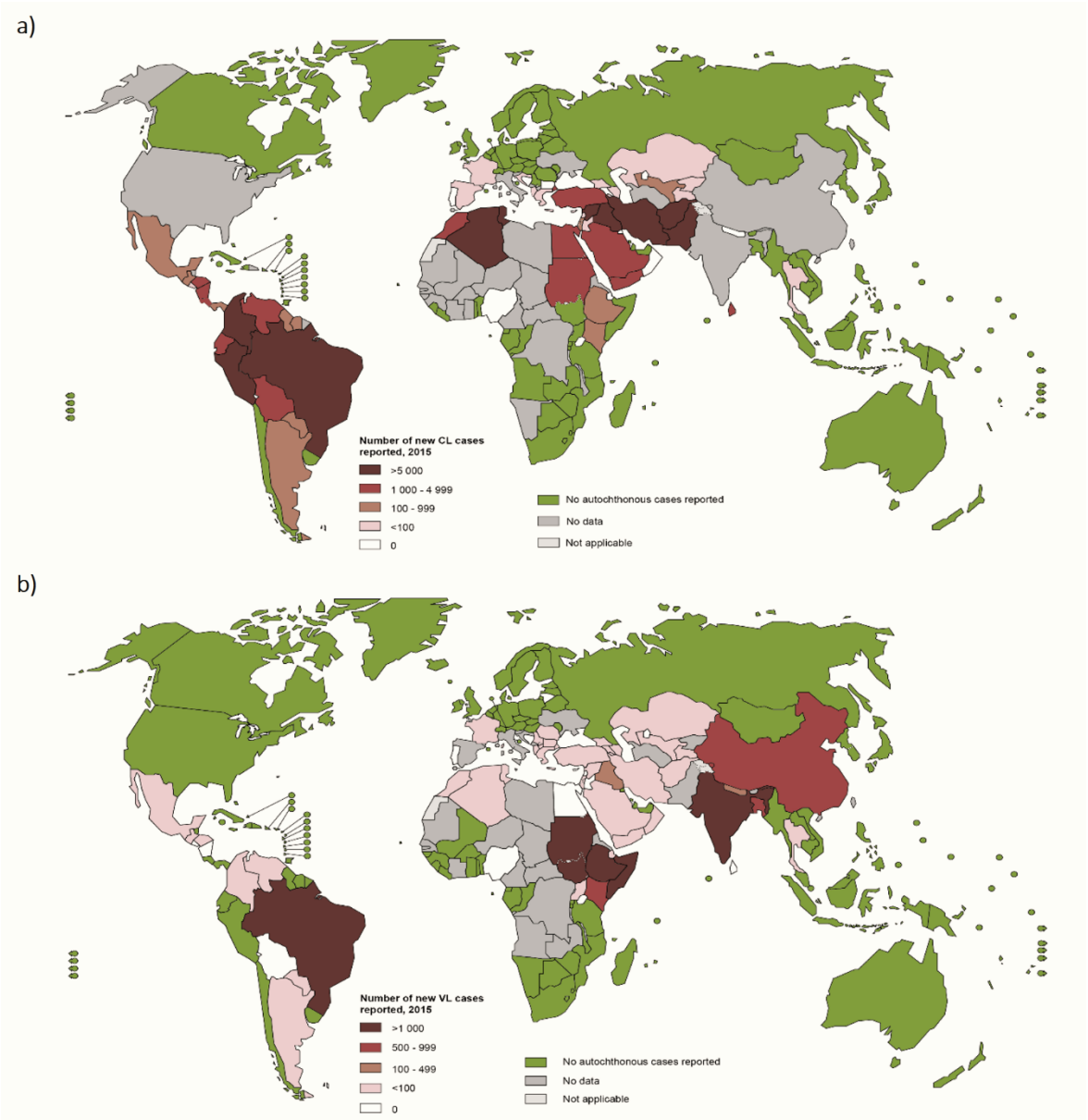


**Figure 5.4:** World map presenting the countries with ongoing transmission of **a)** cutaneous and **b)** visceral leishmaniasis as of 2015. Adapted from Leishmaniasis disease information from World Health Organization website (2017).

## 5.2 Literature Review

### 5.2.1 Human Malaria

It is known that *P. falciparum* parasites gradually modify the infected RBCs (*i*-RBCs) during the intraerythrocytic stage, affecting their mechanical (Nash *et al.*, 1989; Suresh *et al.*, 2005; Maier *et al.*, 2009; Toepfner *et al.*, 2018), magnetic (Trang *et al.*, 2004; Ribaut *et al.*, 2008; Hackett *et al.*, 2009), and dielectric properties (Gascoyne *et al.*, 1997, 2002a). The differences in the biophysical properties of *i*-RBCs and uninfected RBCs (*u*-RBCs) have been exploited for separation using different microfluidic techniques. For instance, Hou *et al.* (2010) presented a

deformability-based separation system, where *P. falciparum i*-RBCs were sorted based on their reduced deformability and in the margination effect (Hou *et al.*, 2010). This is a naturally-occurring effect, observed in blood vessels with a diameter ≤ 300 μm. The Poiseuille flow profile within the vessel generates a pressure gradient directed to the centre, causing migration of smaller and more deformable RBCs to the axial centre of the blood vessel, pushing leukocytes to the side-walls. Whole blood samples can thus be used directly, bypassing dilution or other sample preparation steps. Results from this technique indicated >90% recovery of late stages *i*-RBCs and 75% recovery of ring stage *i*-RBCs. Despite these positive results, the system presented a throughput of only 5 μL/min, requiring a period of 200 min to process 1 mL of blood, the quantity needed to screen for very low levels of parasitaemia. In a more recent work by the same research group, a multiplexed system was used to enrich *i*-RBCs using the margination effect (Kong *et al.*, 2015). While improving the throughput to 10 μL/min, the enrichment factor of ring stage *i*-RBCs was only 1.9 ± 0.2, whereas orders of magnitude are required for low parasitaemia levels (<0.01%).

Guo *et al.* (2016) also investigated using deformability for separation, using a system comprising a tapered constriction and oscillatory flow (Guo *et al.*, 2016). Single cells are deformed along ratchet transportation, which enables continuous separation of cells along the device (**Figure 5.5**). The differential deformation of single cells through constrictions selects *i*-RBCs based on the capability of the cell to squeeze through these micro-gaps, mimicking the transport and sequestration of RBCs in the microvasculature. When testing the device with samples containing early staged *i*-RBCs or samples of extremely low parasitaemia (<0.01%), the authors report enrichment levels between 100x to 2500x. This allows the parasitaemia level to reach values around 1-3%, which can be tested using common methods (such as RDTs). However, the sample throughput of this technique is only 0.5 million cells/h; this translates to 0.1 μL of whole blood per hour, frankly far too low for real-life applications. Other groups have also used deformability for detection with some success (Shelby *et al.*, 2003; Bow *et al.*, 2011). However, *P. vivax i*-RBCs have been reported to present increased deformability (Handayani *et al.*, 2009), rendering a deformability-based detection system for this/multi malaria-causative parasite(s) less effective.

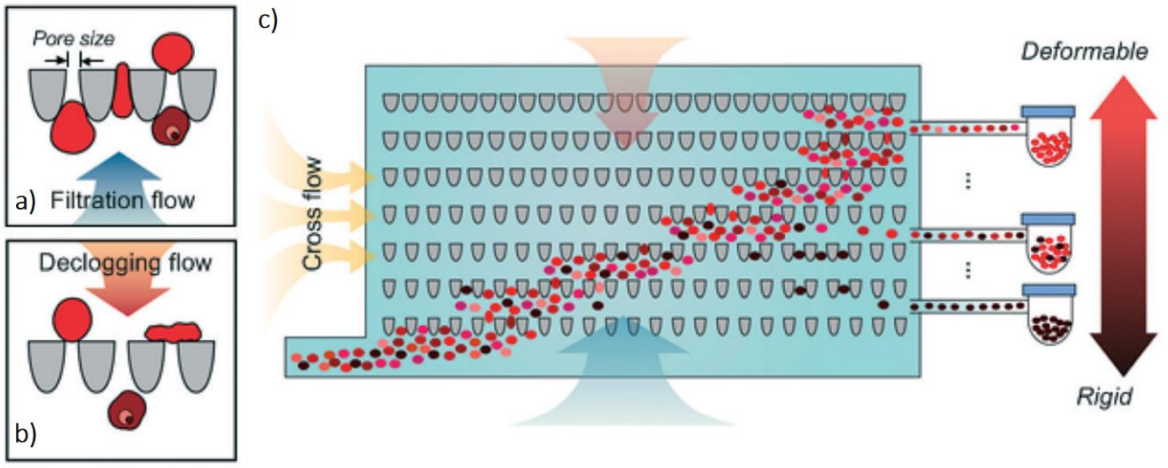


**Figure 5.5:** The deformability-based, ratchet-sorting device for *i*-RBCs enrichment. The tapered constrictions used allow almost unidirectional movement of cells along the device under an oscillating flow which is comprised of **a)** an upward filtration flow and **b)** a downward de-clogging flow. **c)** The cell sample enters the device and under the combined effect of cross flow, filtration flow and de-clogging flow, it form a diagonal trajectory. More deformable cells will travel further upwards the constrictions, being collected at higher outlets, while more rigid cells, as *i*-RBCs, will be blocked midways and separated to lower outlets. Adapted from Guo *et al.* (2016).

A different approach to *i*-RBCs separation was introduced by Zimmerman *et al.* (2006) called magnetic deposition microscopy (Zimmerman *et al.*, 2006). It relies on an increase in magnetic susceptibility caused by haemoglobin digestion by the *Plasmodium* parasite within the *i*-RBC, which generates paramagnetic nanocrystals, or haemozoin, from the heme liberated during digestion. After the application of a strong, narrow magnetic field, *i*-RBCs were concentrated in a small region, followed by fixation and staining for analysis. Results showed a decrease in analysis time and increase in sensitivity. This technique could applied to all *Plasmodium* species, allowing capture of *P. vivax* and *P. falciparum* *i*-RBCs in a common sample (the two most common species). Nonetheless, ring stage *i*-RBC were under-represented, as at this stage the presence of haemozoin is virtually non-existent, greatly limiting the utility of this technique for diagnosis.

Nam *et al.* (2013) further developed magnetic-based separation of *i*-RBCs (Nam *et al.*, 2013). Their system consisted of a microchannel containing a nickel wire, to which a strong magnetic field was applied. This generated a magnetic force that, for *i*-RBCs, was proportional to their magnetic susceptibility, which, in turn, was proportional to the developmental stage of the parasite. Thus *i*-RBCs would be pulled towards the nickel wire, sorting them from *u*-RBCs (**Figure 5.6**). In an attempt to solve the low magnetic susceptibility of ring stage *i*-RBCs, extremely low flow rates were used in order to allow a greater exposure time to the magnetic field.

Despite the high recovery rates for late stage *i*-RBCs (99.2%) and ring stage *i*-RBCs (73%), the optimal flow rate used (0.14 µL/min) limits the applicability of this technique. More recently, Antaki and colleagues proposed a similar system, where multiple ferromagnetic wires distributed along a channel manifold were used (Wu *et al.*, 2016; Blue Martin *et al.*, 2017). High flow rates were used with this approach (77 to 385 µL/min); however, the optimal *i*-RBCs removal efficiency was only 27 ± 2.2%. Multiple passes through the system would be needed to attain total removal, increasing the procedure complexity and time. Moreover, the experiments were conducted with a cell model of *i*-RBCs (methemoglobin RBCs) and not parasite infected cells. As such, it is not possible to assess if such a system would work for all stages of malaria.

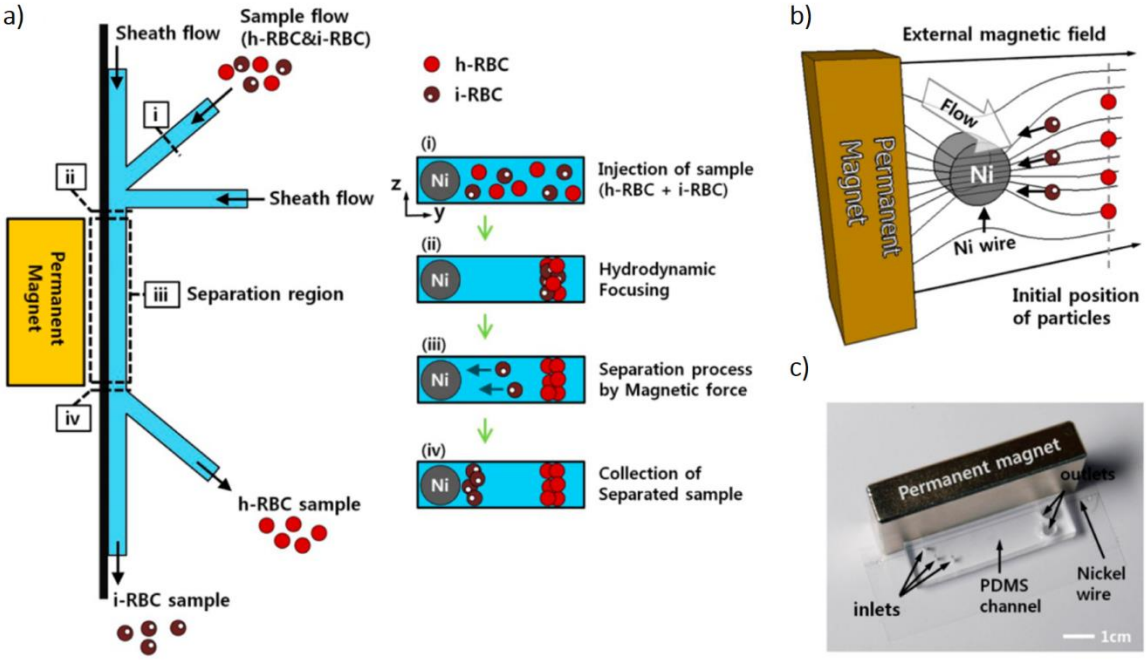


**Figure 5.6: a)** Schematic of the *i*-RBC magnetic-based separation. The sample enters through a central inlet while two sheath flow lanes, entering from side inlets, focus the sample at an optimal distance from the nickel wire. Due to the high magnetic field, paramagnetic *i*-RBCs tend to migrate towards the nickel wire, whereas uninfected one will keep in the focused streamline. **b)** Working principle of the magnetic-based separation, with the magnetic field applied being focused on the nickel wire. **c)** Photograph of the microfluidic device, with the PDMS microchannel, nickel wire and the permanent magnet, which generates the necessary magnetic field. Adapted from Nam *et al.* (2013), where *u*-RBCs were referred to as healthy RBCS – h-RBCs.

AC electrokinetics is a possible approach for detection of parasite-induced changes in the dielectric properties of the *i*-RBC (Gascoyne *et al.*, 1997, 2002a; Gascoyne, Satayavivad and Ruchirawat, 2004; Du *et al.*, 2013). Gascoyne *et al.* (1997) performed the first study using both ROT and DEP, where it was shown that *P. falciparum i*-RBCs exhibited a non-linear DEP crossover frequency response to increasing cell suspension conductivity (Gascoyne *et al.*, 1997). Subsequent to this, a second paper by the same group used two different DEP separator design to isolate *i*-RBCs (Gascoyne *et al.*, 2002a). The first design, an interdigitated electrode array (**Figure 5.7a and b**), was able to trap >95% of *u*-RBCs while ~90% of *i*-RBCs were free to move, allowing for the collection and concentration (50 to 200 fold) of this population. As for the second design (**Figure 5.7c and d**), a spiral microelectrode array with four-phase excitation of the electrodes (Goater, Burt and Pethig (1997)), caused *i*-RBCs to move to the centre of the array due to travelling wave DEP, while *u*-RBCs were trapped at the electrodes edge. This allowed the concentration of ~90% of *i*-RBCs and <0.1% of *u*-RBCs at the centre, thus achieving a concentration factor of ~1000 fold. Further analysis of the DEP levitation and trapping response using iterative multi-shell models, gave the dielectric properties of uninfected and infected RBCs (**Figure 5.7e**). The difference in behaviour between the two cell types was the retention of cytoplasmic ions. While *u*-RBCs were able to maintain a high cytoplasmic conductivity, the cytoplasmic conductivity of the *i*-RBCs fell to that of the low conductivity, isotonic suspending medium. However, heterogeneous populations of *i*-RBCs were measured at various stages making it impossible to determine how the dielectric properties change along the life cycle of the parasite.

More recently, impedance spectroscopy was used to analyse single *i*-RBCs with the aim of discriminating different stages in the parasite life cycle (Du *et al.*, 2013). Small changes in the impedance magnitude were detected between infected and uninfected cells. However, the samples contained a mixture of multi-stage parasites, requiring microscopy images for post-measurement identification of *i*-RBCs. Data was only measured at a single frequency (2 MHz), which measures changes in the cell membrane (Morgan and Green, 2002; Raicu and Feldman, 2015), and very few parasites were measured (for example, 120 *u*-RBcs and 42 *i*-RBCs in one of the experiments). Therefore, there is still a lack of understanding on how the dielectric properties of *i*-RBCs vary at different stages of the parasite life cycle. **Section 5.4** will thus focus on measuring these dielectric properties and determining whether such data could be used as part of a label-free discrimination strategy for enhanced sorting.

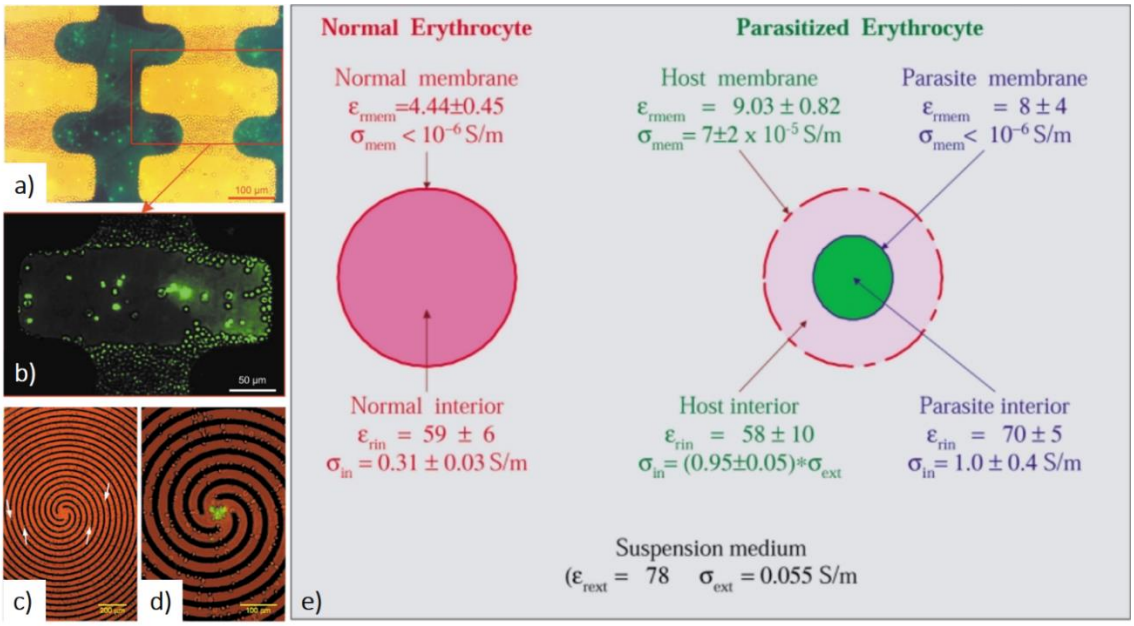


**Figure 5.7: a)** View of the interdigitated electrode array, with a sample of 1.1% *i*-RBCs from approximately 5 x $10^6$ RBCs injected into the chamber. Low-level bright field view of *i*-RBCs exhibiting green fluorescence due to uptake of DiOC6(3) dye, a cationic membrane-permeable potentiometric probe, by the parasite. **b)** Magnified epifluorescence illumination view, confirming concentration of ~95% of parasitized cells. **c)** View of the spiral electrode array, with a sample of 5% *i*-RBCs and the same conditions and staining as in the first design. Before the application of a travelling wave electric field, all *i*-RBCs are spread across the array. **d)** After the application of phase-quadrature signals, *u*-RBCs are trapped at the electrodes edge while *i*-RBCs were moved towards the centre. **e)** Mean dielectric properties of normal and parasitized-RBCs, derived from iterative fitting of shell models. Adapted from Gascoyne *et al.* (2002).

### 5.2.2 Leishmaniasis

The categorization of leishmaniasis as one of the WHO neglected tropical diseases arrives not only from a lack of funding and measures for control and eradication, but also from the fact that there is still a minor interest by the scientific community in developing diagnostic techniques (Hotez *et al.*, 2007). One good example of this is the almost absence of research conducted in the microfluidics and lab-on-a-chip fields on leishmaniasis. Current microfluidic techniques have already shown potential in performing label-free detection and/or enrichment of single cells (Wyatt Shields IV, Reyes and López, 2015; Antfolk and Laurell, 2017; Huang *et al.*, 2017), and, in theory, would be an ideal alternative to standard, low sensitive diagnosis methods. However, there is virtually no published work on leishmaniasis using microfluidics.

The only work was published in 2014 by Costa *et al.*, who used paper-based microfluidic devices to detect anti-Leishmania antibodies in canine sera (Costa *et*

*al.*, 2014). Microfluidic techniques (and paper-based devices in particular), have the potential to meet all the ASSURED criteria for new diagnosis tools (Martinez, Phillips and Whitesides, 2010). Paper devices are inexpensive to fabricate and have a natural porosity amenable to lateral flow assays (Martinez, Phillips and Whitesides, 2010). These do not require syringes, pumps or electrical energy (Martinez *et al.*, 2007), for instance, which is ideal in resource scarce endemic countries. Multiple microchannels can be defined in a single device by patterning its surface with hydrophobic polymers, photoresist or wax, thus creating multiple paths and detection zones for different target compounds (*e.g.*, antibodies or enzymes) (Martinez *et al.*, 2007; Martinez, Phillips and Whitesides, 2010). In their work, Costa *et al.* dotted the paper-platform with antigens to detect anti-*Leishmania* antibodies and ran a test as illustrated in **Figure 5.8a**. Promastigotes of *L. infantum* (**Figure 5.8b**) reference strain were used to produce the antigens. The occurrence of antibody-antigen bio-recognition events was tracked using commercially available anti-dog secondary antibodies. If the dog serum contains anti-Leishmania antibodies, a blue colour develops on the paper surface **Figure 5.8a**. Two sera (plus a control) were tested: one infected with canine leishmaniasis (positive) and another non-infected (negative) (**Figure 5.8c**). There was a statistically significant difference in colour between the three sets of wells, suggesting that anti-Leishmania antibodies in the infected serum attached to the paper-immobilized antigens (**Figure 5.8c**). One drawback with this method is the long incubation time (60 min) needed for testing. Moreover, by relying on colour development, and digital scans for analysis, the applicability of this method is reduced.

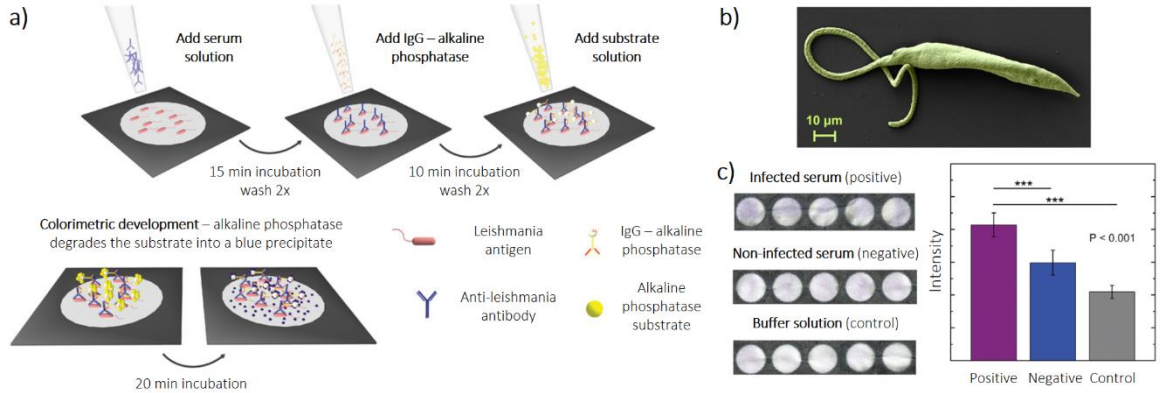


**Figure 5.8: a)** Representation of the paper-based assay developed for the diagnosis of canine leishmaniasis. Colorimetric detection of anti-*Leishmania* antibodies in canine sera is used to detect leishmaniasis. **b)** SEM image of a glutaraldehyde fixed *Leishmania infantum* promastigote. **c)** Colorimetric results from the paper-based assay for detection of anti-*Leishmania* antibodies in canine sera from positive, negative and control wells (N = 5, errors bars represent standard deviation, ***$p$<0.001). Adapted from Costa *et al.* (2014).

Another interesting study, although not focused on leishmaniasis and microfluidics, was published by Hondroulis *et al.* (2017), investigated individual macrophages and their immune response. Macrophages are the host cell of *Leishmania* parasites, playing a crucial part in leishmaniasis. They phagocytose dead cells, bacteria and foreign particles (such as *Leishmania* parasites) (Murray and Wynn, 2012). There is mounting evidence suggesting that macrophages are sensitive to environmental signals that lead to their activation toward the classical M1 phenotype or the alternative M2 phenotype. M1 cells produce pro-inflammatory cytokines and are characterized for a strong antimicrobial and pathogen resistance stance. In contrast, M2 cells are immune-regulatory focused, involved in efficient phagocytosis and parasite elimination (Sica and Mantovani, 2012). Even though phagocytosis has been studied for several decades now, the differing phagocytic activity of M1 and M2 cells remains debatable. There are potential similarities between the two subsets, with mixed M1/M2 phenotypes even being reported (Pettersen *et al.*, 2011; Vogel *et al.*, 2013). Thus, Hondroulis *et al.* (2017) performed comparative single cell tests of M1 and M2 macrophages, when in contact with a foreign agent (*E. coli*, in this case), in droplets, to characterize heterogeneity of the two subsets. A droplet microfluidics-based platform (**Figure 5.9a**) was used to define self-contained regions where macrophages and bacterial cells could interact without interference from external factors. In this platform, droplets containing macrophage were merged with droplets containing bacteria. Loss of *E. coli* due to those interactions was measured as a decrease in GFP fluorescence from bacteria (used for cell count). Quantitatively, a loss of 30% and 33% was observed in co-encapsulated bacteria with M1 and M2 cells respectively; while a combination of both cell types gave a 50% loss (**Figure 5.9b**). Therefore, it is apparent that both activation states have similar efficiency at phagocytosis, at least in respect to *in vitro E. coli*. Moreover, a delay in bacteria uptake was observed for M2 cells in the presence of M1 cells, although there was no difference in overall bacteria clearance. M1 and M2 cells thus seem to have similarities in their phagocytic efficiency while presenting heterogeneity in their behaviour and phenotypic expression. The molecular mechanisms of these effects are not clear at this point, but could be mediated by competitive reactions between existing phenotypes (Villalta *et al.*, 2009). Hence, it would also be interesting to study how M1 and M2 cells differ (or not) in terms of other properties as well. **Section 5.5** will thus also focus on investigating if biophysical properties (as size or dielectric) are altered between M1 and M2 cells upon infection with *L. mexicana*.

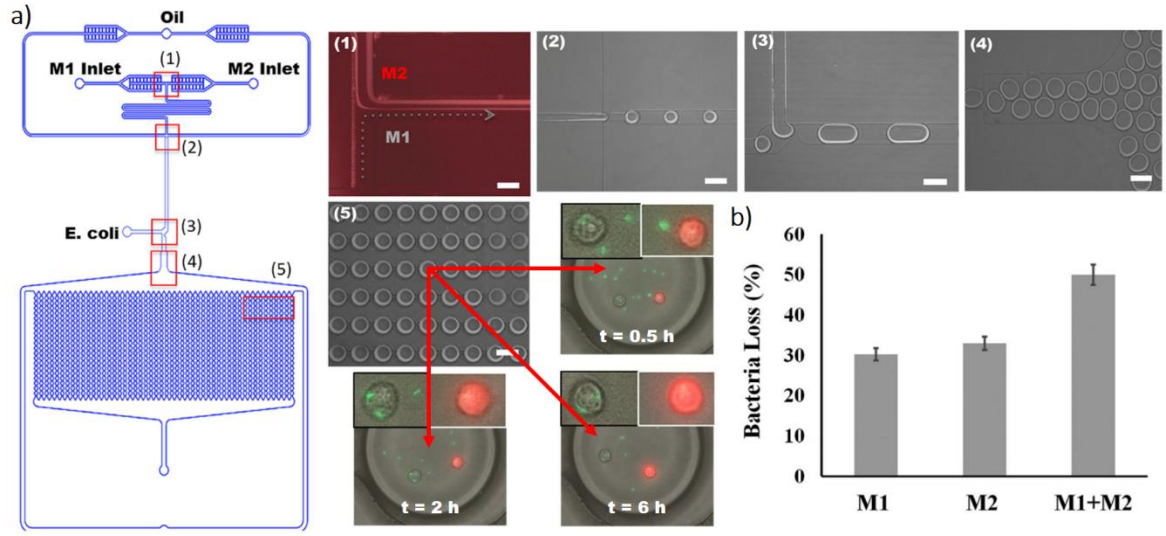


**Figure 5.9: a)** Microfluidic platform design with inlets for M1 and M2 cell types, oil phase and *E. coli*. Images of main device features: (1) laminar flow of M1 and M2 cells at junction 1; (2) droplet generation at junction 2; (3) T-junction for droplet merging (*E.coli* and M1 + M2 cells); (4) merged droplets of consistent volume; (5) droplets halted in docking area, with co-encapsulation at different time points (scale bars = 200 μm). b) Mean loss of *E. coli* in co-encapsulated droplets containing M1, M2 and M1 + M2 cells at t = 6 h. Adapted from Hondroulis *et al.* (2017).

## 5.3 Experimental Methods

### 5.3.1 Sample Preparation

#### 5.3.1.1 *P. falciparum*-infected RBCs

The *P. falciparum* parasites used were kindly supplied by Dr. Lisa Ranford-Cartwright, from the University of Glasgow. Culturing of parasites, sample maintenance and preparation were performed by Lisa Ciuffreda, from the University of Glasgow.

*P. falciparum* parasites were genetically modified to express the fluorescent tag GFP (Kadekoppala *et al.*, 2000) and were grown according to standard protocols (Trager and Jensen, 1976). For time course experiments, MACS columns (Ribaut *et al.*, 2008) were used to purify schizonts from an asynchronous culture. Purified schizonts were then allowed to reinvade fresh red blood cells in a shaking incubator for 4 hours. At the end of the 4 hour incubation, the parasite culture was treated with sorbitol (Lambros and Vanderberg, 1979) to remove all schizont stage parasites that had not burst and reinvaded before that time. Only ring stage parasites survive sorbitol treatment and were used for subsequent measurements. Cultures were grown on and samples removed at 6, 12, 18, 24, 30, 36, 42 hours

post-invasion for time-course measurements. "*Time zero*" (t = 0) was set at the half point of the invasion window, in this way parasites at each time point had a time = hpi ± 2h. A control sample containing uninfected RBCs only was kept under the same conditions and was measured along the time course together with the parasite culture. A Giemsa smear was taken at each time point to assess the parasitaemia and the stage of the parasites. Prior to measurements, all samples were re-suspended in PBS to a final concentration of 500 cells/µL. For experiments conducted with lower conductivity medium, the PBS buffer was diluted 1:3 and 1:2 with a solution of 300 mM D-Mannitol, ensuring an isotonic medium. Polystyrene beads (7 µm diameter) were also added to all samples as reference particles to a final concentration of 100 beads/µL.

#### 5.3.1.2 *L. mexicana*-infected macrophages

The genetically modified GFP-expressing strain of *L. mexicana* was obtained from Dr. Elmarie Myburgh, from the University of York. The parasites used were kindly supplied by Prof. Michael Barrett, from the University of Glasgow. Culturing of parasites, sample maintenance and preparation were performed by Clément Regnault, from the University of Glasgow.

A genetically modified GFP-expressing strain of *L. mexicana* was obtained from Dr. Elmarie Myburgh (University of York). Promastigote forms were cultured in modified Eagle's medium (HOMEM, Invitrogen) supplemented with 1% (v/v), 10% (v/v) heat-inactivated foetal bovine serum (Gibco) and 1% (v/v) penicillin streptomycin solution (Sigma) in non-vented flasks (Corning T25 and T75) at 25ºC.

Murine bone marrow macrophages (BMMs) were harvested from femurs and tibias of female C57 BL/6 mice (Harlan UK Ltd.) aged between 8-12 weeks. After harvest and platting, cells were collected on day 6 of incubation at 37ºC, 5% $CO_2$ in 2 mL of L929-conditionned medium and 8 mL of complete Roswell Park Memorial Institute (RPMI) medium. Viable cells were counted using Trypan Blue (1:1 (v/v) mixture of cell suspension and Trypan Blue) and the concentration was adjusted to 1 x $10^6$ cells/mL. The cell suspension was then transferred to a 24-well plate (Costar) by adding 1 mL of suspension per well. The plates were incubated at 32ºC, 5% $CO_2$ overnight and infections were performed the next day. For classical activation (M1 state), macrophages were treated overnight with IFNγ (Peprotech, 315-05) at a concentration of 0.02 µG/mL (100U/mL), after which LPS (Sigma: *E. coli* 0111:B4, Ref L2630) was added at a concentration of 100 ng/mL. For

alternative activation (M2 state), murine IL-4 was used at a concentration of 20 ng/mL.

Infections were performed with stationary-phase GFP-expressing *L. mexicana* promastigotes at a multiplicity of infection of 1:10 (BMM:parasites). Cells were pelleted by centrifugation (1250 G, 5 min) and washed twice with 32ºC complete RPMI. Cells were re-suspended in complete RPMI (supplemented with IFN$\gamma$/LPS or IL-4 when infections were done in conjunction with immune stimulation) at a density of 1 x $10^7$ cells/mL. After an overnight incubation at 32ºC, the culture medium was removed by aspiration from adherent BMM cultures, and 1 mL of parasite suspension was added to each well. Co-cultures were incubated at 32ºC, 5% $CO_2$ for 24 hours, after which remaining extracellular parasites were removed by three serial washes with 32ºC complete RPMI, and 1 mL fresh complete RPMI (supplemented or not with IFN$\gamma$/LPS or IL-4). From then on, the medium was changed daily (immune stimuli were replaced every time the medium was changed). Co-cultures were grown on and samples removed at 1, 2, 3 and 4 (and 6, for M2 samples) days post-invasion for time-course measurements. A control sample containing uninfected BMMs only was kept under the same conditions and was measured along the time course together with the parasite culture.

Infection ratios were assessed by fluorescence microscopy. Images were acquired on wide-field (grey-scale) and GFP (green) channels using the software Zen (Zeiss). Images were analysed using the software ImageJ. The infection ratio was calculated by dividing the number of GFP-positive cell by the total number of cells in each field (5 or 6 fields analysed; a minimum of 200 cells was counted in each experiment).

Prior to measurements, adherent cells were quickly washed with ice-cold PBS, and 1 mL ice-cold PBS was added to each well for 2 min. Cells were then detached by gentle scraping and transferred to a 15 mL Falcon tube. The wells were rinsed once with 1mL ice-cold PBS, which was added to the Falcon tube, and cells were counted in each sample. Cells were pelleted by centrifugation at 300 G, 5 min and re-suspended in FACS buffer (PBS supplemented with 3% FBS (Gibco) and 1 mM EDTA), to a final concentration of ~500 cells/µL. Polystyrene beads (7 µm diameter) were also added to all samples as reference particles to a final concentration of 100 beads/µL.

### 5.3.2 Data Analysis

Data was processed and analysed using custom scripts written in Matlab (R2016a). The signal from reference beads was used to normalise both the fluorescence and impedance data. Statistical significance of the dielectric properties was assessed using Student's t-test. Results are represented as mean ± standard deviation unless otherwise stated. Scatter plots of infected and uninfected cell populations were drawn with a mean and an elliptical boundary containing 50% of each population (assuming normal distribution). A covariance matrix was first calculated, identifying the directions in which the 2-D data of a single population varied most. The smallest and largest eigen-vector of the matrix give the direction of data spread, while their respective eigen-values give the spread magnitude. Next, based on each population spread and orientation, confidence ellipse, containing within 50% or 1x, 2x and 3x the standard deviation of all events for a given population, for example, can be plotted. The centre of the ellipse gives the population mean position.

### 5.3.3 Statistical Analysis

Statistical analysis was performed using a custom script in Matlab (R2016a). The statistical significance of the differences in parasitaemia obtained from Giemsa-staining/ light microscopy- and fluorescence/ MIC- based methods was assessed using Pearson's chi-squared test, by comparing the proportions of i-RBCs in each RBC populations. The statistical significance of the difference between time-course data (real and imaginary parts) was assessed using Student's t-test, by comparing the mean values of each time-course along the 24 probe frequencies. The statistical significance of the differences in dielectric properties of cells was assessed using Student's t-test, by comparing the values of different cell populations for single time-points. The statistical significance of the differences in dielectric properties of i-RBCs was first assessed by an ANOVA test for differences within the time-points, followed by Tukey's test, by performing pairwise comparisons between each time-point. Results are represented as mean ± standard deviation unless otherwise stated.

### 5.3.4 Optical Flow Cytometry

#### 5.3.4.1 *P. falciparum*-infected RBCs

Conventional flow cytometry analysis of samples containing GFP parasites or 3D7 clone parasites (as a control), at ring and mature stages, was carried out using a BD LSR Fortessa flow cytometer with a 488 nm laser. The measurements were performed by Laura Ciuffreda, from the University of Glasgow. Uninfected RBCs were measured as control samples. Parasite cultures were synchronised with sorbitol the day before the experiment or the same day of the experiment for mature stages and ring stage samples respectively. A Giemsa smear was taken before measurements to assess the parasitaemia and the stages of parasites present. Data were exported as standard FCS files, and the forward and side scattered light (FSC and SSC) and fluorescence (FITC region) signals were analysed using FlowJo, LLC (V.10).

#### 5.3.4.2 *L. mexicana*-infected macrophages

Conventional flow cytometry analysis of samples containing GFP parasites or non-fluorescent parasites (as a control), was carried out using a MACSQuant (Miltenyi) with a 488 nm laser. The measurements were performed by Clément Regnault, from the University of Glasgow. Uninfected macrophages were measured as control samples. Data were exported as standard FCS files, and the forward and side scattered light (FSC and SSC) and fluorescence (GFP region) signals were analysed using FlowJo, LLC (V.10).

### 5.3.5 Isovolumetric sphering of red blood cells

RBCs were sphered following the protocol proposed by Kim and Ornstein (1983). Blood samples originating from freshly collected finger-pricks were used for the process. In a first step, whole blood was diluted 1:50 in a buffer of 0.03 mg/ml sodium dodecyl sulfate (SDS) in PBS. A second dilution step (1:25) was conducted in a buffer of 0.01 mg/ml SDS and 0.1% (v/v) glutaraldehyde in PBS. A final 1:8 dilution in the running PBS buffer was performed, resulting in a final concentration of 500 cells/µL. Fixed RBCs were first diluted 1:50 in PBS only, then 1:25 in a buffer of 0.1% (v/v) glutaraldehyde in PBS, and a final 1:8 dilution in PBS. Normal RBCS were solely diluted in PBS to a final concentration of 500 cells/µl. Polystyrene beads (7 µm diameter) were also added to all samples as reference particles to a final concentration of 100 beads/µL.

## 5.4 Fluorescence-coupled Impedance Cytometry of *P. falciparum*-infected Red Blood Cells

While other researchers have explored the dielectric properties of *i*-RBCs for enrichment, analysis and/or characterization (Gascoyne *et al.*, 1997, 2002a; Du *et al.*, 2013), there is still a lack of understanding on how those properties vary at different stages of the parasite intraerythrocytic life cycle. This section presents the full dielectric characterization of *u*-RBCs and *i*-RBCs using multi-shell models to fit the impedance data. Identification of infected cells through fluorescence detection of parasites that constitutively express GFP within the host cell using the integrated fluorescence MIC system described in **Section 3.4** was used for this work. The analysis of single time-points along the parasite life cycle is then described with the multi-shell modelling. The full list of dielectric properties and discussion of these properties conclude the section.

### 5.4.1 Identification of Infected Red Blood Cells

As the parasite develops within the infected cell there are significant changes in the host cell membrane which manifest as changes in their dielectric properties (Gascoyne *et al.*, 1997, 2002b). These alterations mirror the parasite maturation process and, as such, might not be as perceptible at earlier stages (as 6 or 12 hours post-invasion - hpi) compared to later stages. To uniquely identify the *i*-RBCs, GFP expressing parasites were used in the measurements. Identification of impedance signals from *i*-RBCs followed the protocol summarized in **Figure 5.10**.

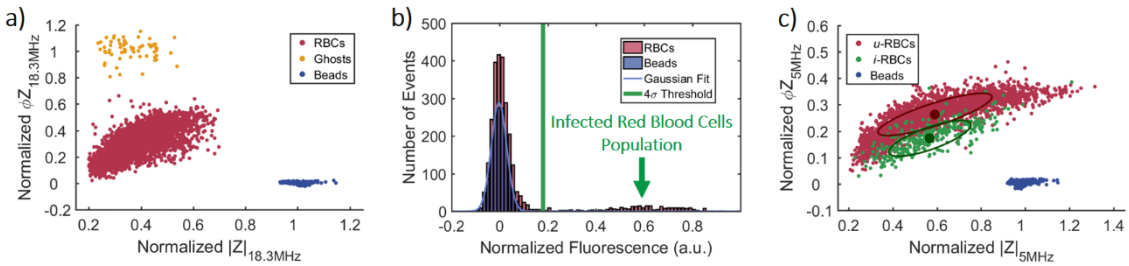


**Figure 5.10:** Identification of infected cells using combined impedance and fluorescence data. **a)** Normalized impedance scatter plot (magnitude |Z| versus phase ΦZ), at the reference frequency (18.3 MHz), of a culture containing parasite-infected cells at 30 hpi, mixed with reference beads. **b)** Normalized fluorescence distributions of reference beads and RBCs, used for identification of infected cells. **c)** Normalized impedance scatter plot (magnitude vs phase), measured at a frequency of 5 MHz for the same blood sample 30 hpi, with reference beads, showing discrimination between *u*-RBCs and *i*-RBCs. The ellipse containing 50% of each population (O) together with the mean (●) are also indicated.

Firstly, the impedance scatter plot was generated at a reference frequency (18.3 MHz). The 7µm reference polystyrene beads added to the sample have a well defined size and dielectric properties, and were used to normalize the magnitude and phase of the impedance signal. **Figure 5.10a** shows the normalized impedance scatter plots for a culture containing parasite-infected cells at 30 hpi, mixed with reference beads. The bead impedance distribution depends on their position in the detection region, *i.e.*, the trajectory of the bead as it flows between the electrodes (Spencer and Morgan, 2011). After correction to compensate for this effect (Spencer *et al.*, 2016), the impedance magnitude of reference beads is distributed normally around a mean value (as seen in **Figure 5.10a and c**). In addition to the bead population, two other clusters were seen: one corresponding to all RBCs and another correspondent to non-viable RBCs, or "*ghosts*". These ghosts are usually present in processed blood samples (as in control samples – **Figure 5.11a**) and as such will be ignored in the remaining analysis.

To uniquely identify infected cells, fluorescence was measured simultaneously with impedance. Conventional flow cytometry confirmed the presence of *i*-RBCs at both early and late stages of infection (see **Figure 5.12**). Fluorescence measurements of the (non-fluorescent) beads were used to set the fluorescence base-level. **Figure 5.10b** shows a histogram of the normalized fluorescence levels for beads and all RBCs. A second, brighter population of RBCs was seen in the histogram, corresponding to the *i*-RBCs. This brighter sub-population was not observed in control samples (**Figure 5.11b and c**).

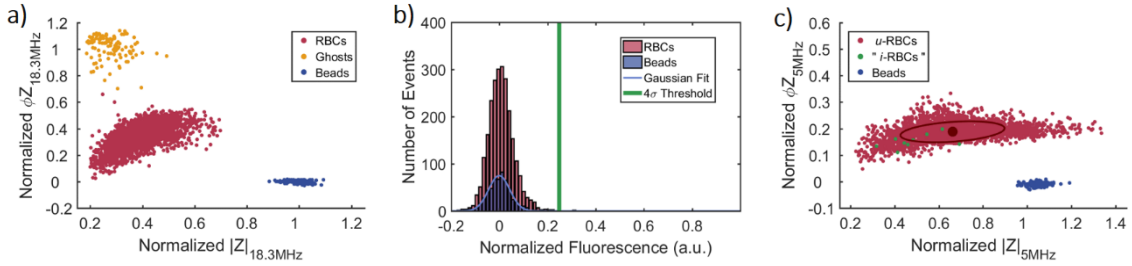


**Figure 5.11:** Infected cell identification process applied to control samples. **a)** Normalized impedance scatter plot (magnitude - |Z| versus phase – ΦZ), at reference frequency (18.3 MHz), of a control sample, mixed with reference beads. **b)** Normalized fluorescence distributions of reference beads and RBCs, used for identification of infected cells. **c)** Normalized impedance scatter plot (magnitude vs phase), measured at a frequency of 5 MHz for the same control sample with reference beads, showing virtually no mislabelled "*i*-RBCs". The ellipse containing 50% of the *u*-RBCs population (O) together with the mean (●) are also indicated.

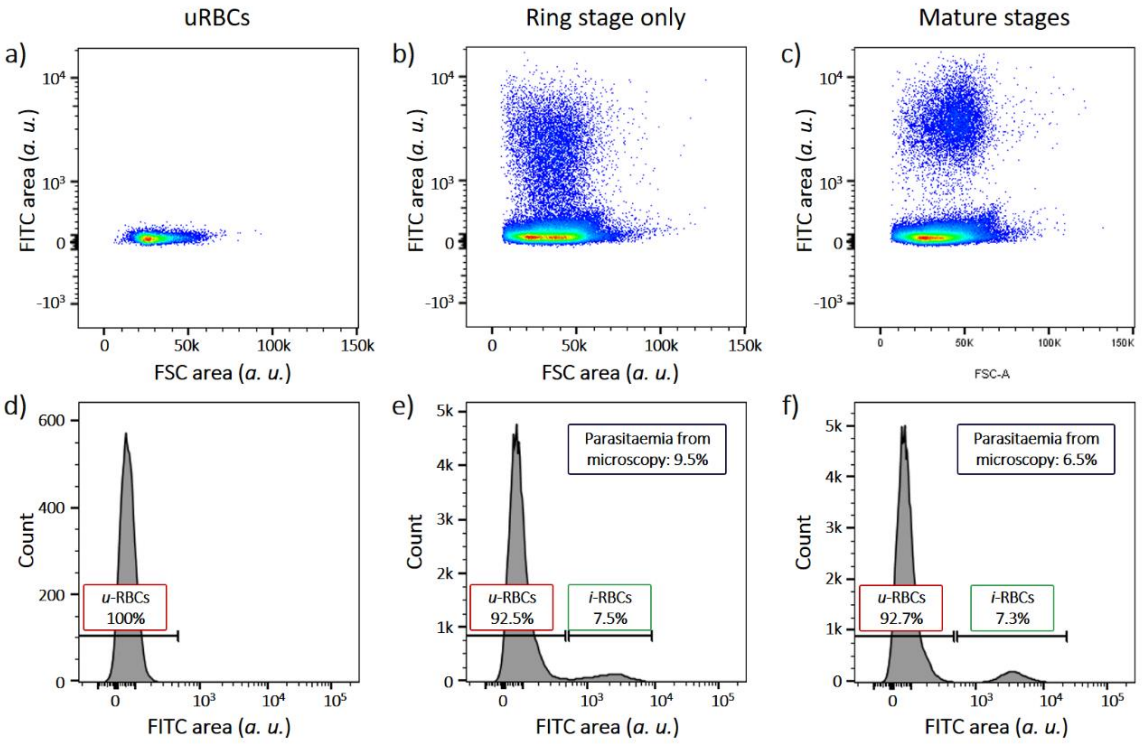


**Figure 5.12:** Conventional flow cytometry data for *u*-RBCs (**a** and **d**), early stage *i*-RBCs (**b** and **e**), and late stage *i*-RBCs (**c** and **f**). Forward scatter – FSC is plotted against fluorescence - FITC region (**a**, **b** and **c**), revealing the presence of GFP-parasites in *i*-RBCs populations only. Parasiatemia levels estimated using histograms of fluorescence (**d**, **e** and **f**) are compared with microscopy-based identification.

To define the division between infected or otherwise, the bead fluorescence data was fitted to a Gaussian distribution. The infected cells were gated from uninfected cells by defining a threshold equal to 4× the standard deviation (σ) away from the mean fluorescence of the beads, giving the scatter plot shown in **Figure 5.10c**. In this way, normalized impedance scatter plots were generated for each probe frequency and each time-point along the infection course.

### 5.4.2 Time-Course Experiments

The different stages of intraerythrocytic growth of the parasite were studied individually by performing measurements every 6 hours along a Time-Course (TC). The first measurement was performed 6 hpi, with the last measurement at 42 hpi (control samples were also measured at the same time-points). Three TC sets of experiments were performed. No significant difference in Real and Imaginary parts was found between the TCs (Student's t-test, N = 24 frequencies; $p \gg 0.05$). For each TC, the parasitaemia, *i.e.*, the percentage of *i*-RBCs within the RBCs population, was measured using standard Giemsa staining and microscopy.

The parasitaemias of each TC were: TC1 – 10.3 ± 0.96%, TC2 – 8.18 ± 0.87%, and TC3 – 5.39 ± 0.71% (mean ± standard error for N = 7 time-points - 1000 RBCs counted per time-point slide). To assess the system sensitivity, the parasitaemia at individual time-points for each TC was calculated using the number of *i*-RBCs identified by fluorescence (from a total of N = 4000 events per time-point). **Figure 5.13** shows the different parasitaemias calculated using both microscopy and fluorescence methods. The mean parasitaemia of each TC calculated by fluorescence was: TC1 – 9.77 ± 1.06%, TC2 – 5.64 ± 0.62%, and TC3 – 4.15 ± 0.63% (N = 7 time-points).

It was observed that certain time-points have lower parasitaemia calculated by fluorescence than based on microscopy (see **Table 5.1**). At early time-points (6 hpi), this difference was significant for 2 of the 3 TCs ($p<0.0001$ for TC2 and $p<0.01$ for TC3; Pearson's chi-squared test for proportions of *i*-RBCs in RBCs populations, N = 7 time-points). One explanation for the discrepancy could be the presence of younger parasites that had yet not produced sufficient GFP to be detected. GFP expression in the parasite line is under the control of the promoter for the histidine rich protein III (*hrpIII:Pf3D7_1372200)* gene, for which RNA-seq data indicates lower expression in the first 5 hpi (Bártfai *et al.*, 2010). Possible differences in parasite invasion window may explain the discrepancies observed between TC1 and TC2/3 at 6 hpi, with parasites at TC2/3 present at an actual time-point < 6 hpi, while TC1 at a time-point ≥ 6 hpi.

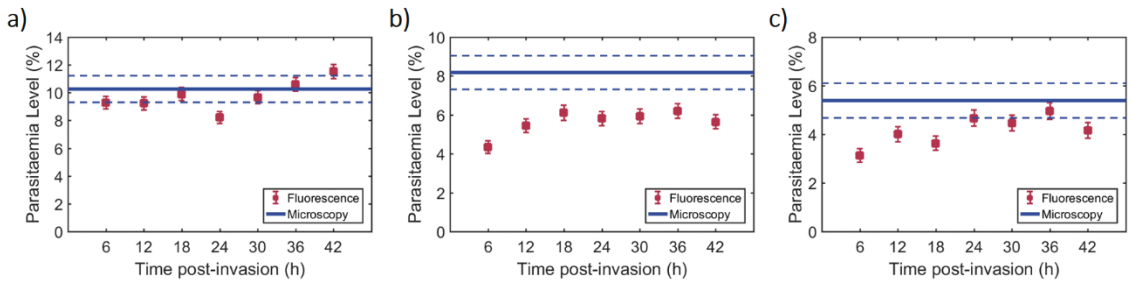


**Figure 5.13:** Parasitaemia levels calculated using microscopy and fluorescence-based methods for **a)** TC1, **b)** TC2 and **c)** TC3. For microscopy, a single mean value (*line*) is calculated for each TC, with a corresponding standard error (*dashed line*) for N=1000 counts. For fluorescence, individual values (*squares*) are calculated for each time-point, with corresponding standard error values (*error bars*) calculated for an average of N=4000 events detected per time-point.

**Table 5.1:** Statistical analysis of Giemsa-staining/ light microscopy- versus fluorescence/MIC- based methods for parasitaemia calculations along the time-course of infection (Pearson's chi-squared test for proportions of *i*-RBCs in RBCs populations, N = 7 time-points, n. s. - not significant, *p<0.05, **p<0.01, ***p<0.001 and ****p<0.0001)

| Time-Course | 6 hpi | 12 hpi | 18 hpi | 24 hpi | 30 hpi | 36 hpi | 42 hpi |
|---|---|---|---|---|---|---|---|
| **1** | n. s. | n. s. | n. s. | n. s. | n. s. | n. s. | n. s. |
| **2** | **** | * | n. s. | * | * | * | ** |
| **3** | ** | n. s. | * | n. s. | n. s. | n. s.. | n. s. |

This phenomenon was also observed by flow cytometry (**Figure 5.12b and e**), where the percentage of *i*-RBCs identified by fluorescence was significantly lower (7.5%) than the one identified by Giemsa staining/light microscopy (9.5%) for early-stage samples ($p$<0.05; Pearson's chi-squared test), while no significant difference was observed for late-stage parasites (p>0.05). In TC2, the difference for most time-points ($p$<0.05) was probably systematic (*e.g.*, a drift in the laser beam focal point, which would affect the sensitivity of the system; or the presence of debris in the detection region). Nevertheless, parasitaemias calculated by fluorescence-coupled MIC were always close to those determined by microscopy. In the case of control samples containing only uninfected RBCs, very small percentages (0.3 ± 0.1 %) of cells were above the threshold fluorescence and classified as "*i*-RBCs" (as seen in **Figure 5.11c** and presented in **Table 5.2**). Thus, the majority of *i*-RBCs were detected for every time-point, in each TC.

As an example, the impedance data of *u*-RBCs and *i*-RBCs populations for all time-points of TC3 are shown in **Figure 5.14**, with similar behaviour observed in TC1 and TC2. For very early stages of infection (6 hpi – **Figure 5.14a**), there was a high degree of overlap between the two cell populations. As the infection runs its course, the *i*-RBCs population shifts in impedance phase (18 hpi – **Figure 5.14c**), and eventually reaches optimal discrimination at later stages of infection (30 hpi – **Figure 5.14e** and 36 hpi – **Figure 5.14f**). Interestingly, discrimination decreased at a very late time-point (42 hpi – **Figure 5.14g**). At this stage, some asynchronous parasites could have already burst from the original host cells and infected new cells, explaining the increased number of *i*-RBCs events overlapping the *u*-RBCs population.

**Table 5.2:** Percentage of mislabelled "*i*-RBCs" calculated for control samples using the fluorescence-based method

| Time-Course | Mislabelled "*i*-RBCs" in control samples (%) | | | | | | | | |
|---|---|---|---|---|---|---|---|---|---|
| | 6 hpi | 12 hpi | 18 hpi | 24 hpi | 30 hpi | 36 hpi | 42 hpi | | |
| 1 | 0.4 | 0.3 | 0.2 | 0.6 | 0.7 | 0.5 | 0.7 | | |
| 2 | 0.2 | 0.3 | 0.4 | 0.7 | 0.1 | 0.1 | 0.0 | Overall Mean | Overall SD |
| 3 | 0.3 | 0.0 | 0.2 | 0.1 | 0.3 | 0.0 | 0.1 | | |
| Mean | 0.3 | 0.2 | 0.3 | 0.4 | 0.4 | 0.2 | 0.3 | 0.3 | 0.1 |
| SD | 0.1 | 0.1 | 0.1 | 0.3 | 0.2 | 0.2 | 0.3 | | |

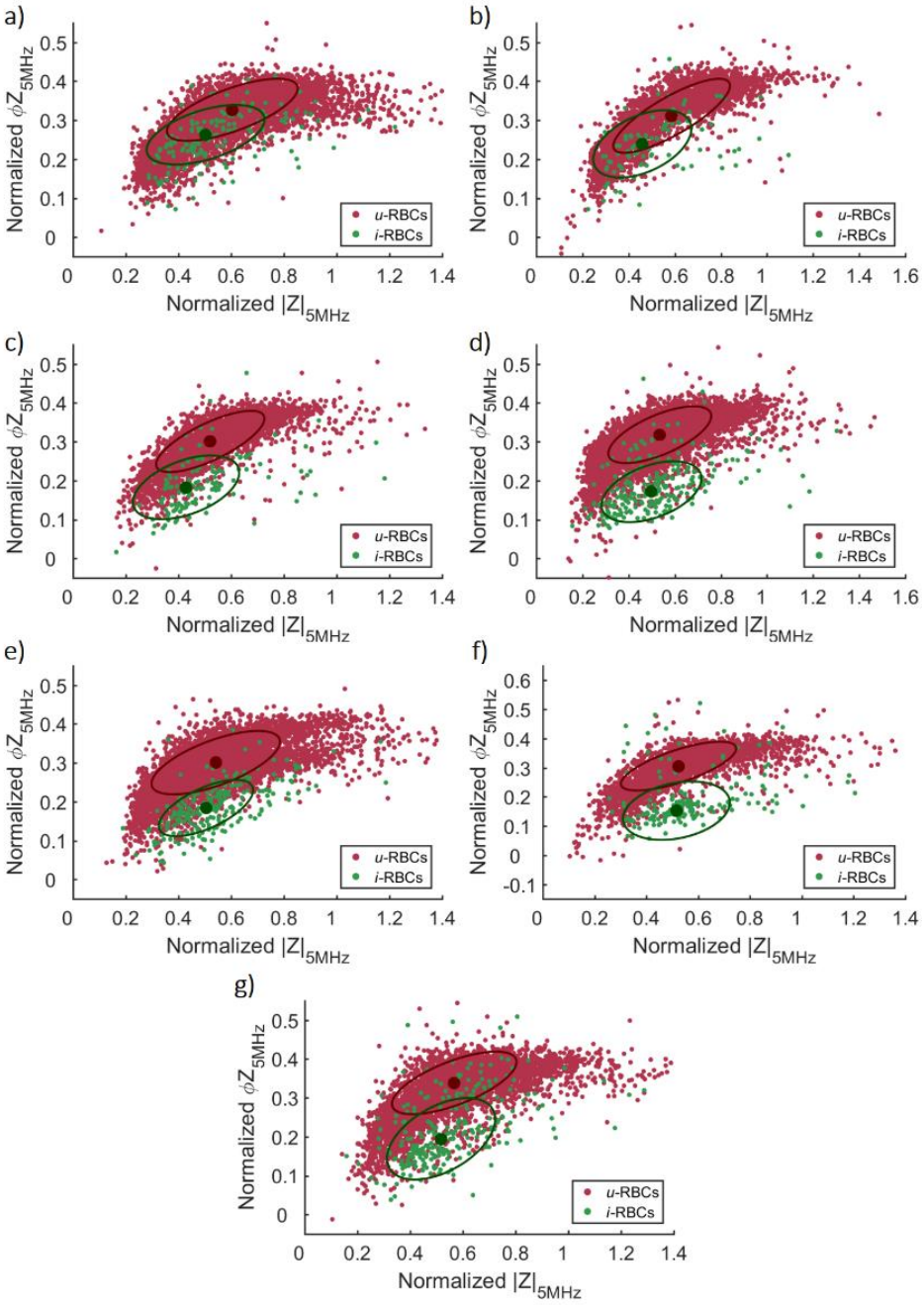


**Figure 5.14:** Normalized impedance scatter plots (magnitude - |Z| versus phase – ΦZ), at probe frequency of 5 MHz, of cultures containing parasite-infected cells at **a)** 6hpi, **b)** 12 hpi, **c)** 18 hpi, **d)** 24 hpi, **e)** 30hpi, **f)** 36 hpi and **g)** 42 hpi showing discrimination between *u*-RBCs and *i*-RBCs. The mean (●) and ellipse containing 50% of each population (O) are also indicated. Data from TC3.

These changes in discrimination were observed at frequencies between 2-8 MHz (**Figure 5.14** presents data at 5 MHz). According to dielectric theory, this range of frequencies measures cell membrane properties (Morgan and Green, 2002; Raicu and Feldman, 2015). Thus, this trend suggests a clear differentiation based on membrane properties as the parasite growth progresses, in accordance with previous literature (Gascoyne *et al.*, 2002b). However, this trend was not reported by Du *et al* (2013) where only a single frequency (2 MHz) was used (Du *et al.*, 2013). The authors measure a difference in impedance magnitude between *i*-RBCs and *u*-RBCs and no difference between the various stages of *i*-RBCs. These observations are contrary to expected, as the parasite induces changes in the mechanical (Nash *et al.*, 1989; Suresh *et al.*, 2005; Maier *et al.*, 2009; Toepfner *et al.*, 2018) and dielectric (Gascoyne *et al.*, 1997, 2002b) properties of *i*-RBCs membrane as it grows within the host cell.

### 5.4.3 Discrimination of Infected Red Blood Cells

Time-course measurements of infected and uninfected showed, as previously presented in **Figure 5.14**, changes in the host cell membrane dielectric properties. These changes allow a visual discrimination between the two cell populations when the magnitude and phase, at frequencies between 2-8 MHz, are presented in a scatter plot. In order to quantify this, an algorithm was developed to automatically define a region of interest, where the majority of *i*-RBCs should be located. Moreover, if an independent method for gating could be developed based on the GFP-parasite, such gates could be feasibly applied to non-fluorescent *i*-RBCs to allow discrimination. However the method's main caveat is that it can only be applied to samples at later stages of infection (≥24 hpi), as for earlier time points there is a large overlap between infected and uninfected cells.

The discrimination method started by applying a similar algorithm to the one developed in **Sections 4.4** and **4.5**. Data from TC3 measurements at 36 hpi and at a frequency of 3.2 MHz (within the frequency range of 2-8 MHz) were used for proof of concept. Briefly, the mean point for each population was first calculated assuming a 2D Gaussian distribution (along magnitude and phase). Three ellipses were then defined containing 50%, 95% and 99% of each population. The intersection of the same ellipse type of each population gave the threshold of equal probability, *i.e.*, it indicated where a detected event has equal probability of belonging to either populations (**Figure 5.15a**).

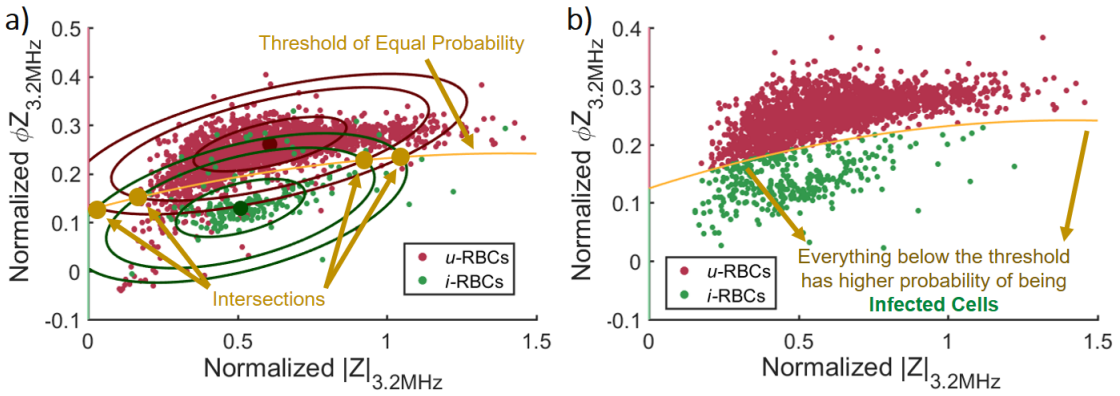


**Figure 5.15:** Normalized impedance scatter plots (magnitude - |Z| versus phase – ΦZ), at probe frequency of 3.2 MHz, of a culture containing parasite-infected cells at 36hpi. **a)** Definition of a threshold of equal probability from the intersection of three ellipses containing 50%, 95% and 99% of cell populations. **b)** Redefinition of infected and uninfected RBCs based on the new threshold. Data from TC3.

This served as an estimate of confidence in the discrimination between infected and uninfected RBCs, and allowed a redefinition of what would be considered infected and uninfected purely looking at impedance data (**Figure 5.15b**). Using this threshold resulted in the gating of approximately 88% of all truly *i*-RBCs, *i.e.*, confirmed by fluorescence, and of approximately 7% of all truly *u*-RBCs. Moreover, ≈50% of gated cells were truly *i*-RBCs, resulting in a ≈10× enrichment from the original sample 5.39 ± 0.71% parasitaemia (mean ± standard error for N = 1000 counts).

With the first threshold defined it was possible to focus on the region of interest and re-analyse the populations using the original fluorescence-based gating of infected and uninfected RBCs (**Figure 5.16a**). It was apparent that there was no real difference at the phase level between the two populations; however, *u*-RBCs seemed to have a lower magnitude value than *i*-RBCs. When plotting the magnitude distribution for both populations (**Figure 5.16b**) this difference was clearer. Taking advantage of the normal distribution of *i*-RBCs along magnitude, a second threshold could thus be defined at one standard deviation below the mean magnitude of *i*-RBCs, effectively removing a majority of *u*-RBCs. As before, infected and uninfected RBCs were redefined according to the new threshold (**Figure 5.16c**). This new region of interest included 78% of all truly *i*-RBCs and 2.7% of all truly *u*-RBCs. In addition, ≈70% of cells within the gate were truly *i*-RBCs, increasing the enrichment level to ≈14×. Looking at how populations distributed in the new threshold using the original fluorescence-based gating, it was apparent that most of *u*-RBCs were removed from the final area of interest (**Figure 5.16d**). Unfortunately, this came at the cost of losing around 20% of all *i*-RBCs, which can

be a critical aspect if dealing with real-life, and low levels of parasitaemia (<0.1%). Nonetheless, this discrimination method seemed to identify correctly most of the *i*-RBCs using impedance data alone.

A possible way to improve discrimination is to enhance the contrast between infected and uninfected cells by altering some of the measurement conditions, specifically the conductivity of the buffer. Maxwell's mixture theory states that the relaxation of particles occurs at lower frequency as the medium conductivity decreases (Maxwell, 1881; Morgan and Green, 2002; Raicu and Feldman, 2015). A single-shell model based on MMT was generated to show this effect in a cell-like particle, as seen on **Figure 5.17** (details are explained in **Section 5.4.4**). This relaxation at a lower frequency means that the interior properties should be probed lower in frequency, which could in theory open the door to using differences between the interior properties of *u*-RBCs (cell cytoplasm) and *i*-RBCs (cell cytoplasm plus parasite properties) as a discrimination factor.

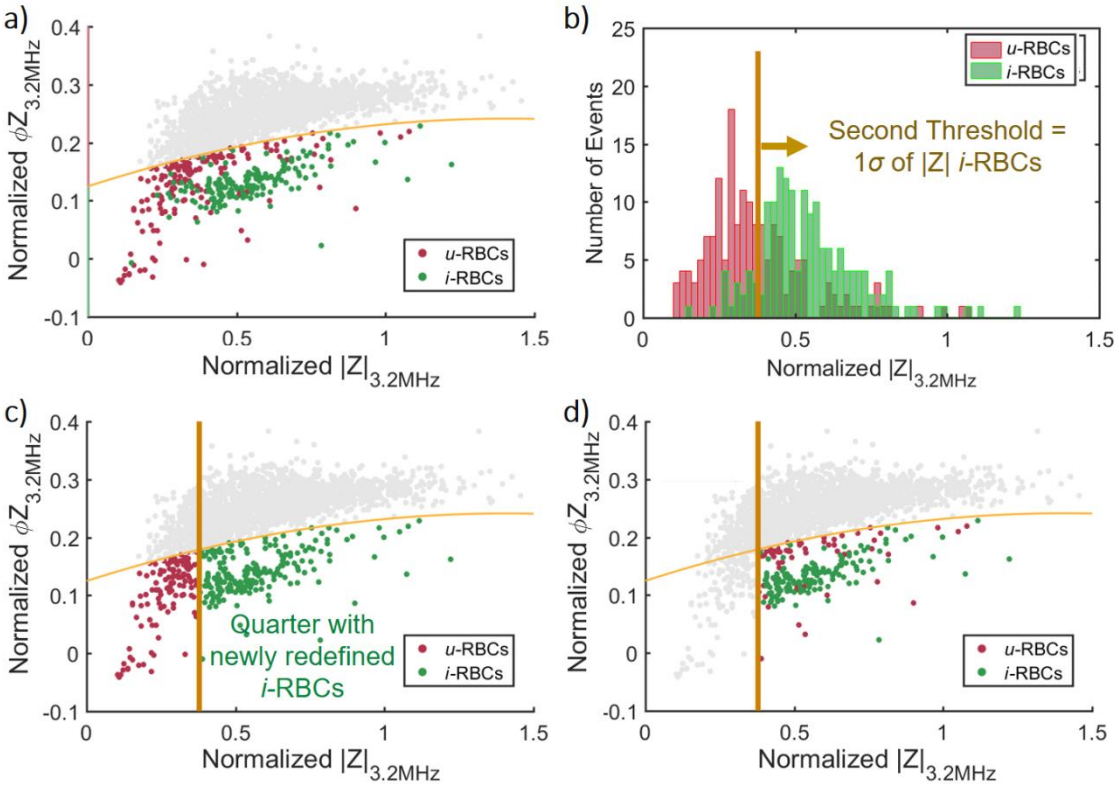


**Figure 5.16:** Normalized impedance scatter plots (magnitude - |Z| versus phase - ΦZ), at probe frequency of 3.2 MHz, of a culture containing parasite-infected cells at 36hpi (**a**, **c** and **d**). **a)** Highlighted area below the threshold of equal probability with original fluorescence-based gating of infected and uninfected RBCs. **b)** Normalized |Z| distributions, at probe frequency 3.2 MHz, of infected and uninfected RBCs, used for the definition of a second discrimination threshold. **c)** Redefinition of infected and uninfected RBCs based on the second threshold. **d)** Highlighted area using both new thresholds with original fluorescence-based gating of infected and uninfected RBCs. Data from TC3.

Moreover, relaxations will have a higher contrast, *i.e.*, the drop in impedance is more evident (see **Figure 5.17a**, where the real part falls from around 0.65 to -0.5 for $\sigma_{medium}$ = 0.3 S/m, but only to around 0 for $\sigma_{medium}$ = 1.1 S/m). This effect enhances any differences in the relaxations curves of the two cell populations.

To test this hypothesis, measurements were conducted using an isotonic medium of lower conductivity: 0.5×PBS ($\sigma_{medium}$ = 0.77 S/m). The sample used in this case contained a heterogeneous population of *i*-RBCs at later stages of invasion, *i.e.*, varying between 24 and 42 hpi. As previously, data was measured for 24 probe frequencies and plotted as impedance magnitude versus phase (**Figure 5.18a**, **b** and **c** present results at 500 kHz, 5 MHz and 50 MHz, respectively). There was a high degree of overlap between infected and uninfected RBCs for measurements at low frequencies (**Figure 5.18a**); a clear separation at mid-range frequencies (**Figure 5.18b**), as expected from previous measurements; and a slight overlap at high frequencies (**Figure 5.18c**). These results at high frequency seemed to suggest that, while there are some differences in dielectric properties between the interior of infected and uninfected cells, these are not sufficient to produce a clear separation between the two populations. A question is whether these differences/similarities are between the cell cytoplasm of both cell types or for a high frequency to probe the parasite dielectric properties directly. The answer is obtained by modelling the two cell populations using multi-shell models, as presented in **Section 5.4.5**.

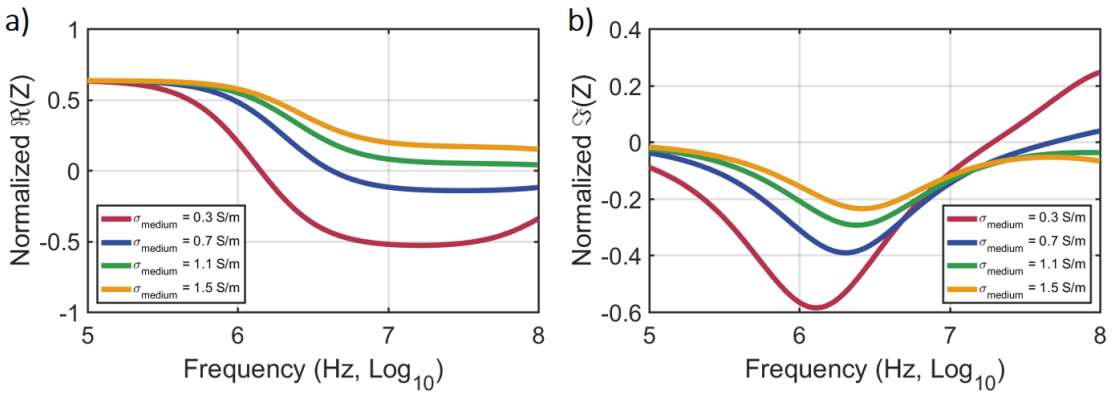


**Figure 5.17:** MMT simulation, using a single-shell model, of relaxation curves in the **a)** real and **b)** imaginary parts of impedance for a cell-like particle in a medium buffer of conductivity between 0.3 - 1.5 S/m. Model parameters: $\varepsilon_{medium}$ = 80, $\varepsilon_{membrane}$ = 8.5, $\varepsilon_{cytoplasm}$ = 85, $\sigma_{membrane}$ ≤$10^{-8}$ S/m, $\sigma_{cytoplasm}$ =1 S/m, $r$ = 3 µm and $d_{membrane}$ = 5 nm.

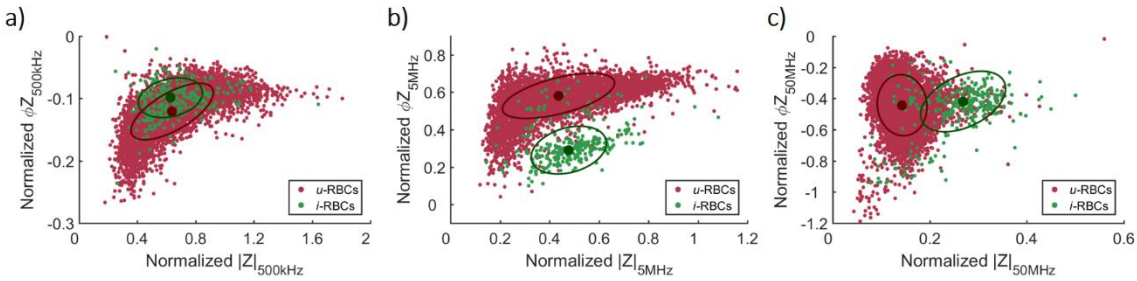


**Figure 5.18:** Normalized impedance scatter plots (magnitude - |Z| versus phase - ΦZ), at probe frequency of **a)** 500 kHz, **b)** 5 MHz and **c)** 50 MHz, of a culture containing late-stage *i*-RBCs in a 0.5xPBS ($\sigma_{medium} = 0.77$ S/m) medium.

The scatterplots measured at higher frequencies did not show a clear separation between infected and uninfected populations, therefore the discrimination algorithm was applied to scatterplots with mid-range frequencies (**Figure 5.19**). Using the threshold of equal probability (**Figure 5.19a**) resulted in the gating of approximately 85% of all truly *i*-RBCs, 6.5% of all truly *u*-RBCs, and an enrichment of ≈7× from the original sample 6.3 ± 0.77% parasitaemia (mean ± standard error for N = 1000 counts) as ≈44% of gated cells are truly *i*-RBCs. The definition of a second threshold was also possible, again set as one standard deviation below the mean magnitude of *i*-RBCs (**Figure 5.19b**). Infected and uninfected RBCs were then redefined according to the second threshold (**Figure 5.19c**). This resulted in the gating of 72% of all truly *i*-RBCs and 1.4% of all truly *u*-RBCs, which in turn meant that ≈75% of cells within the gate are truly *i*-RBCs, increasing the enrichment level to ≈12×. Using a lower conductivity medium has thus not led to any improvements on the current discrimination method.

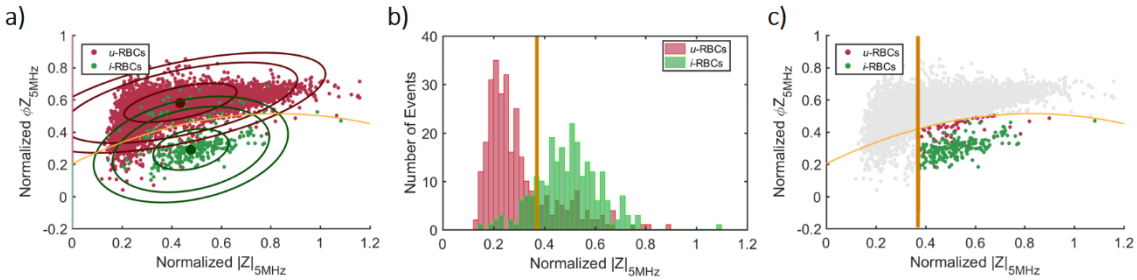


**Figure 5.19:** Normalized impedance scatter plots (magnitude - |Z| versus phase - ΦZ), at probe frequency of 5 MHz, of a culture containing late-stage *i*-RBCs in a 0.5xPBS ($\sigma_{medium} = 0.77$ S/m) medium (**a** and **c**). **a)** Definition of a threshold of equal probability from the intersection of three ellipses containing 50%, 95% and 99% of cell populations. **b)** Normalized |Z| distributions, at probe frequency 5 MHz, of infected and uninfected RBCs, used for the definition of the second discrimination threshold. **c)** Highlighted area using both new thresholds with original fluorescence-based gating of infected and uninfected RBCs.

Another set of measurements were conducted using an isotonic, lower conductivity medium of 0.3×PBS ($\sigma_{medium}$ = 0.53 S/m). In this case, a sample containing a heterogeneous population of early-stage *i*-RBCs (varying between 6 and 18 hpi) was used (5.9 ± 0.75% parasitaemia, mean ± standard error for N = 1000 counts). As before, 24 probe frequencies were measured and scatter plots generated of impedance magnitude versus phase (**Figure 5.20a**, **b** and **c** present results at 500 kHz, 5 MHz and 50 MHz, respectively). These results clearly showed that there was always a considerable overlap between the infected and uninfected RBCs populations. Results in **Figure 5.14** had already shown that the increasing differences between infected and uninfected RBCs membranes enabled discrimination between the two populations for later stages of infection (as seen in **Figure 5.16**). **Figure 5.20b** showed again that these membrane alterations at earlier stages were not substantial enough to allow full discrimination of infected and uninfected cells, thus precluding the implementation of the discrimination algorithm. This further reduction in medium conductivity ($\sigma_{medium}$ = 0.53 S/m) should theoretically facilitate the direct probing of the parasite within *i*-RBCs at higher frequencies due to an earlier relaxation in frequency of the RBC membrane (similarly to what is demonstrated in **Figure 5.17**). This means that, at very high frequencies, impedance should probe cytoplasm properties for the *u*-RBCs case, and parasite properties for the *i*-RBCs case. Thus, even for early-stage *i*-RBCs, if there were clear differences between the *u*-RBCs cytoplasm and the parasite properties, these should be observable through distinct impedance responses. **Figure 5.20c** seems to indicate that this is not the case, as there is still a clear overlap between the *u*-RBC and the *i*-RBCs (parasite) impedance responses at 50MHz (the highest frequency used). In conclusion, *u*-RBcs and parasites seem to have similar dielectric properties. However, to confirm this and arrive at a clearer understanding of the dielectric properties of *u*-RBCs, *i*-RBCs and parasites, accurate modelling must be conducted – see **Sections 5.4.4** and **5.4.5**.

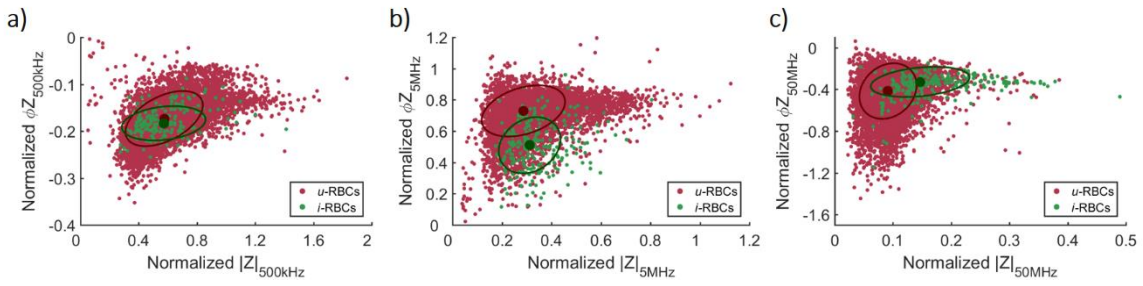


**Figure 5.20:** Normalized impedance scatter plots (magnitude - |Z| versus phase – ΦZ), at probe frequency of **a)** 500 kHz, **b)** 5 MHz and **c)** 50 MHz, of a culture containing early-stage *i*-RBCs in a 0.3×PBS ($\sigma_{medium}$ = 0.53 S/m) medium.

### 5.4.4 Impedance Modelling of Red Blood Cells

As previously discussed in Chapter 3, biological cells in suspension exhibit a dielectric relaxation of the cell membrane(s), termed the β-relaxation by Schwan (Schwan, 1957). Cells are typically modelled as a conducting particle (cell interior) surrounded by an insulating cell membrane, suspended in a conducting medium. This behaviour is often modelled using the so-called multi-shell model which describes the cell as a series of concentric shells with defined dielectric properties (Hanai, Koizumi and Irimajiri, 1975; Irimajiri, Hanai and Inouye, 1979; Huang *et al.*, 1992; Wang *et al.*, 1994). Maxwell's mixture theory (MMT), is used to define the dielectric properties of the cell, the volume fraction and the complex impedance of the suspension (Maxwell, 1881; Morgan and Green, 2002).

Multi shell-models have been used to determine the dielectric properties of cells (Hanai, Koizumi and Irimajiri, 1975; Irimajiri, Hanai and Inouye, 1979; Huang *et al.*, 1992; Wang *et al.*, 1994). One of the most simple and common models approximates biological cells to a spherical particle with a single shell, as presented previously in Chapter 3. This single-shell model is the simplest model that describes the dielectric properties of a cell with a single relaxation. By simplifying the intricacies of a cell to a conductive layer surrounded by a single insulating membrane, it is possible to infer various dielectric properties (see **Figure 5.21**). The presence of the lipid cell membrane means that, in standard PBS buffer medium, cells behave as insulating particles at low frequencies (kHz), however at higher frequencies (MHz) the cell appears progressively more conductive as the electric field probes the intracellular properties (Schwan, 1957; Morgan and Green, 2002; Raicu and Feldman, 2015). In the absence of any substantive membrane conductivity, the cell volume can be measured at low frequencies (<1 MHz), while at intermediate frequencies (1-10 MHz) the membrane capacitance dominates (a measure of invagination, convolution and integrity (Wang *et al.*, 1994; Morgan and Green, 2002; Gascoyne *et al.*, 2013). Cytoplasm properties are measured at still higher frequencies (>10MHz), when the electric field capacitively couples across the membrane and the impedance signal reflects the cell interior properties.

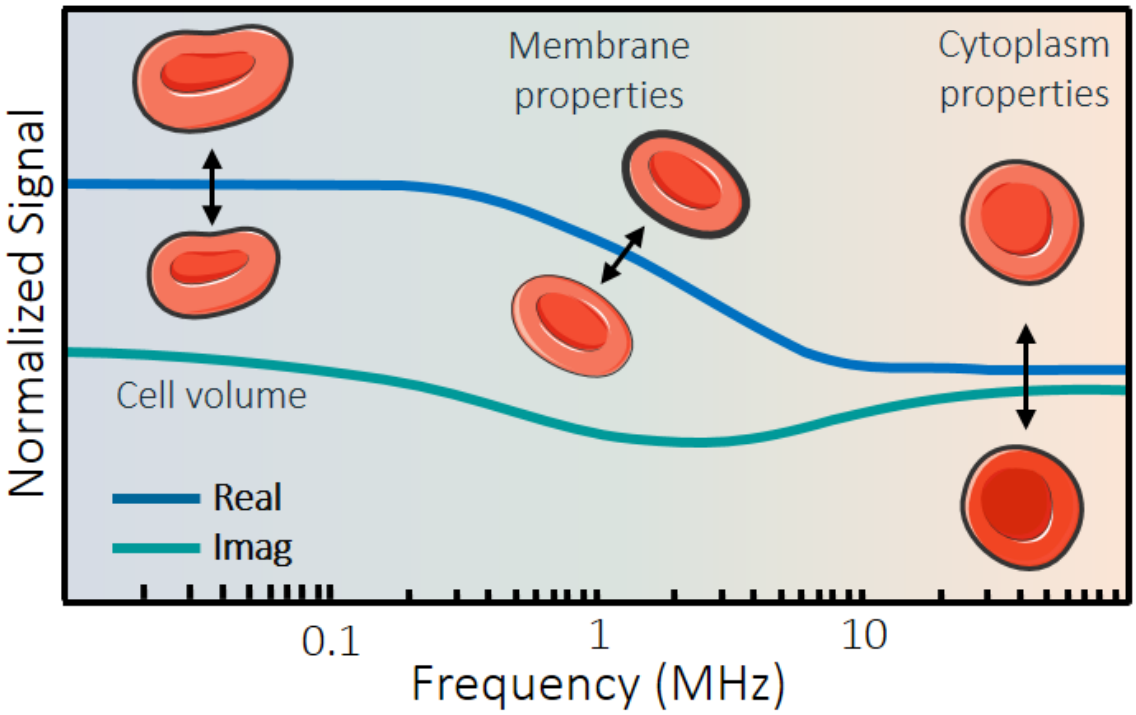


**Figure 5.21:** Illustration of the frequency-dependent dielectric response of a single-shelled particle (as *u*-RBCs), with a single relaxation. The relationships between some of the dielectric properties and behaviour at specific frequencies are highlighted. Note that the frequency window for these relaxations depends on the conductivity of the suspending medium.

Before applying any model to malaria-parasite infected cells, the modelling process was firstly optimized, starting with the application of the spherical single-shell model to normal RBCs. For this process, impedance data of blood samples from fresh finger-pricks were used. As previously described, reference beads were used for data normalization. After identification of the healthy, normal RBC population, the modelling algorithm was applied to the impedance data (**Figure 5.22**).

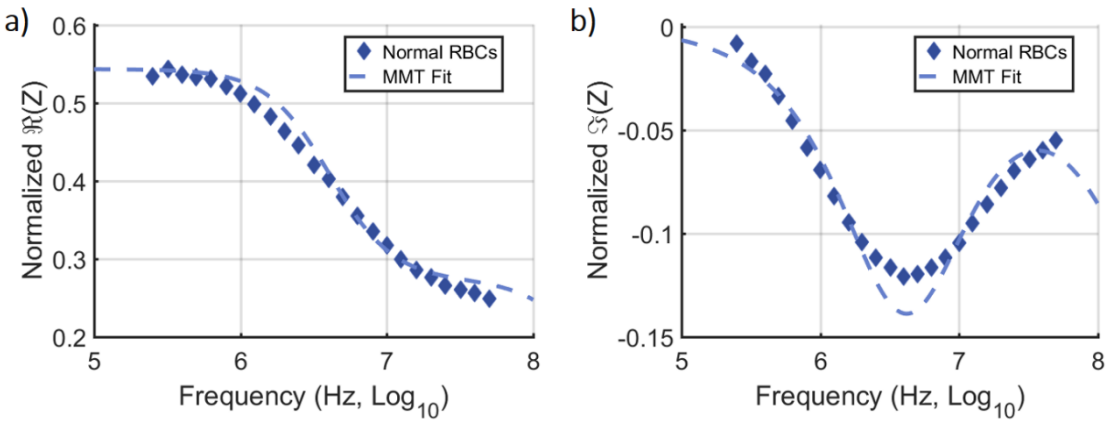


**Figure 5.22:** Normalized **a)** real and **b)** imaginary parts of impedance of normal RBCs, across the measured probe frequency spectrum. The optimal MMT fits (*dashed lines*) using the spherical single-shell model are plotted on top of individual probe frequency mean values (*diamonds*).

Data was modelled using a custom script written in Matlab (R2016a). An iterative algorithm generated multiple relaxation curves based on given mean values for the semi-axis, suspension medium properties (conductivity - $\sigma_{medium} = 1.5$ S/m; permittivity - $\varepsilon_{medium} = 80$), and fixed membrane thickness ($d = 5$ nm) and conductivity ($\sigma_{membrane} \leq 10^{-8}$ S/m). The algorithm used a pattern search function to find the local minimum between a measured data set and the spectrum derived from the model, *i.e.*, what variables generate a relaxation curve that has the minimal difference between data and model. The pattern search function required an initial vector, with starting-points for each variable, *i.e.* for each dielectric property being modelled; as well as two boundaries vectors, defining the maximum and minimum values for each variable. The real and imaginary parts were modelled at the same time, with the local minimum difference being calculated considering the differences in both parts. The fitting process ended when the local difference between the data and model was smaller than a predefined tolerance value, with a $R^2$ value evaluating the goodness of fit.

Each data set comprised the mean values of the real (**Figure 5.22a**) and imaginary (**Figure 5.22b**) parts of impedance, for the 24 probe frequencies analysed. The mean values were derived from a population of usually N = 4,000 events/frequency. While the fit applied to normal RBCs was close to optimal ($R^2$ = 0.9991 ± 0.0001; N = 3 samples; **Figure 5.22**), the estimated dielectric properties of the cells (see **Table 5.3**) were not in agreement with the widely accepted dielectric values for RBCs (Pauly and Schwan, 1966; Takashima, Asami and Takahashi, 1988; Gimsa *et al.*, 1994; Gascoyne *et al.*, 2002b; Katsumoto *et al.*, 2008). An obvious example was the membrane capacitance ($C_{membrane}$) of RBCs which were estimated as 6.37 ± 0.37 mF/m$^2$ (N = 4 samples), compared with accepted values in the range of 7 to 8 mF/m$^2$. Thus, the spherical single-shell model evidently failed to properly model a RBC, probably due to the use of a spherical approximation for the discoid shape of RBCs.

Therefore, further measurements were conducted using sphered RBCs. The protocol of Kim and Ornstein (1983) was used to sphere the cells, as detailed in sub-section 5.3.5. Glutaraldehyde was used to fix the membranes and to prevent lysis during the sphering process. Measurements were also conducted on fixed RBCs to assess the influence of this agent on cell properties. **Figure 5.23** shows a microscope image of the three RBCs populations analysed. The change in cell morphology was visible in sphered cells (**Figure 5.23c**) when compared to normal and fixed ones (**Figure 5.23a and b**, respectively).

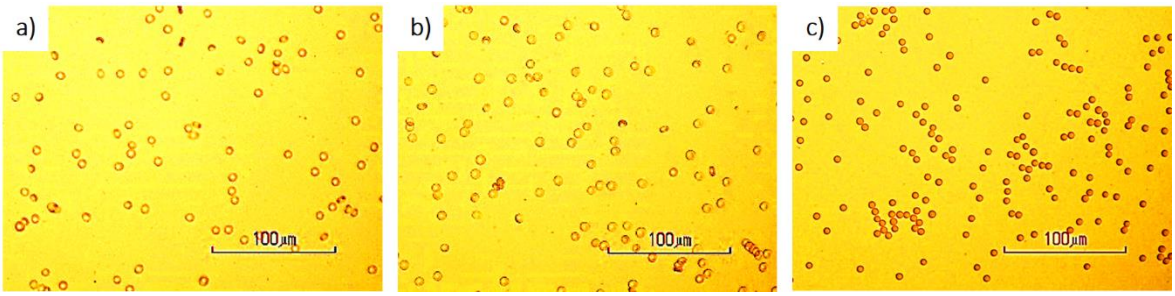


**Figure 5.23:** Microscopy images of the **a)** normal, **b)** fixed and **c)** sphered RBCs.

The algorithm was applied to the impedance data for fixed and spherical RBCs (**Figure 5.24**). For the fixed RBCs, the MMT fit was better than for normal discoid RBCs ($R^2$ = 0.9994 ± 0.0001; N = 3 samples; **Figure 5.24a and b**). The dielectric properties (**Table 5.3**), showed a decrease in the $C_{membrane}$ of fixed cells (5.46 ± 0.23 mF/m², N = 3 samples). This can be explained by the effect of the glutaraldehyde on cells, as it causes the cross-linking of proteins within the cell membrane (Sabatini, Bensch and Barrnett, 1963). It halts membrane channel activity and interaction between the intra- and extra-cellular compartments, resulting in an altered, more rigid and less permeable membrane (Squier, Hart and Churchland, 1976; Marczak and Jóźwiak, 2008). This loss in complexity thus leads to a decrease in $C_{membrane}$ which is linked directly to permittivity (Wang *et al.*, 1994; Morgan and Green, 2002; Gascoyne *et al.*, 2013).

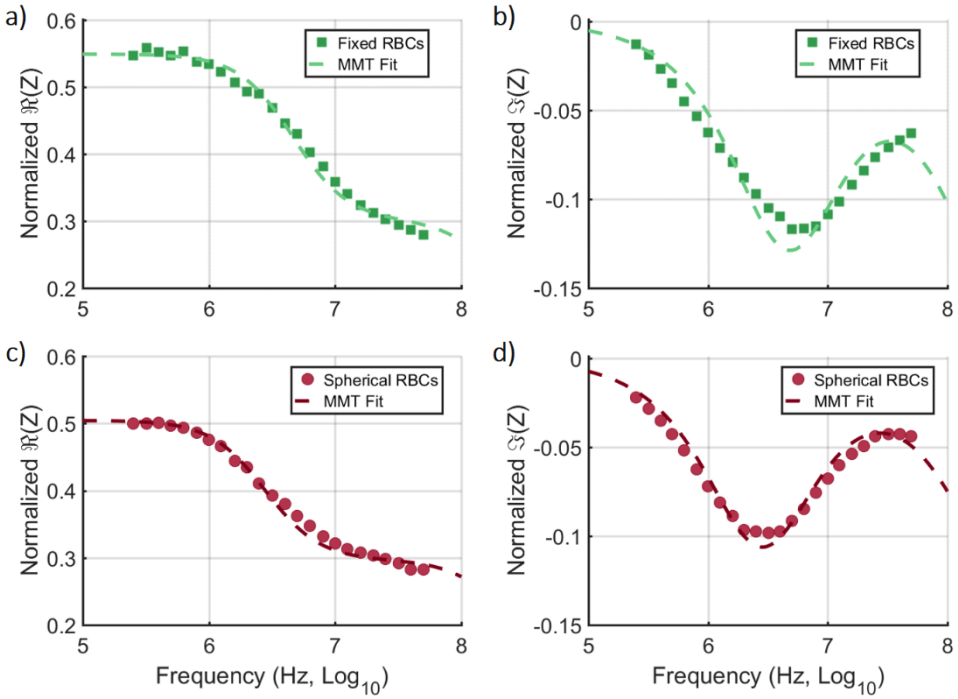


**Figure 5.24:** Normalized real (**a** and **c**) and imaginary (**b** and **d**) parts of impedance of fixed (**a** and **b**) and spherical (**c** and **d**) RBCs, across the measured probe frequency spectrum. The optimal MMT fits (*dashed lines*) using the spherical single-shell model are plotted on top of individual probe frequency mean values (*diamonds*).

**Table 5.3:** Dielectric properties, estimated using the spherical single-shell model, of normal, fixed and spherical RBCs

| Properties | Sample | | |
|---|---|---|---|
| | Normal | Fixed | Spherical |
| $\varepsilon_{membrane}$ | 3.66 ± 0.21 | 3.08 ± 0.13 | 4.71 ± 0.11 |
| $\varepsilon_{cytoplasm}$ | 78.6 ± 2.65 | 77.9 ± 2.44 | 64.9 ± 2.55 |
| $\sigma_{cytoplasm}$ (S/m) | 0.61 ± 0.02 | 0.53 ± 0.04 | 0.43 ± 0.05 |
| $C_{membrane}$ (mF/m$^2$) | 6.47 ± 0.37 | 5.46 ± 0.23 | 8.34 ± 0.20 |

The spherical RBCs gave an optimal MMT fit, with the model fitting both the real and imaginary parts of the impedance ($R^2$ = 0.9998 ± 0.0001; N = 3 samples; **Figure 5.24c and d**). The estimated dielectric properties (**Table 5.3**) are close to the accepted values (Pauly and Schwan, 1966; Takashima, Asami and Takahashi, 1988; Gimsa *et al.*, 1994; Gascoyne *et al.*, 2002b; Katsumoto *et al.*, 2008). These results indicate that it is indeed the morphology of the cell that causes a poor fit (Gimsa *et al.*, 1994). In conclusion the spherical single-shell model fits the impedance data of a spherical cell giving data that matches literature values. However, there is a need for a model which can be used for non-spherical cells.

The ellipsoidal model represented in **Figure 5.25a**, is the most widely used approximation for non-spherical particles (Miller and Jones, 1993; Asami and Yonezawa, 1995; Gimsa *et al.*, 1996; Morgan and Green, 2002). A similar model was used in this work. Consider a homogeneous, ellipsoidal, dielectric particle, of random orientation, with semi-axes $n = a, b$ and $c$. The effective polarisability for each semi-axis ($\tilde{\alpha}_n$) is different and can be calculated through:

$$\tilde{\alpha}_n = 3\,\tilde{\varepsilon}_{medium}\,\widetilde{K}_n \qquad (5.1)$$

where $\tilde{\varepsilon}_{medium}$ is the complex permittivity of the suspending medium. The polarisability magnitude, and thus the effective dipole moment of the particle, is frequency dependent and described by the factor:

$$\widetilde{K}_n = \frac{\tilde{\varepsilon}_{particle} - \tilde{\varepsilon}_{medium}}{3(A_n(\tilde{\varepsilon}_{particle} - \tilde{\varepsilon}_{medium}) + \tilde{\varepsilon}_{medium})} \qquad (5.2)$$

This factor is different for each semi-axis *n*, and depends on a depolarising factor $A_n$. For an oblate spheroid ($a < b = c$), such as RBCs, $A_n$ takes the form:

$$A_a = \frac{1}{1-q^2} + \frac{q}{(1-q^2)^{3/2}} arcos(q) \qquad (5.3)$$

$$A_b = A_c = (1 - A_a)/2$$

where $q$ is the ratio of semi-axis ($a/b$). For the case of spherical particles ($a = b = c$), the depolarising factors are simplified to $A_a = A_b = A_c = 1/3$.

As previously discussed in Chapter 3, the relaxation in the effective polarisability of a particle is described by the complex Clausius-Mossotti factor ($\tilde{f}_{CM}$). This can be determined by taking in consideration the polarisability along each semi-axis:

$$f_{CM} = A_a \, \widetilde{K}_a + A_b \, \widetilde{K}_b + A_c \, \widetilde{K}_c \qquad (5.4)$$

For a particle in a suspending medium at low volume fraction ($\varphi \ll 1$), Maxwell's mixture theory gives the equivalent complex dielectric permittivity of that mixture as:

$$\tilde{\varepsilon}_{mix} = \tilde{\varepsilon}_{medium} \frac{1+2\varphi \, \tilde{f}_{CM}}{1-\varphi \, \tilde{f}_{CM}} \qquad (5.5)$$

This equation gives the dielectric decrement due to the presence of the particle in the suspending medium. With this information, the corresponding relaxation curve can be generated and used to determine the dielectric properties of the particles.

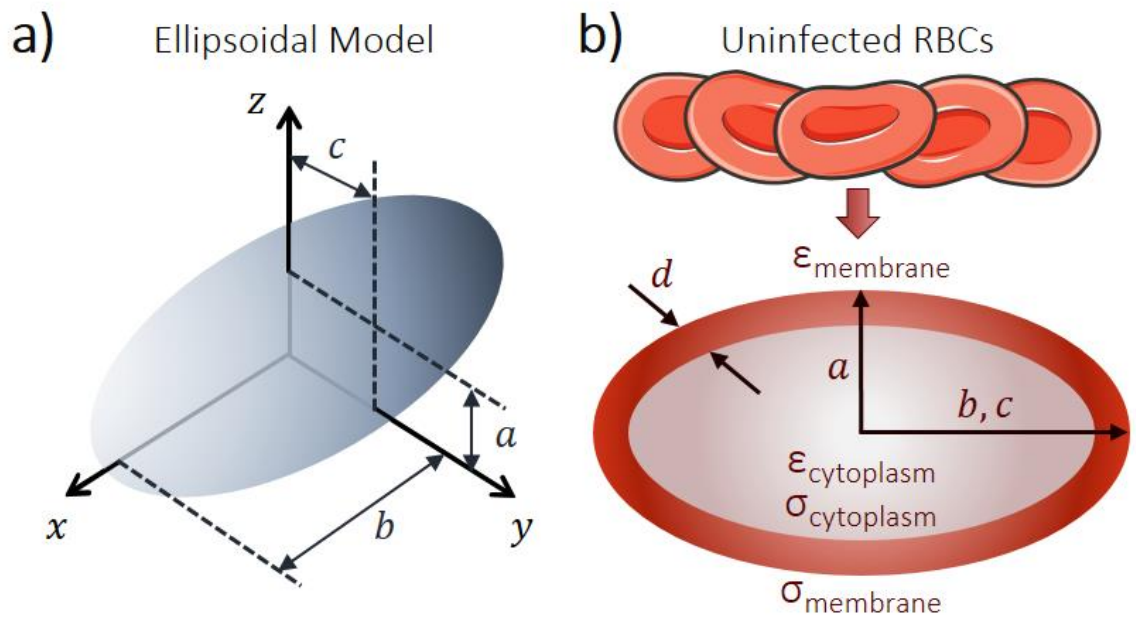


**Figure 5.25: a)** Ellipsoidal model, with semi-axes $a, b$ and $c$ . **b)** Oblate spheroid model implemented for *u*-RBCs, with semi-axes $a < b = c$ (based on the ellipsoidal model), membrane thickness $d$, and dielectric properties modelled are represented.

For the RBC, the ellipsoidal model approximates the cell to a single-shell oblate spheroid, with semi-axes $a < b = c$ (**Figure 5.25b**). The model was first used to estimate the dielectric properties of the TCs control samples, *i.e.*, samples containing only uninfected RBCs, kept under the same conditions as samples containing *i*-RBCs. As an example, **Figure 5.26** presents the MMT fits to impedance data for most time-points of TC2. Optimal fits were obtained for all time-points - $R^2$ = 0.9990 ± 0.0004; N = 7 time-points. The estimated dielectric properties for control RBCs (*c*-RBCs), listed in **Table 5.4**, were in good agreement with the widely accepted dielectric values for RBCs (Pauly and Schwan, 1966; Takashima, Asami and Takahashi, 1988; Gimsa *et al.*, 1994; Gascoyne *et al.*, 2002b; Katsumoto *et al.*, 2008). The model was then implemented for the *u*-RBCs at different TCs. Optimal fits were also obtained for all time-points - $R^2$ = 0.9993 ± 0.0004; N = 7 time-points. **Figure 5.27** shows the MMT fits for most time-points of TC3. Estimated dielectric properties of *u*-RBCs (**Table 5.5**) were also in agreement with accepted literature values for RBCs, suggesting that exposure of uninfected RBC to parasites and their secreted metabolites under culture conditions does not significantly alter the dielectric properties of the RBC (no bystander effect (Paul *et al.*, 2013)).

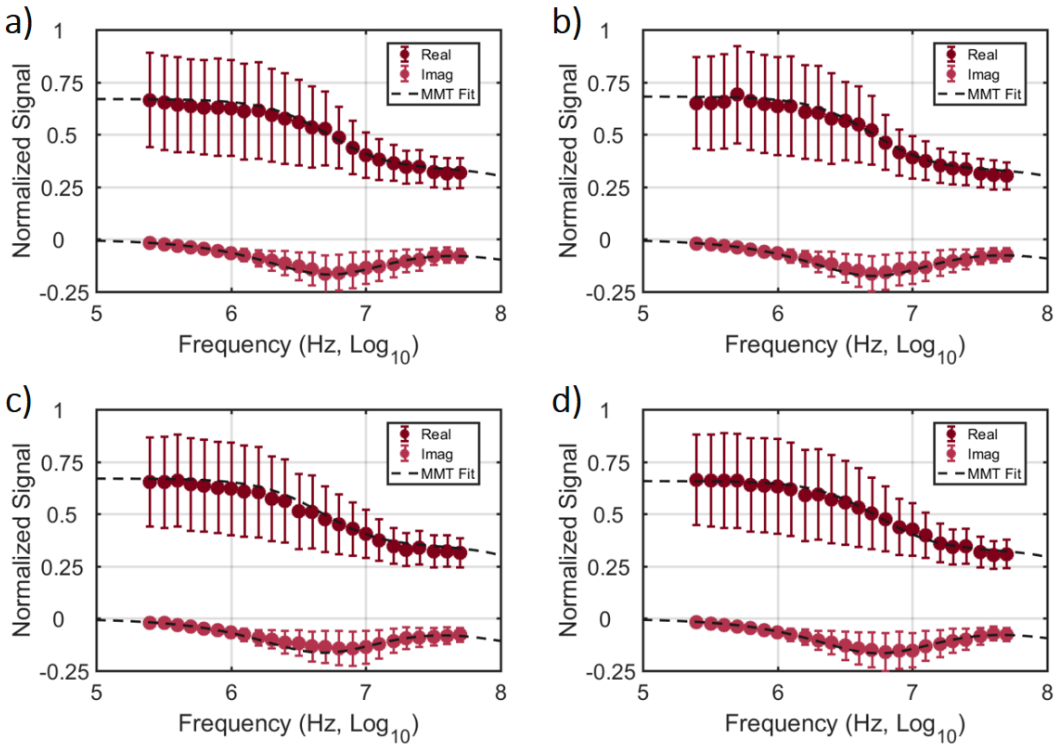


**Figure 5.26:** Normalized real and imaginary parts of impedance of *c*-RBCs, across the measured probe frequency spectrum, of control samples at **a)** 6hpi, **b)** 18 hpi, **c)** 30 hpi and **d)** 42 hpi. Single-shell oblate spheroid models were used to generate each MMT fit. The optimal MMT fits (*dashed lines*) are plotted on top of individual probe frequency mean values (*circles*) and standard deviation (*error bars*) for each time-point. Data from TC2.

**Table 5.4:** Dielectric properties along the TC of infection, estimated using MMT modelling, of *c*-RBCs

| Properties | Period of intraerythrocytic development of parasite | | | | | | |
|---|---|---|---|---|---|---|---|
| | **6 hpi** | **12 hpi** | **18 hpi** | **24 hpi** | **30 hpi** | **36 hpi** | **42 hpi** |
| $\varepsilon_{membrane}$ | 4.24 ± 0.21 | 4.38 ± 0.20 | 4.24 ± 0.22 | 4.10 ± 0.31 | 4.20 ± 0.22 | 4.26 ± 0.22 | 4.13 ± 0.36 |
| $\varepsilon_{cytoplasm}$ | 57.8 ± 4.5 | 56.4 ± 1.9 | 58.3 ± 4.2 | 56.9 ± 2.2 | 59.9 ±4.2 | 62.5 ± 6.2 | 54.4 ± 0.7 |
| $\sigma_{cytoplasm}$ (S/m) | 0.38 ± 0.04 | 0.40 ± 0.04 | 0.43 ± 0.01 | 0.40 ± 0.01 | 0.44 ± 0.05 | 0.40 ± 0.04 | 0.44 ± 0.04 |
| $C_{membrane}$ (mF/m$^2$) | 7.51 ± 0.36 | 7.76 ± 0.35 | 7.51 ± 0.39 | 7.26 ± 0.55 | 7.45 ± 0.40 | 7.54 ± 0.39 | 7.32 ± 0.64 |

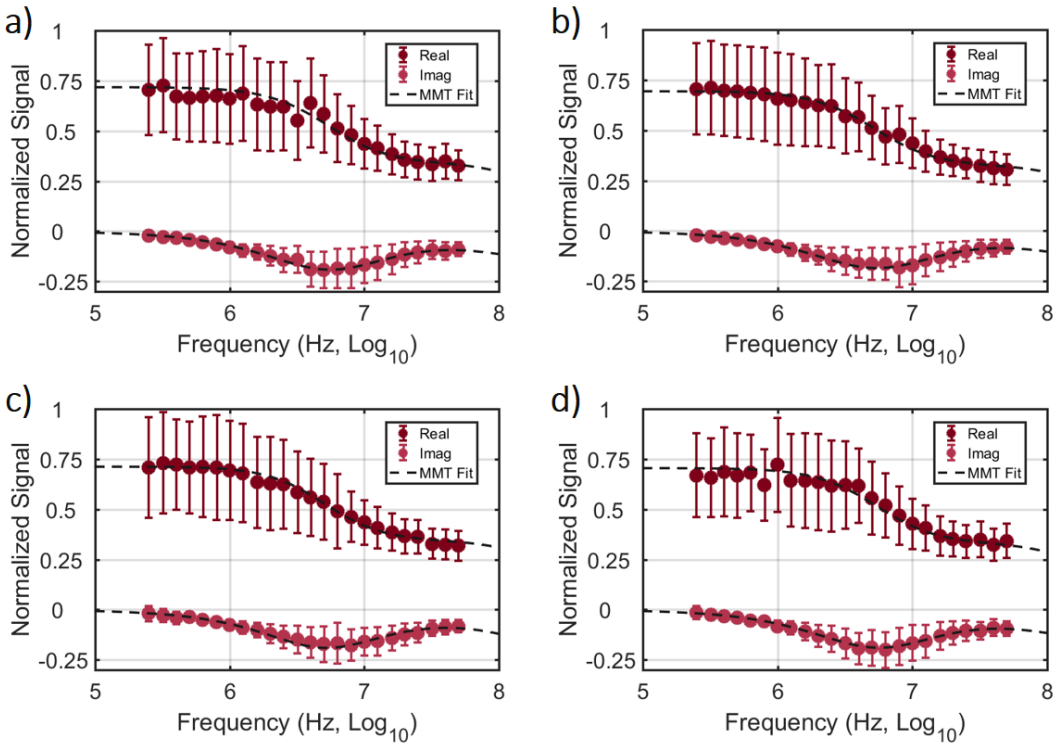


**Figure 5.27:** Normalized real and imaginary parts of impedance of *u*-RBCs, across the measured probe frequency spectrum, of cultures at **a)** 6hpi, **b)** 18 hpi, **c)** 30 hpi and **d)** 42 hpi. Single-shell oblate spheroid models were used to generate each MMT fit. The optimal MMT fits (*dashed lines*) are plotted on top of individual probe frequency mean values (*circles*) and standard deviation (*error bars*) for each time-point. Data from TC3.

**Table 5.5:** Dielectric properties along the TC of infection, estimated using MMT modelling, of *u*-RBCs

| Properties | Period of intraerythrocytic development of parasite | | | | | | |
|---|---|---|---|---|---|---|---|
| | 6 hpi | 12 hpi | 18 hpi | 24 hpi | 30 hpi | 36 hpi | 42 hpi |
| $\varepsilon_{membrane}$ | 4.01 ± 0.05 | 3.95 ± 0.05 | 4.07 ± 0.04 | 4.04 ± 0.17 | 4.10 ± 0.28 | 3.93 ± 0.14 | 4.00 ± 0.05 |
| $\varepsilon_{cytoplasm}$ | 53.7 ± 5.1 | 59.1 ± 4.8 | 60.5 ± 5.0 | 59.2 ± 5.6 | 56.0 ±0.8 | 64.1 ± 2.2 | 60.3 ± 3.1 |
| $\sigma_{cytoplasm}$ (S/m) | 0.41 ± 0.02 | 0.45 ± 0.02 | 0.44 ± 0.03 | 0.43 ± 0.02 | 0.41 ± 0.01 | 0.43 ± 0.01 | 0.43 ± 0.02 |
| $C_{membrane}$ (mF/m$^2$) | 7.10 ± 0.10 | 7.00 ± 0.09 | 7.20 ± 0.07 | 7.15 ± 0.30 | 7.27 ± 0.49 | 6.96 ± 0.25 | 7.09 ± 0.08 |

### 5.4.5 Impedance Modelling of Infected Red Blood Cells

For the case of *i*-RBCs, the presence of the parasite within the host cell complicates the modelling approach. The simplest approach is to use a single-shell oblate spheroid model, where the internal component includes the host cell cytoplasm and the parasite (both membrane and cytoplasm). This model was used to fit to data for early stage (6 hpi – $R^2$ = 0.9984 ± 0.0006; N = 3 TCs; **Figure 5.28a and b**) and late stage infection (36 hpi – $R^2$ = 0.9850 ± 0.0027; N = 3 TCs; **Figure 5.28c and d**). The estimated dielectric properties are presented in **Table 5.6**. With an optimal fit at 6 hpi, the estimated properties are interestingly close to that of uninfected cells (see **Table 5.4** and **Table 5.5**), which seems to indicate a negligible change in the cell due to the parasite at the early infection stage. In constrast, the poor fit at 36 hpi translates to an incorrect estimate of dielectric properties. For example, the estimated $C_{membrane}$ at 36 hpi (5.2 ± 0.5 mF/m$^2$, N = 3 samples) is too low for a viable cell, and does not match with the expected increase in $C_{membrane}$ of *i*-RBCs (Gascoyne *et al.*, 2002b). Furthermore, the estimated dielectric properties (**Table 5.6**) do not give a clear understanding of the alterations of the host cell, as the interior now relates to three different components. For instance, the presence of the parasite membrane effectively reduces the estimated $\sigma_{cytoplasm}$ (the conductivity of the interior), as cell membranes have usually a $\sigma_{membrane}$ value $\leq 10^{-8}$ S/m, making it impossible to correctly estimate the cell cytoplasm conductivity.

**Table 5.6:** Dielectric properties at 6 and 36 hpi, estimated using a single-shell oblate model, with MMT modelling, of *i*-RBCs

| Properties | Period of intraerythrocytic development of parasite | |
|---|---|---|
| | 6 hpi | 36 hpi |
| $\varepsilon_{membrane}$ | 4.20 ± 0.10 | 2.93 ± 0.26 |
| $\varepsilon_{cytoplasm}$ | 72 ± 6.8 | 85.4 ± 6.3 |
| $\sigma_{cytoplasm}$ (S/m) | 0.35 ± 0.02 | 0.29 ± 0.01 |
| $C_{membrane}$ (mF/m$^2$) | 7.50 ± 0.10 | 5.20 ± 0.50 |

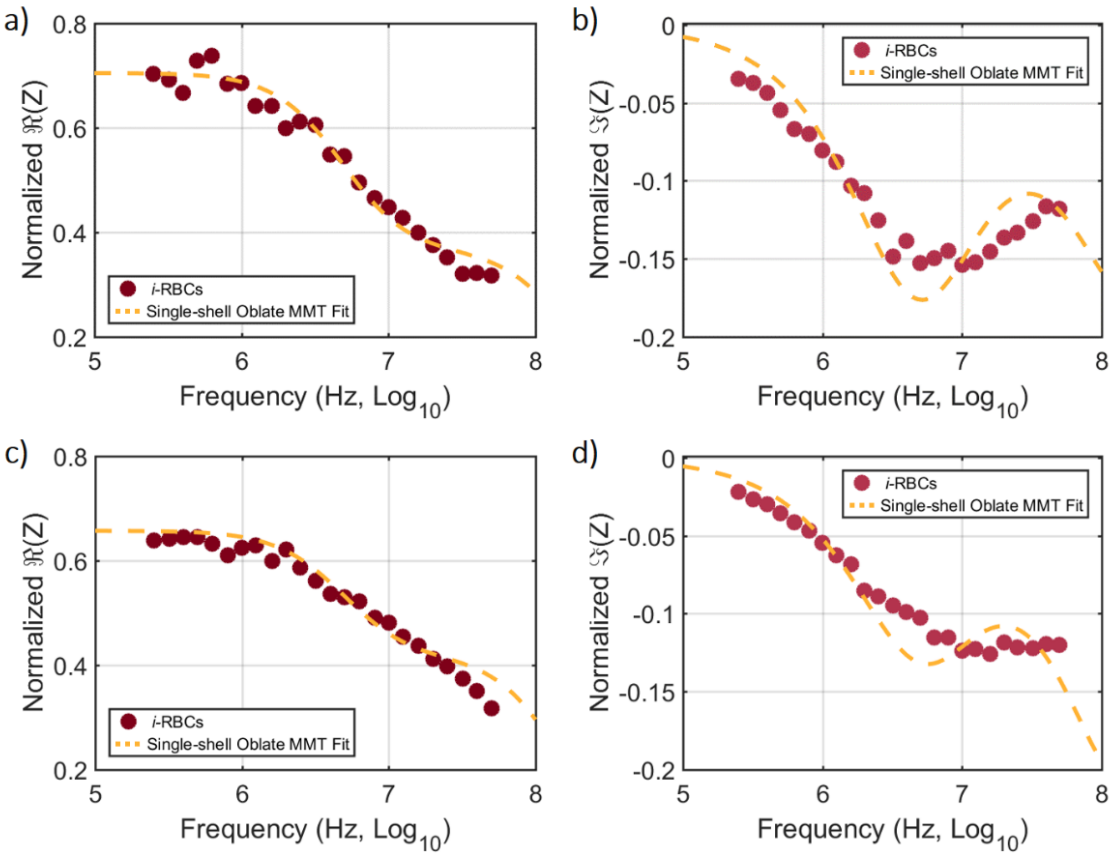


**Figure 5.28:** Normalized real (**a** and **c**) and imaginary (**b** and **d**) parts of impedance of *i*-RBCs, across the measured probe frequency spectrum, of cultures containing parasite-infected cells at 6hpi (**a** and **b**), and 36 hpi (**c** and **d**). Single-shell oblate spheroid models were used to generate each MMT fit. The optimal MMT fits (*dashed lines*) are plotted on top of individual probe frequency mean values (*circles*) and standard deviation (*error bars*) for each time-point. Data from TC3.

The existence of the parasite within the host cell means that the single-shelled particle model is inappropriate. Therefore the double-shell model was used, as it considers both the presence of the host cell membrane and the parasite membrane (**Figure 5.29a**). For higher frequencies (>10 MHz), above the relaxation of the outer membrane, the impedance signal is a function of the cell cytoplasmic properties. As frequency increases, the impedance reflects the properties of the second (internal) shell *i.e.*, the dielectric properties of the parasite, with the second dielectric relaxation occurring at much higher frequencies (Morgan and Green, 2002). The dielectric properties of both host cell and parasite can thus be approximated based on these dielectric relaxations.

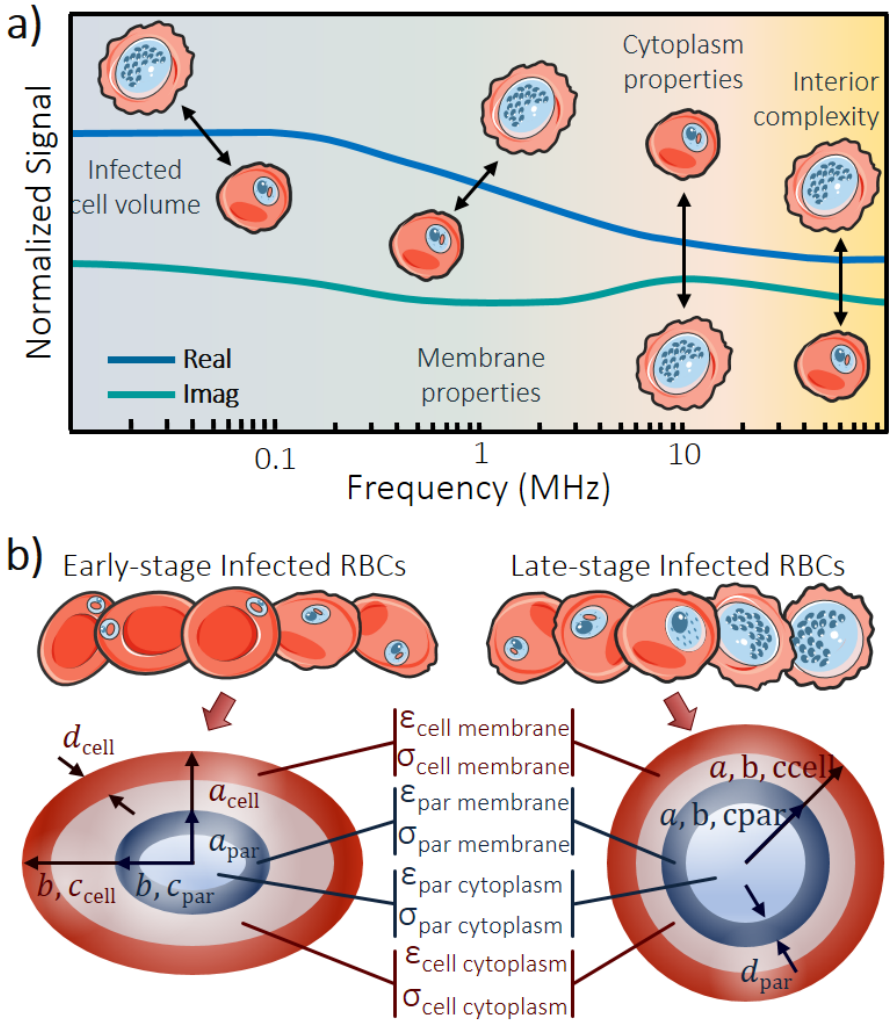


**Figure 5.29: a)** Illustration of the frequency-dependent dielectric response of a double-shelled particle (as *i*-RBCs), with two relaxations. The relationships between some of the dielectric properties and behaviour at specific frequencies are highlighted. Note that the frequency window for these relaxations depends on the conductivity of the suspending medium. **b)** Models implemented for *i*-RBCs: oblate spheroid model for early-stage *i*-RBCs and spherical model for late-stage *i*-RBCs, with semi-axes $a = b = c$ (based on the ellipsoidal model). Membrane thickness of cell ($d_{cell}$) and parasite ($d_{par}$), and dielectric properties modelled are represented.

The wide variations in size and shape of the host cell and parasite throughout the parasite life cycle requires a different modelling approach and two different models were used depending on the stage of infection (**Figure 5.29b**). For early-stage *i*-RBCs, the ellipsoidal model was implemented. Post invasion, the parasite flattens into a thin flat or cup-shaped disc ring, and does not alter the shape of the host cell until later (Bannister *et al.*, 2000; Esposito *et al.*, 2010; Hanssen, McMillan and Tilley, 2010). Thus, a double-shell oblate spheroid model was used. The same initial conditions as used for uninfected RBCs were applied ($\sigma_{medium} = 1.5$ S/m, $\varepsilon_{medium} = 80$, $d = 5$ nm and $\sigma_{membrane} \leq 10^{-8}$ S/m). To reduce the complexity of the modelling process and increase confidence in the results, some variables were fixed (based on values from uninfected RBCs): $\varepsilon_{cell\ cytoplasm} = 60$, $\varepsilon_{par\ cytoplasm} = 60$, $\sigma_{par\ cytoplasm} = 0.40$ S/m. This provided optimal fits for the time-points at early stages of infection: 6 hpi, 12 hpi and 18 hpi ($R^2$ = 0.9978 ± 0.0007; N = 3 time-points; **Figure 5.30**).

The ring-stage parasite gradually changes to a more rounded and irregular trophozoite, and later schizont form. These changes are accompanied by an increase in parasite volume, making the host cell less discoid, at around 24 hpi (Bannister *et al.*, 2000; Esposito *et al.*, 2010; Hanssen, McMillan and Tilley, 2010). At this time-point, the oblate spheroid model might not be the best approach. To test this, both the oblate spheroid and spherical models were used to fit the data at 24 hpi (**Figure 5.31**).

The oblate spheroid model results in a worst fit to the impedance data ($R^2$ = 0.9897 ± 0.0007; N = 3 TCs, **Figure 5.31b**), when compared with the spherical model ($R^2$ = 0.9979 ± 0.0006; N = 3 TCs). The parasite growth and increased deformation of the host cell means that the ellipsoid model is inaccurate, so that for late-stage *i*-RBCs (≥ 24 hpi) the double-shell spherical model was used. This model was based on the existing ellipsoidal model with semi-axes $a = b = c$. Using this model gave optimal fits for the last time-points of infection: 24 hpi, 30 hpi, 36 hpi and 42 hpi ($R^2$ = 0.9967 ± 0.0026; N = 4 time-points; **Figure 5.32**).

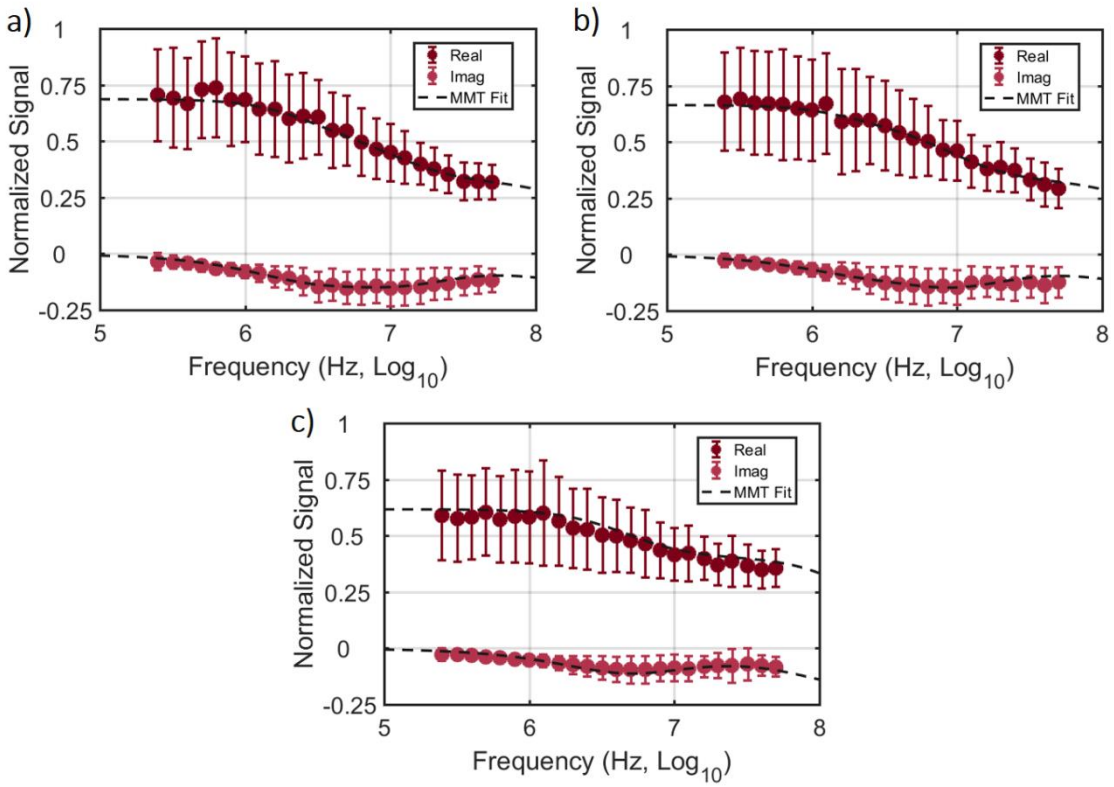


**Figure 5.30:** Normalized real and imaginary parts of the average impedance spectrum of *i*-RBCs, across the measured probe frequency spectrum, of culture containing parasite-infected cells at **a)** 6 hpi, **b)** 12 hpi, and **c)** 18 hpi. Double-shell oblate spheroid model was used to generate each MMT fit. The optimal MMT fits (*dashed lines*) are plotted on top of individual probe frequency mean values (*circles*) and standard deviation (*error bars*) for each time-point. Data from TC1.

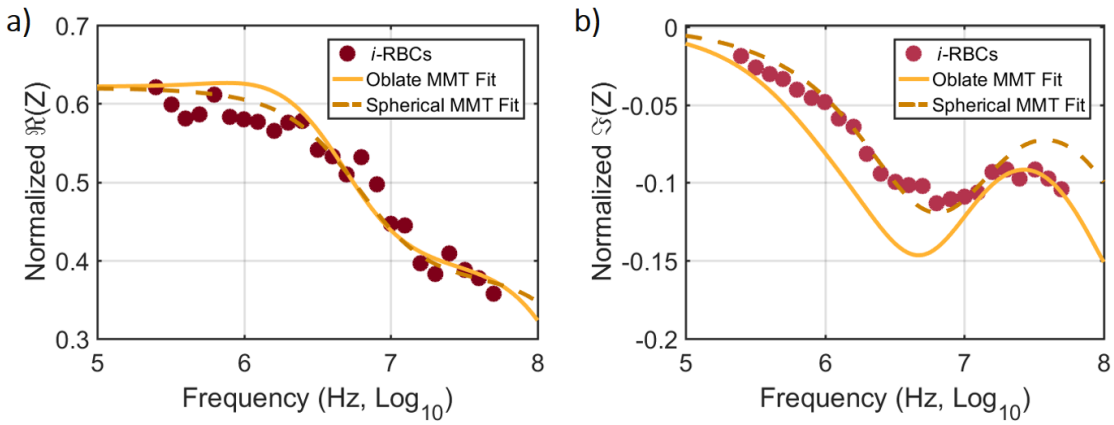


**Figure 5.31:** Normalized **a)** real and **b)** imaginary parts of the average impedance spectrum of *i*-RBCs, across the measured probe frequency spectrum, of a culture containing parasite-infected cells at 24 hpi. Both a double-shell oblate spheroid and spherical model were used to generate MMT fits. The optimal MMT fits (*dashed and full lines*) are plotted on top of individual probe frequency mean values (*circles*). Data from TC3.

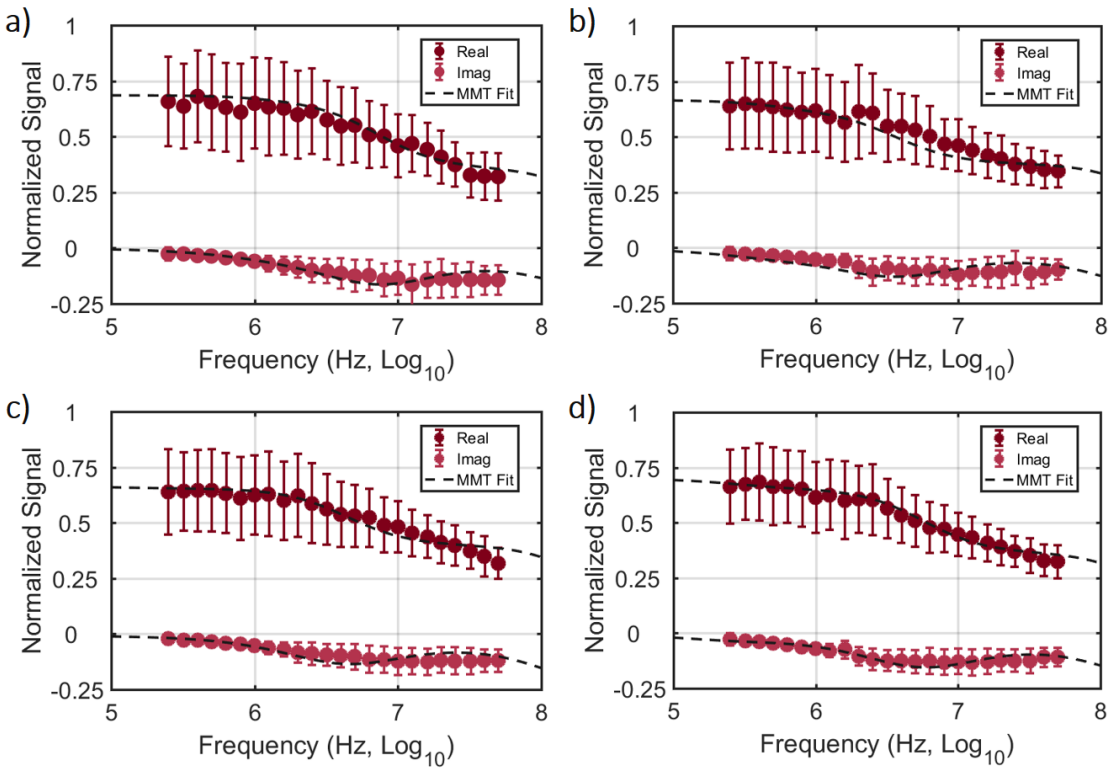


**Figure 5.32:** Normalized real and imaginary parts of the average impedance spectrum of *i*-RBCs, across the measured probe frequency spectrum, of cultures containing parasite-infected cells at **a)** 24 hpi, **b)** 30 hpi, **c)** 36 hpi and **d)** 42 hpi. Double-shell spherical model was used to generate each MMT fit. The optimal MMT fits (*dashed lines*) are plotted on top of individual probe frequency mean values (*circles*) and standard deviation (*error bars*) for each time-point. Data from TC1.

**Figure 5.33** shows how the dielectric properties for *c*-RBCs, *u*-RBCs, *i*-RBCs and parasites as a function of time. Statistical analysis showed no significant difference between the dielectric properties of *u*-RBCs and *c*-RBCs (Student's *t*-test, N = 7 time-points; $p \gg 0.05$). Consequently, these two populations were used for comparison with *i*-RBCs, at different time-points. Statistical analysis showed significant differences in dielectric properties of *i*-RBCs within the TCs (ANOVA test, N = 7 time-points; $p \ll 0.05$). Thus, changes in *i*-RBCs during the infection cycle were statistically assessed by comparing host cell membrane capacitance and cytoplasmic conductivity for *i*-RBCs at individual time-points (Tukey's test, N = 21 pairwise comparisons; **Table 5.7** and **Table 5.8**). The full lists of estimated dielectric properties for *c*-RBCs, *u*-RBCs, and *i*-RBCs and parasite is shown in **Table 5.4**, **Table 5.5** and **Table 5.9**, respectively.

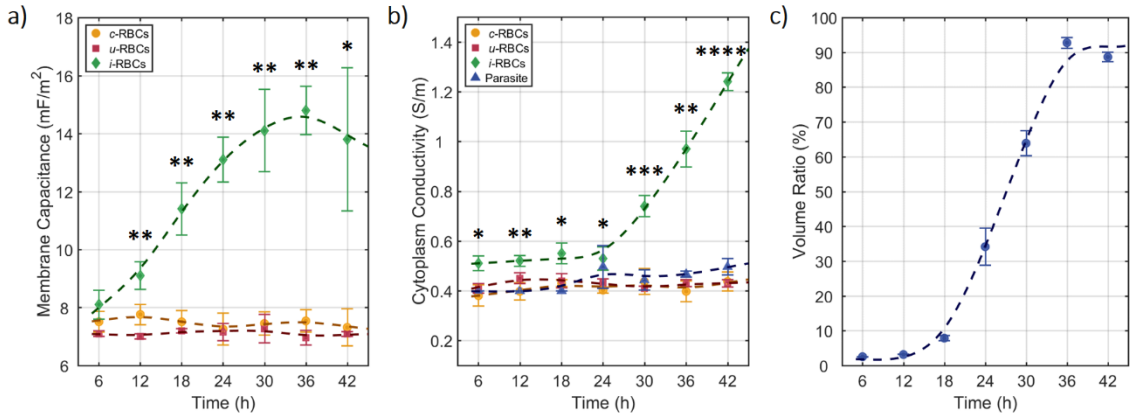


**Figure 5.33:** Dielectric properties, estimated using MMT modelling, during the parasite intraerythrocytic life cycle: **a)** membrane capacitance, **b)** cytoplasm conductivity, and **c)** volume ratio occupied by parasite within the host cell. Mean values from the three TCs (*symbols*) and standard deviation (*error bars*) are plotted for each time-point. Smoothing splines (*dashed lines*) are plotted to represent the overall trend for each population. Statistical significance (*$p$<0.05, **$p$<0.01, ***$p$<0.001 and ****$p$<0.0001) is represented for *i*-RBCs (N=3) versus *c*-RBCs and *u*-RBCs (N=6) at individual time-points.

**Table 5.7:** Statistical analysis of host cell membrane capacitance changes in *i*-RBCs along the time-course of infection (Tukey's test, N = 21 pairwise comparisons; n. s. - not significant, *$p$<0.05, **$p$<0.01)

| $C_{cell\ membrane}$ | 6 hpi | 12 hpi | 18 hpi | 24 hpi | 30 hpi | 36 hpi | 42 hpi |
|---|---|---|---|---|---|---|---|
| **6 hpi** | | n. s. | n. s. | * | ** | ** | ** |
| **12 hpi** | | | n. s. | n. s. | * | ** | * |
| **18 hpi** | | | | n. s. | n. s. | n. s. | n. s. |
| **24 hpi** | | | | | n. s. | n. s. | n. s. |
| **30 hpi** | | | | | | n. s. | n. s. |
| **36 hpi** | | | | | | | n. s. |
| **42 hpi** | | | | | | | |

**Table 5.8:** Statistical analysis of host cell cytoplasmic conductivity changes in *i*-RBCs along the time-course of infection (Tukey's test, N = 21 pairwise comparisons; n. s. - not significant, *$p$<0.05, **$p$<0.01, ***$p$<0.001 and ****$p$<0.0001)

| $\sigma_{cell\ cytoplasm}$ | 6 hpi | 12 hpi | 18 hpi | 24 hpi | 30 hpi | 36 hpi | 42 hpi |
|---|---|---|---|---|---|---|---|
| **6 hpi** | | n. s. | n. s. | n. s. | ** | ** | **** |
| **12 hpi** | | | n. s. | n. s. | ** | ** | **** |
| **18 hpi** | | | | n. s. | ** | ** | **** |
| **24 hpi** | | | | | ** | ** | **** |
| **30 hpi** | | | | | | * | *** |
| **36 hpi** | | | | | | | * |
| **42 hpi** | | | | | | | |

**Table 5.9:** Dielectric properties along the TC of infection, estimated using MMT modelling, of *i*-RBCs

| Properties | Period of intraerythrocytic development of parasite | | | | | | |
|---|---|---|---|---|---|---|---|
| | 6 hpi | 12 hpi | 18 hpi | 24 hpi | 30 hpi | 36 hpi | 42 hpi |
| $\varepsilon_{cell\ membrane}$ | 4.58 ± 0.28 | 5.38 ± 0.36 | 6.43 ± 0.50 | 7.40 ± 0.43 | 7.99 ± 0.80 | 8.32 ± 0.45 | 7.80 ± 1.40 |
| $\varepsilon_{cell\ cytoplasm}$ | 60 (fixed value) | 60 (fixed value) | 60 (fixed value) | 66.7 ± 9.4 | 83.3 ± 4.7 | 86.7 ± 4.7 | 86.7 ± 4.7 |
| $\varepsilon_{par\ membrane}$ | 3.03 ± 0.40 | 3.33 ± 0.47 | 5.83 ± 0.24 | 5.67 ± 0.47 | 5.67 ± 1.70 | 3.50 ± 0.41 | 4.00 ± 0.82 |
| $\varepsilon_{par\ cytoplasm}$ | 60 (fixed value) | 60 (fixed value) | 60 (fixed value) | 76.7 ± 9.4 | 76.7 ± 4.7 | 86.7 ± 4.7 | 86.7 ± 4.7 |
| $\sigma_{cell\ cytoplasm}$ (S/m) | 0.51 ± 0.03 | 0.52 ± 0.02 | 0.55 ± 0.04 | 0.53 ± 0.05 | 0.74 ± 0.04 | 0.97 ± 0.07 | 1.24 ± 0.04 |
| $\sigma_{par\ cytoplasm}$ (S/m) | 0.40 (fixed value) | 0.40 (fixed value) | 0.40 (fixed value) | 0.50 ± 0.09 | 0.44 ± 0.04 | 0.47 ± 0.01 | 0.50 ± 0.03 |
| $C_{cell\ membrane}$ (mF/m$^2$) | 8.1 ± 0.50 | 9.1 ± 0.47 | 11.4 ± 0.88 | 13.1 ± 0.77 | 14.1 ± 1.42 | 14.8 ± 0.83 | 13.8 ± 2.47 |

Alterations in the host cell membrane, as previously discussed (**Figure 5.14**), are one of the aspects that distinguish uninfected and *i*-RBCs. The uninfected RBCs had a membrane capacitance similar to reported values (*c*-RBCs - $C_{membrane}$ = 7.48 ± 0.15 mF/m$^2$; *u*-RBCs - $C_{membrane}$ = 7.11 ± 0.10 mF/m$^2$; N = 7 time-points) (Takashima, Asami and Takahashi, 1988; Gimsa *et al.*, 1994; Gascoyne *et al.*, 2002b; Katsumoto *et al.*, 2008). In contrast, the membrane capacitance of *i*-RBCs varied with time-course, as shown in **Figure 5.33a**. Changes were seen as early as 12 hpi, when the membrane capacitance of *i*-RBCs increased ($C_{cell\ membrane}$ = 9.1 ± 0.47 mF/m$^2$) and was statistically higher than uninfected RBCs ($p$<0.01). The membrane capacitance of *i*-RBCs increased gradually throughout the TC ($p$<0.01 between 6 hpi and 36 hpi), reaching 14.1 ± 1.42 mF/m$^2$ at 30 hpi. Active remodelling of the host cell membrane carried out by the parasite is visible from the very early stages of infection and is likely to be the reason for this gradual change in membrane capacitance (Cranston *et al.*, 1983; Ginsburg *et al.*, 1985; Kirk, 2001). Membrane capacitance is a function of membrane thickness, area and permittivity (Wang *et al.*, 1994; Morgan and Green, 2002). Although the surface area of the RBC is not affected at early stages of infection (Esposito *et al.*, 2010), the host cell membrane lipid composition is modified by the parasite during

infection (Tran *et al.*, 2016), which could alter membrane permittivity, and consequently membrane capacitance. Also, after merozoite invasion and establishment as a ring stage parasite within the RBC, proteins involved in active remodelling of the host cell are produced, transported across the host cell cytoplasm, and inserted in the RBC membrane, modifying its composition and possibly capacitance (Mbengue, Yam and Braun-Breton, 2012). As the parasite develops further, a channel-like system known as the New Permeation Pathway (NPP) appears on the host plasma membrane 10-20 hpi (Kirk, 2001), and results in an increased ability of parasite-infected erythrocytes to take up nutrients, especially anionic compounds (Desai, Bezrukov and Zimmerberg, 2000). Furthermore, accumulation of parasite proteins at the host cell membrane underside causes the appearance of small angular elevations ("*knobs*") at later stages, altering the membrane structure and surface area (Bannister *et al.*, 2000; Hanssen, McMillan and Tilley, 2010), which could increase the capacitance.

One of the consequences of the membrane alterations is a change toward a "*leaky capacitor*" (Morgan and Green, 2002), *i.e.*, an increase in ion exchange activity between the intra- and extra-cellular regions. This effect was observed along the TCs (**Figure 5.33b**). The conductivity of the *i*-RBCs cytoplasm was already different at 6 hpi ($\sigma_{cell\ cytoplasm}$ = 0.51 ± 0.03 S/m, $p$<0.05) when compared with uninfected RBCs (*c*-RBCs: $\sigma_{cytoplasm}$ = 0.38 ± 0.04 S/m; and *u*-RBCs:$\sigma_{cytoplasm}$ = 0.41 ± 0.02 S/m). There was no significant increase in cytoplasmic conductivity during the ring stage of infection, with the *i*-RBCs $\sigma_{cell\ cytoplasm}$ = 0.53 ± 0.05 S/m at 24 hpi. Only after the parasite reaches later stages, was the effect of ion exchange observed. Ions from the high conductivity isotonic medium enter the host cell during the later stages of the life cycle (> 24 hpi), causing an increase in *i*-RBCs cytoplasm conductivity between 24 hpi and 42 hpi ($p$<0.0001). Cytoplasm conductivity increases from $\sigma_{cell\ cytoplasm}$ = 0.74 ± 0.04 S/m at 30 hpi, to values close to that of the medium by 42 hpi - $\sigma_{cell\ cytoplasm}$ = 1.24 ± 0.04 S/m. This was much higher than uninfected RBCs ($p$<0.0001 at 42 hpi), which maintain a constant, much lower value (*c*-RBCs: $\sigma_{cytoplasm}$ = 0.41 ± 0.02 S/m; *u*-RBCs: $\sigma_{cytoplasm}$ = 0.43 ± 0.01 S/m; N = 7 time-points), in agreement with literature (Pauly and Schwan, 1966; Gimsa *et al.*, 1994; Gascoyne *et al.*, 2002b; Katsumoto *et al.*, 2008). The double-shell model was also used to estimate the cytoplasm conductivity of the parasite itself (**Figure 5.33b**). As with uninfected cells, the parasite maintained a stable, lower cytoplasm conductivity at the late stages of TCs: $\sigma_{par\ cytoplasm}$ = 0.48 ± 0.02 S/m; N = 4 time-points (the fixed values for early stages were not considered). This value seems to

confirm the hypothesis that uninfected RBCs and parasites have similar cytoplasm properties. Indeed, the overlap observed in **Figure 5.18c** and **Figure 5.20c** can be explained by the estimated similarities between the dielectric properties of uninfected RBCs (*c*-RBCs: $\sigma_{cytoplasm}$ = 0.41 ± 0.02 S/m; and *u*-RBCs:$\sigma_{cytoplasm}$ = 0.43 ± 0.01 S/m; N = 7 time-points) and parasites.

The observed "*leaky*" behaviour of *i*-RBCs membranes has been reported previously (Ginsburg *et al.*, 1985; Kirk, 2001; Ginsburg and Stein, 2004). It can be attributed to two factors: alterations in membrane lipid content affecting the activity of endogenous channels (to a lesser extent) (Hsiao *et al.*, 1991; Vial and Ancelin, 1998); and, primarily, the appearance of new permeation pathways in the host cell membrane (Ginsburg *et al.*, 1985; Desai, Bezrukov and Zimmerberg, 2000; Kirk, 2001; Ginsburg and Stein, 2004). New permeation pathways display a pore-like behaviour and appear around the trophozoite stage (close to 24 hpi); a stage when the parasite enters a state of intense metabolism, dependent on an ample supply of metabolites and an effective discharge of waste products (Ginsburg *et al.*, 1985; Kirk, 2001; Staines, Ellory and Kirk, 2001; Ginsburg and Stein, 2004). During this period, part of the parasite activity is focused on degrading and digesting RBC proteins, mainly haemoglobin. A decrease in haemoglobin concentration in the *i*-RBCs cytosol leads to an increased influx of anions, compensating for the loss of negative charges, as haemoglobin is negatively charged (Mauritz *et al.*, 2009, 2011). Consequently, this anion influx correlates to the observed sudden increase in cytoplasm conductivity at later stages of infection. *i*-RBCs are thus capable of sustaining a controlled salt composition and osmotic volume, therefore avoiding premature lysis of the host cell before maturation of daughter merozoites (Ginsburg *et al.*, 1985; Kirk, 2001, 2015).

Gascoyne *et al.* (2002) previously reported an opposite phenomenon (Gascoyne *et al.*, 2002b), where they showed how the conductivity of the *i*-RBCs cytoplasm reached 95 ± 5 % of the outside conductivity, when cells were suspended in an iso-osmotic low conductivity medium ($\sigma_{medium}$ = 0.055 S/m). This effect was observed in heterogeneous populations of *i*-RBCs, so it is not clear at what point in the intraerythrocytic cycle this change occurs. The authors attribute this "*leaky*" behaviour by the *i*-RBCs to the presence of the new permeation pathways and changes in the membrane lipid composition. A leaky membrane would explain how those factors would result in a decreased cytoplasmic conductivity, but not how that decrease would fit the known metabolic needs of parasite-infected cells, specifically the necessary increase in anion influx (Ginsburg *et al.*, 1985; Kirk,

2001; Staines, Ellory and Kirk, 2001; Ginsburg and Stein, 2004). Furthermore, the authors state that all stages of parasitized cells lost ions, but fail to describe how ring stage *i*-RBCs would be affected by such membrane changes, which occur later in the infection cycle. Thus, the observed decrease in cytoplasmic conductivity must originate from factors unrelated to the metabolism of parasite-infected cells, but possibly due to the stress on these cells suspended in non-physiological conditions. In these experiments, the cytoplasm conductivity reaches approximately 80% of the medium conductivity only at 42 hpi, staying at approximately 35% during the ring stage, consistent with the described metabolic needs of parasitized cells.

Finally, the volumetric changes in the RBC need to be considered. It has been shown that there is no significant alteration in the *i*-RBC volume when compared with *u*-RBC for *P. falciparum* (Esposito *et al.*, 2010). This absence of volume alteration can also be inferred from the estimated volumes. No statistically significant volume change was measured between *i*-RBCs (94.6 ± 5.14 fL, N = 7 time-points) and uninfected RBCs (96.3 ± 4.25 fL, N = 7 time-points). In contrast, the parasite itself undergoes various volume and growth stages. This can be seen from the parameters in **Figure 5.33c**, where the volume ratio occupied by a parasite within the host cell was calculated and plotted. During early stages (≤ 18 hpi), the parasite activity is focused on creating conditions for survival, by consuming haemoglobin, altering the membrane and re-organizing the host cell interior (Bannister *et al.*, 2000; Kirk, 2001; Maier *et al.*, 2009; Hanssen, McMillan and Tilley, 2010). Thus, it lacks the conditions to grow and occupies a very small portion of the host cell. However, for later stages (≥ 24 hpi), the parasite becomes metabolically more active and starts increasing in size. It eventually starts nuclear division as a preparation for schizogony, *i.e.*, the asexual reproduction process of merozoites creation, and reaches a maximum size between 36 and 42 hpi, occupying most of the host cell volume (Bannister *et al.*, 2000; Hanssen, McMillan and Tilley, 2010). This phenomenon can be clearly seen in **Figure 5.33c**, with the volume ratio varying between less than 10% for early stages (≤ 18 hpi), and around 90% for later stages (36 and 42 hpi).

This full dielectric characterisation of *i*-RBCs provides a thorough description of the time course of changes between infected and uninfected cells over the parasite life cycle. It is clear that there are constant alterations to the host cell dielectric properties, at membrane and/or cytoplasm level, starting from as early as 6 hpi. In addition, contrary to previous studies (Gascoyne *et al.*, 2002b; Du *et al.*, 2013), it

is possible to observe significant changes between the various stages of the parasite life cycle.

These alterations could be exploited to develop label-free analysis and sorting methods using for example AC electrokinetics techniques such as DEP (Huang and Pethig, 1991; Cheng *et al.*, 1998; Lapizco-Encinas *et al.*, 2004a; Gascoyne and Shim, 2014). As previously discussed in **Section 3.2.1**, DEP-based sorting requires two populations of particles to have different dielectric properties (and/or size). Since *i*-RBCs and *u*-RBCs are the same size (Esposito *et al.*, 2010), the differences in dielectric properties could be exploited to identify and sort the *i*-RBCs. However, for the early ring stage *i*-RBCs, the spectrum in differences in dielectric properties would not be sufficient to permit unique identification of infected cells, and thus DEP-based diagnosis would not be possible for *P. falciparum i*-RBCs. Nonetheless, for other *Plasmodium* species, where diagnosis can be performed along the whole infection cycle (as *P. vivax*, for example), sorting of *i*-RBCs at later stages could possibly be achieved. The addition of such a pre-enrichment step would make it possible to increase the sensitivity of the "*gold-standard*" diagnostic method (with a limit of detection of 50 parasites/μL), removing one of the current hurdles to improving the accuracy of diagnosis.

## 5.5 Fluorescence-coupled Impedance Cytometry of *L. mexicana*-infected Macrophages

Enrichment of Leishmania-infected cells using current microfluidic label-free techniques is yet to be accomplished. These could be applied, for example, to the characterization of pure populations of infected cells or to increase the diagnosis sensitivity (Tay *et al.*, 2016). This section focuses on the biophysical properties (size and dielectric properties) of macrophages and how these are modified upon infection with *Leishmania Mexicana*. It also explores whether these could be used as biomarkers for diagnosis. The integrated fluorescence MIC system described in **Section** 3.4 was used for this work. This section describes the setup of the threshold for identification of infected cells using fluorescence detection from the GFP expressing *L. mexicana* parasites. Dielectric analysis was then performed to compare infected and uninfected macrophages, and also cells at different activation states (M0, M1 and M2).

### 5.5.1 Identification of Infected Bone-Marrow Macrophages

Prior to any measurements performed on infected cells, a control sample containing only uninfected bone-marrow macrophages (*u*-BMMs) was first tested. As in previous analysis protocols, 7 µm reference polystyrene beads were used to normalize impedance magnitude and phase, with positional correction taken in consideration (Spencer and Morgan, 2011; Spencer *et al.*, 2016). Impedance scatter plots were then generated at a reference frequency (500 kHz in this case) - **Figure 5.34a** is the normalized impedance scatter plot for the control sample, mixed with reference beads.

Fluorescence measurements were also performed simultaneously with impedance. The non-fluorescent reference beads were used to normalize the fluorescence measurements and defined the base-level. **Figure 5.34b** shows the fluorescence distribution for the sample *u*-BMMs. Contrary to the *u*-RBCs described previously, the unlabelled, uninfected cells have a low level of auto-fluorescence. This was also seen in conventional flow cytometry of control samples (**Figure 5.35a** and **d**) and was not an artefact of the custom optics setup. The GFP gated *u*-BMMs population was plotted using impedance data at different frequencies for further analysis (**Figure 5.34c** illustrated an example at 5 MHz).

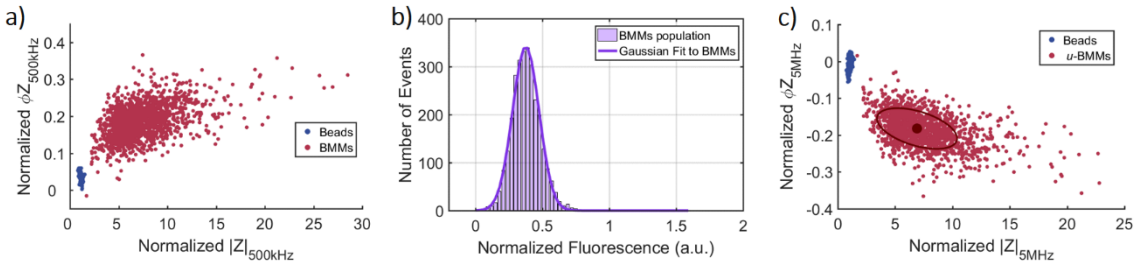


**Figure 5.34: a)** Normalized impedance scatter plot (magnitude |Z| versus phase ΦZ), at 500 kHz, of a control sample, mixed with reference beads. **b)** Normalized fluorescence distribution of the BMMs population. **c)** Normalized impedance scatter plot (magnitude vs phase), measured at 5 MHz for the same control sample, with reference beads, showing only *u*-BMMs. The ellipse containing 50% of the *u*-BMMs population (O) together with the mean (●) are also indicated.

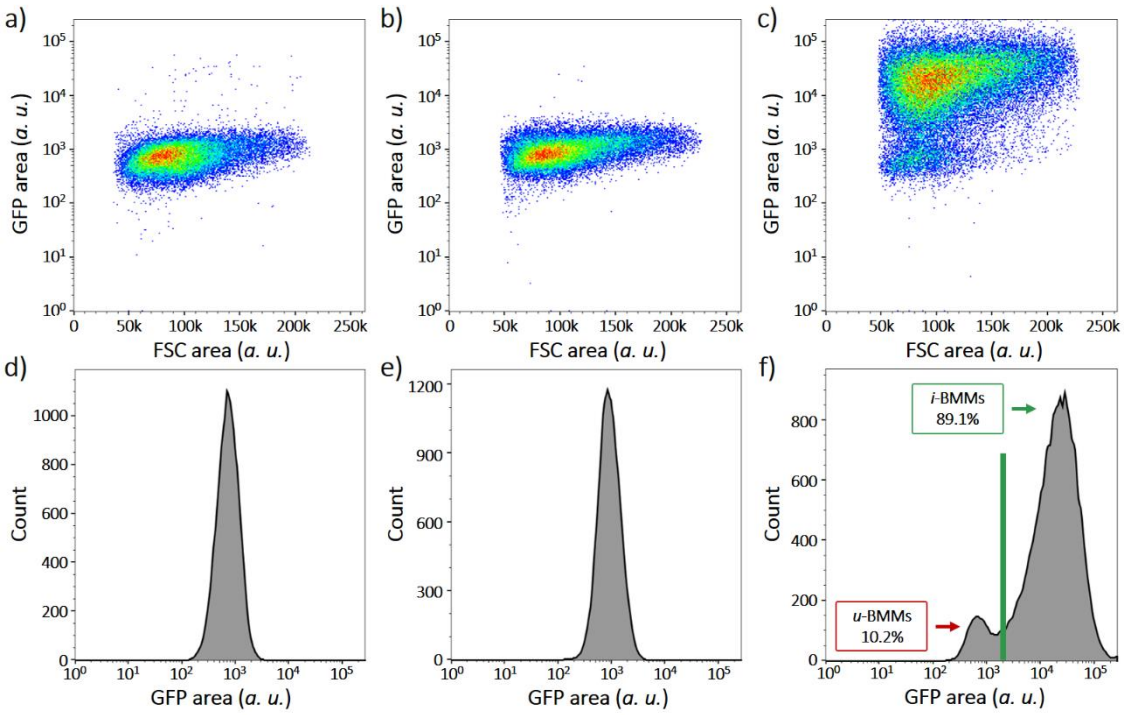


**Figure 5.35:** Conventional flow cytometry data for control, uninfected BMMs (**a** and **d**), non-GFP emitting *i*-BMMs (**b** and **e**), and GFP-emitting *i*-BMMs (**c** and **f**). Forward scatter – FSC is plotted against fluorescence - GFP region (**a**, **b** and **c**), revealing the presence of GFP-parasites in the expected GFP-emitting *i*-BMMs populations only. Histograms of fluorescence show how **d)** control, uninfected BMMs and **e)** non-GFP emitting *i*-BMMs already present auto-fluorescence; but **f)** GFP-emitting *i*-BMMs have a higher level of fluorescent emission, allowing parasitaemia calculation.

Conventional flow cytometry was also performed on samples containing *L. mexicana* infected BMMs (*i*-BMMs) - **Figure 5.35b ,c ,d** and **f**. To uniquely identify *i*-BMMs, parasites that express GFP within the host cell were used. A second, brighter population of cells was clearly seen in FACS data, corresponding to the *i*-BMMs population (**Figure 5.35c** and **f**). This was not observed in control samples (**Figure 5.35a** and **d**); or in samples where non-GFP emitting parasites were used with both *u*-BMMs and *i*-BMMS exhibiting auto-fluorescence (**Figure 5.35b** and **e**). The presence of fluorescent *u*-BMMs was also seen in the samples analysed (**Figure 5.35c** and **f**). Identification of impedance signals from *i*-BMMs followed the protocol summarized in **Figure 5.36**. As previously, normalized impedance data was plotted to identify the populations of BMMs and reference beads (**Figure 5.36a**); and the fluorescence distribution of BMMs was plotted (**Figure 5.36b**). To define a threshold between infected and uninfected cells, the whole BMMs population was first fitted to a double Gaussian distribution, permitting the identification of the two sub-populations. Using the parameters from the model, two new single Gaussian distributions were applied to the infected and uninfected populations.

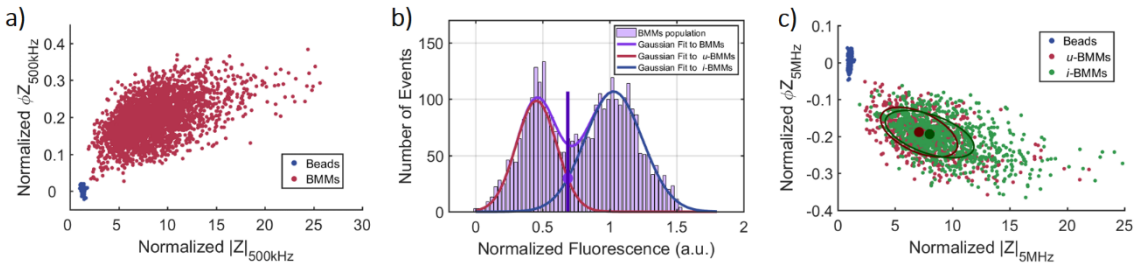


**Figure 5.36:** Identification of infected cells using combined impedance and fluorescence data. **a)** Normalized impedance scatter plot (magnitude |Z| versus phase ΦZ), at 500 kHz, of a M2 sample 3 dpi, mixed with reference beads. **b)** Normalized fluorescence distribution of the BMMs population, used for identification of infected cells. Gaussian fits were used to identify each of the populations present. **c)** Normalized impedance scatter plot (magnitude vs phase), measured at 5 MHz for the same M2 sample 3 dpi, with reference beads, showing discrimination between *u*-BMMs and *i*-BMMs. The ellipse containing 50% of each population (O) together with the mean (●) are also indicated.

An overlap between the two populations was evident (as previously observed in FACS data - (**Figure 5.35f**). The threshold was thus defined as the intersection point between the two Gaussian distributions. This definition led to some mislabelling of events (*i*-BMMs labelled as *u*-BMMs and *vice-versa*); however, the majority of *i*-BMMs were identified for each sample. In this way, scatter plots of impedance data were generated for further analysis (**Figure 5.36c** shows data at 5 MHz, for example).

### 5.5.2 Time-Course Experiments

The different stages of invasion and activation states of BMMs were studied individually by performing measurements every day post-invasion (dpi). Macrophages can be activated by cytokines, dead cells or microbial products; and can adopt the "classical" M1 or "alternative" M2 activation states. M1 and M2 activation is fluid and cells can alter their state depending on the local inflammatory environment (Qualls *et al.*, 2012). Three TC sets of experiments were performed, one for each activation state – M0, M1 and M2. Measurements were performed from the first day post invasion to 4 dpi for the M0 and M1 samples and 6 dpi for the M2 sample. Ideally, both M0 and M1 TCs would have been measured for 6 dpi (or longer), but problems in the maintenance of the samples lead to their discard after day 4. Unfortunately, time constrains made it impossible to repeat these TC sets or perform triplicate measurements.

For each TC, the parasitaemia of infected samples was measured using standard Giemsa staining and microscopy (**Figure 5.37**). Due to the characteristics of each type of macrophage activation state, the parasitaemias for each sample varied

along the TC. For standard M0 samples, the development of the parasite within the host cell follows its natural course (see **Figure 5.3**). Post invasion and transformation to its amastigote form, the parasite multiplies and, upon release to the exterior, the new amastigotes infect other macrophages. When preparing the different samples for analysis, parasites in the promastigote form were left in the medium to infect existing macrophages. Some of the extracellular parasites, which have not infected a cell by the end of day "zero", are capable of persisting in culture, even after multiple washes. As a result, *u*-BMMs can be infected over subsequent days, which explains the observed increase in parasitaemia (**Figure 5.37a**). Furthermore, *u*-BMMs gradually dye in culture, as the lack of external stimuli causes the cells to undergo apoptosis *in vitro* (Moore and Matlashewski, 1994). This leads to the apparent increase in parasitaemia, as more *i*-BMMs remain in culture, as observed in the M0 samples measured, with parasitaemia varying from 35 ± 1.5% at 1 dpi to 67 ± 1.5% at 4 dpi (mean ± standard error for N = 1,000 counts). Fluorescence-based identification of *i*-BMMs was similar to measurement by microscopy: 33.7 ± 0.7% at 1 dpi to 62.6 ± 0.8% at 4 dpi.

For the cases of M1 samples, a decrease in parasitaemia was observed instead (**Figure 5.37b**)**.** This was as expected, as M1 is a pro-inflammatory activation state capable of eliminating intracellular pathogens (Qualls *et al.*, 2012; Kelly and O'Neill, 2015; Van den Bossche, O'Neill and Menon, 2017). This capability arises from some of the key differences between the two activation states. One of the main differences is the Warburg effect, which takes place in M1 BMMs, changing the cell energy metabolism, *i.e.*, the production of ATP from glucose (Otto Warburg, Wind and Negelein, 1927). While M2 (and M0) cells produce ATP by standard oxidative phosphorylation, M1 cells produce ATP through high rates of glycolysis. While a less energy efficient method, it allows M1 cells to quickly produce energy and generate high levels of NADPH as by-products. This metabolite is then used to produce reactive oxygen species that kill intracellular pathogens (Kelly and O'Neill, 2015). Another key pathway for macrophage activation is arginine metabolism (Qualls *et al.*, 2012; Kelly and O'Neill, 2015). In M1 cells, arginine is converted into nitric oxide by the enzyme nitric oxide synthase, which also contributes to the elimination of intracellular pathogens. As a result, *i*-BMMs are cleared out of any parasite by day 2 post-invasion, hence there are only two parasitaemia calculations for these samples: 59 ± 1.6% at 1 dpi and 35 ± 1.5% at 2 dpi through microscopy; and 47.2 ± 0.8% at 1 dpi and 21 ± 0.6% at 2 dpi through fluorescence.

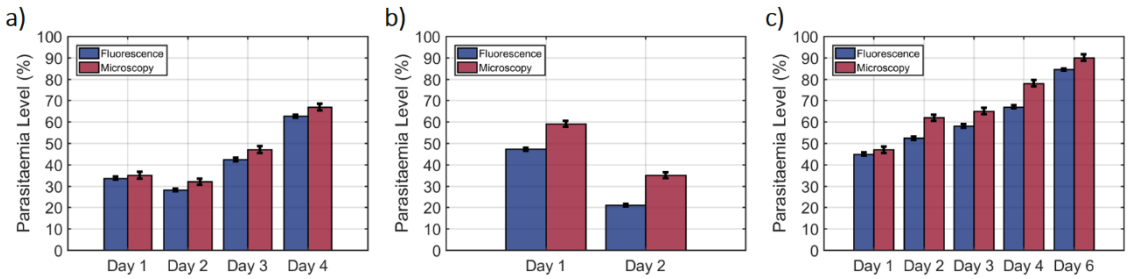


**Figure 5.37:** Bar charts summarizing the parasitaemia levels calculated using microscopy and fluorescence-coupled impedance cytometry-based methods for **a)** M0, **b)** M1 and **c)** M2 samples along the TC. Mean values from each population (N variable for fluorescence; N=1000 for microscopy) and standard error (*error bars*) are plotted for each time-point.

M2 macrophages, on the other hand, work as a counterbalance of the inflammatory response effects, and are involved in tissue repair at the site of inflammation (Qualls *et al.*, 2012; Kelly and O'Neill, 2015; Van den Bossche, O'Neill and Menon, 2017). They are not involved in parasite elimination, as another enzyme, arginase1 (converts arginine into ornithine), inhibits the activity of nitric oxide synthase (and thus nitric oxide production). As such, the parasitaemia of M2 samples varies in a similar fashion to that of M0 samples, *i.e.*, there was an apparent increase in parasitaemia due to the combined factors of late parasite invasion and *u*-BMMs population decay (**Figure 5.37c**). The calculated parasitaemias were: 47 ± 1.6% at 1 dpi and 90 ± 0.9% at 2 dpi through microscopy; and 44.9 ± 0.8% at 1 dpi and 84.4 ± 0.6 at 6 dpi through fluorescence.

### 5.5.3 Dielectric Analysis of Infected Bone-Marrow Macrophages

With *i*-BMMs identified, the impedance data of *u*-BMMs and *i*-BMMs populations was analysed and plotted for all time-points along each TC. **Figure 5.38** shows impedance scatter plots, at different probe frequencies, for the last time-points of each sample. The probe frequencies shown are 500 kHz, 5 MHz and 50 MHz. For each frequency, the population distributions of each cell type considerably overlap each other. Overall, the results of each individual TC seemed to indicate that there are no major differences in the dielectric properties between the infected and uninfected populations. To confirm this hypothesis, it would be necessary to estimate the dielectric properties of each sub-population. The approach previously implemented for the *P. falciparum i*-RBCs, which made use of multi-shell modelling, is unfortunately not a feasible approach in the case of *L. mexicana i*-BMMs. Unlike RBCs, BMMs are nucleated cells, meaning that these cells have two relaxations (cell and nuclear membranes), and have a complex interior.

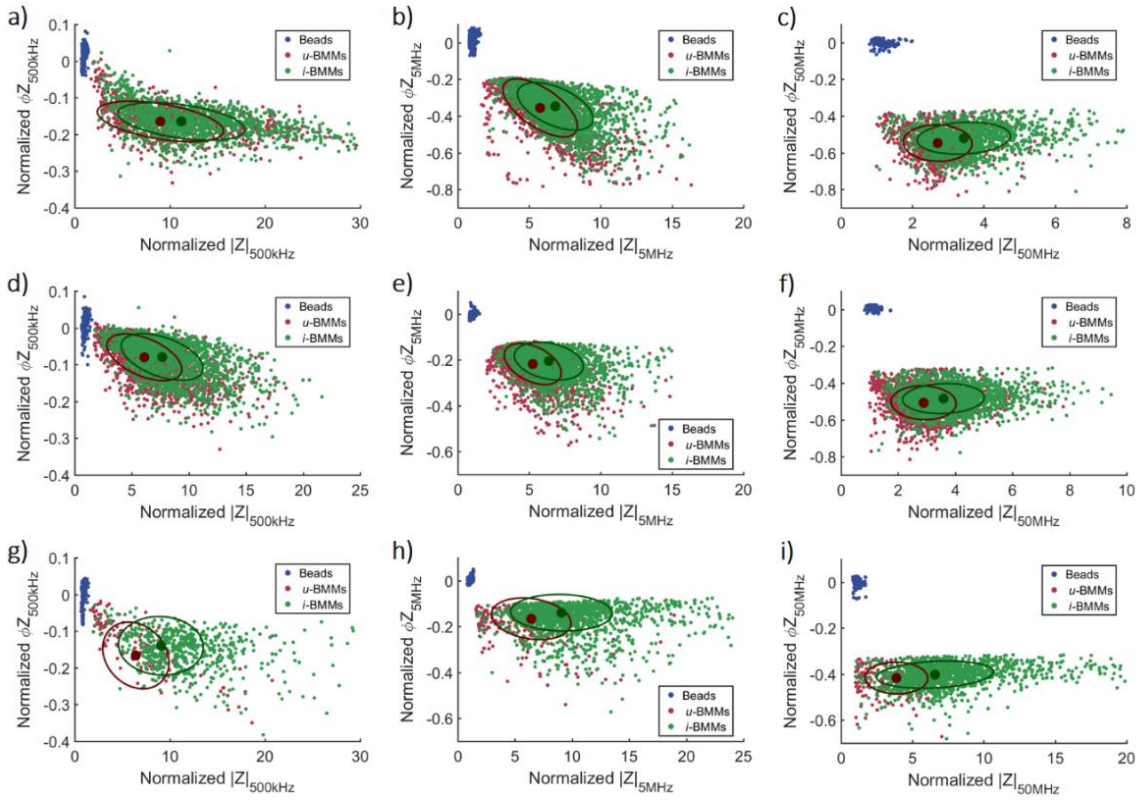


**Figure 5.38:** Normalized impedance scatter plots (magnitude - |Z| versus phase – ΦZ), at probe frequencies 500 kHz (**a**, **d** and **g**), 5 MHz (**b**, **e** and **h**) and 50MHz (**c**, **f** and **i**), of a M0 sample at 4 dpi (**a**, **b** and **c**), a M1 sample at 2dpi (**d**, **e** and **f**), and a M2 sample at 6 dpi (**g**, **h** and **i**), showing discrimination between *u*-BMMs and *i*-BMMs. The mean (●) and ellipse containing 50% of each population (O) are also indicated.

Considering the specific case of *i*-BMMs, a second membrane-enclosed body (parasite) is present within the cell. With both a nucleus and parasite within the cell, it is not possible to approximate their disposition to that of concentric shells. As a result, there is no feasible implementation of a multi-shell model capable of modelling *i*-BMMs.

Nonetheless, impedance data can still be used to evaluate and indirectly estimate some of the cell properties. Size can be easily estimated using impedance data at low frequencies. To calculate size, the cube root of the low frequency impedance, proportional to cell diameter, was normalized against the polystyrene references beads size. Another parameter that can be estimated is the “electrical opacity” of cells, which varies approximately inversely with the cell membrane capacitance. It is the ratio of high to low frequency impedance, in this case 5 MHz and 500 kHz, respectively.

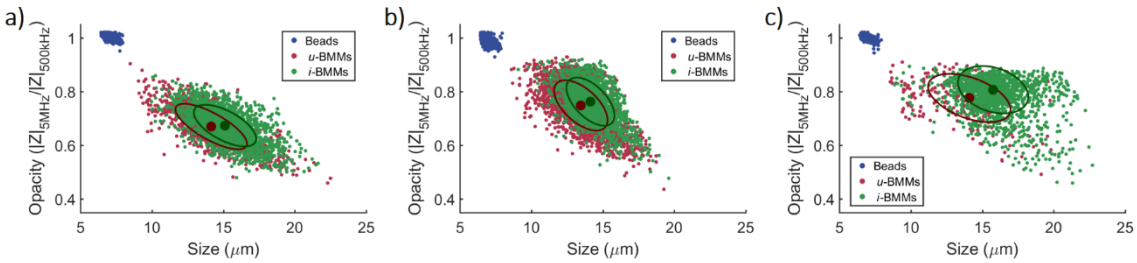


**Figure 5.39:** Scatter plots of opacity (magnitude at 5 MHz - $|Z|_{5MHz}$ over magnitude at 500 kHz - $|Z|_{500kHz}$) versus size (μm) for **a)** M0 sample at 4 dpi, **b)** M1 sample at 2 dpi, and **c)** M2 sample at 6 dpi, showing discrimination between *u*-BMMs and *i*-BMMs. The mean (●) and ellipse containing 50% of each population (O) are also indicated.

**Figure 5.39** shows a scatter plots of electrical opacity vs size for each activation state at the end of the respective TCs. From the three activation states, M2 *i*-BMMs seemed to have a larger size difference compared to *u*-BMMs; but there was virtually no difference in opacity between infected and uninfected BMMs for all cases, meaning that any membrane changes if any were not measurable.

The same analysis was used on all samples and for all time-points. Another set of measurements was performed with BMMs that had phagocytosed heat-killed parasites. These were termed *h*-BMMs and were measured at the three activation states to evaluate the influence that the digestion of external pathogens might have on the properties of macrophages. The presence of the parasite within the cell might permit a more clear understanding of what possible changes could be caused by parasite activity compared to phagocytosis. Unfortunately, lack of sample and time constrains prevented the repetition of the TCs or triplicate measurements, meaning that it was not possible to perform statistical analysis on the values. **Table 5.10** gives the estimation of size and the opacity, along the TC of infection, for the *c*-BMMs, *u*-BMMs, *h*-BMMs and *i*-BMMs populations.

**Figure 5.40** shows the variations in size and opacity along the TC for control BMMs (*c*-BMMs), *u*-BMMs, *h*-BMMs and *i*-BMMs for all activation states. In terms of size, *c*-BMMs (**Figure 5.40a**) seemed to keep a stable value for the M0 sample and the M1 sample, with a slight increase in the M2 sample. The M0 sample had the smallest mean size amongst all activation states. In contrast, in the case of *u*-BMMs (**Figure 5.40c**), there seemed to exist a slight expansion in size for M0. The other samples kept a similar and stable value along the TC. In terms of opacity, there was no change in *c*-BMMs (**Figure 5.40b**), for all activation states. For *u*-BMMs (**Figure 5.40d**), all activation states showed a very small decrease.

**Table 5.10:** Size and opacity along the TC of infection, estimated using impedance data, of *c*-BMMs, *u*-BMMs, *h*-BMMs and *i*-BMMs

| Activation State | Sample | Properties | Period of intraerythrocytic development of parasite | | | | |
|---|---|---|---|---|---|---|---|
| | | | 1 dpi | 2 dpi | 3 dpi | 4 dpi | 6 dpi |
| M0 | *c*-BMMs | Size | 12.5 ± 1.71 | 12.3 ± 1.61 | 13.0 ± 1.54 | 12.7 ± 1.56 | - |
| | | Opacity | 0.67 ± 0.07 | 0.69 ± 0.06) | 0.68 ± 0.07 | 0.70 ± 0.06 | - |
| | *u*-BMMs | Size | 12.8 ± 1.60 | 13.1 ± 1.62 | 13.1 ± 1.47 | 14.6 ± 2.26 | - |
| | | Opacity | 0.70 ± 0.08 | 0.65 ± 0.07) | 0.70 ± 0.06 | 0.65 ± 0.06 | - |
| | *h*-BMMs | Size | 13.3 ± 1.58 | 13.0 ± 1.56 | 13.1 ± 1.76 | 13.4 ± 1.59 | - |
| | | Opacity | 0.69 ± 0.06 | 0.66 ± 0.07) | 0.67 ± 0.07 | 0.68 ± 0.07 | - |
| | *i*-BMMs | Size | 13.6 ± 1.56 | 14.2 ± 1.68 | 14.2 ± 1.58 | 15.3 ± 2.13 | - |
| | | Opacity | 0.69 ± 0.09 | 0.65 ± 0.07) | 0.70 ± 0.07 | 0.66 ± 0.06 | - |
| M1 | *c*-BMMs | Size | 13.2 ± 1.74 | 13.3 ± 1.60 | 13.2 ± 1.64 | 13.9 ± 1.72 | - |
| | | Opacity | 0.70 ± 0.06 | 0.74 ± 0.06) | 0.73 ± 0.07 | 0.70 ± 0.08 | - |
| | *u*-BMMs | Size | 13.1 ± 1.73 | 13.4 ± 1.76 | 12.4 ± 1.53 | 13.4 ± 1.83 | - |
| | | Opacity | 0.77 ± 0.08 | 0.74 ± 0.08) | 0.78 ± 0.06 | 0.74 ± 0.08 | - |
| | *h*-BMMs | Size | 12.5 ± 2.04 | 13.2 ± 1.90 | 13.1 ± 1.79 | 13.3 ± 2.06 | - |
| | | Opacity | 0.79 ± 0.09 | 0.76 ± 0.07) | 0.76 ± 0.08 | 0.75 ± 0.09 | - |
| | *i*-BMMs | Size | 14.1 ± 1.69 | 14.3 ± 1.61 | - | - | - |
| | | Opacity | 0.77 ± 0.08 | 0.75 ± 0.08) | - | - | - |
| M2 | *c*-BMMs | Size | 13.0 ± 1.55 | 13.3 ± 1.60 | 13.5 ± 1.55 | 14.1 ± 1.73 | 14.7 ± 1.83 |
| | | Opacity | 0.72 ± 0.05 | 0.69 ± 0.06) | 0.71 ± 0.06 | 0.70 ± 0.07 | 0.72 ± 0.07 |
| | *u*-BMMs | Size | 13.1 ± 1.56 | 13.2 ± 1.29 | 13.6 ± 1.66 | 13.4 ± 1.58 | 13.8 ± 2.47 |
| | | Opacity | 0.69 ± 0.07 | 0.69 ± 0.06) | 0.70 ± 0.07 | 0.71 ± 0.09 | 0.76 ± 0.08 |
| | *h*-BMMs | Size | 14.6 ± 1.81 | 14.1 ± 1.65 | 14.1 ± 1.60 | 14.4 ± 1.65 | 14.4 ± 1.63 |
| | | Opacity | 0.69 ± 0.06 | 0.72 ± 0.06) | 0.73 ± 0.06 | 0.74 ± 0.08 | 0.72 ± 0.07 |
| | *i*-BMMs | Size | 13.7 ± 1.57 | 13.8 ± 1.41 | 14.2 ± 1.39 | 14.3 ± 1.54 | 16.1 ± 2.04 |
| | | Opacity | 0.69 ± 0.07 | 0.71 ± 0.06) | 0.72 ± 0.07 | 0.72 ± 0.08 | 0.78 ± 0.07 |

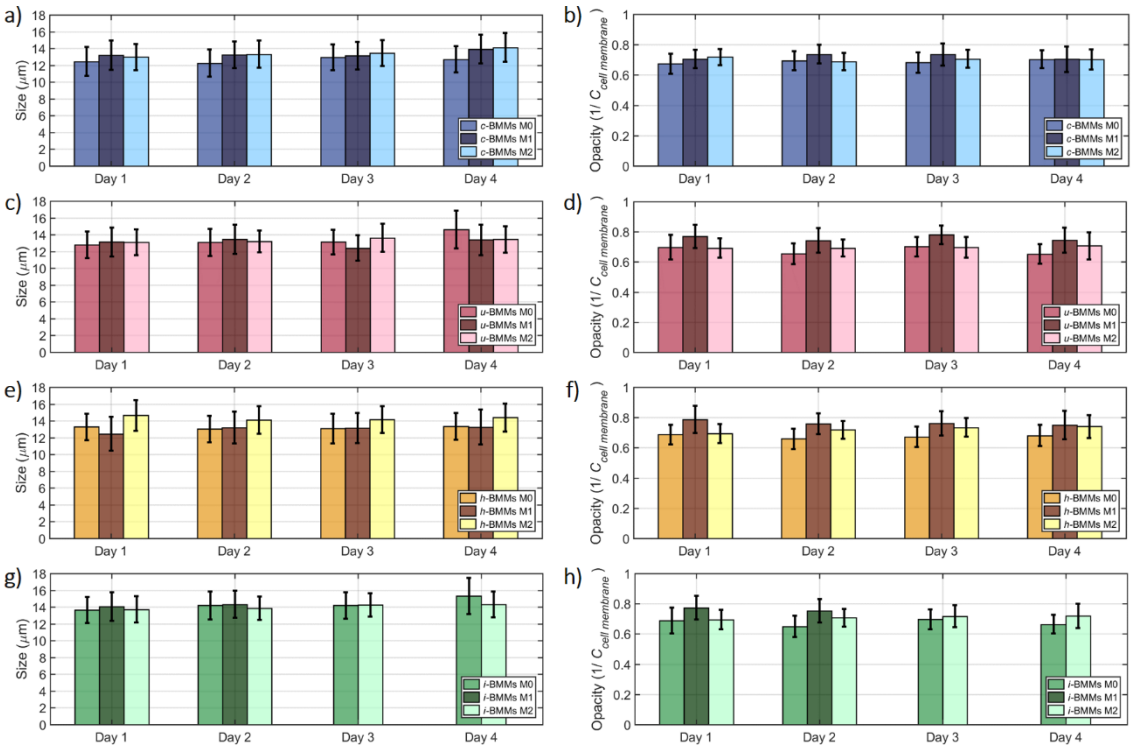


**Figure 5.40:** Bar charts summarizing cell size (**a**, **c**, **e** and **g**) and opacity (**b**, **d**, **f** and **d**) of *c*-BMMs (**a** and **b**), *u*-BMMs (**c** and **d**), *h*-BMMs (**e** and **f**) and *i*-BMMs (**g** and **h**) for M0, M1 and M2 samples along the TC. Mean values from each population (N=1200) and standard deviation (*error bars*) are plotted for each time-point.

In terms of size, *h*-BMMs (**Figure 5.40e**) are unchanged, although differ between activation state: the M2 sample had the largest mean size while the M1 sample the smallest size. However, these values were well within the population standard deviations, meaning that the size difference is probably not significant. Comparing results with *c*-BMMs and *u*-BMMs, where the smallest populations were the M0 and M1/M2 samples, respectively, there is no trend for a specific activation state to increase size, due to either culturing conditions or phagocytosis. Size alterations thus seem to arrive from sample-specific conditions. Regarding opacity variations for *h*-BMMs (**Figure 5.40f**), the M1 sample had a constant, higher mean value than the other two samples. Comparing with *c*-BMMs and *u*-BMMs, M1 samples have a higher mean opacity (lower membrane capacitance) than other activation states across the different cell populations.

For the *i*-BMMs (**Figure 5.40g**) the M1 sample had virtually no size changes during the shorter TC. Both the M0 and M2 samples had a clear size increase from the beginning to the end of the TCs. These alterations could be explained by the presence of the parasite within the cell. The constant growth and divisions of the parasite could cause the cell to stretch and expand, leading to the apparent size increase. In terms of opacity, both the M0 and M1 samples had a decrease in its

value, while the M2 sample increased. This difference seem to indicate that, for the case of the M2 sample, there must be an activation state dependent factor acting on the membrane and causing a decrease in the membrane capacitance.

**Figure 5.41** shows variations in size and opacity for different cell populations at the different activation states. Looking at size alterations for M0 macrophages (**Figure 5.41a**), both infected and uninfected BMMs have higher mean size than *c*-BMMs and *h*-BMMs at the end of the TC. This could indicate that some culturing-specific effect in the sample containing both *i*-BMMs and *u*-BMMs lead to the size increase. One consequence is that it is not apparent if the difference in size between *i*-BMMs and *c*-BMMs is a result of parasite growth within the host cell or another effect.

Regarding the M1 sample, after the second day post-invasion, the pro-inflammatory activity of the macrophages eliminated parasites from the cells. As previously noted, the *i*-BMMs in the M1 sample did not change size or opacity in the short period they were present in sample. For the remainder of the TC, the other measured BMM populations had no difference by the end of the TC, either in terms of size (**Figure 5.41c**) or opacity (**Figure 5.41d**).

As for the M2 state, the *i*-BMMs were characterized by an apparent size expansion along the TC (13.7 ± 1.57 µm at 1 dpi, to 16.1 ± 2.04 µm at 6 dpi). Contrary to what was observed in the M0 sample, *u*-BMMs in the sample did not present a size increase in the same level as *i*-BMMs. In this case, it appears that it was indeed the parasites that led to the expansion of the infected cell. The M2 state is known for its anti-inflammatory characteristics and inability to remove intracellular pathogens (Qualls *et al.*, 2012; Kelly and O'Neill, 2015). Furthermore, M2 *i*-BMMs opacity increased (and thus membrane capacitance decreased) along the TC. This seems to represent a membrane alteration induced specifically by the activation to the M2 state. As a comparison, *c*-BMMs and *h*-BMM did not alter expressively their opacity along the TC.

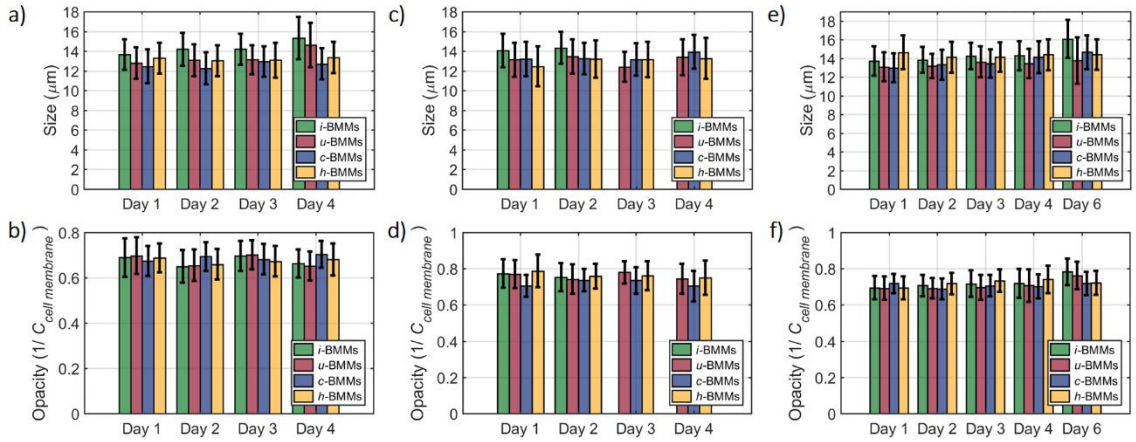


**Figure 5.41:** Bar charts summarizing cell size (**a**, **c** and **e**) and opacity (**b**, **d** and **f**) of M0 (**a** and **b**), M1 (**c** and **d**) and M2 (**e** and **f**) samples along the TC. Mean values from each population (N=1200 for *c*-BMMs, *u*-BMMs and *h*-BMMs; N=750 for *i*-BMMs) and standard deviation (*error bars*) are plotted for each time-point.

Dielectric analysis of *L. mexicana i*-BMMs, at different activation states, showed no major alterations in the size or membrane properties of *i*-BMMs in the M0 and M1 activation states, with only M2 *i*-BMMs presenting alterations. The question of whether such changes could be used for label-free analysis and sorting is, however, still open for debate. AC electrokinetics techniques require the two populations of particles to have different dielectric properties and/or size. Other techniques, such as DLD or inertial microfluidics are also size dependent. If no significant difference exists between the infected and uninfected population, as seems to be the case for M0 and M1 and, to some degree, for M2 samples, enrichment of single *i*-BMMs would not be possible. Unfortunately, the samples were insufficient to enable statistical analysis of the data.

## 5.6 Summary

In this chapter, two of the most life-threatening human parasitic diseases were studied using microfluidic impedance cytometry. Discrimination of parasite-infected RBC could not be achieved by impedance alone. The dielectric properties were determined by MMT and multi-shell modelling. A spherical model was first tested on normal and sphered RBCs, which revealed the need to develop a model that can be used for non-spherical cells (RBCs). An ellipsoid model was developed and used on control samples and uninfected cells. Estimated properties were in agreement with accepted values for RBCs.

In the case of *i*-RBCs, the size and shape variations of host cell and parasite throughout the parasite intraerythrocytic life cycle required two different models:

an oblate spheroid model for early-stage *i*-RBCs and a spherical model for late-stage *i*-RBCs. The dielectric properties showed significant alterations to *i*-RBCs membrane capacitance, increasing gradually throughout the TC ($p$<0.01 between 6 hpi and 36 hpi), reaching 14.1 ± 1.42 mF/m$^2$ at 30 hpi. These changes appear as early as 12 hpi and are significantly higher than uninfected RBCs ($p$<0.01). A consequence of these membrane alterations is an increase in ion exchange activity between the intra- and extra-cellular regions of host cells. Cytoplasm conductivity increased from 0.74 ± 0.04 S/m at 30 hpi, to values close to that of the medium by 42 hpi - 1.24 ± 0.04 S/m. This was much higher than uninfected RBCs ($p$<0.0001 at 42 hpi), which maintain a constant, much lower value (*c*-RBCs: $\sigma_{cytoplasm}$ = 0.41 ± 0.02 S/m; *u*-RBCs: $\sigma_{cytoplasm}$ = 0.43 ± 0.01 S/m; N = 7 time-points), in agreement with literature. As for uninfected cells, the parasite maintains a stable, lower cytoplasm conductivity along the late stages of TCs - 0.48 ± 0.02 S/m Moreover, no significant volumetric changes were observed between uninfected and infected cells. In contrast, the parasite grows along the infection cycle, occupying less than 10% for early stages (≤ 18 hpi), but reaching around 90% for later stages (36 and 42 hpi).

The full dielectric characterization of *i*-RBCs provided a detailed picture of changes occurring at the host cell and parasite level. It was possible to observe significant alterations between the various stages of the parasite intraerythrocytic life cycle. These alterations could possibly be used for label-free analysis and sorting methods. Although cells cannot be uniquely identified during the ring-stage of the infection cycle, *i*-RBCs could be enriched at other points. While this limits the applicability of a DEP-based diagnosis technique for *P. falciparum* *i*-RBCs, the technique could still be promising for other *Plasmodium* species where diagnosis during the 24 hour ring stage is less critical. By adding a pre-enrichment step, the sensitivity of current "*gold-standard*" diagnostic methods could also be improved.

Dielectric analysis of *L. mexicana*-infected macrophages at different activation states showed little changes in biophysical characteristics. Samples containing *i*-BMMs at different activation states were measured along the parasite intra-cellular life cycle every day post-invasion. Samples were measured using a wide spectrum of frequencies to give qualitative dielectric analysis of properties. Overall, the results show no major differences in size or membrane properties of *i*-BMMs in the M0 and M1 activation states, with M2 *i*-BMMs showing a small degree of alteration. The results were not statically assessed, and require further validation before a conclusion of whether such changes could be used for label-free analysis and sorting.

# Chapter 6

# Integrated Single Cell Sorting and Identification

## 6.1 Overview

All the microfluidic techniques for sorting and/or identification described in earlier chapters rely on a unique particle property. Many technologies rely on a single parameter, for example, DLD or inertial microfluidic mostly depend on size (and to a degree, deformability), while DEP and MIC mostly rely on particle dielectric properties.

There are currently few techniques which perform sorting and analysis utilising multiple different properties of particles. Therefore, integration of different microfluidic techniques into a single system could maximise discrimination and separation by utilising multiple biophysical markers. There are very few examples of this in literature; for a recent review see (Yan *et al.*, 2017). One of the most relevant systems for cell separation and analysis was from the group of who developed an integrated system comprised of DLD, inertial focusing and magnetophoresis to enrich cancer cells from large volumes of whole blood (Karabacak *et al.*, 2014; Fachin *et al.*, 2017).

This chapter describes the development of a novel integrated system capable of high-resolution size and shape-based cell sorting using DLD array, together with single cell counting and analysis of the sorted cells. The inclusion of electrodes in the DLD array to enhance separation utilising a DEP force was also investigated. This integrated system was used to perform separation of parasites from the genus Trypanosoma from blood cells, with the enriched parasites identified and counted.

## 6.2 DLD Principles

### 6.2.1 Separation process

The separation mechanism of DLD exploits the interaction of particles as they flow under laminar conditions through an array of micrometre-sized posts fabricated within the fluidic channel, as previously presented in **Section 2.3.2** (**Figure 6.1**). The posts have a specific diameter ($D_p$) and gap distance ($G$); the sum of these two parameters is the distance between post-centres ($\lambda$). Each consecutive row is shifted by a set distance ($\Delta\lambda$) and after a specific number of rows, or period ($N = \lambda/\Delta\lambda$), the posts should return to their initial horizontal position. At typical flowrates, the flow is laminar and at each post the main flow stream is divided in $N$ parallel streamlines or laminae, transporting equal volumetric flow rate. Streamlines next to the posts are wider to accommodate more fluid and satisfy the no-slip boundary condition, while the central streamline has the narrower width and fluid travels at the highest velocity (Davis, 2008).

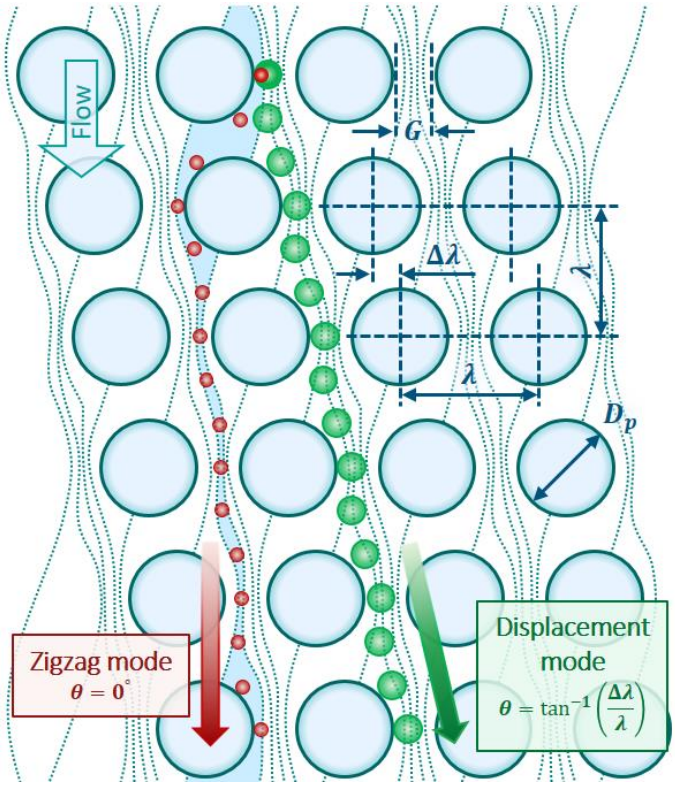


**Figure 6.1:** Schematic illustration of size-based sorting in DLD devices. Particles smaller than the critical size enter "*Zigzag mode*" and follow the direction of the flow; while particles larger than the critical size enter "*Displacement mode*" and follow the rows of posts by a displacement angle. Relevant array geometry parameters are also highlighted.

Consider two differently sized spherical particles following the same streamline when they meet a post (**Figure 6.1**). The interaction of the particles will depend on the size of the particle and the critical diameter ($D_c$) of the post array. Davis, in 2008, empirically deduced a formula to approximate the value of $D_c$ using the geometrical values of the posts and array. By experimenting with over 20 devices of various gaps sizes and testing them with spherical particles of varying size, it was possible to derive the formula as

$$D_c = 1.4 \times G \times N^{-0.48} \qquad (6.1)$$

At each particle-post interaction, two possible outcomes exist. If the hydrodynamic centre of the particle is closer to the post than the critical diameter ( $D_c$), the particle will be mostly affected by the first streamline, remaining in it, and following a "*zigzag*" movement throughout the array. Conversely, larger particles, where the hydrodynamic centre is actually outside $D_c$ range, will be affected by the second streamline, being laterally displaced as they "bump" into the post, moving the particle across and into new streamlines. Both these effects are repeated at each single particle-post interaction. For the first case, called "*Zigzag mode*", particles ultimately follow a straight line along the array, ending in the same streamline. In the second case, named "*Displacement mode*", particles are displaced through an angle ($\theta$), which arises from the lateral row-shifting and is given by

$$\theta = \tan^{-1}\frac{1}{N} = \tan^{-1}\frac{\Delta\lambda}{\lambda} \qquad (6.2)$$

Given adequate time, space and an appropriately designed geometry, particles smaller or larger then $D_c$ will be focused to different outlets, resulting in the complete separation between particles at the end of the array (Huang *et al.*, 2004; Davis *et al.*, 2006).

### 6.2.2 Sidewall Interference

When designing a DLD device, the flow profile close to the edge of the channel must be considered. The sidewall effect in DLD devices is where the flow profile becomes perturbed between the sidewall and the last column of posts. This induces changes in the actual $D_c$ of the array in comparison to the predicted value and was demonstrated by Inglis (2009). To avoid sidewall interference, walls should be designed as if they incorporated a final column of posts, *i.e.*, the sidewall is irregularly shaped rather than a straight wall. By setting the wall at a variable gap from the adjacent post column, the flow streams are not disturbed. Considering a

device sorting from left to right, these gaps can be calculated, depending on their position, left ($G_L$) or right ($G_R$) on the device and the row number ($n$) within a section:

$$G_L = G\sqrt{\frac{n}{N}} \tag{6.3}$$

$$G_R = G\sqrt{2 - \frac{n}{N}} \tag{6.4}$$

### 6.2.3 Post Shape

DLD arrays were first fabricated using circular shaped posts, and have been highly studied, simulated and the flow profiles understood. Subsequently, researchers have attempted to improve performance by changing the post shape. Using a non-circular posts the zero-velocity zones, which occur on top of circular posts, can be minimised or erased, leading to less entrapment of particles in these zones.

One example of a non-circular design was proposed by Loutherback *et al.* (2010), who used triangular posts (**Figure 6.2a**). This design was able to reduce the effects of clogging and the overall hydrodynamic resistance, so lower operating pressures could be used for the same flow rate to be attained. In addition, triangular posts modify the flow profile symmetry, leading to different $D_c$ values in the same array if the flow is reversed. Due to the symmetric nature of circular posts, the stream width near the top or bottom is identical ($W_{circ,top} = W_{circ,bottom}$) (**Figure 6.2a-i**). For tilted triangular posts, at the triangle vertex the flow velocity increases, making the stream narrower at that region ($W_{tri,top} > W_{tri,bottom}$) (**Figure 6.2a-ii**). Consequently, the $D_c$ can be smaller for particles going from left to right compared to the opposite direction. In the case of particles falling between those two $D_c$, it can present a behaviour similar to a "small" particle (going left to right) or "large" particle (reversing right to left) (Loutherback *et al.*, 2009). This effect permits a higher control of the separation process and versatility in its application. For example, a two-tiered separation process could be implemented for a sample containing three differently sized particles: the largest particles ($\gg D_c$) could be first sorted left to right, with the two smaller particles populations being fractioned right to left if one population falls between the two $D_c$.

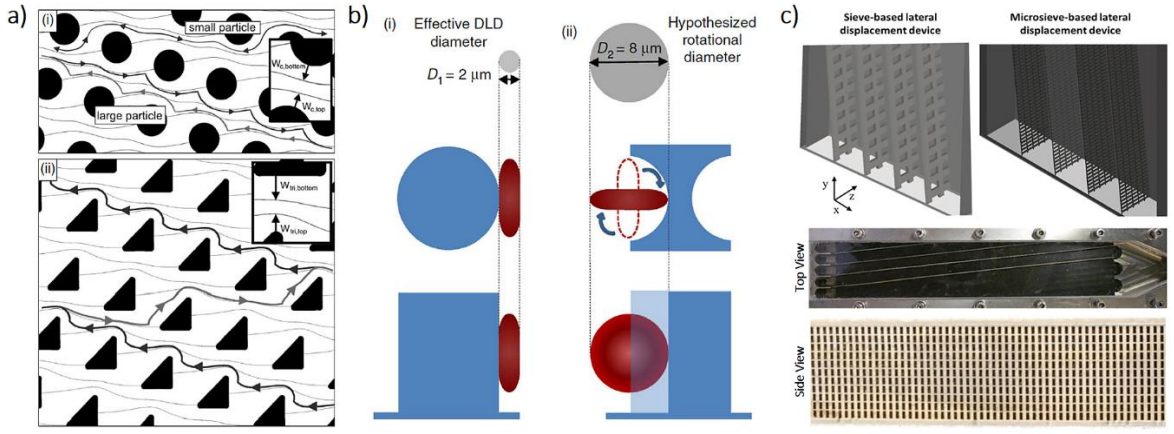


**Figure 6.2: a)** Flow profile alterations due to triangular posts , for *(i)* circular and *(ii)* triangular posts are presented. *(i)* Paths for a small and large particle, moving in both directions, not presenting any alteration. *(ii)* Paths for a particle of medium size, acting as a large particle moving from left to right, while, when the flow reverses, it behaves as a small particle. **b)** Difference between the standard, circular-shaped posts *(i)* and new, I-shaped posts *(ii)*, with both top and cross-section views. The conceptual separation process is based on the induced rotation of non-spherical particles with I-shaped posts, increasing their apparent size. **c)** Representation of the sieve-based and microsieve-based lateral displacement devices for particle separation. Photographs of the top and side view of the device. **a)** Adapted from *Loutherback et al.* (2009); **b)** adapted from Zeming *et al.* (2013); **c)** adapted from Dijkshoorn *et al.* (2017)

Zeming *et al.* (2013) investigated "I-shaped" posts to separate non-spherical and also deformable particles (**Figure 6.2b**). On contact with the posts, non-spherical particles, such as a discoid RBC (**Figure 6.2b-i**) orientate to present the narrower dimension as the effective diameter. By designing the posts as an "I", non-spherical particles are induced to rotate, increasing their apparent hydrodynamic radius to that of their larger dimension (**Figure 6.2b-ii**). Thus, as these particles pass through the constriction zone, they present a $D_c$ greater than they would typically have improving separation. Other examples of studies on different post shapes that have been investigated focused on asymmetrical posts (Au *et al.*, 2017; Hyun *et al.*, 2017), triangular posts (Loutherback *et al.*, 2010; Jiang *et al.*, 2017), parallelogram posts (Lubbersen, Boom and Schutyser, 2014), and "I", "L", "T" and anvil posts (Ranjan *et al.*, 2014). Recently, Dijkshoorn *et al.* (2017) proposed substituting the post array with a sieve mesh consisting of arrays of rectangular openings on vertical frames, effectively working as DLD obstacles (**Figure 6.2c**) (Dijkshoorn *et al.*, 2017). This design has the potential to permit easier fabrication and industrial scale-up of the DLD technology, leading to it applicability to industrially relevant suspensions.

## 6.3 Literature Review

DLD was introduced in 2004 by Huang *et. al.* as a size-based, sorting tool (Huang *et al.*, 2004), although recent studies have shown that other biophysical parameters can be used for example cell deformability (Quek, Le and Chiam, 2011; Beech *et al.*, 2012; Holmes *et al.*, 2014) and shape (Loutherback *et al.*, 2010; Zeming, Ranjan and Zhang, 2013; Beech *et al.*, 2018). An extensive overview of the technique can be found in a recent review (McGrath, Jimenez and Bridle, 2014). DLD has been shown capable of sorting and size-fractioning a varied range of samples including: RBCs, WBCs and platelets from whole blood (Davis *et al.*, 2006); sub-types of WBCs (Inglis *et al.*, 2008); cancer cells (Loutherback *et al.*, 2012; Karabacak *et al.*, 2014); droplets in a two-phase flow (Joensson, Uhlén and Svahn, 2011; Tottori and Nisisako, 2018); nano-sized bioparticles (Zeming *et al.*, 2018); bacteria (Ranjan *et al.*, 2014; Beech *et al.*, 2018); and parasites (Holm *et al.*, 2011, 2016).

Beech *et al.* (2009) proposed the integration of DEP into a DLD device. While DLD is characterized by high precision size-based separation, it lacks the versatility of DEP "tunability" where a different frequency and amplitude of the applied electric field can sort, particles of different volume, shape and electrical properties. The interaction between particle and post can be changed using additional forces (*e.g.* DEP) to create particle displacement. By applying a controlled DEP force across the device, particles can be induced to displace, even if they are considerably smaller than the critical size established by the DLD geometry (**Figure 6.3a**). The authors were able to tune the critical size of separation of polystyrene beads (3 and 5 μm), reducing it from 6 to 3 μm by applying an 100 Hz AC electric field and changing the field strength from 80 to 265 V/cm (**Figure 6.3b** and **c**). The authors also performed further modelling and simulations of particles, proposing a simplified theoretical model of the behaviour of particles. In some of those simulations, for instance, it was possible to visualize the behaviour of the electric field in the posts region (**Figure 6.3d**). The authors hypothesised that the formation of non-uniform regions in the electric field lines between posts that gives rise to the DEP forces influencing the separation process. This work demonstrated that integrating DLD with AC Electrokinetics could be exploited and further explored using other configurations.

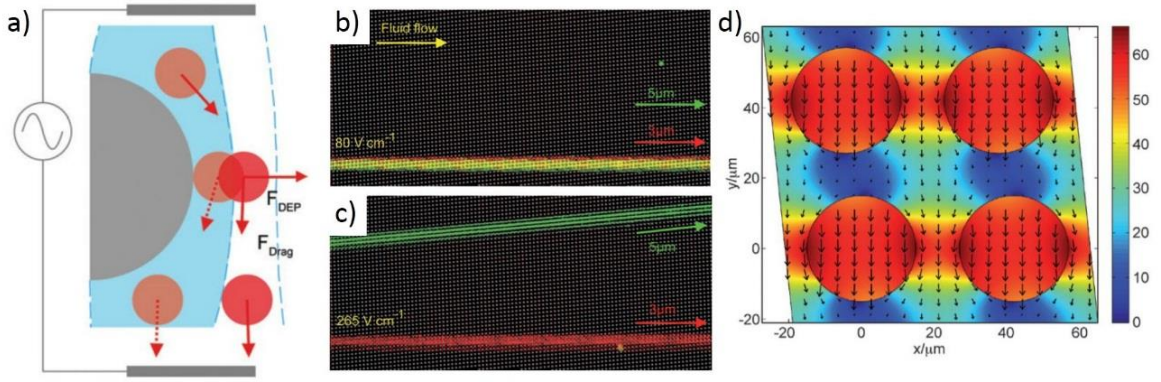


**Figure 6.3: a)** The application of a DEP force pushes the particle out from the post into the neighbouring stream, displacing it despite the fact that its size is below the critical size determined by the device geometry. **b)** Micrograph averaged over 500 frames of the 3 μm (red) and 5 μm (green) beads moving across the device, left to right. The device possesses a $D_c$= 6 μm and an AC field of 80 V/cm at 100 Hz has no effect on the particles trajectories. **c)** After the application of an increased magnitude electric field (265 V/cm), the apparent $D_c$ now decreases so that 5 μm are displaced while 3 μm beads still zigzag along the device. **d)** Results of a simulation on the electric field behaviour in the posts region. The color bar gives the absolute value of the electric field (with a maximum value of 65 V/cm) and the black arrows indicate the direction and magnitude of the electric field. Adapted from Beech *et al.* (2009).

Another approach was recently proposed by Tran *et al.* (2017), where the lid of the DLD devices was removed and capillary flow was used to generate fluid flow and perform separation (Tran *et al.*, 2017). One of the common issues of microfluidic devices using sealed channels is the tendency to clog, especially when dealing with complex (biological) samples. The difficulties of cleaning enclosed devices limits their use for long and repeated use. Thus, the authors proposed an "open" DLD devices concept (**Figure 6.4**), *i.e.*, without a bonded top layer, which are easier to clean and reuse. In addition, paper capillary pumps were used to flow the samples along the device. This configuration was used to separate various particles. As a proof of concept, 3 and 7 μm polystyrene beads were sorted along the device and collected on the paper in outlets pre-defined by wax lines which effectively work as channel walls (**Figure 6.4a**). The device was then used to separate cancer cells (MCF7 cells; diameter 17.3 ± 2.1 μm) and RBCs (diameter 7.8 ± 0.6 μm); WBCs (diameter 12.2 ± 0.9 μm) and RBCs; and even blood-dwelling parasites (*Trypanosoma cyclops*) from RBCs (**Figure 6.4b** and **c**). In the latter case, the orientation of cells was controlled by varying the height of the device, such that in taller devices (24 μm deep; **Figure 6.4b**) both parasites and RBCs follow the flow; while in shallower devices (9 μm deep; **Figure 6.4c**) parasites are displaced (as previously explored in Holm *et al.* (2011, 2016). A DEP-integrated approach was

also tested, where the electrodes were directly dipped within the device (unlike the usual inlet and outlet reservoir mounting) (**Figure 6.4d**). This reduced the distance between electrodes and permitted the generation of higher electric fields. By applying a 400 V AC signal (100 Hz), 4.8 µm carboxy-terminated polystyrene beads were sorted from 3.1 µm sulphate-terminated polystyrene even though the device $D_c$ = 5.1 µm (**Figure 6.4e**). However, the limitations of an open DLD system are evaporation of the sample, contamination and biohazard risk, which could limit its applicability in the field.

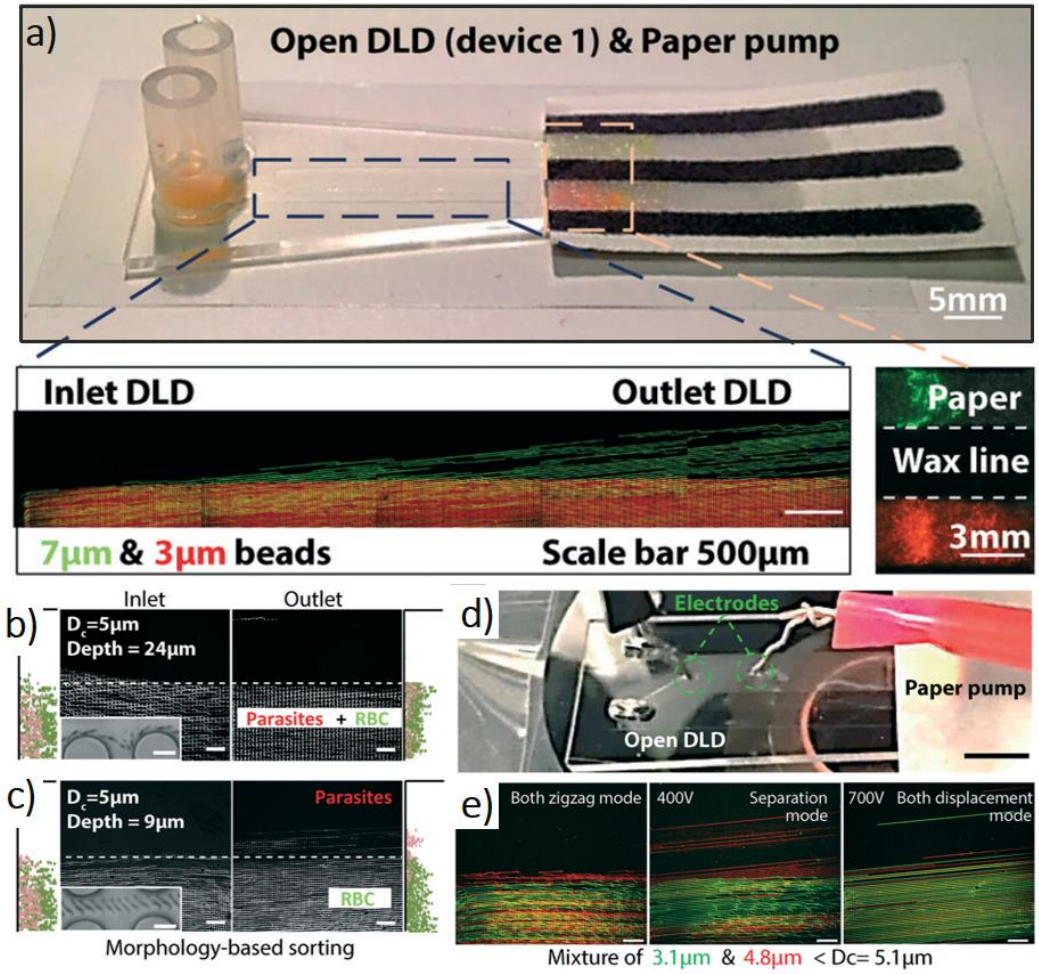


**Figure 6.4:** An overview of the open DLD device layout and applications. **a)** Paper was used both as a capillary pump and for sample collection. Wax lines defined the collection zones where coloured beads were visualized after separation. Time averaged images of fluorescent beads (green 7 µm and red 3 µm) at the beginning and end of the device, showing the trajectory of beads along the device. Parasite sorting in open DLD devices: **b)** in a 24 µm deep devices, cells have the same trajectory, while **c)** in a 9 µm deep devices they are separated. Time averaged micrographs of parasites and RBCs moving through the device, with inlet (*left*) and outlet (*right*) distributions. Integration of AC electrokinetics and open DLD: **d)** the electrodes were positioned directly at any point in the device, permitting the generation of an AC field (100 Hz) at various voltages. **e)** By altering the voltage, beads are induced to displace, even if the bead size is smaller than the pre-defined $D_c$. Adapted from Tran *et al.* (2017).

Other technologies have been integrated with DLD to enhance the system sorting capabilities. Jiang *et al.* (2017) recently proposed an integrated system where an automatic magnetic purifying stage is added after a DLD isolation stage, for the aim of circulating tumour cells (CTCs) enrichment (**Figure 6.5a**). The DLD device was designed as a mirrored array (to double throughput), and triangular posts (**Figure 6.5b**). This had a high throughput (around 1mL/min) of undiluted blood. Afterwards, the isolated sample was directed to the purifying chip, where a permanent magnet was moved in rectangular motions, permitting negative isolation of CTCs (WBCs were tagged by an immunomagnetic marker). The integrated system had a capture rate of around 90% (with >90% viability of isolated cells). However, the capture purity was only ~50%, which means longer processing times to detect significant numbers of CTCs. When dealing with clinical blood samples from patients with advanced metastatic cancers, the system had a capture rate of 83.3%. Nonetheless, the system has some difficulties: first, captured CTCs must be fixed and permeabilized, which limits *in vitro* culture of these cells; second, while less than 1% of WBCs remain post isolation, the high number of WBCs compared with CTCs reduces the capture purity and system efficiency.

More complete integrated systems were developed by Toner *et al.* (Karabacak *et al.*, 2014; Fachin *et al.*, 2017). The most recent system is a high-throughput monolithic device combining DLD, inertial focusing and magnetophoresis depleted blood cells at 15-20 million cells/s (**Figure 6.6a**) (Fachin *et al.*, 2017). The different sorting stages were integrated on a single mass-produced plastic chip, decreasing handling complexity and technical requirements (**Figure 6.6b**). The different sorting stages of the device are presented in **Figure 6.6c**. Blood was pre-labelled with fluorescent tags and magnetic beads against WBCs entered the device and first passed through a DLD stage, where the smaller RBCs, platelets and unbound magnetic beads were removed from the sample. The sorted cells were then accelerated through an inertial focusing stage, which focused the cells to tight streams. The aligned cells were directed to a first MACS stage, through a magnetic field where the magnetic gradient forces the tagged WBCs to focus at the centre of the device. The remaining cells were refocused in a second inertial focusing stage before entering a second MACS stage which removed the remaining labelled cells using a higher magnetic gradient. CTCs are collected in solution with no additional tags, spending less than 8 seconds within the chip. The analysis of over 2,500 CTCs from 38 patient samples showed significant heterogeneity in size and epitope between and within single patients, highlighting the need for further studies and optimization of the integrated system.

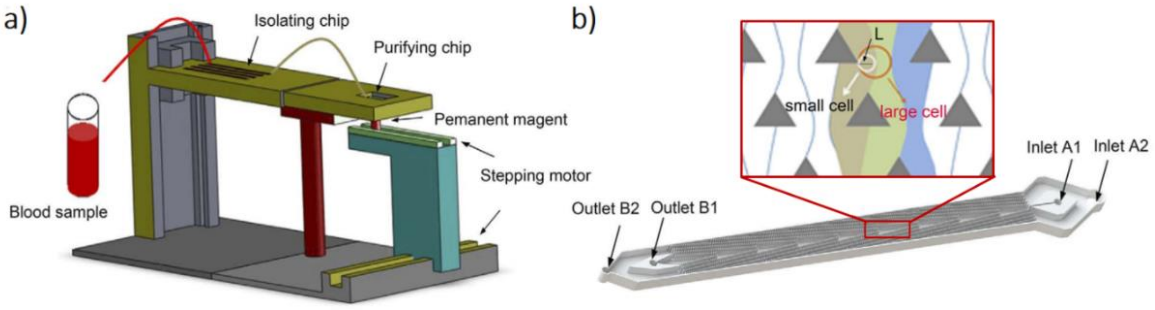


**Figure 6.5: a)** Schematic illustration of the integrated microfluidic device, including the isolation chip and the purifying device (purifying chip, permanent magnet and stepping motor). **b)** Schematic illustration of the DLD device used, consisting of a mirrored triangular post array. The larger cancer cells and some WBCs were concentrated at the centre of the device, while smaller cells (RBCs and most WBCs) will follow the flow direction. Adapted from Jiang *et al.* (2017).

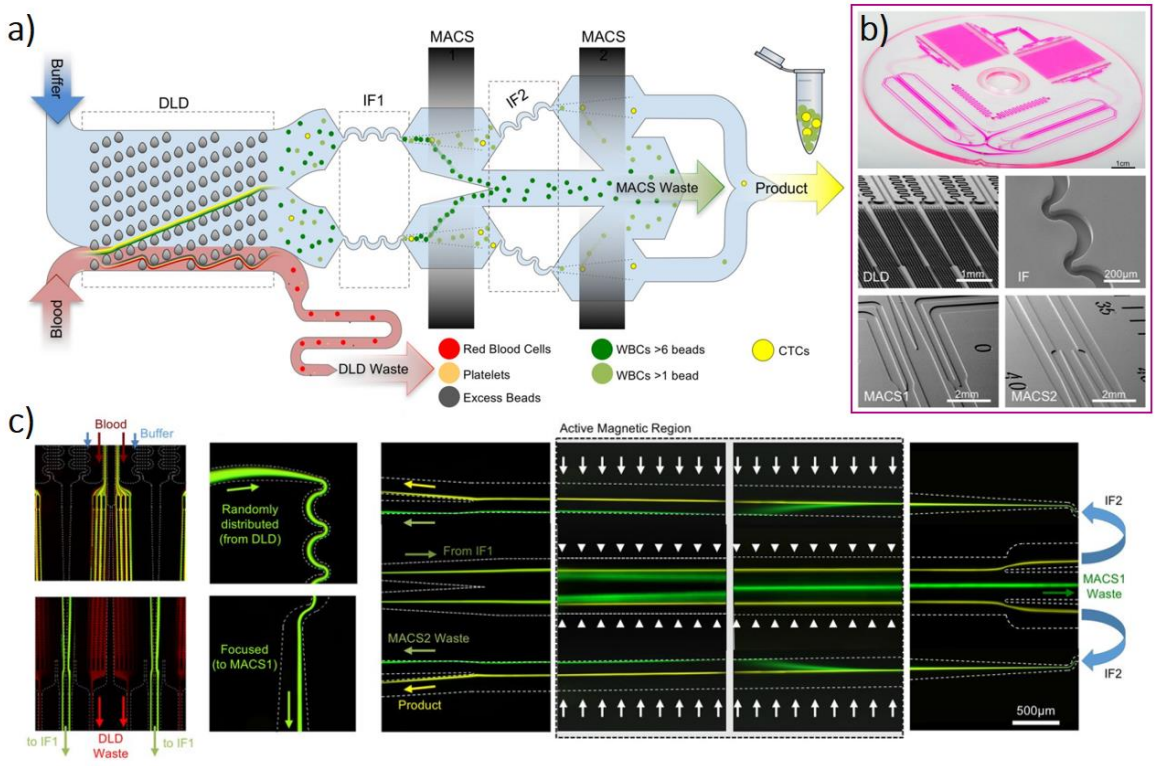


**Figure 6.6: a)** Schematic of the integrated device with the different sorting stages represented. **b)** Photographs of the device (*top*) and SEM micrographs of the different sorting stages: DLD structures (*middle left*); inertial focusing channel (*middle right*); and MACS channels (*bottom*). **c)** Time averaged micrographs of the different sorting stages. First, a blood sample entered the DLD stage, where larger WBCs and CTCs (*green*) were sorted from and RBCs (*red*). Sorted cells were inertially focused to tight streams. These streams finally flowed through sections of low and high gradient MACS, where purified streams of CTCs (*yellow*) were split from the waste WBCs streams (*green*) at the outlet. Adapted from Fachin *et al.* (2017).

## 6.4 AC Electrokinetics-integrated DLD

### 6.4.1 Device Design and Setup

Utilising the high-resolution size and shape-based cell sorting capabilities of DLD, a new integrated system was developed with the inclusion of AC electrokinetic capabilities. The target was to sort cells not only on size but also their dielectric properties, with integrated counting and analysis of the positive cell fraction. Even in non-optimal DLD separation processes it would be possible to quantify the separation efficiency with integrated analysis. The mask design of the integrated system is presented in **Figure 6.7**. This integrated system comprises two components: the chip containing the AC electrokinetics electrodes (red section of **Figure 6.7**) and the DLD device (green section of **Figure 6.7**). To maximize fabrication and system efficiency, two independent devices and sets of electrodes were designed for each single chip. The chip included electrodes capable of performing two different techniques: DEP and MIC. DEP electrodes, 750 µm wide, are located along the device, parallel to the DLD component and permit the generation of an AC field perpendicularly to the flow direction. The DLD device required some adaptations to the traditional system. MIC chips are constructed with two parallel facing electrodes; however, DLD devices are usually fabricated with PDMS bonded to a substrate. Thus, a co-planar conformation was used for MIC, upon which the DLD PDMS device could be attached. Three MIC electrodes (30 µm width and separated by 10 µm) were located just before the measurement outlet, with the AC signal applied to the centre electrode. The electrodes were designed to have a large placement tolerance, minimizing issues with alignment.

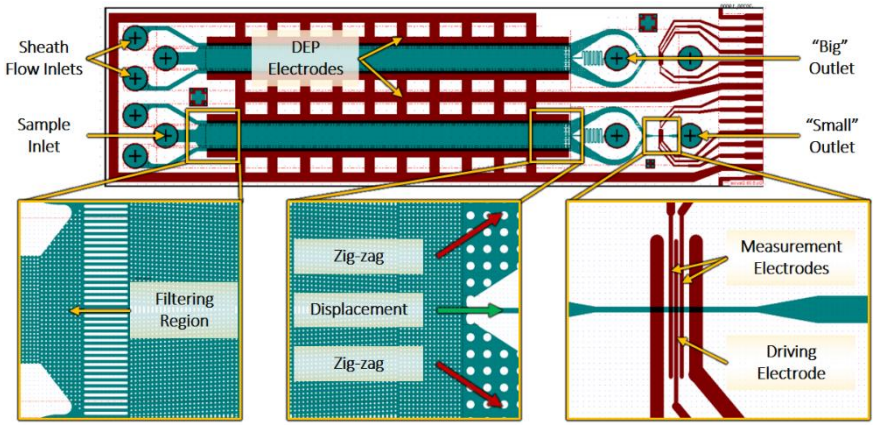


**Figure 6.7:** Mask design of the AC electrokinetics-integrated DLD device. The features in red define the chip containing the AC electrokinetics electrodes. The features in green define the DLD device. Insets present important areas of the device: initial filtering region; final section of sorting in the DLD device; and the MIC region at the measurement outlet.

The device had three independent inlets: one central inlet for sample insertion and two side inlets for sheath flow. The sheath flow lanes overlap the DEP electrodes, which must be in contact with the flow, effectively blocking any particles from interacting directly with the electrodes. A filter region was added after the sample inlet. The DLD post array was designed to displace bigger, non-target particles towards the centre of the device and then to the waste outlet – named "Big" Outlet. Smaller, non-displaced particles emerge at the two side channels, before the channels combining in a single "Small" Outlet and entering the MIC region.

A mirrored design was used, minimizing the migration distance of cells, resulting in a higher throughput (Lubbersen, Boom and Schutyser, 2014). Three different critical diameters were designed: $D_c$ = 6 μm (with $G$ =20 μm, $D_p$ = 20 μm and $N$ = 24); $D_c$ = 5 μm (with $G$ =17.5 μm, $D_p$ = 17.5 μm and $N$ = 27); and $D_c$ = 4 μm (with $G$ =15 μm, $D_p$ = 15 μm and $N$ = 31). This range of $D_c$ covers the dimensions required to separate different blood cells or enrich for bacteria in complex samples, for example. The devices had a uniform length of approximately 31.62 mm, with a total $N$ = 33. Sidewall interference was also taken in consideration, with proper gap adjustments being made for each case (Inglis, 2009). The system was designed to facilitate re-use, thus, the two components were clamped together (**Figure 6.8**) using 3D printed custom pieces. After each experiment the holder was opened and the device removed and cleaned. This reduced the complexity of the system and the turnaround time between experiments.

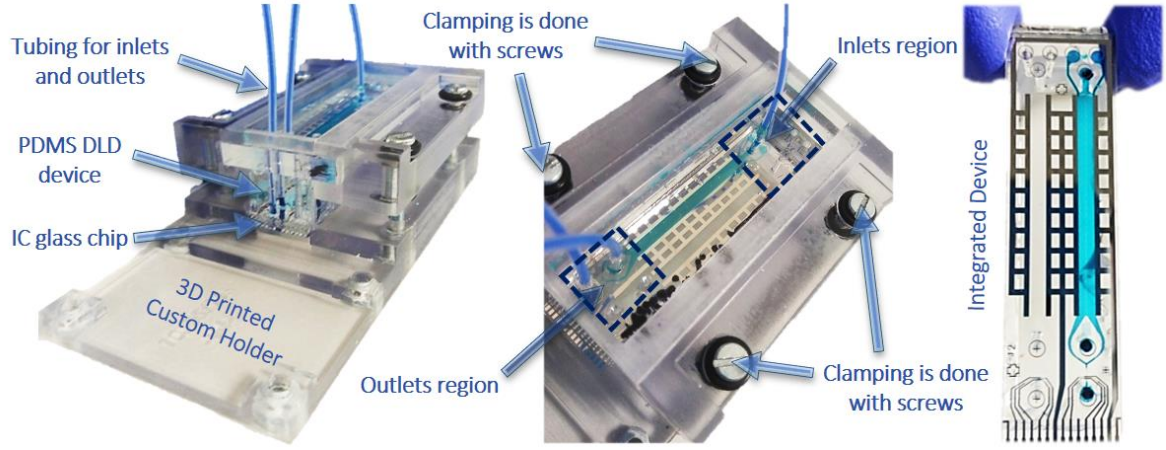


**Figure 6.8:** Photographs of the AC electrokinetics-integrated DLD system. A 3D printed custom holder was designed for the system. The bottom component houses the AC electrokinetics-integrated glass chip and the DLD PDMS device. The top component was screwed, clamping the integrated device. Opening for inlets and outlets tubing are defined on top.

### 6.4.2 Experimental Methods

#### 6.4.2.1 Device Fabrication

The AC electrokinetic-integrated chip (**Figure 6.9a**) followed a fabrication process similar to that of standard MIC chips (Holmes, She, *et al.*, 2007; Spencer, Elliott and Morgan, 2014; Spencer, Hollis and Morgan, 2014). The chips were fabricated using standard photolithography techniques by Ying Tran at the Southampton Nanofabrication Centre, University of Southampton. Electrodes for DEP (750 µm) and impedance detection (30 µm width and separated by 10 µm) were patterned on the glass wafer, with individual chips diced and stored.

The masters for soft lithography were defined with SU8 (SU8-3010) in a 6'' silicon wafer to a thickness of ~17.5 µm. Replicas were created in PDMS by standard replica moulding (Xia and Whitesides, 1998), with an anti-adhesion treatment performed to facilitate demoulding (Beck *et al.*, 2002) (**Figure 6.9b**). CleWin5 (WieWeb Software) was used to draw the photolithographic masks.

#### 6.4.2.2 Experimental Setup

A custom holder was used to house the various system components. The PDMS devices were aligned with the glass chip and clamped by screwing the top component to the holder. To prevent particle adhesion in the devices, a solution of 1% Pluronics F127 in 1x PBS was introduced in the device immediately after assembly and incubated for least 30 min before flushing with PBS for another 30 min. PTFE tubing, 1.5 mm inner diameter connected the inlets and outlets to reservoirs, which were also connected to a pressure control system (OB1 MK3, Elveflow).

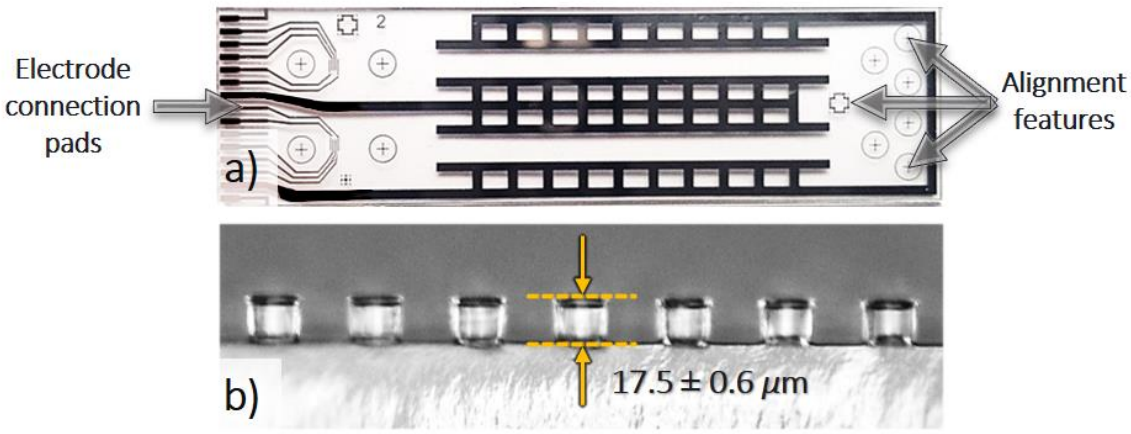


**Figure 6.9: a)** Photograph of the AC electrokinetics integrated DLD glass chip with platinum electrodes. **b)** Micrograph of a DLD device cross-section.

The printed circuit board interfaced to the chip and was connected to a waveform generator (TGA Series, TTi) and a high voltage amplifier (WMA-300, Falco Systems), and to an impedance spectroscope and lock-in amplifier (HF2IS, Zurich Instruments). For DEP measurements, a sinusoidal voltage at varying frequency (1 kHz to 5 MHz) was applied to the electrodes. The high voltage amplifier allows the application of signals up to 300 Vpp. For MIC measurements, sinusoidal voltages at two fixed frequencies were applied to the centre electrode: the first voltage at a frequency of 500 kHz, while the second at a frequency of 5 MHz. The differential signal was acquired from the two side measurement electrodes.

#### 6.4.2.3 Sample Preparation

Buffers of varying conductivity were prepared by diluting 1×PBS solutions ($\sigma$ = 1.5 S/m). Yeast samples were prepared by suspending common baking yeast in a 14% sucrose, PBS solution, and left overnight at 37° while shaking at 200 rpm. After the overnight culture, samples were centrifuged (300 rps, 3 min) and resuspended in the buffer of choice. GFP-expressing *E. coli* samples (Lab strain JM 109) were grown in 20 mL of pre-prepared media of 100 µg/mL Ampicillin, TSB medium. Cultures were kept at 37° while shaking at 130 rpm. Prior to experiments, samples were centrifuged (400 rps, 5 min), and resuspended in the buffer of choice. Polystyrene beads samples, of various sizes (1.5 to 10 µm), were suspended in the buffer of choice to a final concentration of 1500 beads/µL.

#### 6.4.2.4 Optical Flow Cytometry

Conventional flow cytometric analysis of sorted samples was carried out using a BD Accuri C6 (488 nm and 640 nm). Cytometric data was exported as standard FCS files, and the forward and side scattered light (FSC and SSC) signals were analysed using FlowJo, LLC (V.10).

### 6.4.3 Technology Integration: DEP & DLD

The integration of DEP with DLD has been previously explored (Beech, Jönsson and Tegenfeldt, 2009). For the system under study, the field was simulated using finite element simulations (COMSOL Muliphysics), by modelling the electric field in a small section of the device (**Figure 6.10**). The parameters used were: buffer permittivity $\varepsilon_r$ = 80 and conductivity $\sigma$ = 20 mS/m; and PDMS posts permittivity $\varepsilon_r$ = 2.75 and conductivity $\sigma$ = 1 µS/m. A potential of 100 V and 100 Hz applied to the top boundary of the model, with an electrical field generated from the top to

bottom. The model is 2D and does not consider the height of the device or fluid flow, simplifying its implementation.

In the absence of flow (**Figure 6.10**), particles amenable to DEP forces move either to areas of low (nDEP) or high field gradient (pDEP). This depends on the real part of the Clausius-Mossotti factor ($\mathrm{Re}[\tilde{f}_{CM}]$), as previously described (**Section 3.2.1**). An example is presented in **Figure 6.11**, where the behaviour of polystyrene beads and yeast cells was modelled for buffers of varying conductivity. Polystyrene beads were modelled as solid particles with permittivity $\varepsilon_{bead} = 2.5$, conductivity $\sigma_{bead} =$ 2 mS/m and 2 µm diameter. As for yeast cells, a two-shell model (*i.e.*, considering the cell wall and membrane independently) was used. The values used were based on existing literature (Huang *et al.*, 1992): $\varepsilon_{wall} = 60$, $\sigma_{wall} = 1.4\times10^{-2}$ S/m and $d_{wall} = 0.22$ µm; $\varepsilon_{membrane} = 6$, $\sigma_{membrane} = 2.5\times10^{-7}$ S/m and $d_{membrane} = 8$ nm; $\varepsilon_{cytoplasm} = 50$, $\sigma_{cytoplasm} = 0.2$ S/m; and $r_{cell} = 4$ µm. The model showed that the beads undergo nDEP for the frequency range used. As for yeast cells, the behaviour is as expected and observed in biological particles (Markx *et al.*, 1994; Fernandez *et al.*, 2017), *i.e.*, shifting from nDEP to pDEP after a cross-over frequency.

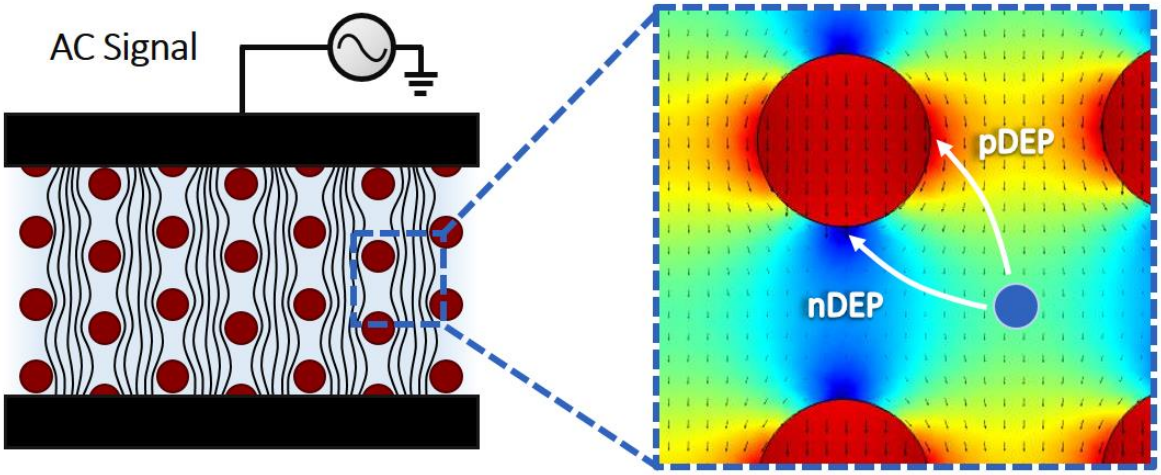


**Figure 6.10:** Schematic of the AC field across the integrated device. An AC signal is applied to electrodes parallel to the DLD post array. Inset shows the simulated electric field. Particles under DEP force will move to areas of low field strength (*blue*) in nDEP or to areas of high field strength (*red*) in pDEP.

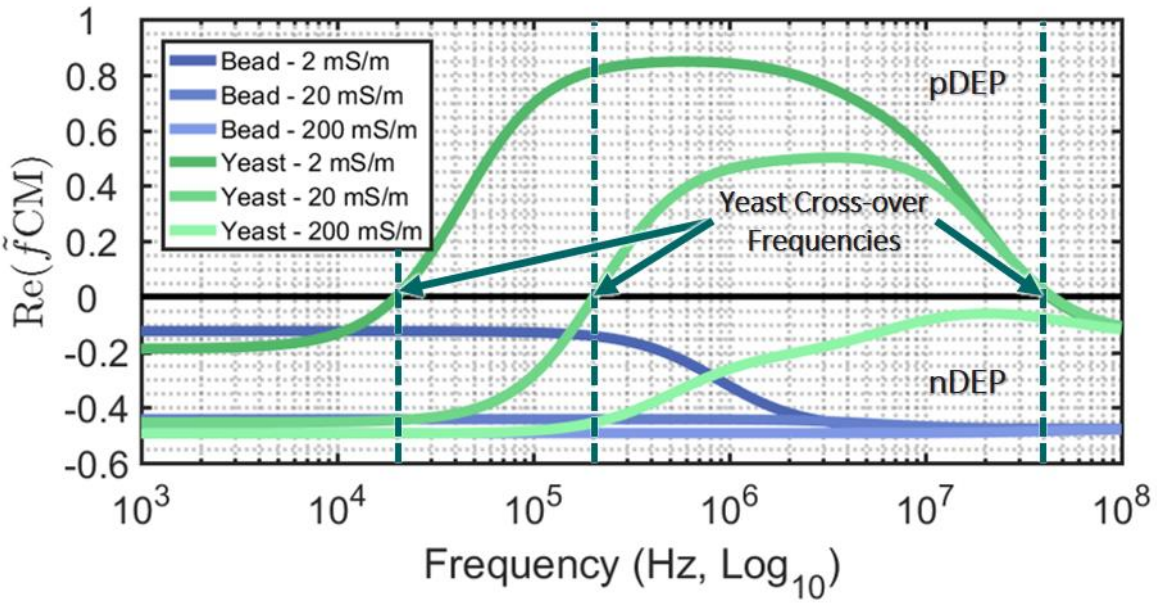


**Figure 6.11:** Real part of the Clausius-Mossotti factor ($\mathrm{Re}[\tilde{f}_{CM}]$) of yeast cells and polystyrene beads, in a medium at different conductivities ($\sigma_{medium}$ = 2, 20 and 200 mS/m), along the frequency spectrum. Polystyrene beads have a constant negative $\mathrm{Re}[\tilde{f}_{CM}]$. Yeast cells go from negative to positive $\mathrm{Re}[\tilde{f}_{CM}]$ at a cross-over frequency around 20 kHz for $\sigma_{medium}$ = 2 mS/m and 200 kHz for $\sigma_{medium}$ = 20 mS/m, but remain negative for $\sigma_{medium}$ = 200 mS/m.

A sample containing fluorescent polystyrene beads (2 µm diameter) and fluorescent tracer particles (100 nm) in a buffer of conductivity $\sigma$ = 3 mS/m was introduced in the device (**Figure 6.12a, b** and **c**). Particles were flushed into the device and allowed to settle. Precise pressure control was exerted to create a static environment, removing any flow. An AC signal of 300 Vpp was applied and the frequency varied. At 100 kHz (**Figure 6.12a**), beads moved from a random distribution to specific positions within the post, corresponding to nDEP behaviour (**Figure 6.10**). As the frequency was increased up to 1MHz, no further movement was observed (**Figure 6.12b** and **c**).

Yeast cells, in an isosmotic buffer of conductivity $\sigma$ = 20 mS/m were introduced in the device and the sample allowed to settle (**Figure 6.12d, e** and **f**). nDEP behaviour was observed when a frequency of 100 kHz was applied (**Figure 6.12d**). However, when the frequency was increased to the region where the cross-over frequency should occur (approximately 200 kHz, **Figure 6.11**), cells were repelled from their position and drifted away from the post (**Figure 6.12e**). This meant that there was little to no DEP force acting on the cells, as predicted. By further increasing the frequency to 1 MHz, yeast cells were attracted to the regions of high field gradient (**Figure 6.12f**).

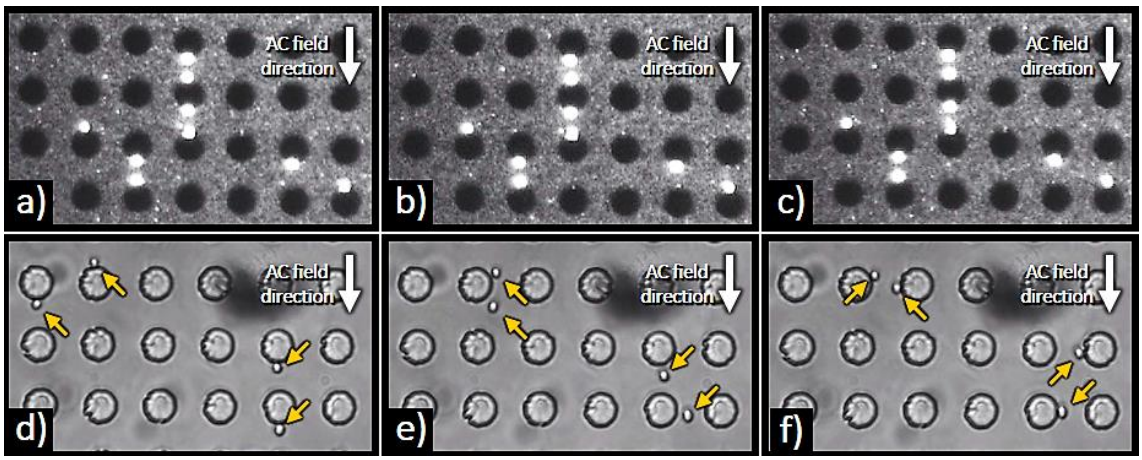


**Figure 6.12:** Micrographs of fluorescent polystyrene beads in a buffer of $\sigma = 3$ mS/m (**a, b** and **c**) and yeast cells in a buffer of $\sigma = 20$ mS/m (**d, e** and **f**) within the integrated device. AC signals (beads – 300 Vpp; yeast – 200 Vpp) at 100 kHz (**a** and **d**), 200 kHz (**b** and **e**) and 1 MHz (**c** and **f**) were used.

Experiments were also conducted with *Escherichia coli* bacteria, which can be found dwelling in blood at extremely low numbers in severe sepsis (Tracey *et al.*, 1987; Jauréguy *et al.*, 2007). An enrichment tool could enrich pathogens at higher numbers for downstream detection. The dielectrophoretic behaviour of *E. coli* was first modelled based on existing literature (Asami, Hanai and Koizumi, 1980; Sanchis *et al.*, 2007). An oblate spheroid model (see **Section 5.4.4**) with three layers (bacteria wall, membrane and cytoplasm) was implemented (**Figure 6.13**). The modelling values used were: $\varepsilon_{wall} = 60$, $\sigma_{wall} = 0.6$ S/m and $d_{wall} = 10$ nm; $\varepsilon_{membrane} = 10$, $\sigma_{membrane} = 1\times10^{-6}$ S/m and $d_{membrane} = 5$ nm; $\varepsilon_{cytoplasm} = 60$, $\sigma_{cytoplasm} = 0.2$ S/m; $a = 1$ µm and $b,\ c = 0.5$ µm.

Modelling results show that pDEP is prevalent for *E. coli* in low conductivity buffer within the maximum frequency range of 50MHz whereas for buffers of higher conductivity (*e.g.* $\sigma = 0.2$ S/m in **Figure 6.13**), the bacteria will experience nDEP at frequencies lower than ~1MHz. The dominance of pDEP for low conductivity buffers is due to the high surface charge characteristic of bacteria (and specifically, *E. coli*) (Markx *et al.*, 1994; Sonohara *et al.*, 1995; Torimura *et al.*, 1999; Buszewski *et al.*, 2003), which means there are more polarisable than the medium and therefore will experience pDEP (see **Section 3.2.1**).

Experiments were conducted with *E. coli* (**Figure 6.14**), suspended in an isosmotic buffer of high conductivity ($\sigma = 180$ mS/m). The *E. coli* was genetically modified to express GFP, facilitating fluorescence identification. Flow was generated by applying 25 mbar to the device inlet (MFCS, Fluigent). AC signals of 300 Vpp were applied to the device and the frequency varied. When a signal of 100 kHz was

applied, bacteria moves from a random distribution (**Figure 6.14a**) to alignment and concentration in the areas of lower electric field gradient (**Figure 6.14b**). Areas of higher field strength were almost deplete of bacteria due to nDEP. Conversely for a 1 MHz signal, a fraction of cells moved from a random distribution (**Figure 6.14c**) to areas of higher field gradient (**Figure 6.14d**), while others remained dispersed within the device. The fact that 1 MHz is close to the cross-over frequency in the buffer used could explain this difference in behaviour. A fraction of cells would then move due to a weak pDEP force, trapping bacteria in-between the posts and forming clusters close to each post.

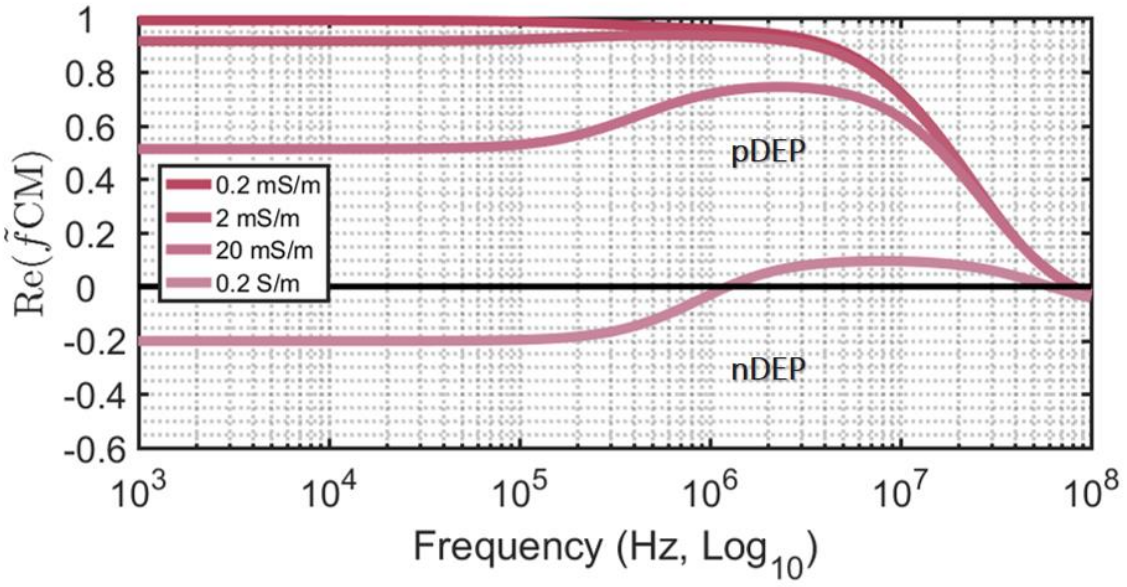


**Figure 6.13:** Real part of the Clausius-Mossotti factor ($\mathrm{Re}[\tilde{f}_{CM}]$) of *E. coli* in a medium at different conductivities ($\sigma_{medium}$ = 0.02 mS/m to 0.2 S/m), along the frequency spectrum.

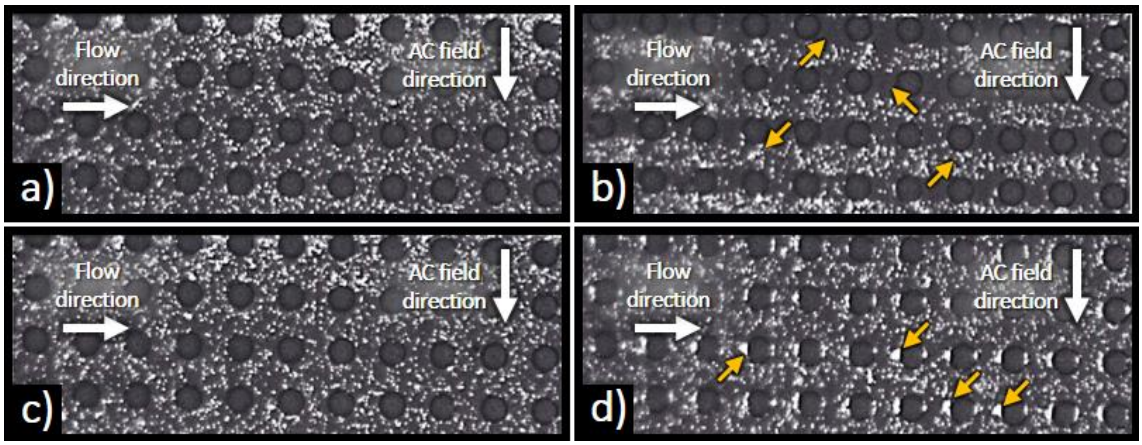


**Figure 6.14:** Micrographs of fluorescent *E. coli* bacteria, in a buffer of $\sigma$ = 180 mS/m, before (**a** and **c**) and after (**b** and **d**) the application of an AC signal (300 Vpp) at **b)** 100 kHz and **d)** 1 MHz. A pressure controller applies 25 mbar pressure to the device, driving a steady flow from left to right, perpendicular to the electric field.

These results could be exploited for the enrichment of pathogenic bacteria in a future integrated device. One possible option would be to explore the apparent nDEP behaviour of *E. coli* at lower frequencies (**Figure 6.14b**). A device could be designed so its $D_c$ is such that any cell present (RBCs or bacteria for example), would zigzag along the device. The zigzag movement requires particles to go around posts after a period $N$ (**Figure 6.1**). On applying an AC field, a nDEP force could be created to repel the bacteria from posts and effectively behave as in displacement mode. Hypothetically, the device could then be designed so that while RBCs and other blood cells zigzag, *E. coli* would be "displaced" to collection outlets due to nDEP and enriched.

A second option would be to take advantage of the pDEP behaviour at higher frequencies (**Figure 6.14d**). The entrapment of bacteria in-between the DLD posts is similar to the observed phenomena named "insulating DEP" (Lapizco-Encinas *et al.*, 2004a, 2004b). The difference is that insulating DEP typically uses DC voltages, applied across a microchannel containing an array of insulating posts etched in glass. The non-uniform electric field near the insulating posts drive DEP as they constrict the field. DI water is used as medium, *i.e.*, a buffer of very low conductivity and pDEP dominates at lower frequencies (as modelled in **Figure 6.13**). With DC voltages applied, this behaviour was confirmed, with live bacteria being trapped in-between posts and enriched, while dead bacteria were removed from the sample. Using this entrapment approach as example, a buffer of low conductivity ($\sigma < 20$ mS/m) could be used in an integrated device where strong electric fields (> 300 Vpp) at low frequency (≤ 100 kHz) would generate a pDEP force sufficiently strong to capture bacteria while other blood cells transverse the device.

However, further studies are required. For example, it is not clear if observed DEP forces would suffice to modulate the displacement of particles when higher pressures and throughputs are required. Furthermore, given the application of strong electric fields across the device, other electrokinetics effects, such as electro-osmosis or electrophoresis, might play a role in the observed movement of particles. Unfortunately, time constraints limited further experiments.

### 6.4.4 Technology Integration: MIC & DLD

The integration of MIC with DLD required alteration of the electrodes to a co-planar conformation, (**Figure 6.15**), onto which the DLD array (fabricated using PDMS) could be bonded. The three electrodes were fabricated just prior to the measurement outlet. An AC signal was applied to the central electrodes and the difference in the current flowing into the two side electrodes was measured using a custom detection circuit. Signal acquisition and processing follows the same steps as in standard MIC (**Section 3.3.1**). Individual signals are thus retrieved for each sorted particle, permitting single-particle counting and analysis. Thus, if the sorting is not perfect (typical for experimental devices), the target cells can still be identified and enumerated from the non-target cells in the positive fraction.

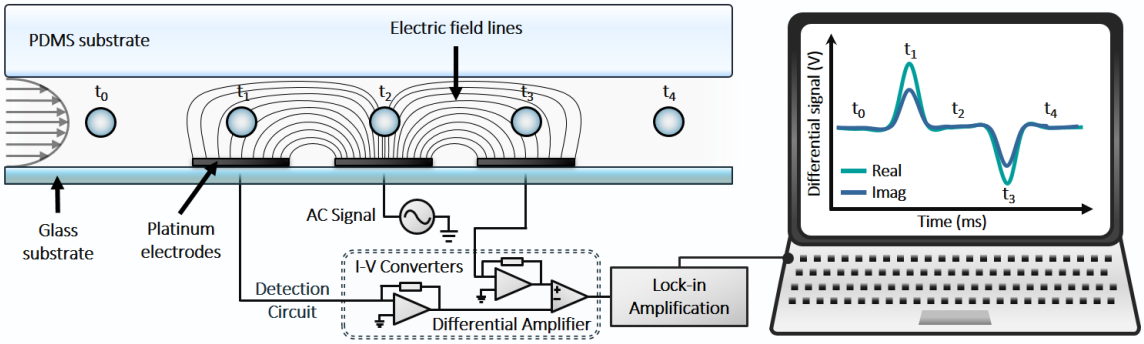


**Figure 6.15:** Representation of the impedance detection section of the integrated system. Particles flow through the microchannel, on top of electrodes, in the detection region. The acquired differential signal is stored for further analysis.

#### 6.4.4.1 Testing the Integrated Device

The sorting efficiency of the three different device types ($D_c$ = 4, 5 and 6 μm) was tested by running samples containing a mixture of two sizes of beads, one below and one above the critical diameter. A pressure of 200 mbar was applied at each inlet to drive the flow. After each experiment, the samples at the outlets reservoirs were collected and measured using optical flow cytometry to quantify sorting efficiency.

For the device with a $D_c$ of 4 μm, the sample at the inlet was 25.9% 3 μm beads and 74.1% 7 μm beads (**Figure 6.16a**). Post sorting, the "displacement" outlet for larger particles (*"Big"* Outlet), contained 15.6% of 3 μm beads and 84.4% of 7 μm beads. The presence of this considerable amount of smaller particles would be expected, as any small particle that enters at the centre of the device will simply zigzag and be collected at this central outlet (see **Figure 6.7**). As for the *"Small"* Outlet, it contained 99.7% of 3 μm beads and only 0.3% of 7 μm beads. The removal of

virtually all larger particles (which are displaced) gave a ratio between bead populations (3 µm : 7 µm) of ~332, resulting in an enrichment of ~950×.

For the device with a $D_c$ of 5 µm (**Figure 6.16b**), the sorting process efficiency was lower, with the ratio at inlet (~0.98) increasing only to ~6.35 at the *"Small"* Outlet (86.4% of 3 µm beads and 13.6% of 7 µm beads), resulting in an enrichment of only ~6.5×. Finally, the $D_c = 6$ µm device (**Figure 6.16c**), had a high enrichment level, around 120×, with the inlet ratio (~0.34) increasing to ~40.7 at the *"Small"* Outlet (97.6% of 5 µm beads and 2.4% of 10 µm beads).

Typically, low pressures of a few hundred mbar are used to drive DLD devices. Further tests were conducted with devices of $D_c = 4$ µm to assess whether higher pressures (and therefore flowrate) could be used without negatively impacting on the enrichment process. Pressures of 300 mbar, 500 mbar and 700 mbar were chosen (compared to the 200 mbar used in previous experiments). Samples of 3 µm beads (49 ± 3 %) and 6 µm fluorescent beads (51 ± 3 %) were used. Optical flow cytometry was used to measure the particle distributions at both outlets (**Figure 6.17**). MIC measurements (integrated into the device) were also made at the same time (see later).

The percentages of particles of each size at the *"Big"* Outlet showed no difference between experiments at different pressures (Student's *t*-test; N = 3 vs 3 experiments), with overall mean populations: 25 ± 4 % of 3 µm beads and 76 ± 4 % of 6 µm beads (N = 9). At the larger particle outlet, the majority of larger beads were being correctly displaced, with very few 6 µm beads being directed to the *"Small"* Outlet (**Figure 6.18a**).

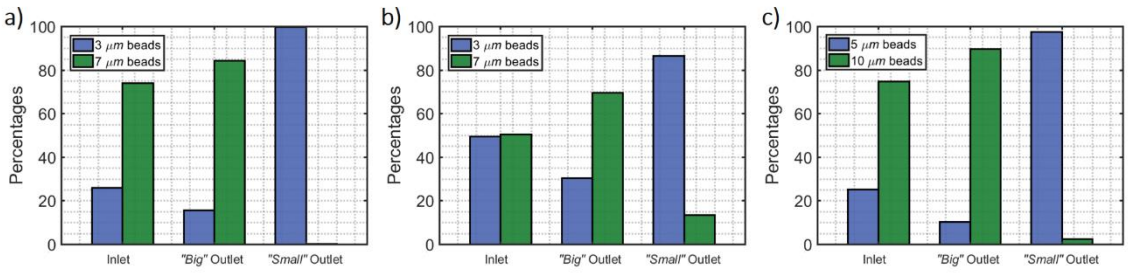


**Figure 6.16:** Percentages of beads populations, determined by optical flow cytometry, at the inlet, outlet for bigger particles (*"Big"* Outlet) and outlet for smaller particles (*"Small"* Outlet), for integrated devices of **a)** $D_c = 4$ µm, **b)** $D_c = 5$ µm and **c)** $D_c = 6$ µm.

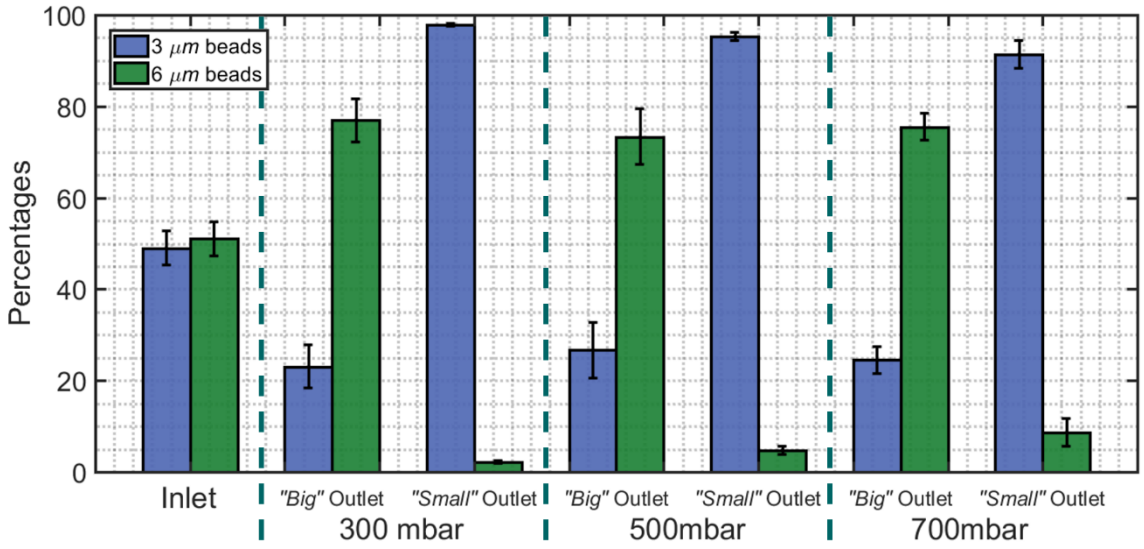


**Figure 6.17:** Percentages of bead populations (3 µm and 6 µm), determined by optical flow cytometry, at the inlet, outlet for larger particles (*"Big"* Outlet) and outlet for smaller particles (*"Small"* Outlet), for an integrated device of $D_c = 4$ µm, at different sample and sheath flow inlet pressures.

A high sorting efficiency was achieved for each pressure, with populations of 3 µm beads of 97.8 ± 0.25 % (enrichment ~46.4 ± 7; N = 3) at 300 mbar, 95.3 ± 0.73 % (enrichment ~21.5 ± 3.6; N = 3) at 500 mbar, and 91.4 ± 2.47 % (enrichment ~11.9 ± 2.9; N = 3) at 700 mbar. Statistical analysis (Student's *t*-test; N = 3 vs 3 experiments), showed only a significant difference between experiments at 300 and 700 mbar ($p$<0.05). Nonetheless, the overall mean populations obtained at this outlet were 94.8 ± 3 % of 3 µm beads and 5.2 ± 3 % of 6 µm beads (N = 9). Thus, higher pressures and therefore higher throughputs could be used in the integrated device.

Impedance cytometry measurements were also made at the *"Small"* Outlet, signal processing followed the methodology introduced in **Section 3.3.2.2.** A running-maximum filter was used to identify the positions of the maximum of the convolution outputs, corresponding to the position of each individual impedance signal (**Figure 6.18b**). Impedance data was acquired at 500 kHz and 5 MHz for each experiment. Using data measured at 500 kHz as reference, the population of 3 µm beads was gated and used to normalize the impedance data in terms of size and opacity (magnitude at 5 MHz over magnitude at 500 kHz). The resulting plot (**Figure 6.18c**) shows the presence of two different populations: one cluster between 2.5 and 5 um (corresponding to the 3 µm beads) and one cluster between 6 and 7um (corresponding to the 6 µm beads). Each clusters appears to contain multiple subpopulations; this is addressed later in **Section 6.4.4.2**. The percentages of each population are presented in **Figure 6.19**, together with the results from

optical flow cytometry, and shows excellent agreement between the integrated inline analysis (MIC) and the offline FACS analysis. The statistical analysis is presented in **Table 6.1**.

**Table 6.1:** Statistical analysis of percentages at the *"Small"* Outlet, at different pressures, for the two detection methods used: MIC and FACS (Student's *t*-test, N=3, n. s. - not significant, *p<0.05)

| Percentages at *"Small"* Outlet | | MIC | | | FACS | | |
|---|---|---|---|---|---|---|---|
| | | 300 mbar | 500 mbar | 700 mbar | 300 mbar | 500 mbar | 700 mbar |
| MIC | 300 mbar | | n. s. | * | n. s. | | |
| | 500 mbar | | | n. s. | | n. s. | |
| | 700 mbar | | | | | | n. s. |
| FACS | 300 mbar | | | | | n. s. | * |
| | 500 mbar | | | | | | n. s. |
| | 700 mbar | | | | | | |

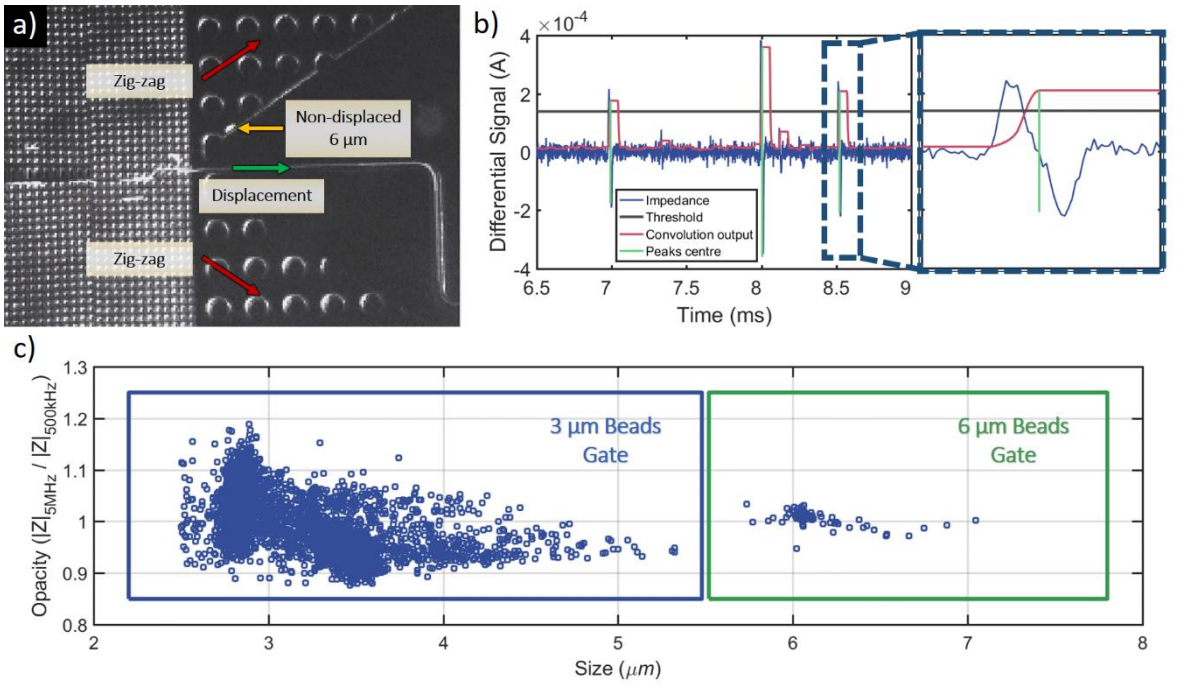


**Figure 6.18: a)** Micrograph of the outlet region of an integrated device with $D_c = 4$ µm. The majority of fluorescent 6 µm beads are displaced to the central zone and collected, with few bigger beads being collected as zigzagging smaller particles. **b)** A section of experimental data showing three individual particles detected by the system, with the threshold level set for identification, the result of the maximum filter applied to the convolution output on the experimental data, and the detected centres for each individual signals. **c)** Scatter plot of opacity (magnitude at 5 MHz - $|Z|_{5MHz}$ over magnitude at 500 kHz - $|Z|_{500kHz}$) versus size (µm) for a measurement at the impedance cytometry region of the integrated device. Gates for classification of smaller, 3 µm beads and bigger, 6 µm beads are presented.

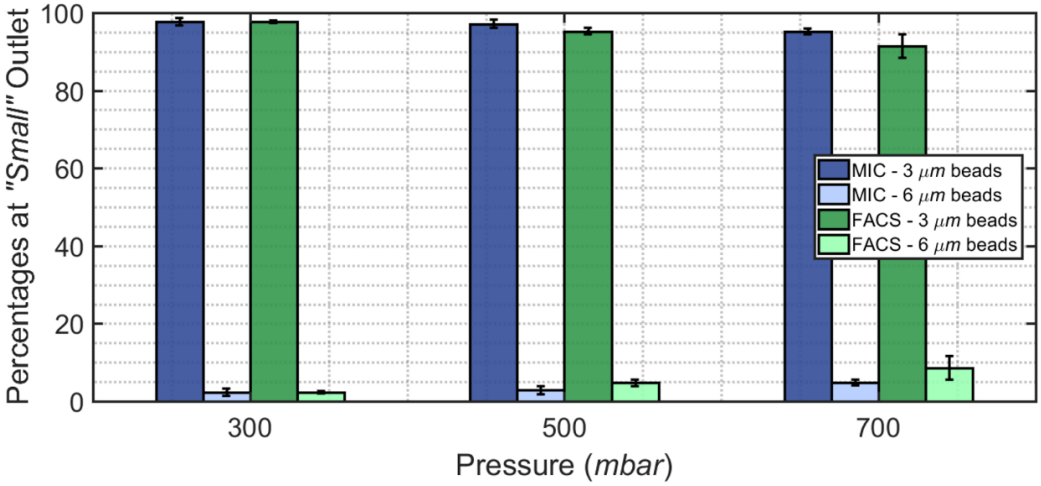


**Figure 6.19:** Percentages of beads populations (3 µm and 6 µm), determined by optical flow cytometry (FACS) and impedance cytometry (MIC), at the outlet for smaller particles (*"Small"* Outlet), for an integrated device of $D_c = 4$ µm, at different sample and sheath flow inlet pressures.

Results from MIC confirmed a high degree of sorting at each tested pressure, with populations of 3 µm beads of 97.7 ± 0.79 % (enrichment ~47.4 ± 10.9; N = 3) at 300 mbar, 97.1 ± 0.85 % (enrichment ~39.4 ± 13.2; N = 3) at 500 mbar, and 95.2 ± 0.59 % (enrichment ~21.3 ± 4.9; N = 3) at 700 mbar. An overall mean population of 96.7 ± 1.3 % (enrichment ~36 ± 15; N = 9) was obtained. Statistical analysis (Student's *t*-test; N = 3 vs 3 experiments), showed again a significant difference between experiments at 300 and 700 mbar ($p$<0.05), but no significant difference when comparing MIC and FACS results directly at each pressure ($p$>0.05). These results indicate that the identification and counting process with the integrated MIC technology is as reliable as the standard optical flow cytometry method, commonly used to assess DLD sorting results. Thus, integration of MIC and DLD could be further explored to enhance current post-experiment DLD protocols by simplifying the assessment of sorting results, reducing turnover times and eliminating the need to move samples of-chip for quantification elsewhere.

#### 6.4.4.2 Positional Correction

As **Figure 6.18c** shows, there is a large distribution in the scatter plot for the monodisperse particles what have a tight distribution in size (as confirmed using the optical flow cytometer). This is also unlike the typical compact distributions seen in previous MIC data. Using the same data from **Figure 6.18c** but zooming in exclusively at the sub-population of 3 µm beads (**Figure 6.20**), the existence of two individual size sub-populations is clear (**Figure 6.20a**). Moreover, when considering a histogram of size distribution (**Figure 6.20b**), if a threshold is set at the expected size (3 µm), approximately 50% of the population is found at each side.

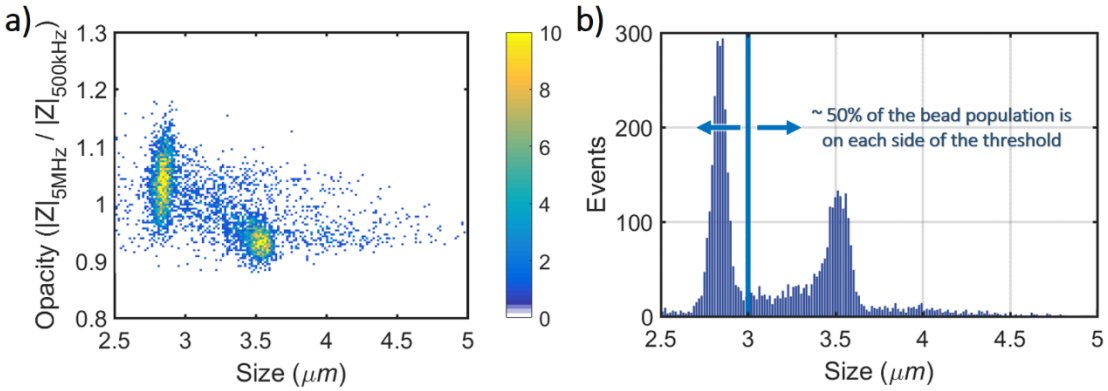


**Figure 6.20: a)** Density scatter plot of opacity (magnitude at 5 MHz - $|Z|_{5MHz}$ over magnitude at 500 kHz - $|Z|_{500kHz}$) versus size (μm) of the 3 μm beads population for a measurement at the impedance cytometry region of the integrated device. **b)** Histogram of size distribution for the 3 μm beads populations. The existence of two individual size sub-populations is clear.

The occurrence of these sub-populations is due to the position dependence of the impedance signal (Spencer and Morgan, 2011), and inertial focusing of particles before the measurement region (Di Carlo, 2009; Di Carlo *et al.*, 2009) as follows: prior to the measurement region, the channel has four lanes of rectangular cross-sections (110 μm × 17.5 μm) and length ~1.2 mm, followed by a wide region of rectangular cross-section (200 μm × 17.5 μm) and length 450 μm, which then funnels until the MIC region (**Figure 6.7**). At intermediate Reynold's numbers, beads migrate into two equilibrium positions within the microchannel (Di Carlo, 2009; Di Carlo *et al.*, 2009; Hur *et al.*, 2011; Spencer and Morgan, 2011). Published work has already addressed the positional dependence of particles in an impedance cytometry microchannel (Gascoyne *et al.*, 2004; Spencer and Morgan, 2011; Errico *et al.*, 2017).

For standard MIC measurements, this effect is automatically compensated in the data processing steps (Spencer *et al.*, 2016). However, for a co-planar electrodes conformation, this effect on particle distribution is much greater due to the non-uniform electric field in the co-planar electrode geometry. Particles can pass though the electrodes at different positions (1, 2 and 3, for example (**Figure 6.21a**) within the microchannel. Since the electric field in the microchannel is not uniform, the particle position will influence differently the differential signal acquired for each particle. Particles flowing at the top of the channel (position 1) interact with a weaker electric field, resulting in weaker signals; with the opposite occurring as particles flow closer (positions 2 and 3) to the electrodes (**Figure 6.21b**).

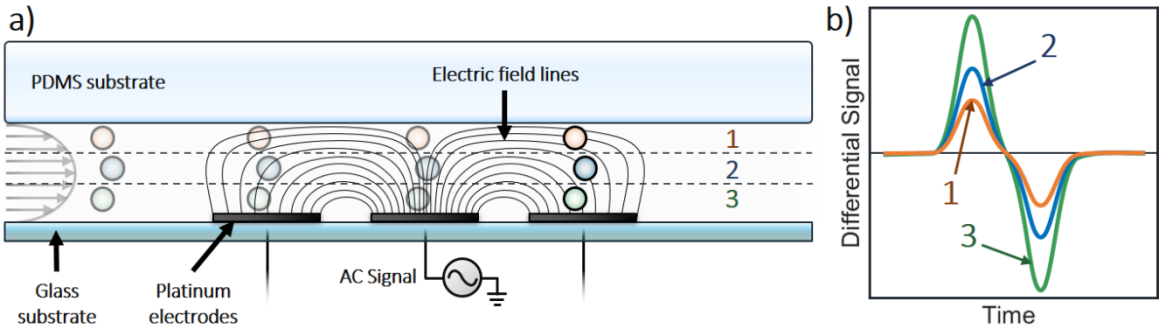


**Figure 6.21:** Signal positional dependence for a typical co-planar electrode conformation in MIC. **a)** The position of particles flowing through a MIC microchannel varies according to its geometry. **b)** Different positions within the microchannel generate Differential Signals of diverse amplitudes, which will translate to different estimated sizes.

This manifests as an apparent error in the measured "electrical size" of the particles. Due to the observed inertial focusing, particles will tend to align at positions 1 and 3 in the microchannel, resulting in very distinct signals and size estimations. This explains the observed two size sub-populations, with the "smaller" and "bigger" beads corresponding to events at positions 1 and 3, respectively.

An algorithm to compensate for this effect was implemented, based on a method recently proposed by Errico *et al.*, (2017). First, single impedance signals were fitted to an anti-symmetric bipolar Gaussian template as represented in **Figure 6.22a**. This template was generated according to:

$$s(t) = a[e^{g+(t)} - e^{g-(t)}] \qquad (6.5)$$

and

$$g \pm (t) = \frac{-(t-(t_c \pm (\delta/2)))^2}{2\Sigma^2} \qquad (6.6)$$

with $t$ being the time variable, $a$ the peak amplitude and $g \pm (t)$ the Gaussian function details, where $t_c$ is the signal centre, $\delta$ the peak-to-peak distance or transit time and $\Sigma$ the peak width. By fitting the template to individual signals (for example, a 7 µm bead, as in **Figure 6.22b**), these different parameters were retrieved.

The estimated size ($D$) of the beads was calculated from the impedance magnitude at low frequency (500 kHz). These values were then normalized by the expected size ($d$) of the beads (7 µm, in this case). A shape parameter was calculated as the ratio between peak width and transit time ($\Sigma/\delta$).

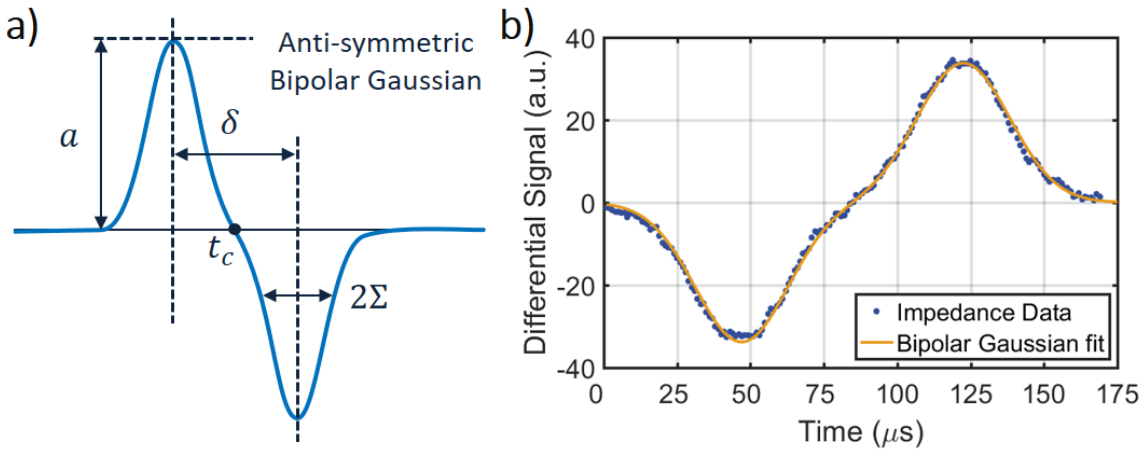


**Figure 6.22: a)** Anti-symmetric Bipolar Gaussian template used as the event fitting function to acquire single impedance signals. **b)** Bipolar Gaussian fit ($R^2$ = 0.9980) to an individual impedance signal of a 7 μm bead.

This parameter is correlated to the particle trajectory within the microchannel, as particles closer to the electrodes will have sharper, less wide peaks, thus presenting smaller shape parameter values (Errico *et al.*, 2017). When plotting the shape parameter versus normalized size (**Figure 6.23a)**, the density of events showed two sub-populations of beads: events with smaller normalized size but higher shape parameter, and vice-versa, corresponding to particles at the top and bottom of the channel, respectively.

A linear regression model was then created to fit the data:

$$D_{est}/d_{exp} = C_1 + C_2\left(\Sigma/\delta\right) \qquad (6.7)$$

from which the corrected estimated size - $D_{corr}$ can be derived:

$$D_{corr} = \frac{D_{est}}{C_1 + C_2\left(\Sigma/\delta\right)} \qquad (6.8)$$

where $C_1$ and $C_2$ are model parameters.

The model was used to fit the data (**Figure 6.23a**) in order to retrieve the parameters (**Table 6.2**). Using **Equation 6.8**, the corrected size distribution can then be calculated (**Figure 6.23b** and **c**). As presented in **Figure 6.23c**, a Gaussian fit ($R^2$ = 0.9322; mean: 7.06 μm; standard deviation: 0.43 μm) applied to the corrected size distribution confirmed a single size distribution.

To further explore the positional dependence effect at different particle sizes, beads of various sizes ranging from 1.5 μm (the limit due to SNR of the measurement system) to 10 μm (upper limit of particle size) were measured. The

linear regression model was applied to the different sized beads populations (**Table 6.2** gives the full list of model parameters). **Figure 6.24** is a plot of the size distributions of the beads before (**Figure 6.24a**) and after (**Figure 6.24b**) the application of the correction algorithm. A vast improvement can be observed, with the corrected size estimation now in accordance to the expected size (**Table 6.2**). This correction method was then used in future experiments with the integrated device, mitigating the positional dependence, and ensuring accurate and reliable numbers for post-sorting data analysis.

**Table 6.2:** Linear Regression fit parameters for each beads population corrected

| Beads Size (µm) | $C_1$ | $C_2$ | $D_{corr}$ (µm) |
|---|---|---|---|
| **10** | 3.3844 | -9.8540 | 9.96 ± 0.41 |
| **7** | 2.6625 | -7.5114 | 7.00 ±0.38 |
| **5** | 2.8805 | -9.2997 | 5.00 ±0.29 |
| **3** | 2.7463 | -9.3344 | 2.99 ±0.27 |
| **1.5** | 1.8397 | -5.0946 | 1.50 ±0.05 |
| **Overall** | 2.7027 ± 0.4989 | -8.2188 ± 1.7520 | |

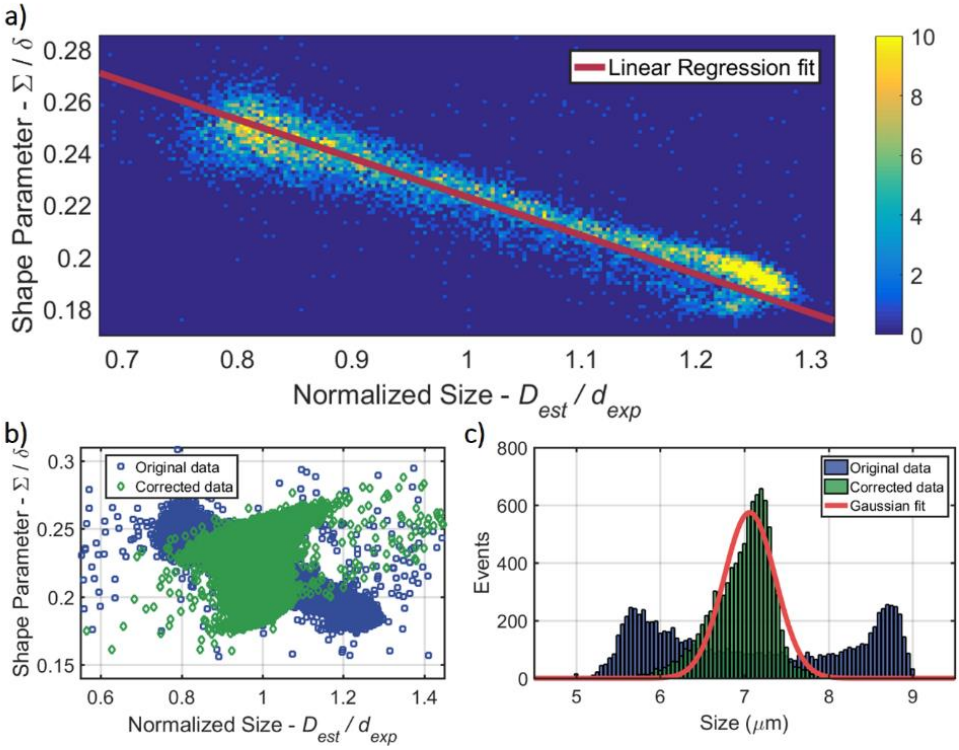


**Figure 6.23:** Density plot of the shape parameter ($\sigma/\delta$) versus the normalized size (estimated size - $D_{est}$ over expected size - $d_{exp}$) for a measurement at the impedance cytometry region of the integrated device of 7 µm beads. The linear regression fit (**Equation 6.7**) is shown in red (fit parameters reported in **Table 6.2**). **b)** Scatter plot of the shape parameter ($\sigma/\delta$) versus the normalized size (estimated size - $D_{est}$ over expected size - $d_{exp}$) of a 7 µm beads sample. The original and corrected data are plotted. **c)** Histogram of size distributions for the original and corrected 7 µm beads populations. A Gaussian fit ($R^2$ = 0.9322) to the corrected data confirms a single size distribution.

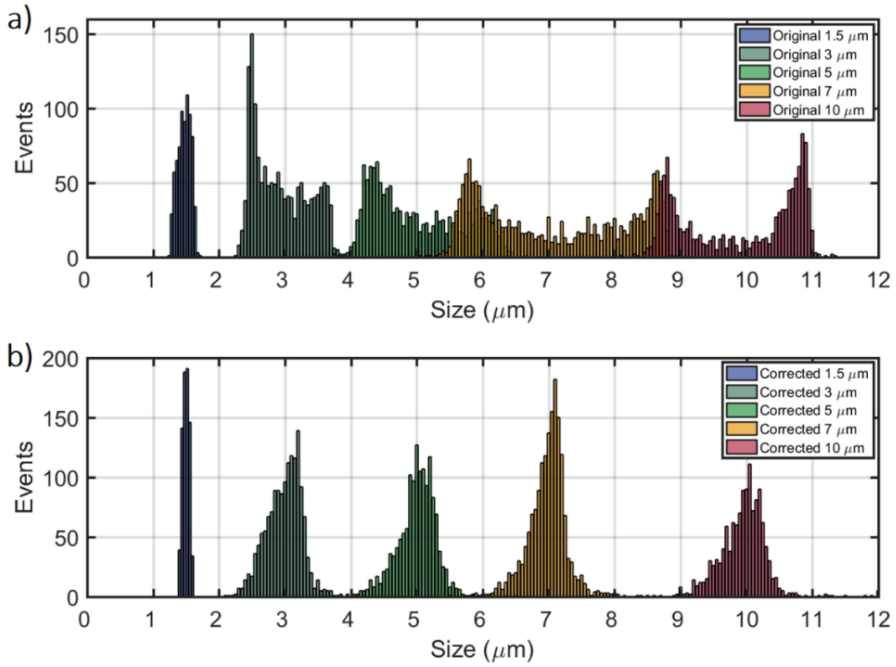


**Figure 6.24:** Histograms of size distributions for the **a)** original and **b)** corrected beads populations (1.5 μm, 3 μm, 5 μm, 7 μm and 10 μm).

#### 6.4.4.3 Setup Optimization

While performing different experiments, the functionality of the custom setup had different drawbacks. One of the main issues was related to the clamping and sealing of the integrated device, where multiple screws were used to clamp the top component to the holder (see **Figure 6.8**). In order to achieve a homogeneous pressure distribution, the screws had to be finely tuned and their individual position controlled. This was time consuming and problematic, leading to recurring leaks in various experiments.

Furthermore, the DLD PDMS device fabrication process lacked reproducibility, so that not all devices had the same dimensions and thickness, further complicated the clamping process. A more reliable and reproducible fabrication method for the DLD PDMS devices was developed, based on the creation of a device frame (**Figure 6.25a** and **b**). This frame was designed so that 12 single devices (53 × 15 mm) could be fabricated at the same time by aligning it with the 6'' Si master (**Figure 6.25a**). Polystyrene was used to fabricate the frame, where 2 mm deep pockets were carved (**Figure 6.25b**) and filled with PDMS to fabricate individual devices. With this process, DLD PDMS devices had a reproducible thickness of ~2.1–2.2 mm (**Figure 6.25c**). Thus, multiple reproducible devices could be fabricated in a single process.

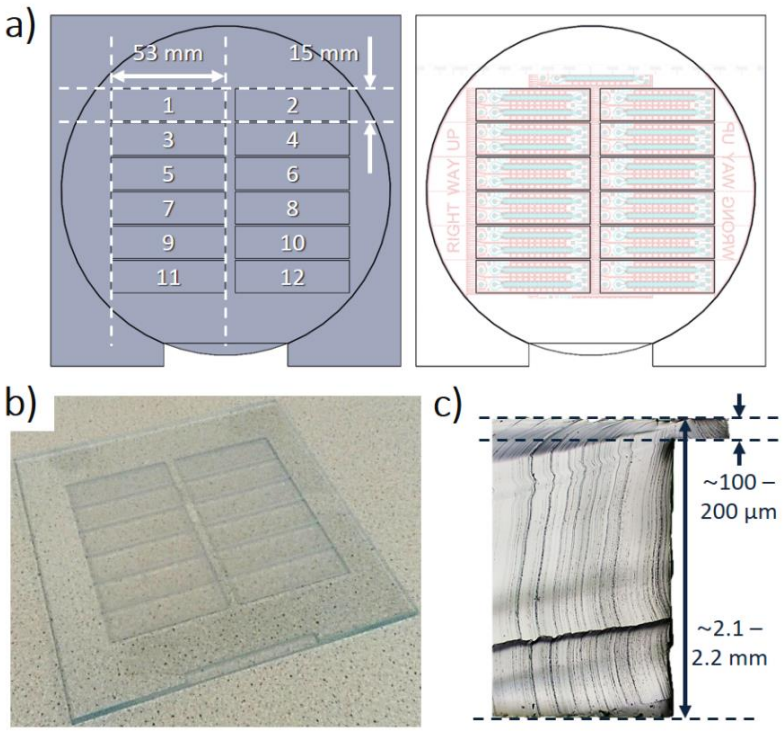


**Figure 6.25: a)** CAD model of the DLD PDMS device frame (*left*), which aligns with the device master for fabrication (*right*). **b)** Polystyrene DLD PDMS device frame. **c)** Micrograph of a DLD PDMS device cross-section.

A holder based on the Fluidic Connect Pro (FCP) frame, from Micronit Microfluidics (Enschede, The Netherlands) was developed. This adaptable frame can be used to house custom holder pieces and completely enclose the integrated device setup. The optimization process was based on the design, fabrication and testing of these custom pieces in collaboration with Micronit Microfluidics, where fabrication of the various pieces was conducted by Dr. Maciej Skolimowski.

The design of the optimized setup is represented in **Figure 6.26**. It comprised three main components: a bottom piece where the glass chip and PDMS device would be located; a top piece with openings for inlets and outlets; and a printed circuit board (PCB) with the electronic components for MIC measurements. By closing the frame, the top component would apply a homogeneous pressure along the integrated device, clamping it together. In addition, the PCB connector pads would be put into contact with the electrodes pads in the glass chip, which would permit the application of AC signals to the device and the performance of impedance measurements.

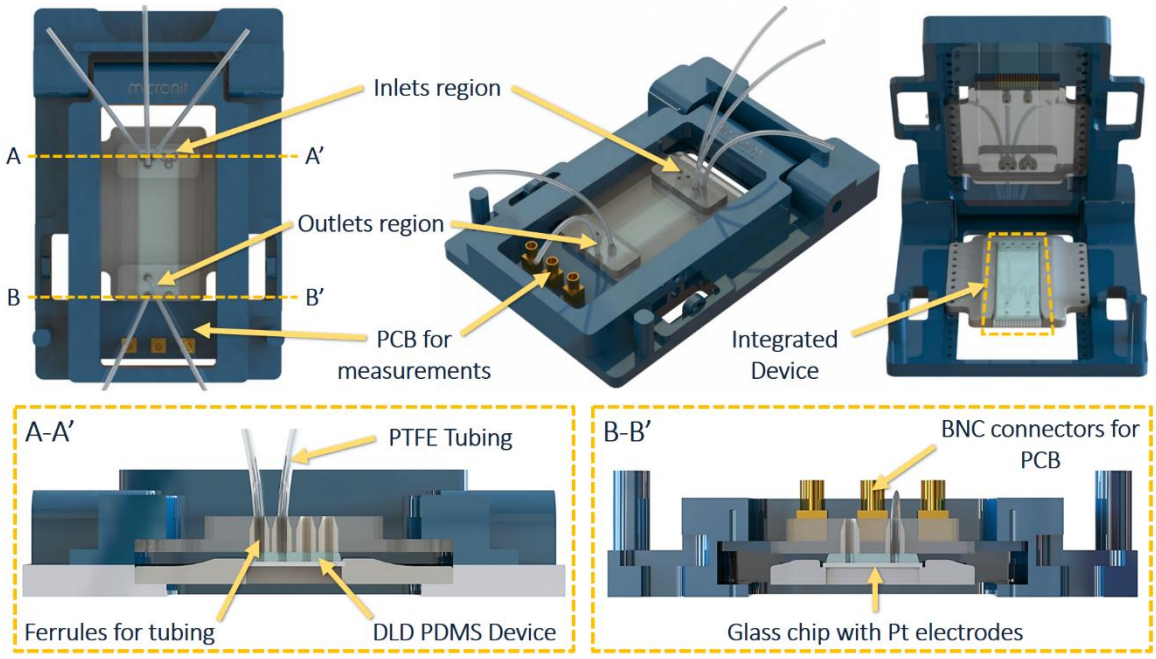


**Figure 6.26:** Concept CAD of the new integrated device setup incorporated in the FCP frame. Cross-sections of the inlets (A-A') and outlets (B-B') region are represented.

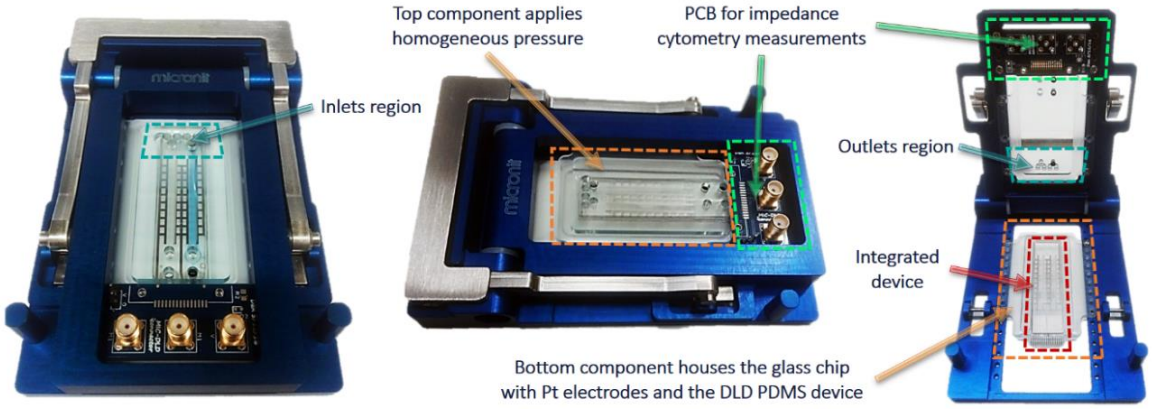


**Figure 6.27:** Photographs of the integrated device experimental setup incorporated in the FCP frame. The bottom component houses the impedance cytometry glass chip and the DLD PDMS device. By closing the frame, the top component applies homogenous pressure to clamp and seal the integrated device. Openings for inlets and outlets are defined at the top component. The PCB for impedance cytometry measurements is also integrated into the frame.

After fabrication of the components and incorporation into the FCP frame - **Figure 6.27**, the new setup was tested by running PBS at various pressures (**Figure 6.28**). The flow rate at the outlet region was measured with a Flow Rate Platform (Fluigent, France). A linear fit ($R^2$ = 0.9788) to the data indicated that the integrated device gave a steady response to the increasing pressure (as expected) and was capable of withstanding pressures up to 1 bar without any leaks or changes to the flow rate. The FCP frame permitted the application of consistent pressure along the

device and drastically reduced the occurrence of leaks during experiments. After experiments, the frame could be opened, the devices easily removed and, if needed, substituted by a new, ready-to-use device. These capabilities simplified the lengthy and complex preparation and clamping processes, making this a feasible setup to implement in future experiments.

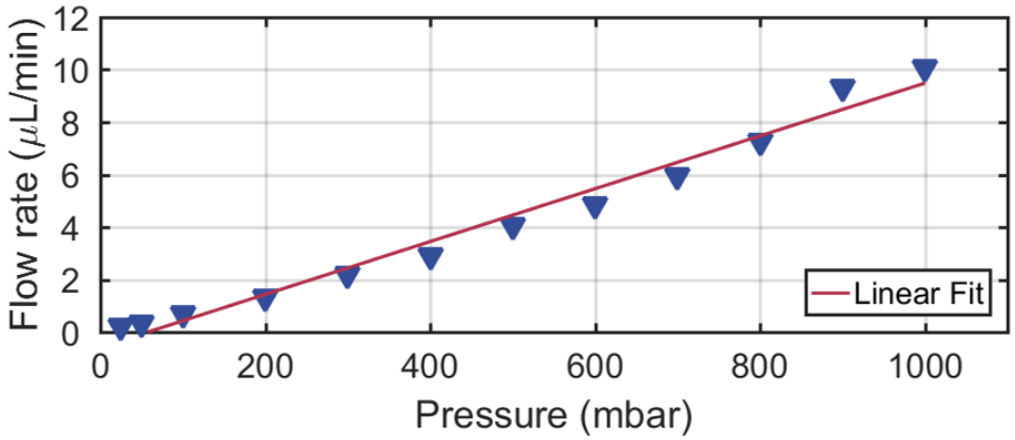


**Figure 6.28:** Plot of flow rate (μL/min) versus pressure (mbar) applied at the sample inlet. A linear fit ($R^2$ = 0.9788) was applied to the data, showing the direct relationship between pressure applied and flow rate at the measurement outlet.

## 6.5 Sorting and Dielectric Analysis of Blood-dwelling Parasitic Protozoa

### 6.5.1 Motivation

Human African trypanosomiasis (HAT) is a fatal parasitic disease endemic to sub-Saharan Africa. It is caused by parasitic protozoa of the *Trypanosoma brucei* subgroup, which are transmitted by the tsetse fly (Barrett *et al.*, 2003). Upon infection, parasites first proliferate in the haemolymphatic system of infected patients (stage 1 of the disease). In stage 2, the parasites invade the central nervous system, causing increased neurological dysfunction. This gives the characteristic changes in the sleep-wake patterns of patients and gives rise to the common name of disease - sleeping sickness. **Figure 6.29** represents a simplified version of the parasite life cycle.

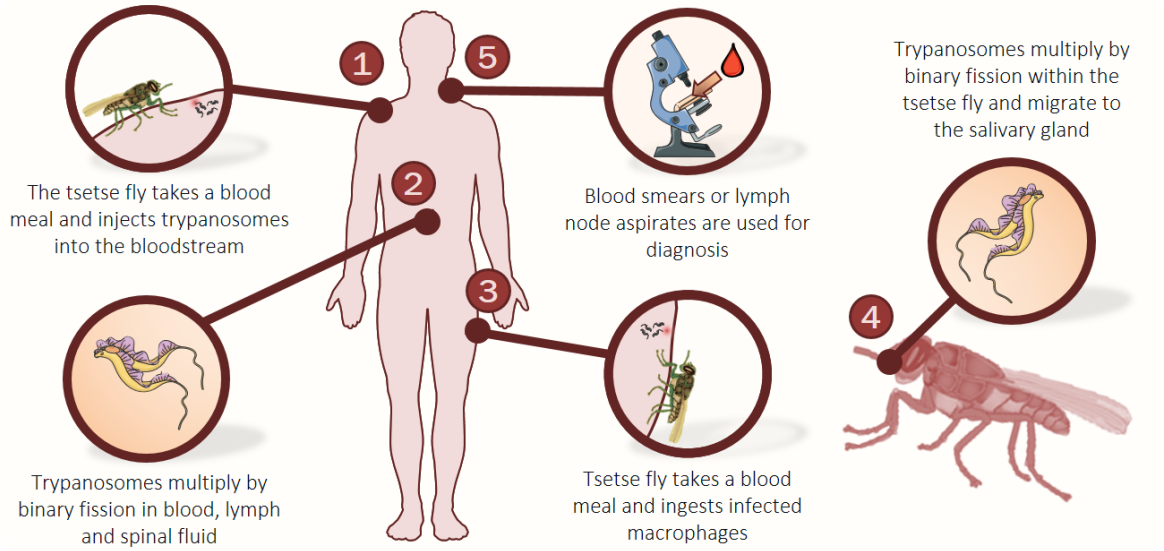


**Figure 6.29:** Representation of the *Trypanosoma* spp. life-cycle in the human host and tsetse fly vector, and the common diagnosis method. This includes: 1 – injection of trypanosomes into the host by a tsetse-fly; 2 – parasite multiplication by binary fission; 3 – ingestion of parasites by a tsetse fly; 4 – release of trypanosomes into the tsetse fly, further multiplication and migration to salivary glands for future invasions; 5 –diagnosis using microscopy, the current "gold-standard" method, to detect infected macrophages in a blood smear or a lymph aspirated sample.

The standard HAT diagnosis still relies on arduous and time-consuming microscopic detection of single parasites within blood smears or lymph node aspirates (Rosenblatt, 2009). Besides the obvious drawbacks of being a lengthy procedure requiring trained technicians, microscopy-based diagnosis has the major disadvantage of struggling when low numbers of parasites are present. Microscopic diagnosis typically has a detection threshold of approximately 10,000 parasites/mL, significantly higher than the lowest parasitaemia level of 100 parasites/mL (Chappuis *et al.*, 2005). The low abundance of parasites in blood has led to development of other technologies (*e.g.,* ion exchange chromatography or centrifugation) to concentrate parasites prior to microscopic inspection (Chappuis *et al.*, 2005). Nonetheless, these are expensive and complex tools, which limit their applicability in the field.

Microfluidic techniques have been proposed as possible alternatives for isolation of trypanosomes, including DEP and DLD - for an overview of these approaches see Barrett *et al.* (Barrett *et al.*, 2017). Following the promising results obtained with DLD separation (Holm *et al.*, 2011, 2016), an Impedance Cytometry-integrated DLD system (IC-DLD) was be developed to enrich and identify parasites without microscopic inspection, thus addressing some of the limitations of current

technologies. The integrated system combines the high-resolution size and shape-based cell sorting of DLD with the label-free single cell counting and analysis capability of MIC. A sample de-complexing step performed by the DLD array removes the majority of RBCs from the detection/analysis region. This step is crucial for impedance cytometry, as individual signals cannot be acquired in the extremely high concentrations of blood cells found in non-sorted samples, rendering detection impracticable. With integrated DLD and MIC, separation and counting can be performed in one step, without the need for microscopes and with better discriminating power.

### 6.5.2 Integrated System Design

The causative pathogens of HAT comprise a taxonomic group that includes subspecies both infectious and non-infectious to man. Given the risks and regulatory constraints associated with working with *T. brucei*, the proof-of-concept experiments were confined to the parasite *T. cyclops*, which has been used as a model system in previous separation studies (Holm *et al.*, 2011, 2016).

The approximate dimensions of a *T. cyclops* parasite are compared with a RBC in **Figure 6.30a**. Previous trypanosomes separation studies have showed that non-spherical particles can be oriented in DLD devices so that they present different dimensions to the device, thus appearing to have different hydrodynamic sizes (**Figure 6.30b**) (Holm *et al.*, 2011, 2016). By tailoring the device depth, the orientation of particles can be controlled and the differences in shape between RBCs and parasites accentuated for improved separation. For shallow devices (depth < 7.5 μm), RBCs orientate such that their largest size (diameter) interacts with the posts, presenting an effective size similar to that of trypanosomes. However, for deeper devices (depth > 7.5 μm), RBCs interact with the pillar and rotate such that the thickness defines effective size defines their hydrodynamic size, which is smaller than the trypanosome's effective size, rendering separation possible. The device used in this work has a depth of ~8.8 – 9.0 μm. At this depth the effective size of the parasites is maximized while the effective size of the RBCs is minimized, allowing for maximum separation. Moreover, a shallow device should minimize/eliminate the occurrence of inertial focusing (observed in the previous integrated device – **Section 6.4.4.2**) (Di Carlo, 2009; Di Carlo *et al.*, 2009; Hur *et al.*, 2011; Spencer and Morgan, 2011). Furthermore, the electric field in shallower devices is almost uniform when compared with deeper devices. Thus, no positional dependence compensation will be required in this case.

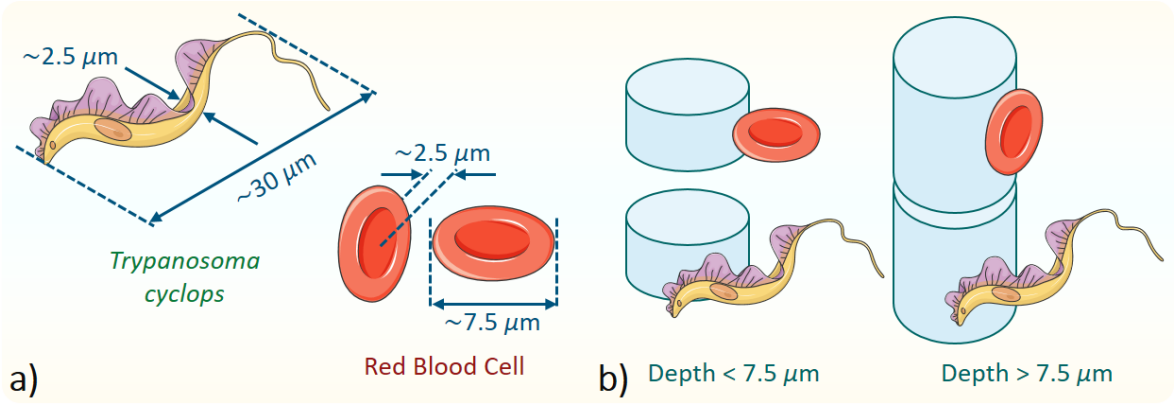


**Figure 6.30: a)** Approximate dimensions of *T. cyclops* parasites and RBCs. **b)** Schematic of how orientation changes the effective size of particles of different shape. RBCs and trypanosomes have distinct shape and dimensions. In a shallow device, RBCs have an effective size corresponding to their diameter, which is similar to the trypanosomes effective size. In a deeper device, RBCs rotate and have a smaller effective size, permitting sorting between parasites and RBCs.

The IC-DLD device design is shown in **Figure 6.31**. The device was designed to process blood with low concentration of parasites and to perform enrichment of parasites free of any contaminating blood cells. The device had three independent inlets: a central inlet for sample, and two side inlets for sheath flow. Each inlet branches into multiple individual inlet channels at the entrance of the DLD device, resulting in an overall ratio of sample to sheath of 40:24. At each inlet there is filter comprising of an array of posts separated by 12 μm, to remove any large debris or cells clusters that would block the main DLD array. The separation post array was designed to displace the enriched target cells to the channel walls, creating an enriched stream at both sides of the device. The design is mirrored design which minimises the migration distance of cells to the nearest wall, doubling throughput (Lubbersen, Boom and Schutyser, 2014). Sheath flow at each side is used to ensure the sample flows in the centre of the device, and the sides of the device will be free of non-displaced cells. As previously described, the device was fabricated with a depth of ~8.8 – 9.0 μm, which causes RBCs to rotate and behave like particles of effective size 2.5 μm while trypanosomes move in such a way that their effective size is larger. The critical diameter of the device was defined as $D_c$ = 3.5 μm (with $G$ =12 μm and a post diameter of 20 μm). In principle, only trypanosomes are displaced and collected at the outlet channels. The outlet region is a 4:56 ratio of collection channels (channels 1, 2, 59 and 60, for trypanosomes) to waste channels (channels 3 to 58, for RBCs). The collection outlet directs the trypanosomes to the impedance detection region for identification.

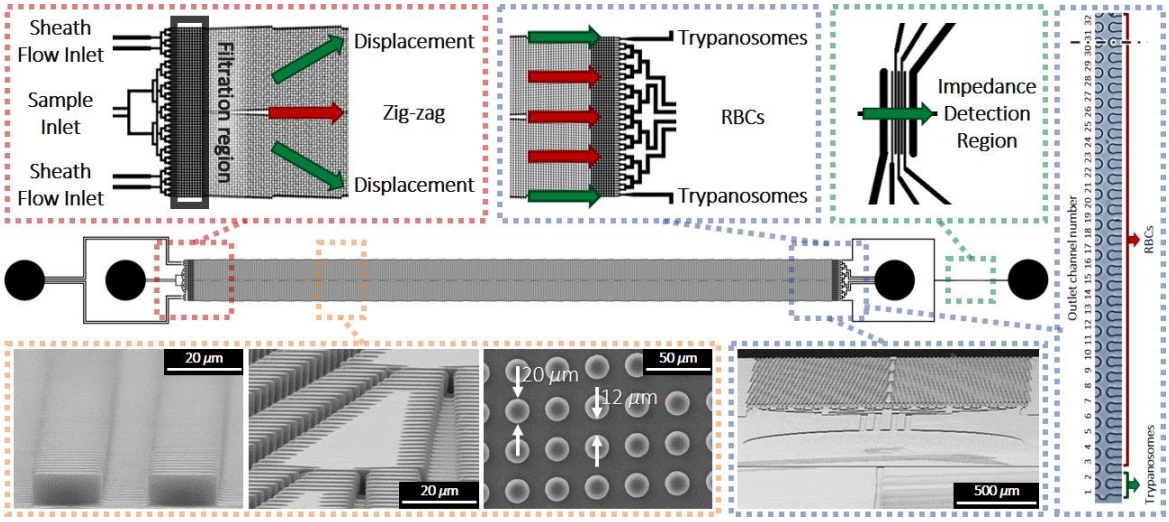


**Figure 6.31:** Schematic overview of the IC-DLD device. Particles enter the device through a central inlet, bounded by sheath flow inlets. A filtration region removes large debris and cells clusters at the start of the device. Cells larger than the critical diameter are laterally displaced towards the channel walls. Displaced target cells are collected at the outlet region and directed to the impedance detection region, where single cells are measured and counted. SEM micrographs of relevant features of a PDMS device are also presented.

The integrated system concept can be found in **Figure 6.32a**. The system was implemented using the previously presented Fluidic Connect PRO frame (Micronit, Enschede, The Netherlands). Custom pieces were designed in SolidWorks (Dassault Systèmes, Vélizy-Villacoublay, France) and fabricated from polystyrene. The bottom component housed the glass chip for impedance cytometry and the DLD PDMS device.

The PDMS devices were oxygen plasma bonded to the glass chips. The bonding process allowed full adhesion between substrates during experiments but was reversed after overnight immersion of bonded devices in 99.7% ethanol. After alignment between these two parts, the frame was closed, applying homogenous pressure across the device and sealing it. A printed circuit board was designed to integrate into the frame and connect to the electrode pads, apply the AC signal, and measure the differential signal. After each experiment, the frame was opened, the DLD device was removed, and if needed substituted by a new device. This reduced the complexity of the system and the turnaround time between experiments. The experimental setup is shown in **Figure 6.32b**.

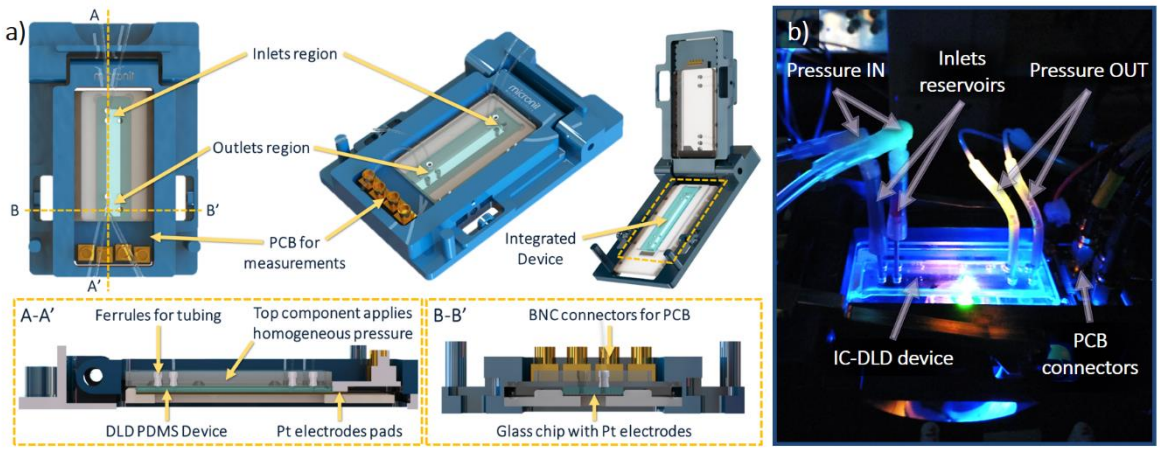


**Figure 6.32: a)** Concept CAD of the IC-DLD integrated device setup incorporated in the FCP frame. The different holder parts, the integrated device and the printed circuit board (PCB) for impedance cytometry were designed to fit the frame. A cross-section along the frame (A-A') shows how all the parts and the integrated device fit within the frame. A cross-section of the outlets region (B-B') is also represented. **b)** Photograph of the IC-DLD setup during an experiment. PEEK tubing, lined with silicon tubing, was used as inlets reservoirs. The inlets and outlets were then coupled to the pressure control system.

### 6.5.3 Experimental Methods

#### 6.5.3.1 Device fabrication

The fabrication details of the IC-DLD electrode-patterned glass chips also followed previously reported procedures (**Section 6.4.1**). Electrodes for impedance detection (30 µm width and separated by 10 µm) were patterned on the glass wafer (**Figure 6.33a**). Individual chips were then diced from the wafer. Fabrication of the soft lithography master and PDMS devices (**Figure 6.33b**) followed the protocols previously reported (**Section 6.4.1**). CleWin5 (WieWeb Software, Hengelo, the Netherlands) was used to draw the photolithographic masks.

#### 6.5.3.2 Experimental setup

To prevent cell adhesion in the devices, a solution of 1% Pluronics in 1x PBS (Pluronic F-127, Sigma-Aldrich, Merck KGaA, Darmstadt, Germany) was introduced immediately after the bonding and clamping process. The solution was allowed to rest for 30 min before flushing with Cunningham's medium15 for another 30 min. PEEK tubing (1.5 mm inner diameter), lined with silicon tubing (5 mm inner diameter) was connected to the device via a pressure controller (MFCS-EZ, Fluigent, Paris, France). Individual pressures were controlled to attain a balanced sample stream. The pressures used were: sample inlet = 500 ± 50 mbar; sheath flow inlets = 500 ± 100 mbar; waste outlets = -800 ± 100 mbar; collection outlets = -500 ±

300 mbar (N = 9). Different pressures at the outlets were used to attain a balanced throughput and properly focused streams at the outlet region.

In MIC measurements with standard chips to characterise cells prior to the integrated DLD-mic system (parallel measurement), sinusoidal voltages at two frequencies (500 kHz and 5 MHz) were applied to both top electrodes, with impedance data acquired as described previously. In IC-DLD impedance measurements (co-planar), the printed circuit board for impedance cytometry measurements was connected to the impedance spectroscope and lock-in amplifier (HF2FLI, Zurich Instruments). Sinusoidal voltages at the two fixed frequencies (500 kHz and 5 MHz) were applied to the central electrode. The differential signal was acquired from the two side measurement electrodes, with the real and imaginary parts of the signal, at each frequency, being stored for data analysis.

Videos and still images were collected using an inverted Nikon Eclipse TE2000-U microscope (Nikon Corporation, Tokyo, Japan) and a Andor iXon EMCCD camera (Andor Technology, Belfast, Northern Ireland). Differential Interference Contrast (DIC) was used to ensure adequate contrast of blood cells and trypanosomes.

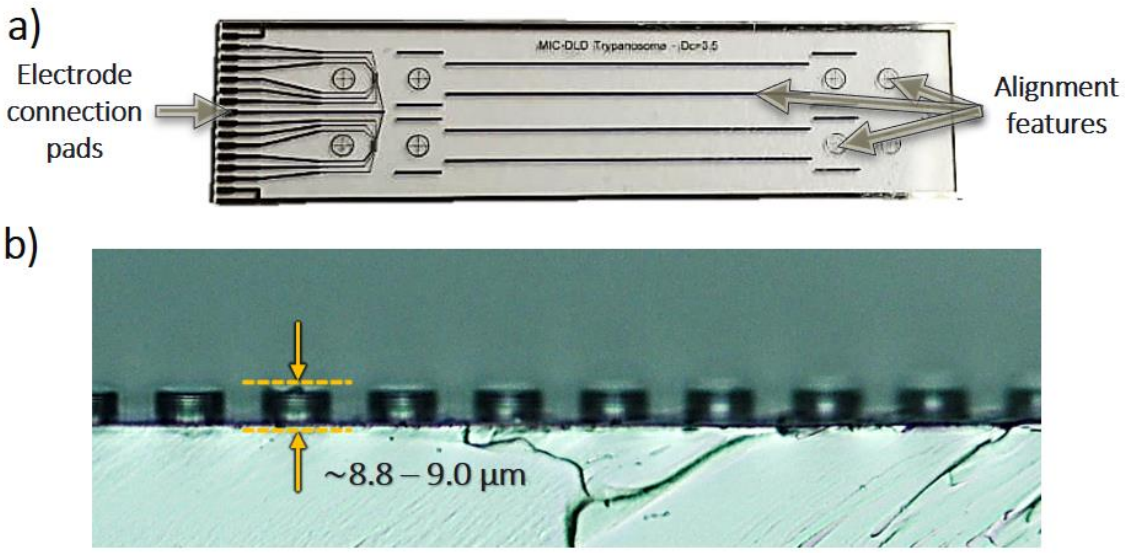


**Figure 6.33: a)** Photograph of the IC-DLD glass chip with platinum electrodes. **b)** Micrograph of a DLD device cross-section.

#### 6.5.3.3 Sample preparation

The *Trypansoma cyclops* parasites used were kindly supplied by Prof. Michael Barrett, from the University of Glasgow. Culturing of parasites, sample maintenance and preparation were performed by Clément Regnault, from the University of Glasgow. *T. cyclops* parasites were stored at -80 ˚C in 10% dimethyl sulfoxide (DMSO, Fluka, St Louis, MO, USA). After thawing, trypanosomes were incubated in Cunningham's medium with 20% Fetal Calf Serum (FCS, Sigma-Aldrich, St Louis, MO, USA) at 28 ˚C allowing the parasites to proliferate (Cunningham, 1977). Blood samples were extracted *via* finger pricking (Haemolance, MedCore AB, Kista, Sweden) of healthy volunteers from which informed consent was obtained. Samples were diluted 20× in AutoMACS running buffer (Miltenyi Biotech, Auburn, CA, USA) to facilitate particle tracking. Because blood serum is known to lyse *T. cyclops* (Weinman, 1972), serum was removed and blood cells were resuspended in AutoMACS.

For DLD-only experiments to test the separation array preformance, 500× and 50× diluted blood samples were mixed with trypanosomes at ~1,500 cells/μL; while for IC-DLD experiments, 20× diluted blood samples were spiked with trypanosomes at ~500 cells/μL and ~50 cells/μL. The suspending medium was a 50:50 mixture of AutoMACS running buffer and Cunningham's medium. For MIC-only experiments, trypanosomes and RBCs were re-suspended in Cunningham's medium to a final concentration of ~1,500 cells/μL and ~500 cells/μL, respectively. Polystyrene beads (7 μm diameter) were also added as reference particles to a final concentration of 100 beads/μL.

#### 6.5.3.4 Data analysis

The lateral distributions of cells were characterized at the outlets of the device through analysis of videos. This was performed by Dr. Stefan Holm, from Lund University. A particle tracking algorithm, custom written in Matlab (The MathWorks, Natick, MA, USA) was used to quantify the distribution of RBCs in blood samples (Holm *et al.*, 2016). While this allowed for the correct quantification of a large number of cells, it was not able to discriminate between different cell types. Consequently to quantify mixed samples manual counting was employed.

Impedance cytometry data was processed and analysed using a custom script written in Matlab. For MIC measurements, the signal from reference beads was used to normalise impedance data; while for IC-DLD measurements, the signal from the RBCs was used instead. Results are represented as mean ± standard deviation

unless otherwise stated. To identify the positions of equal probability deviation between two clusters, as previously implemented (**Section 4.3.2**). The intersection of the equivalent confidence ellipses (1×, 2× and 3× standard deviation) defined the boundary where a data point has equal probability of belonging to either population. A line of equal probability deviation was then fitted to the points of intersection.

### 6.5.4 Impedance Analysis of Trypanosomes

Prior to experiments with the IC-DLD system, samples containing trypanosomes and RBCs were measured with the standard MIC system (Spencer *et al.*, 2016; McGrath *et al.*, 2017; Xavier *et al.*, 2017), to qualitatively determine the dielectric behaviour of trypanosomes. The process of population identification is summarized in **Figure 6.34**. Firstly, the impedance data was plotted using the reference frequency (500 kHz) (data not shown) and the data normalized against the 7 µm reference beads. In addition to the bead population, two other populations can be observed; one that corresponds to the RBCs and the another the trypanosomes. Gates were generated to define these three populations (**Figure 6.34a**). Impedance scatter plots were generated of size versus opacity; again three populations were identified and a second set of gates drawn (**Figure 6.34b**). The final scatter plot and population definition was attained by intersecting the two sets of gates for the three different populations (**Figure 6.34c**). This intersection gives more confidence to the gating process, as mislabelled events in one of the gates will be removed from the final group of events.

The mean sizes of the cell populations were: RBCs = 5.71 ± 0.02 µm; and trypanosomes = 3.97 ± 0.01 µm (N = 3), based on the electrical data. By approximating the particles to a sphere, the estimated volumes of each population were: RBCs = 97 ± 1 fL; and trypanosomes = 33 ± 1 fL (N = 3) (see **Figure 6.34d**). These volumes obtained are similar to values found in literature: RBCs = 80-96 fL (Vajpayee, Graham and Bem, 2011) and trypanosomes = 16 – 33 fL (Webster and Griffithst, 1994). The estimated mean size of RBCs (~5.7 µm) was used in IC-DLD experiments for normalization of all data. Furthermore, the MIC data showed that RBCs and trypanosomes have clear differences in membrane dielectric properties. The opacity data shows clear discrimination between the two cell populations. The mean normalized opacities of the cells populations were: RBCs = 0.78 ± 0.01 and trypanosomes = 0.96 ± 0.07 (N = 3) - these differences were exploited in the IC-DLD experiments.

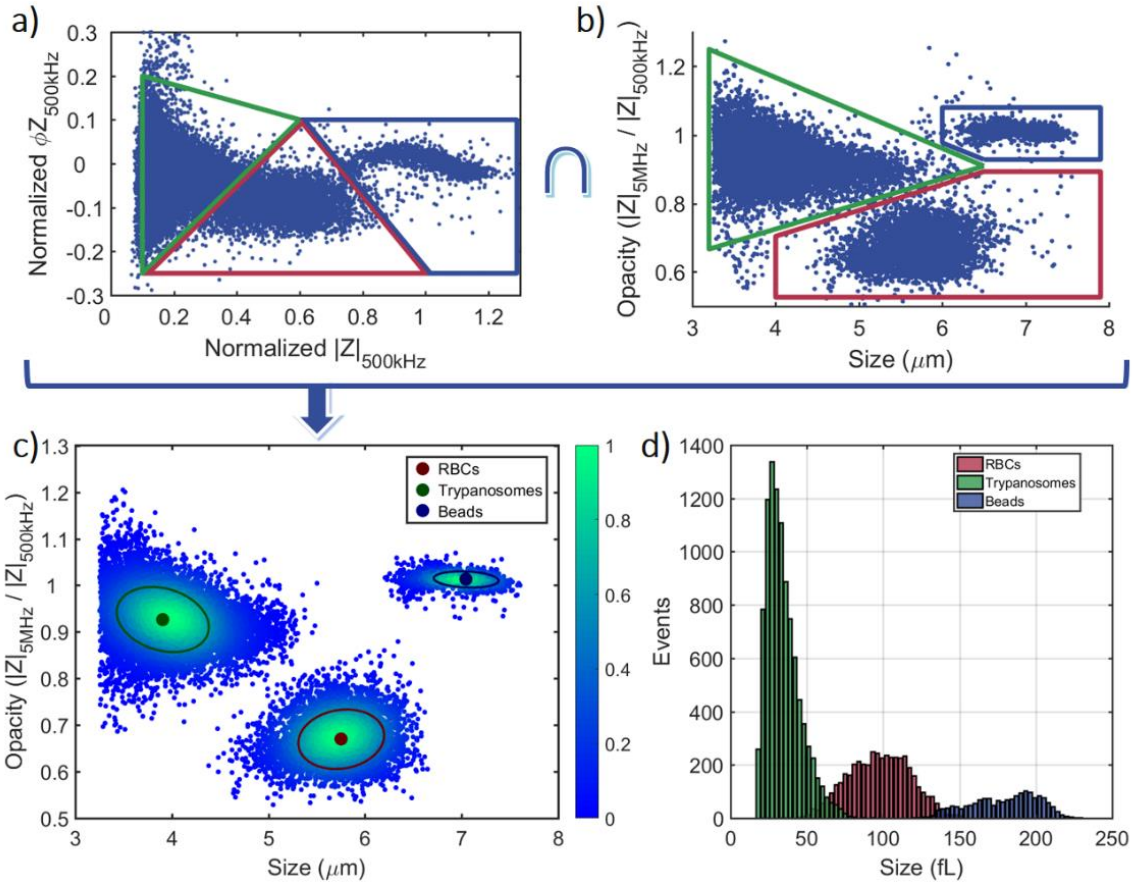


**Figure 6.34:** Gating process for the identification of cell populations using MIC data. **a)** Normalized impedance scatter plot (magnitude |Z| versus phase ΦZ), at the reference frequency (500 kHz), of a sample containing RBCs and trypanosomes, mixed with reference beads. The first set of gates is defined in this scatter plot. **b)** Impedance scatter plot of size (µm) versus opacity (magnitude at 5 MHz - $|Z|_{5MHz}$ over magnitude at 500 kHz - $|Z|_{500kHz}$). The second set of gates is defined in this scatter plot. **c)** Impedance scatter plot of size (µm) versus opacity (magnitude at 5 MHz - $|Z|_{5MHz}$ over magnitude at 500 kHz - $|Z|_{500kHz}$) of the gates intersection. The three particle populations are identified. Density represents the probability of an event belonging to the corresponding population. Ellipses containing 50% of each population together with the mean (●) are also indicated. **d)** Histogram of electrical size (fL) of the three particle populations.

### 6.5.5 DLD Separation Efficiency

The sorting capability of the DLD device was evaluated using spiked human blood (500× and 50× blood dilutions; trypanosomes at ~1,500 cells/µL). The distribution of each cell population along the outlet region and the sorting efficiency of the device is presented in **Figure 6.35**. Individual particles were identified and tracked at the outlet region as shown in **Figure 6.35a**, which is combined image of the tracks taken by RBCs (in red) and trypanosomes (in green) at the end of the device for one experiments (N = 140 total cells counted). The figure show approximately

half of the device. Due to the mirrored conformation of the array to increase throughput, identical effects were observed in the other half. Single cell tracking of each cell type at each outlet channel was quantified for diluted blood samples - **Figure 6.35b**. The data demonstrates that outlets channels 1 and 2 contain the majority of all displaced trypanosomes, with only a small number of outliers seen in the other outlet channels. Platelets are mostly found at outlets channels 2 to 10, while most of the RBCs are distributed along the waste channels (3 to 30). Interestingly, despite the trypanosomes being considerably smaller electrical size/volume than the RBCS, they displace more, highlighting the importance of morphology on DLD sorting.

Repeated measurements enabled calculation of the fraction of the population displaced towards the collection outlet for each cell type, as shown in **Figure 6.35c**. From the population of RBCs counted (N = 501 cells for 3 samples at 500× dilution; N = 524 cells for 3 samples at 50× dilution), only 3.1 ± 0.3% (N = 3 samples at 500× dilution) and 3.6 ± 1.0% (N = 3 samples at 50× dilution) were displaced to the collection outlet. For the trypanosomes, 91.3 ± 2.4% (from 245 cells counted; N = 3 samples at 500× dilution) and 95.7 ± 3.0% (from 51 cells counted; N = 3 samples at 50× dilution) were displaced to the collection outlet. These fractions represent an enrichment of approximately 30× when comparing trypanosomes and RBCs percentages, for both cases. Furthermore, the removal of ~96.7 ± 0.8% (N = 6 samples) of RBCs to the waste outlets indicates high specificity in the sorting process. The device also presented high separation sensitivity, with ~93.5 ± 3.5% (N = 6 samples) of trypanosomes being displaced to the collection outlet.

The presence of platelets was also observed (N = 63 cells for 3 samples at 500× dilution; N = 18 cells for 3 samples at 50× dilution), with 65.8 ± 30% (N = 3 samples at 500× dilution) and 60.2 ± 40% (N = 3 samples at 50× dilution) exiting through the collection outlet. The high variation in the fractions obtained for this cell type is explained by two factors. First, the low numbers counted mean that the percentage varies depending on the displacement of only a few cells. Second, the fact that many of the observed platelets were non-spherical and irregular in shape, or sometimes clustered or adhering to debris altered their effective size and leading to displacement into the collection outlet. As for other blood cells, such as leukocytes, their size (usually >10μm) and low numbers meant that virtually all of them are stuck immediately at the inlet and filtration regions. Thus, no other cell types were observed at the outlets of the IC-DLD device. Therefore, the DLD array proved to be effective at the removal of the majority of RBCs, decomplexing the sample and enriching for trypanosomes.

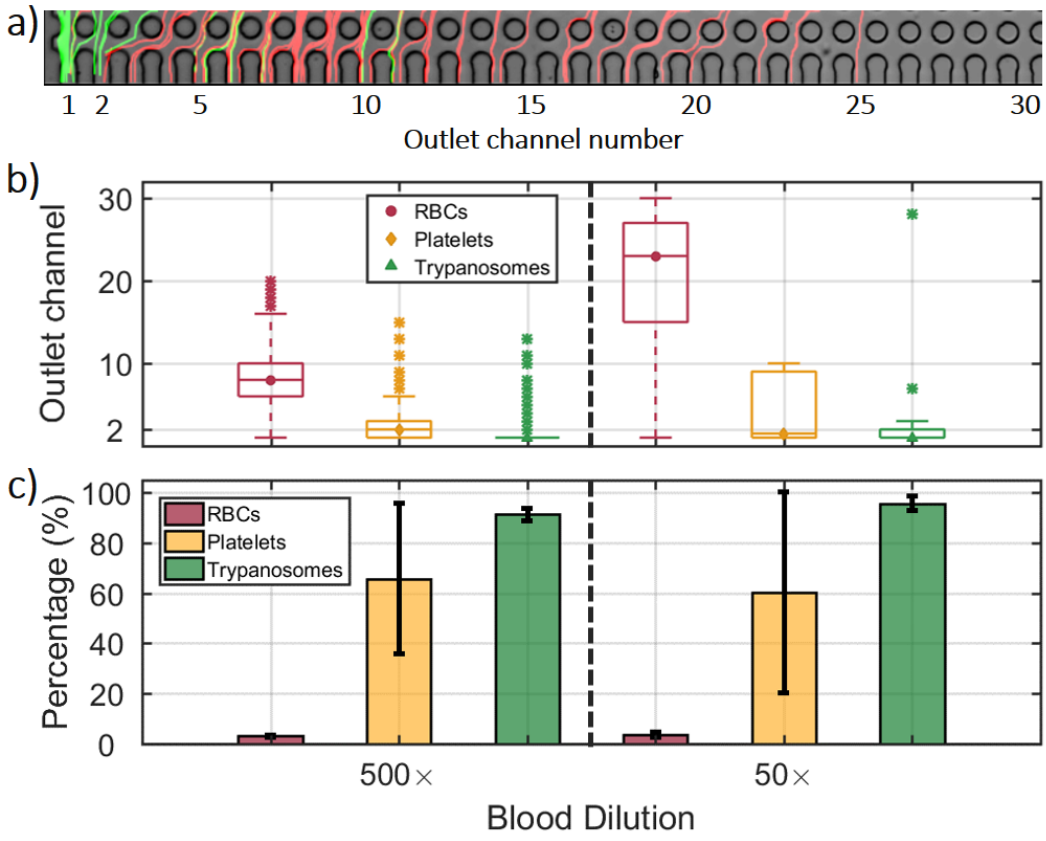


**Figure 6.35: a)** Combined micrograph of video frames of the outlet region for a sample of 500× diluted blood spiked with trypanosomes. Pathways taken by RBCs (red) and trypanosomes (green) at the outlet region are represented. **b)** Distribution of each cell population (RBCs, platelets and trypanosomes) at the outlet region, for the two blood dilutions tested (500× and 50×; N = 3 samples per dilution). The central line of each boxplots represents the median, with the box edges representing 25$^{th}$ and 75$^{th}$ percentiles, whiskers represent data within 3× standard deviation and individual markers represent outliers. **c)** Fraction sorted to the collection outlet for each cell population (RBCs, platelets and trypanosomes), for the two blood dilutions tested (500× and 50×; N = 3 samples per dilution).

### 6.5.6 Integrated Separation and Readout

The integrated impedance cytometry analysis was tested with 20× diluted blood spiked with trypanosomes (at 500 cells/µL and 50 cells/µL). The impedance data was plotted using the reference frequency (500 kHz) normalized against the RBCs population (reference polystyrene beads not used in IC-DLD experiments). Three cell populations were identified and gated: RBCs, trypanosomes and platelets (**Figure 6.36a**)

Impedance scatter plots were generated from opacity vs electrical size, and new gates used to define the three populations (**Figure 6.36b**). Size estimation was based on the mean size of RBCs (~5.7 µm) calculated previously from experiments with the standard MIC system. The intersection of these gates gives a more accurate

identification of the different cell populations (**Figure 6.36c**). Data was acquired for 3 minutes for each sample, with a throughput of ~18 ± 12 cells per second (N = 6 samples) at the detection region.

Control samples of 20× diluted blood, with no trypanosomes, were also tested. As expected, individual cell tracking revealed that the DLD process effectively removes the majority of RBCs and platelets from the collection outlet (outlet channels 1 and 2) (**Figure 6.37a**). Using the impedance data analysis protocol, the RBC and platelets populations were also clearly identified (**Figure 6.37b**). The presence of virtually no events within the trypanosomes gate in the control samples tested (N = 3 samples) confirms that the trypanosomes identified in non-control samples correspond to the enriched parasites.

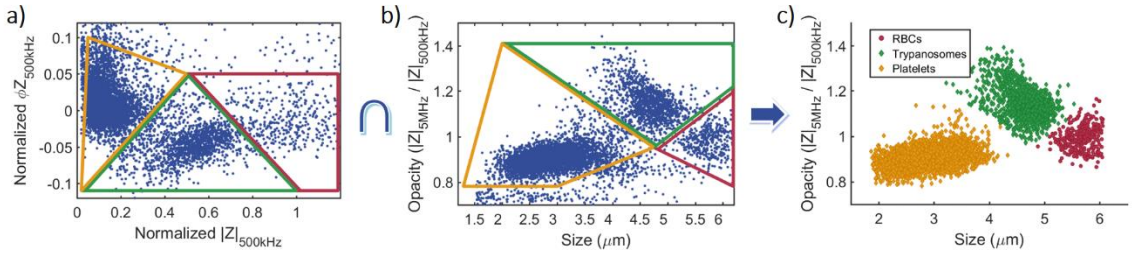


**Figure 6.36:** Gating process for the identification of cell populations using impedance cytometry data on IC-DLD experiments. **a)** Normalized impedance scatter plot (magnitude |Z| versus phase ΦZ), at the reference frequency (500 kHz), of a 20× diluted blood sample spiked with trypanosomes at 500 cells/µL. The first set of gates is defined in this scatter plot. **b)** Impedance scatter plot of size (µm) versus opacity (magnitude at 5 MHz - $|Z|_{5MHz}$ over magnitude at 500 kHz - $|Z|_{500kHz}$). The second set of gates is defined in this scatter plot. **c)** Intersection of gates identifies the three cell populations: RBCs, trypanosomes and platelets.

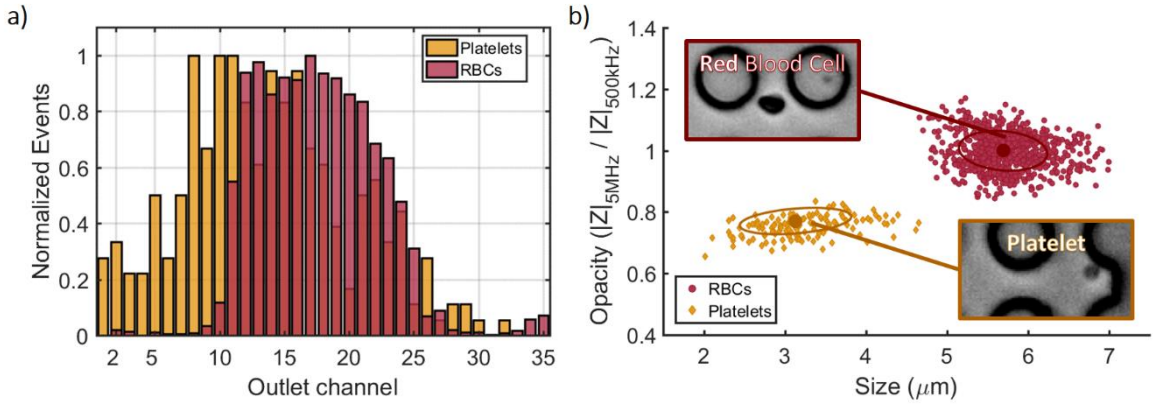


**Figure 6.37: a)** Distributions of platelets and RBCs at the outlet region for a control sample (20× diluted blood sample). **b)** Impedance scatter plot of size (µm) versus opacity (magnitude at 5 MHz - $|Z|_{5MHz}$ over magnitude at 500 kHz - $|Z|_{500kHz}$) of a control sample (20× diluted blood sample). Inserts show micrographs of identified cells within the device. Ellipses containing 50% of each population together with the mean (●) are also indicated.

In order to increase the confidence in the identification process, a refined gating process was executed using previously implemented thresholds of equal probability between different populations (**Section 4.3.2**) (van Berkel *et al.*, 2011; McGrath *et al.*, 2017). Using the thresholds of equal probability, optimal gates were determined for each cell population. Details on the generation of these thresholds are also detailed in **Figure 6.38**.

**Figure 6.39** shows the final thresholds between the trypanosomes population and the RBCs/platelets populations (for one of the 20× diluted blood samples spiked with trypanosomes at 500 cells/µL - **Figure 6.39a**, and at 50 cells/µL **Figure 6.39b**). With refined gates for each sample, the percentages of each cell population in the analysed samples were calculated (**Table 6.3**). By comparing the percentages at the sample inlet and the collection outlet, the enrichment numbers for each cell type were also calculated (**Table 6.3** and **Figure 6.40**).

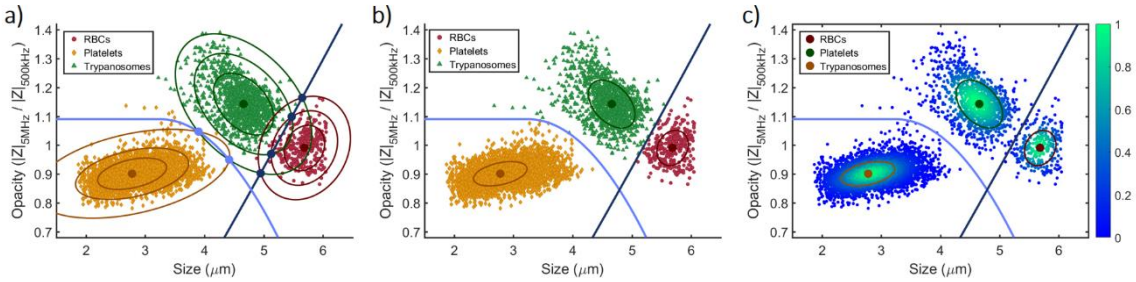


**Figure 6.38:** Refined gating process for the identification of cell populations using impedance cytometry data on IC-DLD experiments. Impedance scatter plots of size (µm) versus opacity (magnitude at 5 MHz - $|Z|_{5MHz}$ over magnitude at 500 kHz - $|Z|_{500kHz}$) of a 20× diluted blood sample spiked with trypanosomes at 500 cells/µL were used. **a)** Based on the 2-D Gaussian distribution of single populations, confidence ellipses containing events within 1×, 2× and 3× standard deviations of the mean were plotted. The intersection of equivalent confidence ellipses identifies the positions of equal probability deviation between two clusters. **b)** Thresholds of equal probability deviation, *i.e.*, the boundaries where a data point has equal probability of belonging to either population, are then fitted to the points of intersection. These lines define the final gates for cell population identification. **c)** Density scatter plot of size versus opacity, with density representing the probability of an event belonging to the corresponding population. Ellipses containing 50% of each population together with the mean (●) are also indicated.

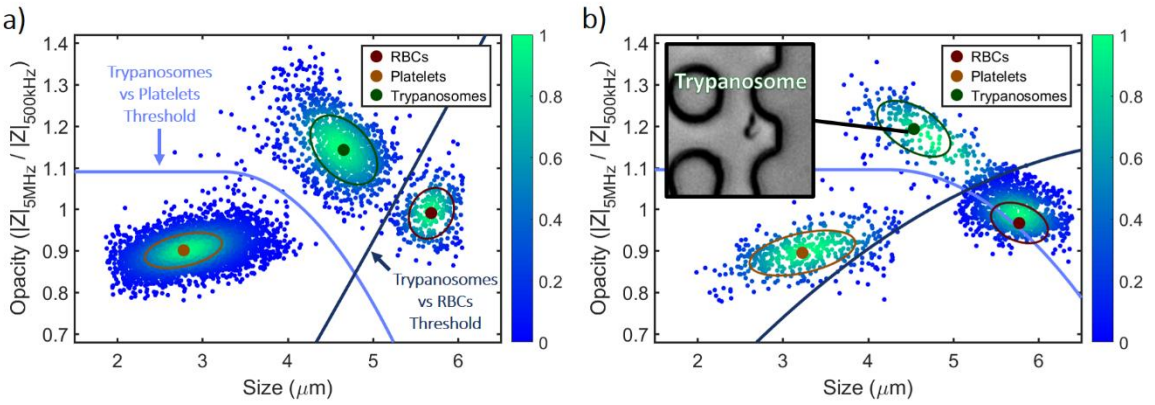


**Figure 6.39:** Density scatter plots of size (μm) versus opacity (magnitude at 5 MHz - $|Z|_{5MHz}$ over magnitude at 500 kHz - $|Z|_{500kHz}$) of 20× diluted blood samples spiked with trypanosomes at **a)** 500 cells/μL and **b)** 50 cells/μL. Density represents the probability of an event belonging to the corresponding population. Gates between populations were defined as thresholds of equal probability. Ellipses containing 50% of each population together with the mean (●) are also indicated. Insert in **b)** shows a micrograph of a trypanosome within the device.

The effective removal of RBCs from the enriched sample is clear for samples with trypanosomes at 500 cells/μL, with RBCs accounting for less than 10% of the identified cells. For samples at 50 trypanosomes/μL, RBCs are more evident. Furthermore, as previously seen in **Figure 6.35** and **Figure 6.37a**, a considerable amount of platelets were displaced towards the collection outlet. The majority of the parasites were concentrated in the collection outlet, with enrichment of ~160 and ~800 for samples with 500 trypanosomes/μL and 50 trypanosomes/μL.

The numbers obtained confirm that the integrated system was capable of effective decomplexing of blood samples containing trypanosomes, and separating and discriminating parasites based on their dielectric properties. By removing the majority of blood cells from the positive target sample outlet, an impedance-based identification of single cells was possible. If for example the separation process was incomplete or ineffective, the overwhelming presence of RBCs and other blood cells at the measurement region would result in multiple cells traversing the electrodes area at the same time, making any meaningful identification of parasites extremely difficult. Furthermore, the high separation sensitivity observed and promising high enrichment numbers obtained suggest that the system should be able to properly enrich and identify parasites, even in cases of the low parasitaemia levels currently limiting standard microscopy diagnosis.

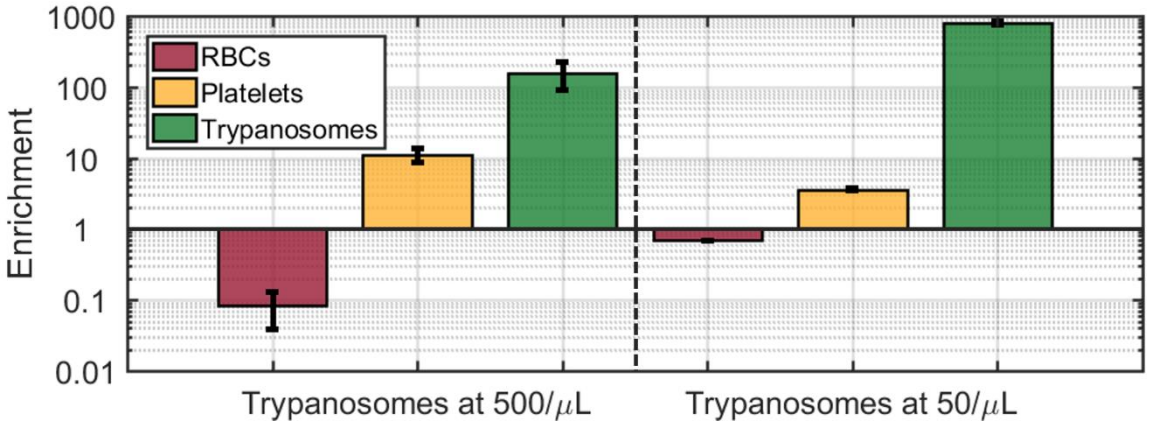


**Figure 6.40:** Enrichment numbers for 20× diluted blood samples spiked with trypanosomes at 500 cells/μL and 50 cells/μL (N = 3 samples per dilution). Error bars represent 1× standard deviation for each cell population. The enrichment number relates to the percentage of each cell type at the collection outlet versus its theoretical percentage at the sample inlet.

**Table 6.3:** Percentages at sample inlet and at collection outlet for the identified cell populations. The enrichment number, *i.e.*, the comparison between the percentages at the collection outlet versus its theoretical percentage at sample inlet, is also presented for each cell population.

| Samples | Sample Inlet (%) | | | Collection Outlet (%) | | | Enrichment (Outlet % vs Inlet %) | | |
|---|---|---|---|---|---|---|---|---|---|
| | RBCs | Platelets | Trypanosomes | RBCs | Platelets | Trypanosomes | RBCs | Platelets | Trypanosomes |
| Trypanosomes at 500/μL | 94.16 | 5.65 | 0.19 | 7.81 | 45.44 | 46.75 | 0.08 | 8.04 | 248 |
| | 94.16 | 5.65 | 0.19 | 12.32 | 62.67 | 25.01 | 0.13 | 11.09 | 133 |
| | 94.16 | 5.65 | 0.19 | 4.16 | 79.31 | 16.53 | 0.04 | 14.04 | 88 |
| **Mean** | 94.16 | 5.65 | 0.19 | 8.10 ± 3.34 | 62.48 ± 13.83 | 29.43 ± 12.73 | 0.09 ± 0.04 | 11.06 ± 2.45 | 156 ± 68 |
| Trypanosomes at 50/μL | 94.32 | 5.66 | 0.02 | 63.44 | 20.21 | 16.35 | 0.67 | 3.57 | 867 |
| | 94.32 | 5.66 | 0.02 | 64.66 | 20.04 | 15.30 | 0.69 | 3.54 | 811 |
| | 94.32 | 5.66 | 0.02 | 65.07 | 20.98 | 13.95 | 0.69 | 3.71 | 740 |
| **Mean** | 94.32 | 5.66 | 0.02 | 64.39 ± 0.69 | 20.41 ± 0.41 | 15.20 ± 0.98 | 0.68 ± 0.01 | 3.61 ± 0.07 | 806 ± 52 |

## 6.6 Summary

The integration of single cell sorting and identification was accomplished, with the design, development and optimization of the novel integrated system described in this chapter. Exploring the high-resolution size and shape-based cell sorting capabilities of DLD, a new integrated system was developed with the inclusion of AC electrokinetics capabilities through DEP and MIC integration. Cells could in theory, be sorted based not only on size but also their dielectric properties, with the cells of interest counted and analysed as they are sorted.

The inclusion of DEP in the integrated system was first demonstrated. Experiments with yeast cells and polystyrene beads, performed in a static environment, showed that these particles were amenable to DEP forces, following modelled behaviour. Beads in a buffer of low conductivity ($\sigma$ = 3 mS/m) moved from a random distribution to specific positions corresponding to nDEP behaviour regardless of the applied frequency; while yeast cells, in a different buffer ($\sigma$ = 20 mS/m), went from nDEP to pDEP as the applied signal frequency increased. Experiments were also conducted with *E. coli* bacteria suspended in a buffer of high conductivity ($\sigma$ = 180 mS/m). As expected from modelled behaviour, *E. coli* was concentrated due to nDEP forces for low frequency signals, while a weak pDEP force trapped a fraction of cells in-between the posts for high frequency signals.

The MIC capability of the integrated device was initially tested with two sets of beads with sizes below and above the device critical diameter. The sorting efficiency was assessed first by optical flow cytometry and compared with impedance cytometry measurements on the integrated device. The integrated device showed a high efficiency in separation, with approximately 97% of smaller beads being collected at the appropriate outlet. Overall, the results indicated that the identification and counting process with the integrated MIC technology was as reliable as the standard optical flow cytometry method.

However, the acquired impedance data revealed that, due to inertial focusing at the outlet region, the same type of beads were measured as two independent populations differing in size. This was due to the known particle positional dependence of impedance cytometers using co-planar electrode conformations. A new positional correction algorithm was thus developed. Measurements conducted with beads of various sizes (1.5 to 10 μm) were successfully corrected, with the corrected size estimation in accordance to the expected size. The integrated system was also further optimized, being re-designed to simplify both fabrication

and operational procedures. By integrating all components in a holding frame and clamping the different pieces together, PDMS DLD devices were easily fabricated and replaced when needed (reducing the turnaround time between experiments). This is an important aspect for future field diagnosis tools, as a reusable system would minimize production costs.

With an optimized experimental system, a revised integrated device was designed to perform separation and enrichment of blood dwelling parasites (*T. cyclops*) from a diluted blood sample background. MIC technology was again integrated as a post-separation analysis tool, enabling single cell counting and identification of sorted cells. The device had an optimal depth of ~9.0 µm, permitting the separation of parasites from other cells. With this integrated system, separation and counting in a single device with improved discrimination power was possible, eliminating the need for post-sorting analysis (*e.g.* with optical flow cytometry) for parasite quantification.

Experiments showed a high specificity in the separation process, with the removal of ~97% of RBCs from the enriched sample. In addition, the presence of ~94% of all trypanosomes at the collection outlet indicated high separation sensitivity. By defining thresholds of equal probability between the cells populations found in the analysed samples, it was possible to confidently quantify each cell type at the enriched sample. It was calculated that, compared with theoretical initial values at the sample inlet, trypanosomes were enriched up to 800×. This indicates that the integrated system might match the limit of detection of current microscopy-based methods (approximately 10,000 parasites/mL); and even cope with the cases of low parasitaemia (as low as 100 parasites/mL) found in the field, being capable of enriching and identifying any parasite present in sample.

# Chapter 7

# Conclusions and Future Direction

This work describes label-free methods for analysis, characterization and sorting of rare particles. Rare particles of interest included human pathogens (or pathogen-infected cells) such as waterborne pathogenic protozoa, malaria parasite-infected red blood cells, leishmania parasite-infected macrophages and blood dwelling parasites (trypanosomes). This chapter summarises the achievements and highlights further opportunities for development of label-free, integrated devices towards sample-to-answer systems for PoC field detection.

Microfluidic impedance cytometry is a powerful tool to analyse the dielectric properties of single particles at high throughput. This technique was used to determine whether different cell characteristics (*e.g.*, size or dielectric properties) and conditions (*e.g.*, viability, species or parasitization) could be used as an alternative detection method based on impedance data.

The water-borne protozoan *Cryptosporidium parvum* was the first analysed pathogen recurring to MIC (**Chapter 4**). The impedance data of *C. parvum* oocysts of varying source, strain and age were measured. The impedance of untreated and heat-inactivated oocysts (modelling natural loss of viability) was measured in buffers of different conductivity. Current standard detection techniques do not confer any species-level information or viability status of recovered pathogens. However, when suspended in higher conductivity buffer (5× PBS), results showed a high degree of discrimination (over 90%). The proposed hypothesis for this optimal discrimination at high conductivity is based on the loss of ion transfer regulation capability by heat-treated, *i.e.*, non-viable, parasites. With their ion regulation compromised, an inward flux of ions from the buffer to the oocyst ensues. This effect is detectable by MIC, as this technique is capable of probing different layers of the oocyst structure depending on the frequency used. By applying high frequency (~50 MHz) signals, a clear electrical “contrast” between the internal

properties of untreated and heat-inactivated oocysts was observed, making discrimination possible.

In addition, measurements were performed on other water-borne protozoan species suspended in 1× PBS. Species discrimination is not possible with standard detection techniques. Using impedance data from both low and high frequencies (thus probing both size and internal properties), discrimination between pathogenic (*C. parvum* and *Giardia lamblia*) and non-pathogenic (*C. muris*) species was observed at high level (>93%). Besides *C. parvum*, other species, such as *C. hominis* or *C. meleagridis* have been associated with human infection, representing together over 90% of human cases of cryptosporidiosis (Bouzid *et al.*, 2013; Chalmers and Katzer, 2013). All these major human-pathogenic species have similarities in their shape and size (~ 4.0-5.0 × 5.0-5.5 µm) (Chalmers and Katzer, 2013), suggesting that MIC may be able to discriminate these from other species outside this size range that pose little to no risk to human health (*e.g.*, *C. andersoni*, *C.muris* or the smaller *C. xiaoi* and *C. ryanae*).

For a future widespread application of this technique in water monitoring and in-field facilities, the suitability of MIC for discrimination of viability and species must be first assessed using environmental samples. If suitable, MIC technology could potentially be useful for water utilities in, for example, a warning system which more rapidly identifies single pathogenic (oo)cysts in a standard post-recovery sample. As demonstrated, the system can simultaneously provide an indication of the viability and species of recovered (oo)cysts, which may reduce the requirement for skilled microscopists and the associated labour demands.

MIC technology was also used to analyse two of the most life-threatening human parasitic diseases: human malaria and leishmaniasis **(Chapter 5**). In both cases, intracellular parasites (*Plasmodium falciparum* and *Leishmania mexicana*, respectively) invade host cells (RBCs and macrophages, respectively), in order to replicate and produce new parasites. To independently discriminate infected from non-infected cells, parasites that constitutively express GFP were used in the MIC measurements. GFP fluorescence could then work as reference in the measurements, confirming the identification of target parasites. To detect fluorescence signals, a novel portable fluoresce-coupled MIC system was developed (**Chapter 3**). A portable system could be set-up in any scenario or location (such as a biological safety cabinet), allowing for its utilization in the restricted environments where experiments with human pathogens must take place.

Experiments showed that discrimination between malaria parasite-infected RBCs and uninfected RBCs was found to not be possible using impedance data alone. This was especially evident at the early stages of invasion, the point where standard diagnosis takes place. Thus, an impedance-based detection tool for *P. falciparum*-infected RBCs seems to be ruled out as an alternative.

Nonetheless a full dielectric characterisation of uninfected and infected RBCs along the invasion process was achieved. Maxwell's mixture theory and multi-shell models were used and refined using uninfected cells data. A simple spherical model was implemented for normal and sphered RBCs, revealing the need for a more suitable model for non-spherical RBCs. An ellipsoid model was then developed and tested on control samples and uninfected cells. The estimated dielectric properties were in agreement with accepted values for RBCs, confirming its feasibility as a modelling solution.

For the parasite-infected RBCs alterations of the host cell and parasite during the invasion process required the implementation of two models: an ellipsoid model for early-stage infected cells and a spherical model for late-stage infected cells. The estimated dielectric properties indicated significant alterations to the infected RBC membrane capacitance, appearing as early as 12 h post-invasion and increasing along the time-course of invasion. As a consequence of these membrane alterations, there was an increase in ion exchange activity between the intra- and extra-cellular regions of host cells, resulting in a higher cytoplasm conductivity when compared with control and uninfected RBCs. In addition, no significant volumetric changes were observed between uninfected and infected RBCs. In contrast, the parasite growth during the time-course of invasion was clearly detected, occupying less than 10% for early stages (≤ 18 hpi), but reaching around 90% for later stages (36 and 42 hpi).

These biophysical changes could possibly be exploited in other label-free AC electrokinetics technique such as DEP. With a limited applicability for the cases of *P. falciparum*-infected RBCs, this technique could maybe be promising for other *Plasmodium* species (such as *P. vivax*) where diagnosis during the early-stage of invasion (first 24 h) is less critical. Future experiments should then focus on the impedance analysis and dielectric characterization of other *Plasmodium* species parasitized cells. Upon these studies, a DEP-based enrichment device could be created, permitting the separation of infected cells from the remaining background. The addition of such a pre-enrichment step prior to impedance or microscopy detection, for example, would make it possible to increase the

sensitivity of existing "*gold-standard*" diagnostic methods (currently ~50 parasites/μL).

As for the dielectric analysis of leishmania parasite-infected macrophages, no major alterations in the biophysical properties were observed between uninfected and infected cells at different activation states measured along the parasite intra-cellular life cycle every day post-invasion. Results showed small differences in size or membrane properties for infected cells in the M0 and M1 state; while M2 infected cells presented a small degree of alteration. However, these differences were not statistically assessed and could be not significant. Therefore, future work should focus on repeating these experiments before a conclusion could be made regarding the feasibility of using AC electrokinetics-based analysis and sorting as a future detection alternative.

This thesis concluded with the design, development and optimization of a novel integrated system combining label-free single cell sorting and identification (**Chapter 6**). Size- and shape-based sorting was performed using DLD. Electrodes for AC electrokinetics were integrated to enhance the system through DEP. Electrodes for MIC was also integrated for particle identification, removing the necessity of post-experimental offline analysis. Experiments with integrated DEP showed that static particles within the device were responsive to DEP forces. Experiments with *E. coli* bacteria conducted in a buffer of high conductivity revealed that, at low frequency, nDEP forces concentrated cells, while at high frequencies a weak pDEP force trapped a fraction of cells in-between the posts. These results could be explored for the enrichment of human pathogenic bacteria in a future integrated device by specifically influencing the displacement of bacteria during a DLD-based enrichment step. Nonetheless, further studies are required to confirm whether observed DEP forces would suffice to displace particles under high flow pressure; and if other electrokinetics effects, such as electro-osmosis or electrophoresis, would interfere in the movement of particles.

Experiments with integrated MIC showed that identification and counting process with integrated impedance cytometry was as reliable as the standard optical flow cytometry method. Integrated devices showed a high efficiency in separation of beads of various sizes, with ~97% of smaller particles being collected at the appropriate outlet. However, inertial focusing at the outlet region resulted in measurement errors due to the positional dependence of impedance cytometers using co-planar electrode conformations. A novel algorithm was thus developed to correct the system positional dependence, solving a common issue found in

impedance cytometers. Furthermore, the integrated system was re-designed to include all components in a holding frame and clamping the different pieces together. The new system design simplified fabrication and operational procedures, making use of simple replica moulded parts. PDMS DLD devices could be easily replaced when needed, while the more expensive MIC glass chips could be reused. This not only reduced the overall costs and the turnaround time between experiments, but rendered the system portable, making it usable in the field.

A revised integrated device was designed to perform enrichment of *T. cyclops*, a blood dwelling human parasite, from diluted blood samples and to identify sorted cells. The device was fabricated to an optimal depth of ~9.0 μm, inducing orientation of both parasites and RBCs to maximise separation. Results showed a high sensitivity in the separation process, with the presence of ~94% of all trypanosomes at the collection outlet. Moreover, the removal of ~97% of RBCs from the enriched sample indicated high separation specificity. It was also calculated that, compared with theoretical initial values at the sample inlet, trypanosomes were enriched up to 800×, suggesting that, in cases of low parasitaemia commonly found in the field, the integrated system could be a valuable alternative. Further tests should focus on clinical samples, ideally with whole blood or less diluted samples at low parasitaemia levels. Whole blood/ less diluted samples would probably require a system of parallel DLD devices, capable of withstanding the larger volume of cells without clogging issues. Moreover, as separation was only demonstrated for *T. cyclops*, other strains of trypanosomes must also be tested.

Before an integrated separation and readout system can be used in the field for detection of trypanosomiasis there are still a few aspects to consider. Whilst the integrated device addresses many of the limitations with current detection techniques, further testing and optimization is required. One main aspect to revise is the fabrication process of devices. For example, DLD devices are commonly fabricated using soft lithography, which lacks the necessary scalability for in field use, while MIC chips are still only produced in small batches. This is a critical aspect of production, as large numbers of devices should be made available at low-cost for the usually resource scarce settings where parasitic diseases are found. Thus, different fabrication techniques (such as injection moulding) could be explored to cheaply mass-produce the devices. Finally, the experimental setup as a whole must be further simplified and rendered fully portable. This not only involves the creation of a portable setup for the electronics of the system, required for impedance data

acquisition, but also designing a simpler pressure controller system to drive the samples though the device.

In summary, label-free methods for analysis, characterization and sorting of rare particles were explored. Impedance cytometry was used to identify, discriminate and dielectrically characterize different human protozoan pathogens. A novel portable fluorescence-coupled impedance cytometry system was developed and used to confirm identification of pathogens. Furthermore, AC electrokinetics-based techniques for separation and analysis were integrated with single cell sorting in a custom system. For the first time DLD sorted particles were immediately detected and counted, avoiding the need for post-sorting offline analysis. In conclusion, microfluidic techniques for label free single cell sorting and analysis were explored, with novel systems designed and tested. Ultimately, by continuing to explore these different techniques, the next generation of systems would then be one-step closer to the ultimate goal of this project: to develop field-ready tools capable of performing point-of-care diagnosis and revolutionize the realm of diagnostics.

# References


Alvar, J. *et al.* (2012) 'Leishmaniasis worldwide and global estimates of its incidence', *PLoS ONE*, 7(5). doi: 10.1371/journal.pone.0035671.

Antfolk, M. and Laurell, T. (2017) 'Continuous flow microfluidic separation and processing of rare cells and bioparticles found in blood – A review', *Analytica Chimica Acta*. Elsevier Ltd, 965, pp. 9–35. doi: 10.1016/j.aca.2017.02.017.

Asami, K., Hanai, T. and Koizumi, N. (1980) 'Dielectric analysis of Escherichia coli suspensions in the light of the theory of interfacial polarization', *Biophysical Journal*, 31(2), pp. 215–228. doi: 10.1016/S0006-3495(80)85052-1.

Asami, K. and Yonezawa, T. (1995) 'Dielectric behavior of non-spherical cells in culture', *BBA - General Subjects*, 1245(3), pp. 317–324. doi: 10.1016/0304-4165(95)00116-6.

Athanassiou, G. A. *et al.* (2010) 'Red blood cell deformability in patients with human immunodeficiency virus infection', *European Journal of Clinical Microbiology and Infectious Diseases*, 29(7), pp. 845–849. doi: 10.1007/s10096-010-0936-9.

Au, S. H. *et al.* (2017) 'Microfluidic isolation of circulating tumor cell clusters by size and asymmetry', *Scientific Reports*. Springer US, 7(1), pp. 1–10. doi: 10.1038/s41598-017-01150-3.

Bannister, L. H. *et al.* (2000) 'A brief illustrated guide to the ultrastructure of Plasmodium falciparum asexual blood stages', *Parasitology Today*, 16(10), pp. 427–433. doi: 10.1016/S0169-4758(00)01755-5.

Barabino, G. A., Platt, M. O. and Kaul, D. K. (2010) 'Sickle Cell Biomechanics', *Annual Review of Biomedical Engineering*, 12(1), pp. 345–367. doi: 10.1146/annurev-bioeng-070909-105339.

Barrett, M. P. *et al.* (2017) 'Microfluidics-Based Approaches to the Isolation of African Trypanosomes', *Pathogens*, 6(4), p. 47. doi: 10.3390/pathogens6040047.

Bártfai, R. *et al.* (2010) 'H2A.Z demarcates intergenic regions of the Plasmodium falciparum epigenome that are dynamically marked by H3K9ac and H3K4me3', *PLoS Pathogens*, 6(12). doi: 10.1371/journal.ppat.1001223.

Baruch, D. I. (1999) 'Adhesive receptors on malaria-parasitized red cells', *Bailliere's Best Practice and Research in Clinical Haematology*, 12(4), pp. 747–761. doi: 10.1053/beha.1999.0051.

Bates, P. A. (2008) 'Europe PMC Funders Group Leishmania sand fly interaction : progress and challenges', *Current Opinion in Microbiology*, 11(4), pp. 340–344. doi: 10.1016/j.mib.2008.06.003.Leishmania.

Beck, M. *et al.* (2002) 'Improving stamps for 10 nm level wafer scale nanoimprint lithography', *Microelectronic Engineering*, 61–62, pp. 441–448. doi: 10.1016/S0167-9317(02)00464-1.

Beebe, D. J., Mensing, G. A. and Walker, G. M. (2002) 'Physics and Applications of Microfluidics in Biology', *Annual Review of Biomedical Engineering*, 4(1), pp. 261–286. doi: 10.1146/annurev.bioeng.4.112601.125916.

Beech, J. P. *et al.* (2012) 'Sorting cells by size, shape and deformability', *Lab on a Chip*, 12(6), p. 1048. doi: 10.1039/c2lc21083e.

Beech, J. P. *et al.* (2018) 'Separation of pathogenic bacteria by chain length', *Analytica Chimica Acta*, 1000, pp. 223–231. doi: 10.1016/j.aca.2017.11.050.

Beech, J. P., Jönsson, P. and Tegenfeldt, J. O. (2009) 'Tipping the balance of deterministic lateral displacement devices using dielectrophoresis.', *Lab on a chip*, 9(18), pp. 2698–2706. doi: 10.1039/b823275j.

Benazzi, G. *et al.* (2007) 'Discrimination and analysis of phytoplankton using a microfluidic cytometer', *IET nanobiotechnology*, 1(6), pp. 94–101. doi: 10.1049/iet-nbt.

Berendt, A. R., Ferguson, D. J. P. and Newbold, C. I. (1990) 'Sequestration in Plasmodium falciparum malaria: Sticky cells and sticky problems', *Parasitology Today*. Elsevier Current Trends,

6(8), pp. 247–254. doi: 10.1016/0169-4758(90)90184-6.

van Berkel, C. *et al.* (2011) 'Integrated systems for rapid point of care (PoC) blood cell analysis', *Lab on a Chip*, 11(7), p. 1249. doi: 10.1039/c0lc00587h.

Bern, C., Maguire, J. H. and Alvar, J. (2008) 'Complexities of assessing the disease burden attributable to leishmaniasis', *PLoS Neglected Tropical Diseases*, 2(10). doi: 10.1371/journal.pntd.0000313.

Bezuneh, A. *et al.* (2014) 'Comparison of point-of-care tests for the rapid diagnosis of visceral leishmaniasis in east African patients', *American Journal of Tropical Medicine and Hygiene*, 91(6), pp. 1109–1115. doi: 10.4269/ajtmh.13-0759.

Bhagat, A. A. S. *et al.* (2010) 'Microfluidics for cell separation', *Medical and Biological Engineering and Computing*, 48(10), pp. 999–1014. doi: 10.1007/s11517-010-0611-4.

Blewett, D. (1988) 'Proceedings of the First International Workshop on Cryptosporidiosis', in *Edinburgh: The Animal Disease Research Association*, pp. 85–95.

Blue Martin, A. *et al.* (2017) 'Development of a High-Throughput Magnetic Separation Device for Malaria-Infected Erythrocytes', *Annals of Biomedical Engineering*, 45(12), pp. 2888–2898. doi: 10.1007/s10439-017-1925-2.

Boeck, G. (2001) 'Current status of flow cytometry in cell and molecular biology.', *International review of cytology*, 204, pp. 239–98. Available at: http://www.ncbi.nlm.nih.gov/pubmed/11243596 (Accessed: 25 May 2018).

Van den Bossche, J., O'Neill, L. A. and Menon, D. (2017) 'Macrophage Immunometabolism: Where Are We (Going)?', *Trends in Immunology*. Elsevier Ltd, 38(6), pp. 395–406. doi: 10.1016/j.it.2017.03.001.

Bouzid, M. *et al.* (2013) 'Cryptosporidium pathogenicity and virulence', *Clinical Microbiology Reviews*, 26(1), pp. 115–134. doi: 10.1128/CMR.00076-12.

Bow, H. *et al.* (2011) 'A microfabricated deformability-based flow cytometer with application to malaria', *Lab Chip*, 11, pp. 1065–1073. doi: 10.1039/c0lc00472c.

Bridge, J. W. *et al.* (2010) 'Engaging with the water sector for public health benefits: Waterborne pathogens and diseases in developed countries', *Bulletin of the World Health Organization*, 88(11), pp. 873–875. doi: 10.2471/BLT.09.072512.

Bridle, H. *et al.* (2012) 'Detection of Cryptosporidium in miniaturised fluidic devices', *Water Research*, 46(6), pp. 1641–1661. doi: 10.1016/j.watres.2012.01.010.

Bridle, H., Miller, B. and Desmulliez, M. P. Y. (2014) 'Application of microfluidics in waterborne pathogen monitoring: A review', *Water Research*. Elsevier Ltd, 55(0), pp. 256–271. doi: 10.1016/j.watres.2014.01.061.

Bruus, H. (2008) *Theoretical Microfluidics*. Oxford University Press. doi: 10.1017/CBO9781107415324.004.

Burguillos, M. a. *et al.* (2013) 'Microchannel Acoustophoresis does not Impact Survival or Function of Microglia, Leukocytes or Tumor Cells', *PLoS ONE*, 8(5), pp. 1–11. doi: 10.1371/journal.pone.0064233.

Buszewski, B. *et al.* (2003) 'Separation of bacteria by capillary electrophoresis', *Journal of Separation Science*, 26(11), pp. 1045–1049. doi: 10.1002/jssc.200301442.

Di Carlo, D. *et al.* (2007) 'Continuous inertial focusing, ordering, and separation of particles in microchannels.', *Proceedings of the National Academy of Sciences of the United States of America*, 104(48), pp. 18892–18897. doi: 10.1073/pnas.0704958104.

Di Carlo, D. (2009) 'Inertial microfluidics.', *Lab on a chip*, 9(21), pp. 3038–3046. doi: 10.1039/b912547g.

Di Carlo, D. *et al.* (2009) 'Particle segregation and dynamics in confined flows', *Physical Review Letters*, 102(9), pp. 1–4. doi: 10.1103/PhysRevLett.102.094503.

Chalmers, R. M. and Katzer, F. (2013) 'Looking for Cryptosporidium: The application of advances in detection and diagnosis', *Trends in Parasitology*. Elsevier Ltd, 29(5), pp. 237–251. doi:

10.1016/j.pt.2013.03.001.

Chappuis, F. *et al.* (2005) 'Options for Field Diagnosis of Human African Trypanosomiasis', *Clinical Microbiology Reviews*, 18(1), pp. 133–146. doi: 10.1128/CMR.18.1.133.

Cheng, J. *et al.* (1998) 'Preparation and hybridization analysis of DNA/RNA from E. coli on microfabricated bioelectronic chips', *Nature biotechnology*, 16(June), pp. 541–546.

Chin, C. D. *et al.* (2011) 'Microfluidics-based diagnostics of infectious diseases in the developing world', *Nature Medicine*. Nature Publishing Group, 17(8), pp. 1015–1019. doi: 10.1038/nm.2408.

Costa, M. N. *et al.* (2014) 'A low cost, safe, disposable, rapid and self-sustainable paper-based platform for diagnostic testing: Lab-on-paper', *Nanotechnology*, 25(9). doi: 10.1088/0957-4484/25/9/094006.

Coulter, W. H. (1956) 'High speed automatic blood cell counter and size analyzer', in *Proc Natl Electron Conf*, pp. 1034–1040. doi: 10.1038/205820a0.

Cowman, A. F. *et al.* (2016) 'Malaria: Biology and Disease', *Cell*. Elsevier Inc., 167(3), pp. 610–624. doi: 10.1016/j.cell.2016.07.055.

Craighead, H. (2006) 'Future lab-on-a-chip technologies for interrogating individual molecules', *Nature*, 442(7101), pp. 387–393. doi: 10.1038/nature05061.

Cranston, H. A. *et al.* (1983) 'Plasmodium falciparum Maturation Abolishes Physiologic Red Cell Deformability', *Science*, 223, pp. 401–403.

Cunningham, I. (1977) 'New Culture Medium for Maintenance of Tsetse Tissues and Growth of Trypanosomatids', *The Journal of Protozoology*, 24(2), pp. 325–329. doi: 10.1111/j.1550-7408.1977.tb00987.x.

Dalton, C. *et al.* (2001) 'Parasite viability by electrorotation', *Colloids and Surfaces A: Physicochemical and Engineering Aspects*, 195(1–3), pp. 263–268. doi: 10.1016/S0927-7757(01)00850-0.

Dalton, C. *et al.* (2004) 'Analysis of parasites by electrorotation', *Journal of Applied Microbiology*, 96(1), pp. 24–32. doi: 10.1046/j.1365-2672.2003.02113.x.

Davies, A. P. and Chalmers, R. M. (2009) 'Cryptosporidiosis.', *BMJ (Clinical research ed.)*, 339(October), p. b4168. doi: 10.1136/bmj.b4168.

Davis, J. A. (2008) *Microfluidic Separation of Blood Components through Deterministic Lateral Displacement*, *PhD Thesis*. PhD Thesis, Princeton University.

Davis, J. a *et al.* (2006) 'Deterministic hydrodynamics: taking blood apart.', *Proceedings of the National Academy of Sciences of the United States of America*, 103(40), pp. 14779–14784. doi: 10.1073/pnas.0605967103.

Debye, P. and Falkenhagen, H. (1928) 'Dispersion of the Conductivity and Dielectric Constants of Strong Electrolytes', *Phys*, 29.

Desai, S. A., Bezrukov, S. M. and Zimmerberg, J. (2000) 'A voltage-dependent channel involved in nutrient uptake by red blood cells infected with the malaria parasite', *Nature*, 406(6799), pp. 1001–1005. doi: 10.1038/35023000.

Didar, T. F. and Tabrizian, M. (2010) 'Adhesion based detection, sorting and enrichment of cells in microfluidic Lab-on-Chip devices', *Lab on a Chip*, 10(22), p. 3043. doi: 10.1039/c0lc00130a.

Dijkshoorn, J. P. *et al.* (2017) 'Reducing the critical particle diameter in (highly) asymmetric sieve-based lateral displacement devices', *Scientific Reports*. Springer US, 7(1), pp. 1–10. doi: 10.1038/s41598-017-14391-z.

Dittrich, P. S. and Manz, A. (2006) 'Lab-on-a-chip: microfluidics in drug discovery', *Nature Reviews Drug Discovery*. Nature Publishing Group, 5, p. 210. Available at: http://dx.doi.org/10.1038/nrd1985.

Du, E. *et al.* (2013) 'Electric impedance microflow cytometry for characterization of cell disease states.', *Lab on a chip*, 13(19), pp. 3903–9. doi: 10.1039/c3lc50540e.

Elmahallawy, E. K. *et al.* (2014) 'Diagnosis of leishmaniasis', *Journal of Infection in Developing*

*Countries*, 8(8), pp. 961–972. doi: 10.3855/jidc.4310.

Errico, V. *et al.* (2017) 'Mitigating positional dependence in coplanar electrode Coulter-type microfluidic devices', *Sensors and Actuators, B: Chemical*. Elsevier B.V., 247, pp. 580–586. doi: 10.1016/j.snb.2017.03.035.

Esposito, A. *et al.* (2010) 'Quantitative imaging of human red blood cells infected with Plasmodium falciparum.', *Biophysical journal*. Biophysical Society, 99(3), pp. 953–60. doi: 10.1016/j.bpj.2010.04.065.

Fachin, F. *et al.* (2017) 'Monolithic Chip for High-throughput Blood Cell Depletion to Sort Rare Circulating Tumor Cells', *Scientific Reports*. Springer US, 7(1), pp. 1–11. doi: 10.1038/s41598-017-11119-x.

Fayer, R. (1994) 'Effect of High Temperature on Infectivity of Cryptosporidium parvum Oocysts in Water', *Applied and Environmental Microbiology*, 60(8), pp. 2732–2735.

Fayer, R. and Xiao, L. (2012) *Cryptosporidium and Cryptosporidiosis*. Second Edi. Taylor & Francis.

Fernandez, R. E. *et al.* (2017) 'Review: Microbial analysis in dielectrophoretic microfluidic systems', *Analytica Chimica Acta*. Elsevier Ltd, 966, pp. 11–33. doi: 10.1016/j.aca.2017.02.024.

Fuhr, G. *et al.* (1991) 'Asynchronous traveling-wave induced linear motion of living cells', *Stud Biophys*, 140(2), pp. 79–102.

Gascoyne, P. *et al.* (1997) 'Dielectrophoretic detection of changes in erythrocyte membranes following malarial infection', *Biochimica et Biophysica Acta*, 1323(2), pp. 240–252. doi: 10.1016/S0005-2736(96)00191-5.

Gascoyne, P. *et al.* (2002a) 'Microsample preparation by dielectrophoresis: isolation of malaria.', *Lab on a chip*, 2(2), pp. 70–5. doi: 10.1039/b110990c.

Gascoyne, P. *et al.* (2002b) 'Microsample preparation by dielectrophoresis: isolation of malaria.', *Lab on a chip*, 2(2), pp. 70–75. doi: 10.1039/b110990c.

Gascoyne, P. *et al.* (2004) 'Particle Impedance Sensor'. doi: 10.1016/j.(73).

Gascoyne, P. *et al.* (2013) 'Correlations between the Dielectric Properties and Exterior Morphology of Cells Revealed by Dielectrophoretic Field-Flow Fractionation', *Electrophoresis*, 34(7), pp. 1–20. doi: 10.1158/2326-6066.CIR-13-0034.PD-L1.

Gascoyne, P. R. C. and Shim, S. (2014) 'Isolation of circulating tumor cells by dielectrophoresis', *Cancers*, 6(1), pp. 545–579. doi: 10.3390/cancers6010545.

Gascoyne, P., Satayavivad, J. and Ruchirawat, M. (2004) 'Microfluidic approaches to malaria detection', *Acta tropica*, 89(3), pp. 357–369. doi: 10.1016/j.actatropica.2003.11.009.

Gawad, S., Schild, L. and Renaud, P. (2001) 'Micromachined impedance spectroscopy flow cytometer for cell analysis and particle sizing', *Lab on a Chip*, 1(1), p. 76. doi: 10.1039/b103933b.

Gimsa, J. *et al.* (1994) 'Dielectric spectroscopy of human erythrocytes: investigations under the influence of nystatin', *Biophysical Journal*, 66(4), pp. 1244–1253. doi: 10.1016/S0006-3495(94)80908-7.

Gimsa, J. *et al.* (1996) 'Dielectric spectroscopy of single human erythrocytes at physiological ionic strength: dispersion of the cytoplasm.', *Biophysical journal*, 71(1), pp. 495–506. doi: 10.1016/S0006-3495(96)79251-2.

Ginsburg, H. *et al.* (1985) 'Characterization of Permeation Pathways Appearing in the Host Membrane of Plasmodium Falciparum Infected Red Blood Cells', *Molecular and Biochemical Parasitology*, 14, pp. 313–322.

Ginsburg, H. and Stein, W. D. (2004) 'The New Permeability Pathways Induced by the Malaria Parasite in the Membrane of the Infected Erythrocyte: Comparison of Results Using Different Experimental Techniques', *Journal of Membrane Biology*, 197(2), pp. 113–122. doi: 10.1007/s00232-003-0646-7.

Goater, a D. and Pethig, R. (1998) 'Electrorotation and dielectrophoresis.', *Parasitology*, 117 Suppl, pp. S177–S189. doi: 10.1017/S0031182099004114.

Goater, A. D., Burt, J. P. H. and Pethig, R. (1997) 'A combined travelling wave dielectrophoresis and electrorotation device: applied to the concentration and viability determination of Cryptosporidium', *Journal of Physics D: Applied Physics*, 30, pp. L65–L69. doi: Doi 10.1088/0022-3727/30/18/001.

Gossett, D. R. *et al.* (2010) 'Label-free cell separation and sorting in microfluidic systems', *Analytical and Bioanalytical Chemistry*, 397(8), pp. 3249–3267. doi: 10.1007/s00216-010-3721-9.

Grützkau, A. and Radbruch, A. (2010) 'Small but mighty: How the MACS1-technology based on nanosized superparamagnetic particles has helped to analyze the immune system within the last 20 years', *Cytometry Part A*, 77(7), pp. 643–647. doi: 10.1002/cyto.a.20918.

Guo, Q. *et al.* (2016) 'Deformability based sorting of red blood cells improves diagnostic sensitivity for malaria caused by Plasmodium falciparum', *Lab Chip*. Royal Society of Chemistry, 16(4), pp. 645–54. doi: 10.1039/C5LC01248A.

Hackett, S. *et al.* (2009) 'Magnetic susceptibility of iron in malaria-infected red blood cells', *Biochimica et Biophysica Acta - Molecular Basis of Disease*, 1792(2), pp. 93–99. doi: 10.1016/j.bbadis.2008.11.001.

Hanai, T., Koizumi, N. and Irimajiri, A. (1975) 'A method for determining the dielectric constant and the conductivity of membrane-bounded particles of biological relevance', *Biophysics of Structure and Mechanism*, 1(4), pp. 285–294. doi: 10.1007/BF00537642.

Handayani, S. *et al.* (2009) 'High deformability of Plasmodium vivax-infected red blood cells under microfluidic conditions.', *The Journal of infectious diseases*, 199(3), pp. 445–450. doi: 10.1086/596048.

Hänscheid, T. and Grobusch, M. P. (2002) 'How useful is PCR in the diagnosis of malaria?', *Trends in Parasitology*, 18(9), pp. 395–398. doi: 10.1016/S1471-4922(02)02348-6.

Hanssen, E., McMillan, P. J. and Tilley, L. (2010) 'Cellular architecture of Plasmodium falciparum-infected erythrocytes', *International Journal for Parasitology*, 40(10), pp. 1127–1135. doi: 10.1016/j.ijpara.2010.04.012.

Hauke, G. (2008) *An Introduction to Fluid Mechanics and Transport Phenomena*. New York: Springer US.

Hawkes, J. J. and Coakley, W. T. (2001) 'Force field particle filter, combining ultrasound standing waves and laminar flow', *Sensors and Actuators, B: Chemical*, 75, pp. 213–222. doi: 10.1016/S0925-4005(01)00553-6.

Herricks, T., Antia, M. and Rathod, P. K. (2009) 'Deformability limits of Plasmodium falciparum - infected red blood cells', *Cellular Microbiology*, 11(9), pp. 1340–1353. doi: 10.1111/j.1462-5822.2009.01334.x.

Holm, S. H. *et al.* (2011) 'Separation of parasites from human blood using deterministic lateral displacement.', *Lab on a chip*, 11(7), pp. 1326–1332. doi: 10.1039/c0lc00560f.

Holm, S. H. *et al.* (2016) 'Simplifying microfluidic separation devices towards field-detection of blood parasites', *Anal. Methods*, 8(16), pp. 3291–3300. doi: 10.1039/C6AY00443A.

Holmes, D., She, J. K., *et al.* (2007) 'Bead-based immunoassays using a micro-chip flow cytometer.', *Lab on a chip*, 7(8), pp. 1048–1056. doi: 10.1039/b707507n.

Holmes, D., Sun, T., *et al.* (2007) 'Label-free differential leukocyte counts using a microfabricated, single-cell impedance spectrometer', *Proceedings of IEEE Sensors*, pp. 1452–1455. doi: 10.1109/ICSENS.2007.4388687.

Holmes, D. *et al.* (2009) 'Leukocyte analysis and differentiation using high speed microfluidic single cell impedance cytometry.', *Lab on a chip*, 9(20), pp. 2881–2889. doi: 10.1039/b910053a.

Holmes, D. *et al.* (2014) 'Separation of blood cells with differing deformability using deterministic lateral displacement(†).', *Interface focus*, 4(6), p. 20140011. doi: 10.1098/rsfs.2014.0011.

Holmes, D. and Morgan, H. (2010) 'Single cell impedance cytometry for identification and counting of CD4 T-cells in human blood using impedance labels', *Analytical Chemistry*, 82(4), pp. 1455–1461. doi: 10.1021/ac902568p.

Holzel, R. (1997) 'Electrorotation of Single Yeast Cells at Frequencies Between', *Biophysical Journal*, 73(February), pp. 1103–1109.

Hommel, M. (1999) 'Visceral leishmaniasis: Biology of the parasite', *Journal of Infection*, 39(2), pp. 101–111. doi: 10.1016/S0163-4453(99)90000-2.

Hondroulis, E. *et al.* (2017) 'A droplet-merging platform for comparative functional analysis of m1 and m2 macrophages in response to *e. coli* -induced stimuli', *Biotechnology and Bioengineering*, 114(3), pp. 705–709. doi: 10.1002/bit.26196.

Hotez, P. J. *et al.* (2007) 'Control of Neglected Tropical Diseases', *The New England Journal of Medicine*, 357, pp. 1018–1027. doi: 10.1056/NEJMra064142.

Hou, H. W. *et al.* (2010) 'Deformability based cell margination--a simple microfluidic design for malaria-infected erythrocyte separation.', *Lab on a chip*, 10(19), pp. 2605–2613. doi: 10.1039/c003873c.

Hou, H. W. *et al.* (2013) 'Isolation and retrieval of circulating tumor cells using centrifugal forces.', *Scientific reports*, 3, p. 1259. doi: 10.1038/srep01259.

Houssin, T. *et al.* (2010) 'Label-free analysis of water-polluting parasite by electrochemical impedance spectroscopy', *Biosensors and Bioelectronics*, 25(5), pp. 1122–1129. doi: 10.1016/j.bios.2009.09.039.

Hsiao, L. L. *et al.* (1991) 'Modification of host cell membrane lipid composition by the intraerythrocytic human malaria parasite Plasmodium faciparum', *Biochem. J*, 274, pp. 121–132. doi: 10.1042/bj2740121.

Huang, L. *et al.* (2017) 'Microfluidics cell sample preparation for analysis: Advances in efficient cell enrichment and precise single cell capture', *Biomicrofluidics*, 11(1). doi: 10.1063/1.4975666.

Huang, L. R. *et al.* (2004) 'Continuous particle separation through deterministic lateral displacement.', *Science (New York, N.Y.)*, 304(5673), pp. 987–990. doi: 10.1126/science.1094567.

Huang, Y. *et al.* (1992) 'Differences in the AC electrodynamics of viable and non-viable yeast cells determined through combined dielectrophoresis and electrorotation studies.', *Physics in medicine and biology*, 37(7), pp. 1499–1517. doi: 10.1088/0031-9155/37/7/003.

Huang, Y. and Pethig, R. (1991) 'Electrode design for negative dielectrophoresis', *Measurement Science and Technology*, 2, pp. 11142–1146.

Hur, S. C. *et al.* (2011) 'Deformability-based cell classification and enrichment using inertial microfluidics', *Lab on a Chip*, 11(5), p. 912. doi: 10.1039/c0lc00595a.

Hyun, J. chul *et al.* (2017) 'Improved pillar shape for deterministic lateral displacement separation method to maintain separation efficiency over a long period of time', *Separation and Purification Technology*. Elsevier B.V., 172, pp. 258–267. doi: 10.1016/j.seppur.2016.08.023.

Ibrahim, F. *et al.* (2015) 'The Application of Biomedical Engineering Techniques to the Diagnosis and Management of Tropical Diseases: A Review', *Sensors*, 15(3), pp. 6947–6995. doi: 10.3390/s150306947.

Inglis, D. W. *et al.* (2008) 'Microfluidic device for label-free measurement of platelet activation', *Lab on a Chip*, 8(6), p. 925. doi: 10.1039/b800721g.

Inglis, D. W. (2009) 'Efficient microfluidic particle separation arrays', *Applied Physics Letters*, 94(1), pp. 2007–2010. doi: 10.1063/1.3068750.

Irimajiri, A., Hanai, T. and Inouye, A. (1979) 'A dielectric theory of "multi-stratified shell" model with its application to a lymphoma cell', *Journal of Theoretical Biology*, 78(2), pp. 251–269. doi: 10.1016/0022-5193(79)90268-6.

Jauréguy, F. *et al.* (2007) 'Host and bacterial determinants of initial severity and outcome of Escherichia coli sepsis', *Clinical Microbiology and Infection*, 13(9), pp. 854–862. doi: 10.1111/j.1469-0691.2007.01775.x.

Jiang, J. *et al.* (2017) 'An integrated microfluidic device for rapid and high-sensitivity analysis of circulating tumor cells', *Scientific Reports*. Nature Publishing Group, 7(February), pp. 1–11. doi: 10.1038/srep42612.

Joensson, H. N., Uhlén, M. and Svahn, H. A. (2011) 'Droplet size based separation by deterministic lateral displacement—separating droplets by cell-induced shrinking', *Lab on a Chip*, 11(7), p. 1305. doi: 10.1039/c0lc00688b.

Johnson, K. W., Dooner, M. and Quesenberry, P. J. (2007) 'Fluorescence activated cell sorting: A window on the stem cell', *Current Pharmaceutical Biotechnology*, 8(3), pp. 133–139. doi: 10.2174/138920107780906487.

Kadekoppala, M. *et al.* (2000) 'Stable expression of a new chimeric fluorescent reporter in the human malaria parasite Plasmodium falciparum.', *Infection and immunity*, 68(4), pp. 2328–32. doi: 10.1128/IAI.68.4.2328-2332.2000.

Kapishnikov, S., Kantsler, V. and Steinberg, V. (2006) 'Continuous particle size separation and size sorting using ultrasound in a microchannel', *Journal of Statistical Mechanics: Theory and Experiment*, 2006(01), pp. P01012–P01012. doi: 10.1088/1742-5468/2006/01/P01012.

Karabacak, N. M. *et al.* (2014) 'Microfluidic, marker-free isolation of circulating tumor cells from blood samples.', *Nature protocols*. Nature Publishing Group, 9(3), pp. 694–710. doi: 10.1038/nprot.2014.044.

Katsumoto, Y. *et al.* (2008) 'Dielectric cytometry with three-dimensional cellular modeling', *Biophysical Journal*, 95(6), pp. 3043–3047. doi: 10.1529/biophysj.108.132019.

Kelly, B. and O'Neill, L. A. J. (2015) 'Metabolic reprogramming in macrophages and dendritic cells in innate immunity', *Cell Research*. Nature Publishing Group, 25(7), pp. 771–784. doi: 10.1038/cr.2015.68.

Kim, D. *et al.* (2010) 'Measurement of single-cell deformability using impedance analysis on microfluidic chip', *Japanese Journal of Applied Physics*, 49(12). doi: 10.1143/JJAP.49.127002.

Kim, Y. R. and Ornstein, L. (1983) 'Isovolumetric Sphering of Erythrocytes for More Accurate and Precise Cell Volume Measurement by Flow Cytometry'', *Solutions*, 3(6), pp. 419–427.

King, B. J. and Monis, P. T. (2007) 'Critical processes affecting Cryptosporidium oocyst survival in the environment', *Parasitology*, 134(3), pp. 309–323. doi: 10.1017/S0031182006001491.

Kirk, K. (2001) 'Membrane Transport in the Malaria-Infected Erythrocyte', *Physiol Rev*, 81(2), pp. 495–537.

Kirk, K. (2015) 'Ion Regulation in the Malaria Parasite', *Annual Review of Microbiology*, 69(1), pp. 341–359. doi: 10.1146/annurev-micro-091014-104506.

Kong, T. F. *et al.* (2015) 'Enhancing malaria diagnosis through microfluidic cell enrichment and magnetic resonance relaxometry detection', *Scientific Reports*. Nature Publishing Group, 5(January), pp. 1–12. doi: 10.1038/srep11425.

Kostrzynska, M. *et al.* (1999) 'Three sample preparation protocols for polymerase chain reaction based detection of Cryptosporidium parvum in environmental samples', *Journal of Microbiological Methods*, 35(1), pp. 65–71. doi: 10.1016/S0167-7012(98)00106-7.

Kuntaegowdanahalli, S. S. *et al.* (2009) 'Inertial microfluidics for continuous particle separation in spiral microchannels', *Lab on a Chip*, 9(20), p. 2973. doi: 10.1039/b908271a.

Küttel, C. *et al.* (2007) 'Label-free detection of Babesia bovis infected red blood cells using impedance spectroscopy on a microfabricated flow cytometer', *Acta Tropica*, 102(1), pp. 63–68. doi: 10.1016/j.actatropica.2007.03.002.

Lambros, C. and Vanderberg, J. P. (1979) 'Synchronization of Plasmodium Falciparum Erythrocytes Stages in Culture', *The Journal of Parasitology*, 65(3), pp. 418–420.

Lapizco-Encinas, B. H. *et al.* (2004a) 'Dielectrophoretic Concentration and Separation of Live and Dead Bacteria in an Array of Insulators', *Analytical Chemistry*, 76(6), pp. 1571–1579. doi: 10.1021/ac034804j.

Lapizco-Encinas, B. H. *et al.* (2004b) 'Insulator-based dielectrophoresis for the selective concentration and separation of live bacteria in water', *Electrophoresis*, 25, pp. 1695–1704. doi: 10.1002/elps.200405899.

Laurell, T., Petersson, F. and Nilsson, A. (2007) 'Chip integrated strategies for acoustic separation

and manipulation of cells and particles.', *Chemical Society reviews*, 36(3), pp. 492–506. doi: 10.1039/b601326k.

LeChevallier, M., Norton, W. and Lee, R. (1991) 'Occurrence of Giardia and Cryptosporidium spp. in surface water supplies', *Applied and Environmental Microbiology*, 57(9), pp. 2610–2616.

Leirião, P. *et al.* (2004) 'Survival of protozoan intracellular parasites in host cells', *EMBO Reports*, 5(12), pp. 1142–1147. doi: 10.1038/sj.embor.7400299.

Lenshof, A. and Laurell, T. (2011) 'Emerging Clinical Applications of Microchip-Based Acoustophoresis', *Journal of Laboratory Automation*. Elsevier Inc, 16(6), pp. 443–449. doi: 10.1016/j.jala.2011.07.004.

Lenshof, A. and Laurell, T. (2010) 'Continuous separation of cells and particles in microfluidic systems', *Chemical Society Reviews*, 39(3), p. 1203. doi: 10.1039/b915999c.

Lenshof, A., Magnusson, C. and Laurell, T. (2012) 'Acoustofluidics 8: Applications of acoustophoresis in continuous flow microsystems', *Lab on a Chip*, 12(7), p. 1210. doi: 10.1039/c2lc21256k.

Linder, V. (2007) 'Microfluidics at the crossroad with point-of-care diagnostics', *The Analyst*, 132(12), p. 1186. doi: 10.1039/b706347d.

Liu, C. and Hu, G. (2017) 'High-throughput particle manipulation based on hydrodynamic effects in microchannels', *Micromachines*, 8(3). doi: 10.3390/mi8030073.

Loutherback, K. *et al.* (2009) 'Deterministic microfluidic ratchet', *Physical Review Letters*, 102(4), pp. 1–4. doi: 10.1103/PhysRevLett.102.045301.

Loutherback, K. *et al.* (2010) 'Improved performance of deterministic lateral displacement arrays with triangular posts', *Microfluidics and Nanofluidics*, 9(6), pp. 1143–1149. doi: 10.1007/s10404-010-0635-y.

Loutherback, K. *et al.* (2012) 'Deterministic separation of cancer cells from blood at 10 mL/min.', *AIP advances*, 2(4), p. 42107. doi: 10.1063/1.4758131.

Lubbersen, Y. S., Boom, R. M. and Schutyser, M. a I. (2014) 'High throughput particle separation with a mirrored deterministic ratchet design', *Chemical Engineering and Processing: Process Intensification*. Elsevier B.V., 77, pp. 42–49. doi: 10.1016/j.cep.2014.01.007.

Lumsden, W. H. R. *et al.* (1979) 'Trypanosoma brucei: miniature-anion exchange centrifugation technique for detection of low parasitaemias: adaptation for field use', *T.Roy.Soc.Trop.Med.H.*, 73(3), pp. 312–317.

Lumsden, W. H. R., Kimber, C. D. and Strange, M. (1977) 'Trypanosoma brucei: detection of low parasitaemias in mice by a miniature anion-exchanger/centrifugation technique', *Transactions of the Royal Society of Tropical Medicine and Hygiene*. No longer published by Elsevier, 71(5), pp. 421–424. doi: 10.1016/0035-9203(77)90043-8.

Maier, A. G. *et al.* (2009) 'Malaria parasite proteins that remodel the host erythrocyte', *Nature reviews. Microbiology*, 7. doi: 10.1038/nrmicro2110.

Manz, A., Graber, N. and Widmer, H. M. (1990) 'Miniaturized Total Chemical Analysis Systems : a Novel Concept for Chemical Sensing', *Sensors and Actuators B: Chemical*, pp. 244–248.

Marczak, A. and Jóźwiak, Z. (2008) 'The interaction of DNR and glutaraldehyde with cell membrane proteins leads to morphological changes in erythrocytes', *Cancer Letters*, 260(1–2), pp. 118–126. doi: 10.1016/j.canlet.2007.10.027.

Mark, D. *et al.* (2010) 'From microfluidic application to nanofluidic phenomena issue', *Chemical Society reviews*, 39(3), pp. 1153–82. doi: 10.1039/b820557b.

Markx, G. H. *et al.* (1994) 'Dielectrophoretic characterization and separation of micro-organisms', *Microbiology*, 140, pp. 585–591.

Martinez, A. W. *et al.* (2007) 'Patterned paper as a platform for inexpensive, low-volume, portable bioassays', *Angewandte Chemie - International Edition*, 46(8), pp. 1318–1320. doi: 10.1002/anie.200603817.

Martinez, A. W., Phillips, S. T. and Whitesides, G. M. (2010) 'Diagnostics for the Developing World :

Microfluidic Paper-Based Analytical Devices', *Analytical chemistry*, 82(1), pp. 3–10. doi: 10.1021/ac9013989.

Masuda, S., Washizu, M. and Iwadare, M. (1987) 'Separation of Small Particles Suspended in Liquid by Nonuniform Traveling Field', *IEEE Transactions on Industry Applications*, IA-23(3), pp. 474–480. doi: 10.1109/TIA.1987.4504934.

Mauritz, J. M. A. *et al.* (2009) 'The homeostasis of Plasmodium falciparum-infected red blood cells.', *PLoS computational biology*, 5(4), p. e1000339. doi: 10.1371/journal.pcbi.1000339.

Mauritz, J. M. A. *et al.* (2011) 'X-ray microanalysis investigation of the changes in Na, K, and hemoglobin concentration in plasmodium falciparum-infected red blood cells', *Biophysical Journal*. Biophysical Society, 100(6), pp. 1438–1445. doi: 10.1016/j.bpj.2011.02.007.

Maxwell, J. C. (1881) *A treatise on electricity and magnetism*, *A treatise on electricity and magnetism*. Clarendon Press. doi: 10.1017/CBO9781107415324.004.

Mbengue, A., Yam, X. Y. and Braun-Breton, C. (2012) 'Human erythrocyte remodelling during Plasmodium falciparum malaria parasite growth and egress', *British Journal of Haematology*, 157(2), pp. 171–179. doi: 10.1111/j.1365-2141.2012.09044.x.

McGrath, J., Jimenez, M. and Bridle, H. (2014) 'Deterministic lateral displacement for particle separation: a review', *Lab Chip*. Royal Society of Chemistry, 14(21), pp. 4139–4158. doi: 10.1039/C4LC00939H.

McGrath, J. S. *et al.* (2017) 'Analysis of Parasitic Protozoa at the Single-cell Level using Microfluidic Impedance Cytometry', *Scientific Reports*, 7(1). doi: 10.1038/s41598-017-02715-y.

McMorrow, M. L., Aidoo, M. and Kachur, S. P. (2011) 'Malaria rapid diagnostic tests in elimination settings-can they find the last parasite?', *Clinical Microbiology and Infection*. European Society of Clinical Microbiology and Infectious Diseases, 17(11), pp. 1624–1631. doi: 10.1111/j.1469-0691.2011.03639.x.

Miller, L. H. *et al.* (2002) 'The pathogenic basis of malaria', *Nature*. Nature Publishing Group, 415, pp. 673–679. Available at: http://dx.doi.org/10.1038/415673a.

Miller, R. D. and Jones, T. B. (1993) 'Electro-orientation of ellipsoidal erythrocytes. Theory and experiment.', *Biophysical Journal*. Elsevier, 64(5), pp. 1588–1595. doi: 10.1016/S0006-3495(93)81529-7.

Moore, K. J. and Matlashewski, G. (1994) 'Intracellular infection by Leishmania donovani inhibits macrophage apoptosis', *The Journal of Immunology*, 152(6), pp. 2930–2937. Available at: http://www.ncbi.nlm.nih.gov/entrez/query.fcgi?cmd=Retrieve&db=PubMed&dopt=Citation&list_uids=8144893.

Morgan, H. *et al.* (1997) 'Large-area travelling-wave dielectrophoresis particle separator', *Journal of Micromechanics and Microengineering*, 7(2), pp. 65–70. doi: 10.1088/0960-1317/7/2/004.

Morgan, H. *et al.* (2007) 'Single cell dielectric spectroscopy', *Journal of Physics D: Applied Physics*, 40, pp. 61–70. doi: 10.1088/0022-3727/40/1/S10.

Morgan, H. and Green, N. G. (2002) *AC Electrokinetics: colloids and nanoparticles*. Baldock, Hertfordshire, UK: Research Studies Press Ltd.

Morton, K. J. *et al.* (2008) 'Crossing microfluidic streamlines to lyse, label and wash cells.', *Lab on a chip*, 8(9), pp. 1448–1453. doi: 10.1039/b805614e.

Mosadegh, B. *et al.* (2011) 'Next-generation integrated microfluidic circuits', *Lab on a Chip*, 11(17), p. 2813. doi: 10.1039/c1lc20387h.

Murray, H. W. *et al.* (2005) 'Advances in leishmaniasis', *Lancet*, 366(9496), pp. 1561–1577. doi: 10.1016/S0140-6736(05)67629-5.

Murray, P. J. and Wynn, T. A. (2012) 'Protective and pathogenic functions of macrophage subsets', *Nature Reviews Immunology*, 11(11), pp. 723–737. doi: 10.1038/nri3073.Protective.

Nam, J. *et al.* (2013) 'Magnetic separation of malaria-infected red blood cells in various developmental stages', *Analytical Chemistry*, 85(15), pp. 7316–7323. doi: 10.1021/ac4012057.

Nash, G. B. *et al.* (1989) 'Abnormalities in the Mechanical Properties of Red Blood Cells Caused by

Plasmodium Falciparum', *Blood*, 74(2), pp. 855–861.

Neitzke-Abreu, H. C. *et al.* (2013) 'Detection of DNA from Leishmania (Viannia): Accuracy of Polymerase Chain Reaction for the Diagnosis of Cutaneous Leishmaniasis', *PLoS ONE*, 8(4), pp. 1–7. doi: 10.1371/journal.pone.0062473.

Nguyen, N.-T. and Wereley, S. T. (2006) *Fundamentals and Applications of Microfluidics*. Second Edi. Boston: Artech House.

Nichols, R. A. B. *et al.* (2010) 'Identification of Cryptosporidium species and genotypes in Scottish raw and drinking waters during a one-year monitoring period', *Applied and Environmental Microbiology*, 76(17), pp. 5977–5986. doi: 10.1128/AEM.00915-10.

Nikolic-Jaric, M. *et al.* (2009) 'Microwave frequency sensor for detection of biological cells in microfluidic channels', *Biomicrofluidics*, 3(3). doi: 10.1063/1.3187149.

Okhuysen, P. C. *et al.* (1999) 'Virulence of three distinct Cryptosporidium parvum isolates for healthy adults.', *The Journal of infectious diseases*, 180(4), pp. 1275–81. doi: 10.1086/315033.

Ostyn, B. *et al.* (2011) 'Incidence of symptomatic and asymptomatic Leishmania donovani infections in High-Endemic foci in India and Nepal: A prospective study', *PLoS Neglected Tropical Diseases*, 5(10), pp. 1–7. doi: 10.1371/journal.pntd.0001284.

Otto Warburg, B., Wind, F. and Negelein, N. (1927) 'The Metabolism of Tumors in the Body', *The Journal of General Physiology*, 309(2), pp. 397–519. doi: 10.1097/00000441-193107000-00022.

Pace, D. (2014) 'Leishmaniasis', *Journal of Infection*, 69(S1), pp. S10–S18. doi: 10.1016/j.jinf.2014.07.016.

Paul, A. *et al.* (2013) 'The bystander effect in optically trapped red blood cells due to plasmodium falciparum infection', *Transactions of the Royal Society of Tropical Medicine and Hygiene*, 107(4), pp. 220–223. doi: 10.1093/trstmh/trt010.

Pauly, H. and Schwan, H. P. (1966) 'Dielectric Properties and Ion Mobility in Erythrocytes', *Biophysical Journal*. Elsevier, 6(5), pp. 621–639. doi: 10.1016/S0006-3495(66)86682-1.

Petersson, F. *et al.* (2007) 'Free flow acoustophoresis: microfluidic-based mode of particle and cell separation.', *Analytical chemistry*, 79(14), pp. 5117–23. doi: 10.1021/ac070444e.

Pethig, R. (1979) *Dielectric and Electric Properties of Biological Materials*. John Wiley & Sons.

Pethig, R. *et al.* (2010) 'Dielectrophoresis: A review of applications for stem cell research', *Journal of Biomedicine and Biotechnology*, 2010. doi: 10.1155/2010/182581.

Pethig, R. (2010) 'Dielectrophoresis: Status of the theory, technology, and applications', *Biomicrofluidics*, 4(2), pp. 1–35. doi: 10.1063/1.3456626.

Pettersen, J. S. *et al.* (2011) 'Tumor-associated macrophages in the cutaneous SCC microenvironment are heterogeneously activated', *Journal of Investigative Dermatology*, 131(6), pp. 1322–1330. doi: 10.1038/jid.2011.9.

Qu, B. Y. *et al.* (2008) 'A glass microfluidic chip for continuous blood cell sorting by a magnetic gradient without labeling', *Analytical and Bioanalytical Chemistry*, 392(7–8), pp. 1317–1324. doi: 10.1007/s00216-008-2382-4.

Qualls, J. E. *et al.* (2012) 'Sustained generation of nitric oxide and control of mycobacterial infection requires argininosuccinate synthase 1', *Cell Host and Microbe*. Elsevier Inc., 12(3), pp. 313–323. doi: 10.1016/j.chom.2012.07.012.

Quek, R., Le, D. V. and Chiam, K. H. (2011) 'Separation of deformable particles in deterministic lateral displacement devices', *Physical Review E - Statistical, Nonlinear, and Soft Matter Physics*, 83(5), pp. 1–7. doi: 10.1103/PhysRevE.83.056301.

Raicu, V. and Feldman, Y. (2015) *Dielectric Relaxation in Biological Systems*. Oxford, Oxfordshire, UK: Oxford University Press.

Ranjan, S. *et al.* (2014) 'DLD pillar shape design for efficient separation of spherical and non-spherical bioparticles', *Lab Chip*. Royal Society of Chemistry, 14(21), pp. 4250–4262. doi: 10.1039/C4LC00578C.

Ribaut, C. *et al.* (2008) 'Concentration and purification by magnetic separation of the erythrocytic stages of all human Plasmodium species', *Malaria Journal*, 5, pp. 1–5. doi: 10.1186/1475-2875-7-45.

Rodriguez-Trujillo, R. *et al.* (2007) 'Low cost micro-Coulter counter with hydrodynamic focusing', *Microfluidics and Nanofluidics*, 3(2), pp. 171–176. doi: 10.1007/s10404-006-0113-8.

Rosenblatt, J. E. (2009) 'Laboratory Diagnosis of Infections Due to Blood and Tissue Parasites', *Clinical Infectious Diseases*, 49(7), pp. 1103–1108. doi: 10.1086/605574.

Russom, A. *et al.* (2009) 'Differential inertial focusing of particles in curved low-aspect-ratio microchannels', *New Journal of Physics*, 11(075025), pp. 1–11. doi: 10.1088/1367-2630/11/7/075025.Differential.

Sabatini, D. D., Bensch, K. and Barrnett, R. J. (1963) 'Cytochemistry and electron microscopy. The preservation of cellular ultrastructure and enzymatic activity by aldehyde fixation.', *The Journal of cell biology*, 17, pp. 19–58. doi: 10.1083/jcb.17.1.19.

Sanchis, A. *et al.* (2007) 'Dielectric characterization of bacterial cells using dielectrophoresis.', *Bioelectromagnetics*, 28(5), pp. 393–401. doi: 10.1002/bem.20317.

Schwan, H. P. (1957) *Advances in Biological and Medical Physics*. 5th edn. Edited by C. A. Tobias and J. H. Lawrence. New York: Academic Press Inc.

Scottish Water (2013) 'Annual Water Quality Report 2013', p. 30.

Segré, G. and Silberberg, A. (1961) 'Radial particle displacements in poiseuille flow of suspensions', *Nature*, 189(4760), pp. 209–210. doi: 10.1038/189209a0.

Shafiee, H. *et al.* (2010) 'Selective isolation of live/dead cells using contactless dielectrophoresis (cDEP)', *Lab on a Chip*, 10(4), p. 438. doi: 10.1039/b920590j.

Shapiro, H. M. (2003) *Practical Flow Cytometry*. Fourth Edi. Hoboken, New JErsey: John Wiley & Sons, Inc.

Sheetz, M. P. and Singer, S. J. (1976) 'Equilibrium and kinetic effects of drugs on the shapes of human erythrocytes', *The Journal of cell biology*, 70, pp. 247–251. doi: 10.1177/030857591203600211.

Shelby, J. P. *et al.* (2003) 'A microfluidic model for single-cell capillary obstruction by Plasmodium falciparum- infected erythrocytes', *Proceedings of the National Academy of Sciences of the United States of America*, 100(25), pp. 14618–14622.

Sia, S. K. and Kricka, L. J. (2008) 'Microfluidics and point-of-care testing', *Lab on a Chip*, 8(12), p. 1982. doi: 10.1039/b817915h.

Sibley, L. D. (2011) 'Invasion and Intracellular Survival by Protozoan Parasites', *Immunological Reviews*, 240(1), pp. 72–91. doi: 10.1002/nbm.3066.Non-invasive.

Sica, A. and Mantovani, A. (2012) 'Macrophage plasticity and polarization: in vivo veritas', *Journal of Clinical Investigation*, 122(3), pp. 787–795. doi: 10.1172/JCI59643DS1.

Singh, B. *et al.* (1999) 'A genus-and species-specific nested polymerase chain reaction malaria detection assay for epidemiologic studies', *The American journal of tropical medicine and hygiene*, 60(4), pp. 687–692. doi: 10.4269/ajtmh.1999.60.687.

Song, H. *et al.* (2013) 'A microfluidic impedance flow cytometer for identification of differentiation state of stem cells.', *Lab on a chip*, 13(12), pp. 2300–10. doi: 10.1039/c3lc41321g.

Sonohara, R. *et al.* (1995) 'Difference in surface properties between Escherichia coli and Staphylococcus aureus as revealed by electrophoretic mobility measurements', *Biophysical Chemistry*, 55(3), pp. 273–277. doi: 10.1016/0301-4622(95)00004-H.

Sorger, P. K. (2008) 'Microfluidics closes in on point-of-care assays', *Nature Biotechnology*, 26(12), pp. 1345–1346. doi: 10.1038/nbt1208-1345.

Spencer, D. *et al.* (2016) 'High accuracy particle analysis using sheathless microfluidic impedance cytometry', *Lab Chip*. Royal Society of Chemistry, 16(13), pp. 2467–2473. doi: 10.1039/C6LC00339G.

Spencer, D., Elliott, G. and Morgan, H. (2014) 'A sheath-less combined optical and impedance

micro-cytometer.', *Lab on a chip*, 14(16), pp. 3064–3073. doi: 10.1039/c4lc00224e.

Spencer, D., Hollis, V. and Morgan, H. (2014) 'Microfluidic impedance cytometry of tumour cells in blood', *Biomicrofluidics*, 8(6), p. 064124. doi: 10.1063/1.4904405.

Spencer, D. and Morgan, H. (2011) 'Positional dependence of particles in microfludic impedance cytometry.', *Lab on a chip*, 11(7), pp. 1234–1239. doi: 10.1039/c1lc20016j.

Squier, C. A., Hart, J. S. and Churchland, A. (1976) 'Changes in red blood cell volume on fixation in glutaraldehyde solutions', *Histochemistry*, 48(1), pp. 7–16. doi: 10.1007/BF00489711.

Squires, T. M. and Quake, S. R. (2005) 'Microfluidics: Fluid physics at the nanoliter.pdf', *Reviews of Modern Physics*, 77(July).

Srivastava, P. *et al.* (2011) 'Diagnosis of visceral leishmaniasis', *Transactions of the Royal Society of Tropical Medicine and Hygiene*. Royal Society of Tropical Medicine and Hygiene, 105(1), pp. 1–6. doi: 10.1016/j.trstmh.2010.09.006.

Staines, H. M., Ellory, J. C. and Kirk, K. (2001) 'Perturbation of the pump-leak balance for Na(+) and K(+) in malaria-infected erythrocytes.', *American journal of physiology. Cell physiology*, 280(6), pp. 1576–1587.

Su, Y.-H. *et al.* (2014) 'Quantitative dielectrophoretic tracking for characterization and separation of persistent subpopulations of Cryptosporidium parvum.', *The Analyst*, 139(1), pp. 66–73. doi: 10.1039/c3an01810e.

Sun, T., Bernabini, C. and Morgan, H. (2010) 'Single-colloidal particle impedance spectroscopy: Complete equivalent circuit analysis of polyelectrolyte microcapsules', *Langmuir*, 26(6), pp. 3821–3828. doi: 10.1021/la903609u.

Sundar, S. and Rai, M. (2002) 'Laboratory Diagnosis of Visceral Leishmaniasis Laboratory Diagnosis of Visceral Leishmaniasis', *Clinical and Diagnostic Laboratory Immunology*, 9(5), pp. 951–958. doi: 10.1128/CDLI.9.5.951.

Suresh, S. *et al.* (2005) 'Connections between single-cell biomechanics and human disease states: Gastrointestinal cancer and malaria', *Acta Biomaterialia*, 1, pp. 15–30. doi: 10.1016/j.actbio.2015.07.015.

Suresh, S. (2010) 'Biomechanics and biohysics of cancer cells', *Materials Science*, 3(4), pp. 413–438. doi: 10.1016/j.actbio.2007.04.002.Biomechanics.

Tabeling, P. and Chen, S. (2005) *Introduction to Microfluidics*. Oxford, Oxfordshire, UK: OUP.

Takashima, S., Asami, K. and Takahashi, Y. (1988) 'Frequency domain studies of impedance characteristics of biological cells using micropipet technique. I. Erythrocyte', *Biophysical Journal*, 54(6), pp. 995–1000. doi: 10.1016/S0006-3495(88)83037-6.

Tay, A. *et al.* (2016) 'Advances in microfluidics in combating infectious diseases', *Biotechnology Advances*, 34(4), pp. 404–421. doi: 10.1016/j.biotechadv.2016.02.002.

Terry, S. C., Jerman, J. H. and Angell, J. B. (1979) 'A gas chromatographic air analyzer fabricated on a silicon wafer', *IEEE Transactions on Electron Devices*, 26(12). doi: 10.1109/T-ED.1979.19791.

The malERA Consultative Group on Diagnoses (2011) 'A research agenda for malaria eradication: Diagnoses and diagnostics', *PLoS Medicine*, 8(1). doi: 10.1371/journal.pmed.1000396.

Thiel, A., Scheffold, A. and Radbruch, A. (1998) 'Immunomagnetic cell sorting-pushing the limits', *Immunotechnology*, 4(2), pp. 89–96. doi: 10.1016/S1380-2933(98)00010-4.

Toepfner, N. *et al.* (2018) 'Detection of human disease conditions by single-cell morpho-rheological phenotyping of blood', *eLife*, 7, p. e29213. doi: 10.7554/eLife.29213.

Torimura, M. *et al.* (1999) 'Surface characterization and on-line activity measurements of microorganisms by capillary zone electrophoresis', *Journal of Chromatography B: Biomedical Applications*, 721(1), pp. 31–37. doi: 10.1016/S0378-4347(98)00490-3.

Tottori, N. and Nisisako, T. (2018) 'High-throughput production of satellite-free droplets through a parallelized microfluidic deterministic lateral displacement device', *Sensors and Actuators, B: Chemical*. Elsevier B.V., 260, pp. 918–926. doi: 10.1016/j.snb.2018.01.112.

Tracey, K. J. *et al.* (1987) 'Anti-cachectin/TNF monoclonal antibodies prevent septic shock during lethal bacteraemia', *Nature*, 330(6149), pp. 662–664. doi: 10.1038/330662a0.

Trager, W. and Jensen, J. B. (1976) 'Human Malaria Parasites in Continuous Culture', *Science*, 193(4254), pp. 673–675.

Tran, P. N. *et al.* (2016) 'Changes in lipid composition during sexual development of the malaria parasite Plasmodium falciparum', *Malaria Journal*. BioMed Central, 15(1), p. 73. doi: 10.1186/s12936-016-1130-z.

Tran, T. S. H. *et al.* (2017) 'Open channel deterministic lateral displacement for particle and cell sorting', *Lab Chip*. doi: 10.1039/C7LC00707H.

Trang, D. T. X. *et al.* (2004) 'One-step concentration of malarial parasite-infected red blood cells and removal of contaminating white blood cells', *Malaria Journal*, 3, pp. 1–7. doi: 10.1186/1475-2875-3-1.

Turchetti, V. *et al.* (1997) 'Variations of erythrocyte morphology in different pathologies.', *Clinical hemorheology and microcirculation*, 17(3), pp. 209–15. Available at: http://www.ncbi.nlm.nih.gov/pubmed/9356785.

United Kingdom Environment Agency (2010) *Methods for the Examination of Waters and Associated Materials*.

United States Environmental Protection Agency (2012) *Method 1623.1: Cryptosporidium and Giardia in Water by Filtration/IMS/FA*.

Unni, H. N. *et al.* (2012) 'Characterization and separation of Cryptosporidium and Giardia cells using on-chip dielectrophoresis', *Biomicrofluidics*, 6(012805), pp. 1–14. doi: 10.1063/1.3671065.

Vajpayee, N., Graham, S. S. and Bem, S. (2011) 'Basic Examination of Blood and Bone Marrow', in *Henry's Clinical Diagnosis and Managment by Laboratory Methods*. 22nd edn. Philadelphia, PA: Elsevier/Saunders.

Vial, H. J. and Ancelin, M. L. (1998) 'Malaria Lipids', in Sherman, I. W. (ed.) *Malaria: Parasite Biology, Pathogenesis, and Protection*. Washington DC: American Society of Microbiology, pp. 159–175.

Villalta, S. A. *et al.* (2009) 'Shifts in macrophage phenotypes and macrophage competition for arginine metabolism affect the severity of muscle pathology in muscular dystrophy', *Human Molecular Genetics*, 18(3), pp. 482–496. doi: 10.1093/hmg/ddn376.

Vogel, D. Y. S. *et al.* (2013) 'Macrophages in inflammatory multiple sclerosis lesions have an intermediate activation status', *Journal of Neuroinflammation*, 10(35), pp. 1–12. doi: 10.1186/1742-2094-10-35.

Voldman, J. (2006) 'Electrical Forces for Microscale Cell Manipulation', *Annual Review of Biomedical Engineering*, 8(1), pp. 425–454. doi: 10.1146/annurev.bioeng.8.061505.095739.

Wang, X. B. *et al.* (1994) 'Changes in Friend murine erythroleukaemia cell membranes during induced differentiation determined by electrorotation', *BBA - Biomembranes*, 1193(2), pp. 330–344. doi: 10.1016/0005-2736(94)90170-8.

Weatherall, D. J. *et al.* (2002) 'Malaria and the red cell.', *Hematology / the Education Program of the American Society of Hematology. American Society of Hematology. Education Program*, pp. 35–57. doi: 10.1182/asheducation-2002.1.35.

Webster, P. and Griffithst, G. (1994) 'A novel method for mean cell volume estimation', 174(March 1993), pp. 85–92.

Weinman, D. (1972) 'Trypanosom cyclops N. SP.: A Pigmented Trypanosome From the Malaysian Primates Macaca Nemestrina and M. Ira', *Transactions of the Royal Society of Tropical Medicine and Hygiene*, 66(4), pp. 628–633. doi: 10.1016/j.trstmh.2009.07.024.

Wongsrichanalai, C. *et al.* (2007) 'A review of malaria diagnostic tools: Microscopy and rapid diagnostic test (RDT)', *American Journal of Tropical Medicine and Hygiene*, 77(6), pp. 119–127. doi: 10.3126/ajms.v1i2.2965.

World Health Organization (2016) 'World malaria report 2016', pp. 17–18. doi: 10.4135/9781452276151.n221.

World Health Organization (2017a) *Leishmaniasis*. Available at: http://who.int/leishmaniasis/en/ (Accessed: 1 December 2017).

World Health Organization (2017b) *World Health Statistics 2017*.

World Health Organization (2017c) *World Malaria Report 2017*. doi: http://www.who.int/malaria/publications/world-malaria-report-2017/report/en/.

Wu, W.-T. *et al.* (2016) 'Design of microfluidic channels for magnetic separation of malaria-infected red blood cells', *Microfluidics and Nanofluidics*, 20(2), pp. 444–454. doi: 10.1158/1940-6207.CAPR-14-0359.Nrf2-dependent.

Wunsch, B. H. *et al.* (2016) 'Nanoscale lateral displacement arrays for the separation of exosomes and colloids down to 20nm', *Nature Nanotechnology*. Nature Publishing Group, 11(11), pp. 936–940. doi: 10.1038/nnano.2016.134.

Wyatt Shields IV, C., Reyes, C. D. and López, G. P. (2015) 'Microfluidic cell sorting: a review of the advances in the separation of cells from debulking to rare cell isolation', *Lab Chip*. Royal Society of Chemistry, 15, pp. 1230–1249. doi: 10.1039/C4LC01246A.

Xavier, M. *et al.* (2017) 'Size and dielectric properties of skeletal stem cells change critically after enrichment and expansion from human bone marrow: Consequences for microfluidic cell sorting', *Journal of the Royal Society Interface*, 14(133), p. 20170233. doi: 10.1098/rsif.2017.0233.

Xia, Y. and Whitesides, G. M. (1998) 'Soft Lithography', *Annual Review of Materials Science*. Annual Reviews 4139 El Camino Way, PO Box 10139, Palo Alto, CA 94303-0139, USA, 28(1), pp. 153–184. doi: 10.1146/annurev.matsci.28.1.153.

Yager, P. *et al.* (2006) 'Microfluidic diagnostic technologies for global public health', *Nature*, 442(7101), pp. 412–418. doi: 10.1038/nature05064.

Yan, S. *et al.* (2017) 'Hybrid microfluidics combined with active and passive approaches for continuous cell separation', *Electrophoresis*, 38(2), pp. 238–249. doi: 10.1002/elps.201600386.

Yang, J. *et al.* (1999) 'Dielectric Properties of Human Leukocyte Subpopulations Determined by Electrorotation as a Cell Separation Criterion', *Biophysical Journal*, 76(6), pp. 3307–3314. doi: 10.1016/S0006-3495(99)77483-7.

Zborowski, M. and Chamers, J. J. (2011) 'Rare Cell Separation and Analysis by Magnetic Sorting', *Analytical Chemistry*, 83(21), pp. 8050–8056. doi: 10.1021/ac200550d.

Zeming, K. K. *et al.* (2018) 'Fluorescent label-free quantitative detection of nano-sized bioparticles using a pillar array', *Nature Communications*, 9(1). doi: 10.1038/s41467-018-03596-z.

Zeming, K. K., Ranjan, S. and Zhang, Y. (2013) 'Rotational separation of non-spherical bioparticles using I-shaped pillar arrays in a microfluidic device.', *Nature communications*. Nature Publishing Group, 4, p. 1625. doi: 10.1038/ncomms2653.

Zimmerman, P. A. *et al.* (2006) 'Diagnosis of malaria by magnetic deposition microscopy', *American Journal of Tropical Medicine and Hygiene*, 74(4), pp. 568–572.

**"The mystery of life isn't a problem to solve, but a reality to experience."**

*Frank Herbert, Dune*